

Direct syngas-to-fuel: integration of Fischer-Tropsch synthesis and hydrocracking in micro-structured reactors

zur Erlangung des akademischen Grades eines
DOKTORS DER INGENIEURWISSENSCHAFTEN (Dr.-Ing.)

der KIT-Fakultät für Chemieingenieurwesen und Verfahrenstechnik des
Karlsruher Instituts für Technologie (KIT)

genehmigte
DISSERTATION

von

M. Sc. Chenghao Sun
aus Shandong, VR China

Referent: Prof. Dr.-Ing. Roland Dittmeyer

Korreferent: Prof. Dr.-Ing. Thomas Turek

Tag der mündlichen Prüfung: 15. December 2017

Erklärung

Ich versichere, dass die hier vorliegende Dissertation mit dem eingereichten und genehmigten Prüfungsexemplar der Doktorarbeit übereinstimmt.

Chenghao Sun

Ort und Datum

Acknowledgements

First of all, I would like to express my deep gratitude to Prof. Dr.-Ing. Roland Dittmeyer for the opportunity to accomplish my doctoral thesis with this interesting and challenging topic under his supervision. His support, understanding and confidence in me have encouraged me during the entire doctoral study. In addition, I would especially thank my group leader Prof. Dr.-Ing. Peter Pfeifer for his valuable instruction and advices. His rich knowledge and experience has greatly helped the successful implementation of my doctoral research. Moreover, I would like to thank Prof. Dr.-Ing. Thomas Turek from Technische Universität Clausthal for his valuable comments and suggestions regarding my work. I would like to thank Prof. Dr.-Ing. Steffen Grohmann, and Prof. Dr. Matthias Franzreb for undertaking to be examiners.

I would like to thank Dr.-Ing. Paolo Piermartini for his support at the first stage of my doctoral study. I would thank Dipl.-Ing. Heinz Lambach, Mr. Matthias Schöffler, Mrs. Sabine Schweikert-Joß, Dipl.-Ing. Robin Dürschnabel and Mrs. Cornelia Schorle for their help with the design, fabrication and maintenance of the reactors, and Dipl.-Ing. Uta Gerhards and Mr. Florian Messerschmidt for their help with SEM measurement. I would thank Dr.-Ing. Joachim Binder and Dr.-Ing. Christian Kohler from Institute for Applied Materials, Karlsruhe Institute of Technology for their help with screen-printing. I would also thank my students Mr. Zhuohui Luo, Ms. Tiantian Zhan and Ms. Ting Xu for their contribution to this work. And many thanks to all colleagues for the support, encouragement and shared time during my doctoral study.

Moreover, I would like to thank the China Scholarship Council (CSC) for providing the financial support.

Finally, I would like to express my sincere thanks to my family, in particular my parents, grandparents, sister and wife, for their unconditional and eternal love throughout my life.

Karlsruhe, December 2017

Chenghao Sun

Abstract

To meet the increasing energy demand and to reduce the greenhouse gas emissions, energy system decarbonization and more efficient energy utilization are required for the energy transition towards a low-carbon future. An increasing share of renewables (solar energy, wind energy, biomass, etc.) has been widely approved. Renewables are mainly used for power generation. However, the highly distributed and unsteady properties of renewables lead to the emerging need for energy storage technologies and grid expansion to secure power supply and make use of the full potential of the renewables. The power-to-fuel process has been proposed where surplus electricity would be used to produce H₂ via electrolysis and non-fossil energy based CO₂ could be used as carbon source to realize a closed carbon cycle. In the power-to-fuel process, Fischer-Tropsch synthesis (FTS) is adopted to convert syngas into value-added clean fuels. To improve the yield of the liquid fuels, hydrocracking (HC) is required to convert heavy hydrocarbons from FTS into middle distillates. Considering the typical power range and the isolated location of renewables, tailored small-scale plants with simplified and intensified processes are of great importance for power-to-fuel applications in this context. Modular micro-structured reactors with high space time yield and dynamic operability would be a promising solution for compact power-to-fuel applications.

Process simplification by integrating FTS with HC in micro-structured reactors was targeted in this dissertation with a view to the feasibility of one-stage syngas-to-fuel conversion for decentralized small-scale power-to-fuel plants. The integration was achieved by arranging FTS and HC catalysts in different configurations. Both powder and wall-coated catalysts were adopted. For integration with powder catalysts, sequential and hybrid configurations were studied. For integration with wall-coated catalysts, sequential, face-to-face, dual-layer and hybrid configurations were investigated. Both experimental studies and computational analysis were carried out to understand the implications of the integrated process. The performance of different integration configurations and catalyst types was compared regarding selectivity and productivity of liquid fuels (C₅-C₂₀), and the influence of the operating conditions was investigated.

For the targeted process simplification, micro packed-bed (for powder catalyst) and microchannel (for wall-coated catalyst) reactors were designed. An experimental setup able to accommodate the different reactor types was built. Isothermal operation was obtained in the micro-structured reactors due to the enhanced heat transfer. Home-made FTS and HC

catalysts were developed to meet the requirements of both catalyst types. For powder type, the catalysts were pelletized and crushed to 50-100 μm particles. Screen-printing was adopted and optimized to prepare catalyst layers in the microchannel. Catalyst layers with uniform thickness (20-50 μm) and reasonable mechanical stability were obtained. Different integration configurations were achieved by easily changing the assembly of the catalyst-coated foils.

The feasibility of the integrated FTS-HC process was verified in a two-stage reactor system with powder catalysts. Different from the conventional HC process, all components from FTS, including H_2 , CO, H_2O and light hydrocarbons ($\text{C}_1\text{-C}_{20}$), are passed over the HC catalyst in the integrated system, among which CO and H_2O have proved to be negative for HC. The influence of the FTS performance (concentration of residual H_2 and CO as well as amount of heavy hydrocarbons) on HC was studied, and the overall performance of the integrated process was analyzed regarding the liquid fuel ($\text{C}_5\text{-C}_{20}$) selectivity and productivity. Sufficient cracking of the C_{21+} fraction was achieved under FTS conditions, and primary cracking proved to be dominant. Higher temperature has a positive effect on HC, but too high temperature would turn out to increase the $\text{C}_1\text{-C}_4$ selectivity, and a maximum of 70 wt.% $\text{C}_5\text{-C}_{20}$ was obtained. Slightly negative effects on HC were observed at higher H_2 partial pressure. An increase of the CO partial pressure obviously inhibits the cracking performance. The wax flow rate study revealed a quite selective cracking of the FTS wax.

One-stage sequential and hybrid integration with powder catalysts were compared in an annular micro packed-bed reactor. The influence of the operating conditions was investigated targeting liquid fuel synthesis ($\text{C}_5\text{-C}_{20}$). It was proved that FTS plays the determining role in the integrated process and HC exhibits a promoting function. Good performance was obtained in both the sequential and the hybrid system. With an increase of temperature, the liquid fuel selectivity reaches a plateau value of around 70% at 230-250 $^\circ\text{C}$, depending on the integration pattern and the syngas space velocity. H_2/CO ratio and pressure only have limited influence on the fuel selectivity. FTS and HC were enhanced in the hybrid configuration. Catalyst stability in both configurations was analyzed, and a reasonable and comparable long-term stability was obtained.

Due to condensation of long-chain hydrocarbons, a liquid phase would be formed in the catalyst pores, as well as in the catalyst bed. Accumulation of liquid hydrocarbons in FTS catalyst pores was studied using a pore filling model, where the accumulation of heavy hydrocarbons is given by the interplay of formation in the pore and evaporation out of the pore. It was found that for the 100 μm catalyst particles even at the reactor inlet, i.e. with

extremely low liquid fraction in the surrounding fluid, complete pore filling would occur within several hours. Hence, complete liquid filling was assumed for both FTS and HC catalysts over the entire reactor length.

Computational analysis was applied to aid the study of the integrated FTS-HC process. The reaction kinetics of FTS and HC were regressed based on the experimental data. The influence of the liquid filling of the catalyst particles was studied using a heterogeneous model solving the reaction-diffusion equations. Despite liquid filling, limited influence of internal diffusion was observed on both FTS and HC owing to the small particle size. Deviation between experimental data and simulated results was noticed for both FTS and HC when the liquid fraction rose to relatively high values. A simplified model was created to investigate the experimentally observed FTS and HC performance in presence of larger amounts of liquid. It is assumed that part of the catalyst bed would be blocked if the liquid fraction exceeds a threshold. The liquid blocking would cause enlarged diffusion resistance or even inaccessible regions in the catalyst bed, particularly in micro-structured reactors with broad flat slits such as the annular geometry of this study. Significant mass transport limitation is found for FTS in the assumed liquid-filled spots. Hydrocracking exhibits limited response to internal diffusion limitation. Good agreement with experimental data was obtained by assuming inaccessible local regions in the packed bed. Identical cross section-averaged effectiveness factors of 0.6-0.7 were obtained for the liquid-filled sections in both FTS and HC.

Compared to the micro packed-bed reactor with powder catalysts, the microchannel reactor with wall-coated catalysts maintains even better heat transfer and eliminates liquid blocking. The FTS performance for 20 and 40 μm thick catalyst layers was evaluated. Similar CO conversion and hydrocarbon selectivity were obtained for both cases, which indicates that the layer thickness, within the studied range, has little influence on the FTS performance. Used wall-coated FTS catalyst foils were cut and characterized. Complete filling of liquid hydrocarbons inside the catalyst layer was observed. According to the simulation using a heterogeneous model solving the reaction-diffusion equations in the cylindrical catalyst layer, the limited influence of the layer thickness was confirmed. For the FTS with powder catalysts in the micro packed-bed reactor, positive effects of CO conversion on the chain growth probability were obtained, which could be attributed to competitive adsorption of water and olefins. For the FTS with wall-coated catalysts in the microchannel reactor, steady C_{5+} selectivity and increasing CH_4 selectivity were observed with increasing CO conversion. Compared to the small voids in the packed-bed, the large free space in the microchannel

suggests reduced capillary condensation effects, which would lead to a lower liquid phase fraction and hence to reduced water and olefin concentration compared to the packed-bed case. Accordingly, it is therefore assumed that the adsorption of water and olefins would be suppressed in the microchannel reactor.

Process integration was also analyzed with wall-coated catalysts in the microchannel reactor. Significant improvement of the liquid fuel selectivity was obtained. The performance of different configurations was compared at 30 and 20 bar, respectively. Identical CO conversion as for the FTS reference was observed for the sequential integration. At 30 bar, increasing CO conversion and HC efficiency were obtained from face-to-face over dual-layer to hybrid integration. The fuel selectivity remained constant at 70% over 225-260 °C for the parallel FTS-HC integration (face-to-face, dual-layer and hybrid), but the quality of the produced liquid fuels would be different. Compared to the integration with powder catalysts in the packed-bed, a lower temperature is required to reach the maximum fuel selectivity. At 20 bar, improved HC efficiency, but reduced CO conversion, were observed from face-to-face over dual-layer to hybrid integration. Almost all C₂₁₊ hydrocarbons were eliminated. The catalyst stability was analyzed in all configurations, and a reasonable and comparable long-term stability was obtained. A microchannel reactor with separate heating of two adjacent catalyst-coated plates enabled flexible adjustment of the FTS and HC activity. Independent temperatures were applied for FTS and HC in sequential and face-to-face integration using circulating thermal oil and electric heating cartridges, respectively. Optimization of selectivity, productivity and composition of the liquid fuels was achieved by individually changing FTS or HC temperatures.

Both FTS and HC were affected in the integration with parallel FTS and HC. It is assumed that local HC of FTS hydrocarbons would change the composition (total molar amount, molar fraction, relative ratio, etc.), which would influence both reactions. A simplified heterogeneous model for the hybrid configuration was created to investigate the influence of the changed syngas concentration and H₂/CO ratio on the FTS performance. Effective cracking of heavy hydrocarbons was observed in the hybrid integration, which consequently leads to a slower increase of the liquid fraction. The changed syngas concentration and H₂/CO ratio caused by local cracking of hydrocarbons in the parallel FTS-HC integration system proved to have only limited influence on CO conversion. Adsorption of olefin and water was assumed to be responsible for the experimentally observed results, which differed from the model predictions.

The FTS-HC integration with both powder and wall-coated catalysts exhibits a significant improvement of the C₅-C₂₀ selectivity. Reasonable feasibility was achieved for the one-stage hydrocarbon upgrading. The parallel FTS-HC integration provides the possibility to further increase the yield of liquid fuels.

Zusammenfassung

Um dem stetig steigenden Energiebedarf unter Berücksichtigung der Reduktion von Treibhausgasen zu begegnen bedarf es einer effizienteren Energienutzung und der dekarbonisierung des Energiesektors. Biomasse, Solar- und Windkraft wird vielerorts bereits zur Stromerzeugung genutzt und weiter ausgebaut. Die Herausforderung beim zunehmenden Umstieg auf diese Energiequellen stellen deren dezentrales und zeitlich fluktuierendes Auftreten dar. Um in absehbarer Zeit Abhilfe zu schaffen, müssen Energiespeichertechnologien verbessert und Energienetze ausgebaut werden, sodass eine sichere Versorgung gewährleistet ist und das Potential der Erneuerbaren voll ausgeschöpft werden kann. In einem „Power-to-Fuel“-Prozess kann überschüssige elektrische Energie genutzt werden, um Wasserstoff (H_2) mittels Elektrolyse zu gewinnen und mit aktiviertem Kohlenstoffdioxid (CO_2) als Kohlenstoffquelle innerhalb eines geschlossenen Kohlenstoffkreislaufs Kraftstoffe herzustellen. Hierbei spielt die Fischer-Tropsch-Synthese (FTS) eine maßgebliche Rolle, um Synthesegas (CO/H_2) zu hochwertigen, sauberen Kraftstoffen zu konvertieren. Um hierbei die Ausbeute an flüssigen Produkten zu erhöhen, wird eine hydrierende Spaltung (sog. Hydrocracking, HC) benötigt, bei welcher die langkettige Produktfraktion der FTS zur Mitteldestillatfraktion gespalten wird. Um dem typischen Leistungsbereich, dem üblicherweise dezentrale Auftreten und den oben erwähnten Fluktuationen der erneuerbaren Energien Rechnung zu tragen, rücken maßgeschneiderte Anlagen kleinerer Produktkapazitäten mit vereinfachten und intensivierten Prozessabläufen immer mehr in den Vordergrund. Modular einsetzbare mikrostrukturierte Reaktoren mit einer hohen Raum-Zeit-Ausbeute und der Möglichkeit einer dynamischen Betriebsweise stellen eine vielversprechende Lösung für kompakte Power-to-Fuel-Anwendungen dar.

Diese Dissertation befasst sich mit der Prozessvereinfachung durch die Verbindung der FTS mit HC in mikrostrukturierten Reaktoren mit Hinblick auf die Etablierung einer einstufigen Synthesegasumwandlung zu Kraftstoff in dezentralen Kleinanlagen. Die Kombination beider Verfahren in einem Prozessschritt wurde durch die Kombination der zu verwendenden Katalysatoren über die Integration als Wandbeschichtung oder als Schüttungen in unterschiedlichen Konfigurationen realisiert. Wandbeschichtungen der beiden Katalysatoren wurden sequentiell, gegenüberliegend, als Doppelschicht oder als hybride Schicht eingebracht. Im Falle der Schüttungen wurden die sequentielle und die hybride Konfiguration untersucht. Durch Experiment und Simulation wurden die Auswirkung der Katalysatorkonfigurationen

auf die Selektivität und Produktivität hin zu flüssigen Kraftstoffen (C_5 - C_{20}) untersucht und der Einfluss verschiedener Prozessparameter evaluiert. Dafür wurden entsprechende Reaktoren sowohl für die Untersuchungen am Festbett (Ringspalt-Mikrofestbettreaktor) als auch für die Wandbeschichtungen (Mikrokanalreaktor) entworfen und getestet. Durch die hohe Wärmeübertragungsleistung der mikrostrukturierten Reaktoren konnte ein isothermer Betrieb gewährleistet werden. Eigens hergestellte Katalysatoren wurden den Bedürfnissen der unterschiedlichen Katalysatorintegrationen angepasst. Für die Untersuchungen im Festbett wurden 100-150 μm große Katalysatorpartikel durch Pelletieren und Zerkleinern hergestellt. Ein Siebdruckverfahren wurde optimiert, um Katalysatorschichten mit einheitlicher Schichtdicke (20-50 μm) und mechanischer Stabilität in die Mikrokanäle einzubringen. Hierbei konnte durch entsprechende Folienanordnung auf einfache Art und Weise unterschiedliche Katalysatorkonfigurationen erreicht werden.

Die Durchführbarkeit des integrierten FTS-HC-Prozess wurde zunächst in einem zweistufigen Reaktorsystem mit Katalysatorschüttungen getestet. Anders als in herkömmlichen HC-Prozessen wurden das gesamte FTS-Produktgemisch (inklusive H_2 , CO , H_2O , kurzkettige Kohlenwasserstoffe (C_1 - C_{20})) über den HC-Katalysator geführt, wobei vor allem CO und H_2O einen negativen Einfluss auf das HC zeigten. Der Einfluss der FTS (insbesondere die Konzentration an nicht umgesetztem H_2 und CO , sowie die der langkettigen Kohlenwasserstoffe) auf die HC-Stufe wurde untersucht und die Gesamtleistung des integrierten Prozesses hinsichtlich seiner Selektivität zu flüssigen Kraftstoffen (C_5 - C_{20}) ermittelt. Die C_{21+} -Fraktion der FTS-Produkte wurde bei FTS-Bedingungen erfolgreich gespalten, wobei das Primär cracking dominierte. Mit zunehmender Temperatur zeigte sich ein Anstieg in der HC-Aktivität mit einem Selektivitätsmaximum von 70 wt.% an C_5 - C_{20} . Jedoch zeigt sich bei zu hohen Temperaturen auch eine Erhöhung der Selektivität zu C_1 - C_4 . Ein leichter negativer Effekt auf das HC wurde bei höheren H_2 - und CO -Partialdrücken beobachtet. Bei Variation der Kontaktzeit des Waxes im HC-Teil zeigte sich ein davon unabhängiges selektives Spalten des FTS-Waxes.

Die einstufige Integration FTS-HC auf Basis von Katalysatorschüttungen in Form der sequentiellen und hybriden Schüttung wurde im Ringspalt-Mikrofestbettreaktor verglichen und der Einfluss der Betriebsparameter auf die Zielkomponenten (flüssige Treibstoffe, C_5 - C_{20}) untersucht. Es konnte gezeigt werden, dass die FTS hinsichtlich der Produktivität die größte Rolle spielt, während das HC die Selektivität beeinflusst. Sowohl für das sequentielle, als auch für das hybride System wurde eine zufriedenstellende Leistung ermittelt. Durch eine Erhöhung der Temperatur auf 230-250 $^{\circ}\text{C}$ konnte ein Maximum von etwa 70 wt.% für die

Kraftstoffselektivität erreicht werden, welches jedoch abhängt von der verwendeten Katalysatorkonfiguration und der Raumgeschwindigkeit des Eduktgases. Das Verhältnis an H_2/CO und der Gesamtdruck haben nur begrenzt Einfluss auf die Kraftstoffselektivität. Für beide Konfigurationen konnte eine vergleichbare und zufriedenstellende Langzeitstabilität nachgewiesen werden.

Durch Kondensation der langkettigen Kohlenwasserstoffe bildete sich in den Katalysatorporen und im Bett zwischen den Partikeln eine Flüssigphase. Die Ansammlung der Flüssigphase in den Poren wurde mittels eines Modells zur Beschreibung der Porenfüllung untersucht, bei welchem die Ansammlung der flüssigen Kohlenwasserstoffe als ein Zusammenspiel aus deren Bildung in den Poren mit der Verdampfung aus der Pore heraus abgebildet wird. Es wurde festgestellt, dass selbst 100 μm große Partikel am Reaktoreingang, d.h. bei einem niedrigen Flüssiganteils im umgebenden Fluid, innerhalb weniger Stunden komplett mit Flüssigkeit gefüllt werden. Daher wurde eine komplette Füllung beider Katalysatoren (FTS und HC) über die gesamte Reaktorlänge angenommen.

Oben erwähnte Studien wurden mit Simulation gestützt. Die Reaktionskinetiken beider Prozessschritte wurden an experimentelle Daten angeglichen und der Einfluss der Flüssigphase mithilfe eines heterogenen Reaktions-Diffusions-Modells implementiert. Trotz der Füllung der Poren durch die Flüssigphase wurde ein beschränkter Einfluss der internen Diffusion sowohl bei der FTS als auch beim HC festgestellt, was auf die geringe Partikelgröße zurückgeführt wurde. Abweichungen zwischen Simulation und Experiment wurden für relativ hohe Flüssigphasenanteile beobachtet. Um diese experimentell beobachteten Ergebnisse bei hohen Flüssiganteilen beschreiben zu können wurde ein vereinfachtes Modell erstellt. Dabei wurde angenommen, dass ein Teil des Katalysators blockiert wird, sobald die Flüssigphase einen Grenzwert überschreitet, was sich in einem erhöhten Diffusionswiderstand oder unzugänglichen Bereichen im Katalysatorbett niederschlägt, besonders in breiten, flachen Strömungskanälen wie sie in dem in dieser Arbeit verwendeten Ringspaltreaktor vorliegen. Die Folge ist eine signifikante Limitierung im Stofftransport der FTS in den Bereichen in denen Flüssigfüllung angenommen wird, während im Bereich des HC nur eine bedingte Anfälligkeit für interne Diffusionslimitierung vorliegt. Die Modellintegration von unzugänglichen Bereichen im Festbett brachte eine gute Übereinstimmung der Simulationsergebnisse mit den experimentellen Daten.

Verglichen mit dem Festbettreaktor zeigte der Mikrokanalreaktor mit Wandbeschichtung bessere Eigenschaften in der Wärmeübertragung und verhinderte Blockaden durch

Kondensation. Die FTS wurde für eine Schichtdicke von 20 und 40 μm bei identischen Prozessbedingungen untersucht. Nachdem in beiden Fällen ähnliche CO-Umsätze und Selektivitäten festgestellt wurden, kann der Schichtdicke als Parameter – zumindest in den untersuchten Bereichen – nur ein geringfügiger Einfluss auf die FTS zugeschrieben werden. Bereits in der Reaktion genutzte, beschichtete Folien wurden zerschnitten und untersucht, wobei eine vollständige Füllung an flüssigen Kohlenwasserstoffen innerhalb der Katalysatorschicht festgestellt werden konnte. Die Simulation gemäß des heterogenen Modells zur Beschreibung der Reaktions-Diffusions-Gleichungen bestätigte den geringen Einfluss der Schichtdicke.

Im Mikrofestbettreaktor wurde ein positiver Effekt des CO-Umsatzes auf die Kettenwachstumswahrscheinlichkeit festgestellt, was auf die konkurrierende Adsorption von Wasser und Olefinen zurückzuführen ist. Mit steigendem CO-Umsatz im beschichteten Mikrokanalreaktor konnte eine gleichbleibende C_{5+} -Selektivität und eine steigende CH_4 -Selektivität bei steigendem Umsatzgrad beobachtet werden. Verglichen mit den kleinen Hohlräumen innerhalb des Festbetts kann für den Mikrokanalreaktor durch die großen Freiräume nur ein geringfügiger Effekt der Kapillarkondensation angenommen werden was wiederum zu einem geringeren Flüssigphasenanteil und somit zu geringeren Wasser- und Olefinkonzentration führt.

Die Prozessintegration in einem Mikrokanalreaktor mit beschichteten Kanalwänden zeigte maßgebliche Verbesserungen in der Kraftstoffselektivität bei den untersuchten Drücken von 30 und 20 bar, wobei im Vergleich zum FTS Referenzsystem identische CO-Umsätze erreicht wurden. Bei 30 bar zeigte sich der höchste Umsatz und der höchste HC-Wirkungsgrad für die hybride Beschichtung gefolgt von der Doppelschichtanordnung und gegenüberliegenden Anordnung. Die Kraftstoffselektivität verblieb zwischen 225 und 260 $^{\circ}\text{C}$ konstant bei 70 wt.% für alle parallelen FTS-HC-Kombinationen (gegenüberliegend, Doppelschicht, Hybrid), wobei die Zusammensetzung der Kraftstoffe jedoch unterschiedlich war. Verglichen mit der Festbettanordnung wird eine geringere Temperatur benötigt, um die maximale $\text{C}_5\text{-C}_{20}$ Selektivität zu erreichen. Bei 20 bar wurde ebenfalls der höchste HC-Wirkungsgrad für die hybride Beschichtung gefunden, gefolgt von der Doppelschichtanordnung und gegenüberliegenden Anordnung, wobei hier der CO-Umsatz dem entgegengesetzten Trend folgte. Nahezu alle C_{21+} -Kohlenwasserstoffe konnten durch die HC Integration gespalten werden. Die Katalysatorstabilität wurde untersucht, wobei für alle Anordnungen über 15 Tage hinweg eine vergleichbare und gute Stabilität ermittelt werden konnte.

Für die gegenüberliegende und sequentielle Anordnung wurden durch separate Beheizung (durch Thermoöl und Heizkartuschen) voneinander unabhängige Temperaturen der FTS und der HC Zonen angewendet. So konnten die Selektivität und Produktivität zu C₅-C₂₀ sowie die Zusammensetzung der Flüssigkraftstoffe durch die individuelle Temperierung weiter optimiert werden.

Es zeigte sich somit, dass sowohl FTS als auch HC durch die Parallelintegration beeinflusst werden. Es wird angenommen, dass das Spalten der FTS Kohlenwasserstoffe die jeweilige Zusammensetzung lokale ändert (molare Gesamtmenge, molare Anteile, etc.), was wiederum beide Teilreaktionen beeinflusst. Daher wurde ein vereinfachtes, heterogenes Reaktionsmodell für die hybride Katalysatorintegration erstellt, um den Einfluss der veränderten Synthesegaskonzentration und dem H₂/CO-Verhältnis auf die Leistung der FTS zu ermitteln. Demnach werden länger-kettige Kohlenwasserstoffe effektiv gespalten, was in der Hybridanordnung zu einer langsameren Zunahme der Flüssigfraktion führt. Die veränderte Synthesegaskonzentration durch lokales Spalten in der parallelen FTS-HC-Anordnung hat so nur einen geringen Einfluss auf den CO-Umsatz. Vielmehr kann angenommen werden, dass unterschiedliche Adsorptionseffekte von Olefinen und Wasser für die Abweichung der Ergebnisse aus Experiment und Modellvorhersage verantwortlich sind.

Die Integration beider Reaktionen sowohl über Festbettkatalysatoren als auch über katalytisch aktive Wandbeschichtungen führte zu einer signifikanten Erhöhung der C₅-C₂₀-Selektivitäten. Die Realisierbarkeit einer einstufigen Kohlenwasserstoff-Synthese (FTS) mit integrierter Produktaufbereitung (HC) konnte gezeigt werden. Die parallele Anordnung beider Reaktionen (FTS-HC) ermöglichte darüber hinaus eine weitere Erhöhung der Kraftstoffausbeute.

Parts of this dissertation have been published in:

1. C. Sun, T. Zhan, P. Pfeifer, R. Dittmeyer, Influence of Fischer-Tropsch synthesis (FTS) and hydrocracking (HC) conditions on the product distribution of an integrated FTS-HC process, *Chem. Eng. J.* 310, Part 1 (2017) 272-281.
2. C. Sun, P. Pfeifer, R. Dittmeyer, One-stage syngas-to-fuel in a micro-structured reactor: investigation of integration pattern and operating conditions on the selectivity and productivity of the liquid fuel, *Chem. Eng. J.* 326 (2017) 37-46.
3. C. Sun, Z. Luo, A. Choudhary, P. Pfeifer, R. Dittmeyer, Influence of the condensable hydrocarbons on an integrated Fischer-Tropsch synthesis and hydrocracking process: simulation and experimental validation, *Ind. Eng. Chem. Res.* (2017) (DOI: 10.1021/acs.iecr.7b01326).
4. C. Sun, M. Klumpp, J. Binder, P. Pfeifer, R. Dittmeyer, One-stage syngas-to-fuel conversion with printed catalyst layers in microstructured reactors, *Chem. Ing. Tech.* 89 (2017) 894-902.

Content reproduced with the permission of Elsevier, American Chemical Society and John Wiley & Sons.

Contents

Erklärung	i
Acknowledgements	ii
Abstract	iii
Zusammenfassung	viii
Contents	xiv
1. Introduction	1
1.1 Background and motivation.....	1
1.2 Fischer-Tropsch synthesis in micro-structured reactors	5
1.3 Objectives of this dissertation.....	12
2. Experimental procedures and catalyst characterization results	14
2.1 Lab-scale micro-structured reactors	14
2.1.1 Annular micro packed-bed reactor	14
2.1.2 Wall coated microchannel reactor	16
2.2 Material preparation and characterization	19
2.2.1 Preparation of FTS and HC catalysts	19
2.2.2 Optimization of catalyst pastes for screen-printing.....	20
2.2.3 Physical properties of original and coated catalysts.....	23
2.2.4 Different configurations of wall-coated catalyst layers	26
2.3 Experimental setup	28
2.4 Analysis methods.....	30
2.4.1 Product analysis.....	30
2.4.2 Data analysis	32
2.5 Experimental conditions	33

3.	FTS-HC integration in micro-structured reactors	34
3.1	Computational analysis.....	34
3.1.1	FTS and HC reaction kinetics	34
3.1.2	Vapor-liquid equilibrium.....	40
3.1.3	Reaction-diffusion in the catalyst.....	42
3.1.4	Reactor modelling	45
3.1.5	Pore filling model.....	46
3.2	FTS reference of different catalyst configurations	47
3.2.1	FTS reference with powder catalyst in the micro packed-bed reactor	47
3.2.2	FTS reference with wall-coated catalyst in the microchannel reactor I.....	50
3.2.3	Estimation of the FTS kinetics	53
3.2.4	Accumulation of liquid hydrocarbons	54
3.2.5	Influence of the liquid hydrocarbons on FTS.....	56
3.3	Two-stage FTS-HC integration with powder-type catalysts	60
3.3.1	Two-stage reactor system.....	61
3.3.2	Influence of the HC temperature	62
3.3.3	Influence of the H ₂ partial pressure on HC	64
3.3.4	Influence of the CO partial pressure on HC	66
3.3.5	Influence of the wax space velocity on HC.....	67
3.3.6	Stability of the catalysts	69
3.4	One-stage FTS-HC integration with powder-type catalysts.....	70
3.4.1	Comparison of FTS performance	71
3.4.2	Influence of temperature and syngas space velocity on fuel synthesis	73
3.4.3	Influence of the pressure on fuel synthesis	75
3.4.4	Influence of the H ₂ /CO ratio on fuel synthesis	77
3.4.5	Stability of the catalysts	78
3.4.6	Interaction between FTS and HC in the integrated process	80

3.4.7	Estimation of HC kinetics	81
3.4.8	Influence of the liquid hydrocarbons on HC	82
3.5	One-stage FTS-HC integration with printed catalyst layers.....	85
3.5.1	Interaction between FTS and HC in different catalyst configurations.....	86
3.5.2	Performance at 30 bar	88
3.5.3	Performance at 20 bar	91
3.5.4	Stability of the catalysts	94
3.5.5	Integration performance with independent temperature control of FTS and HC...	95
3.5.6	Computational analysis of the wall-coated FTS-HC integration system	98
3.6	Discussion of the different integration options.....	101
4.	Summary and conclusions.....	104
5.	Outlook.....	107
	Nomenclature	108
	Symbols.....	108
	Subscripts and superscripts	109
	Abbreviations	110
	References	112
	Appendix	134
	A1 Optimization of screen-printing pastes.....	134
	A1.1 Optimization of Al ₂ O ₃ paste.....	134
	A1.2 Optimization of H-ZSM-5 paste.....	135
	A2 Gas chromatography.....	136
	A3 Blank test of syngas activity of Pt-ZSM-5	138
	A4 Experimental conditions.....	138
	Curriculum Vitae.....	143

1. Introduction

1.1 Background and motivation

Energy plays an essential role in the global development. The growing population and economy lead to a growing energy demand. Over last five decades the primary energy consumption increased by 359% (Figure 1-1a) [1]. Fossil fuels had a share of 86% of the global energy consumption in 2015 (oil 32.9%, coal 29.2%, natural gas 23.8%), while renewables only accounted for 14%. Liquid fuels hold 36% of the final energy consumption, which is twice the share of electricity (18%). According to consumption rates in 2015, the proved reserves of oil, coal and natural gas are only available for 50.7, 114 and 52.8 years, respectively.

In addition to energy demand, greenhouse gas emissions is another big issue accompanying current worldwide growth. As shown in Figure 1-1b, a significant increase of the global anthropogenic CO₂ emissions (~ 96% of total greenhouse gas emissions) was observed with the same trend as energy consumption, owing to the fossil fuel combustion. In 2015 the worldwide CO₂ emissions reached 33.5 Gt [1]. While relatively steady CO₂ emissions was recorded in Europe. Since 1975, the average global temperature on earth has increased by about 0.53 °C. Be aware even a tiny change would lead to serious impacts. A one- to two-degree temperature drop would plunge the earth into the Little Ice Age [2].

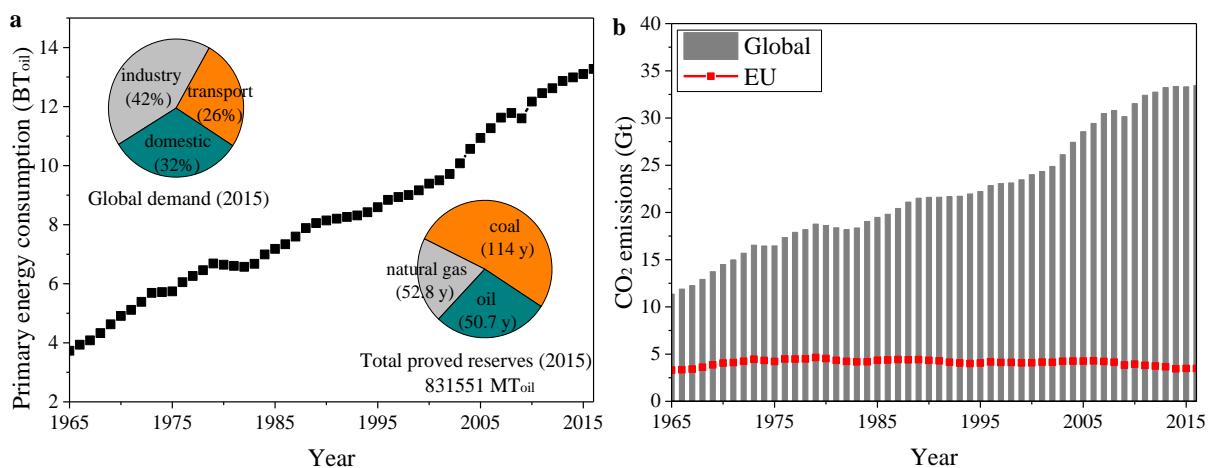


Figure 1–1 Global energy consumption (a) and CO₂ emissions (b) (Gt refers to Gigatonne) [1]

To meet the increasing energy demand and reduce the greenhouse gas emissions, energy system decarbonization and more efficient energy utilization are required. Great efforts are being exerted in the energy transition towards a low-carbon future [3-6]. According to the

energy strategy of the European Union (EU), 40% reduction in CO₂ emissions (compared to 1990 levels) and a 30% EU-wide share for renewables (solar energy, wind energy, biomass, etc.) are targeted by 2030. The greenhouse gas emissions are to be reduced by 80-95% until 2050 [7]. Progress has been made towards an energy system largely based on renewables. Wind energy and photovoltaics are undergoing major growth of installed capacity year by year. Accordingly, electricity becoming a primary form of energy has been expected. Germany leads the pace and has reached a share of 31.7% electricity consumption from renewables in 2016 (Figure 1-2) [8-10]. 100% electricity supply and minimum 80% share of the total energy consumption from renewables are targeted by 2050 (Energiewende [11]).

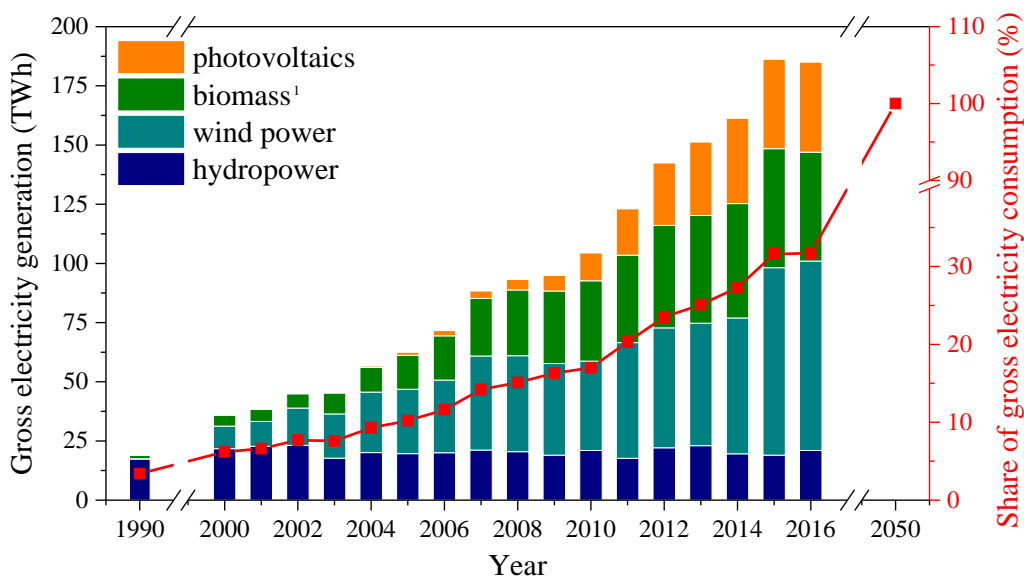


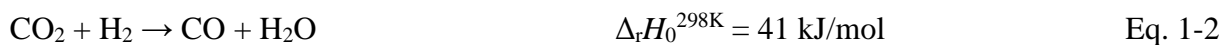
Figure 1–2 Development of electricity generation and share of electricity consumption from renewables in Germany (¹ solid and liquid biomass, biogas, sewage and landfill gas, biogenic fraction of waste) [8-10]

However, the large scale installation of renewable energy would face unavoidable constraints. Very often renewables (wind energy, solar energy, biomass, etc.) are distributed and highly unsteady with limited availability [12], which thereby can split the overall energy supply into small units and lead to stability issues of the electrical grid. Energy loss would be resulted if the variable renewable supply exceeds the demand. Moreover, attentions should be paid to other energy forms (heat, gas, liquid, etc.) when electricity becomes a primary one. A smart energy system with efficient utilization of renewables and effective conversion between different energy forms is of great importance for the ongoing energy transition. Energy storage technologies and grid expansion are required.

Considering the compatibility with existing infrastructures for storage and distribution, chemical energy carriers (fuels) would be attractive options for flexible generation of power and heat. The power-to-fuel process has been proposed to stabilize the electrical grid by converting the surplus energy into methane (power-to-gas, PtG) or liquid fuels (power-to-liquid, PtL). The power-to-fuel process mainly consists of two parts: conversion of the power and carbon source to syngas (H₂ and CO) and conversion of the syngas to fuels. Surplus electricity from renewables would be used to produce H₂ via water or steam electrolysis (Eq. 1-1). The syngas could be produced from non-food biomass (wood, straw, etc.) by gasification [13, 14] or from CO₂ and H₂ by reverse water-gas-shift (Eq. 1-2) [15], which not only offers a better utilization of excess energy, but also reduces the CO₂ footprint.

Due to technical limitations, liquid fuels (gasoline, diesel, kerosene, methanol, etc.) will remain as transportation fuels in the near future, especially for propulsion of heavy duty trucks and airplanes where other technologies are unsuitable [16]. The potential to substitute fossil fuels and their derived products gives additional interests to the PtL process. In the PtL process, two paths have been applied in the syngas-to-liquid process (Figure 1-3). The Fischer-Tropsch synthesis (FTS, Eq. 1-3) route [17] is an ideal way to produce clean liquid fuels because the hydrocarbon products obtained are oxygen, nitrogen and sulfur-free. Methanol synthesis also has been widely used, where the methanol can then be mixed with conventional liquid fuels.

FTS is a surface catalyzed polymerization reaction. It can convert syngas into a wide range of hydrocarbons from methane to heavy wax, which can be described by the Anderson-Schulz-Flory (ASF) distribution (Figure 1-4) [18]. The hydrocarbon selectivity is characterized by the chain growth probability (α). With an increase of the chain growth probability, a shift towards heavier hydrocarbons would be expected. For the low-temperature Fischer-Tropsch (LTFT, 200-250 °C) process, the chain growth probability is around 0.85-0.95, which limits the selectivity of liquid fuels (C₅-C₂₀) to 26-68 wt.% (according to the ideal ASF distribution). A conventional way to improve the yield of liquid fuels is to separate the FTS wax and feed it into a hydrocracking (HC) unit. With additional H₂ the FTS wax would be cracked into middle distillates (Eq. 1-4) [19-25].



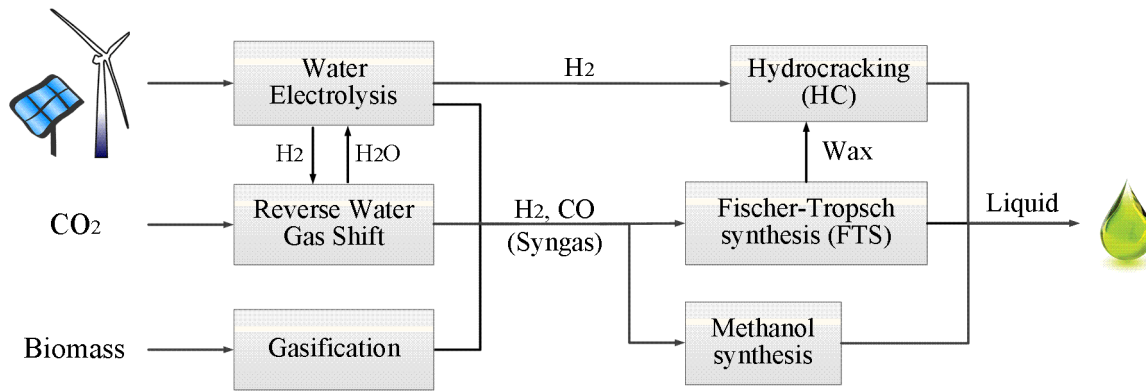


Figure 1–3 An overview of PtL process options

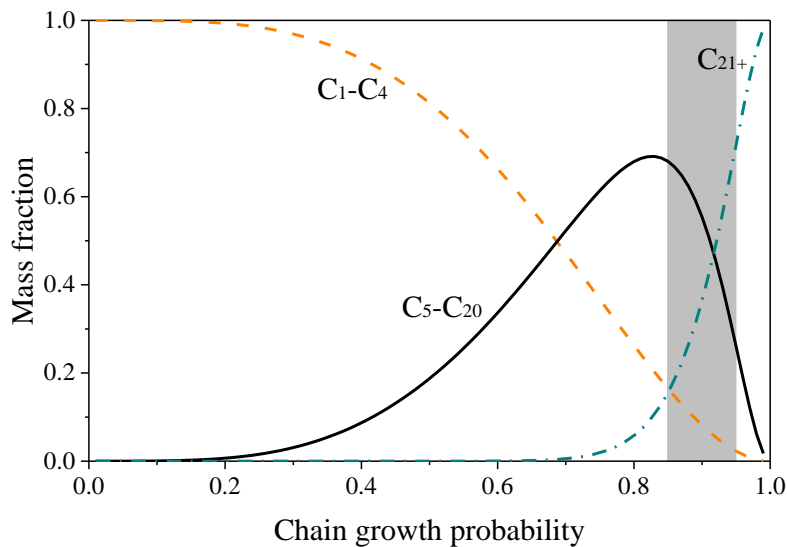


Figure 1–4 Ideal ASF distribution of FTS hydrocarbons [18]

As mentioned above, the highly unsteady and highly distributed characteristics of renewables split the overall energy supply into small-scale units with dynamic operation. Traditional large-scale syngas-to-liquid plants are not economically feasible. Therefore, tailored cost-effective small-scale plants with simplified and intensified processes and enhanced dynamic operability are of great importance for PtL applications.

On one hand, modular micro-structured reactors with enhanced heat transfer performance are being developed to cope with the highly exothermic or endothermic reactions and to improve the operation under dynamic conditions [26-32]. The advanced temperature control of micro-structured reactors suits the highly exothermic FTS reaction ($\Delta H = -167$ kJ/mol) well. The high volumetric productivity, compared to conventional reactors, makes the micro-structured reactor a promising option for process intensification and cost reduction.

On the other hand, the opportunity for process integration, such as by combining FTS with HC, is drawing more and more attention [33-45]. HC is a decomposition reaction to crack long chain hydrocarbons into short ones [46]. The first integration of FTS with HC was

reported in the 1970s [33]. Multifunctional catalysts with both FTS and HC active species were proposed, e.g., where the FTS catalyst was encapsulated by a HC catalyst to form a core-shell structure [37, 42, 43, 47, 48] or where the FTS active metal was dispersed on a HC catalyst support [40, 41, 44, 49]. Meanwhile, sequential or hybrid catalyst bed concepts, where the FTS catalyst is followed by or mixed with the HC catalyst, have been studied [34-36, 38, 39, 50-52]. Both catalyst and process level combinations exhibited an improvement of the middle distillate selectivity. However, there is still a lot unknown when targeting deeper understanding and practical application of simplified processes for decentralized small-scale PtL plants.

1.2 Fischer-Tropsch synthesis in micro-structured reactors

FTS converts syngas into a wide range of hydrocarbons, which offers a crude oil free route for the production of value-added molecules. The temperature-sensitive FTS chain growth probability (α) leads to the requirement of (near-) isothermal operation for the desired selectivity of hydrocarbons. Considering the highly exothermic nature of FTS, efficient removal of the reaction heat turns out to be the most critical demand of industrial FTS reactors. Large-scale FTS has been commercialized in South Africa (Sasol), Malaysia (Shell) and Qatar (Sasol and Shell) for fuel production (12000 – 140000 bpd) [53], which indicates only a few gas fields in the world (< 10%) are capable of supplying such big facilities. Compact and modular micro-structured reactors with intensified heat and mass transfer properties could ideally suit the challenges of FTS, particularly for decentralized small-scale gas sources (CO₂, biomass, natural gas, etc.).

Research efforts in micro-structured reactors fall in novel reactor concepts, catalyst development, scale-up and commercialization. FTS was carried out in micro-structured reactors with both powder-form and wall-coated catalysts. Significant improvement of catalyst activity, selectivity and stability was obtained in micro-structured reactors, which is attributed to the increase of mass and heat transfer in microchannel flows [27, 54-62]. As reported by Cao et al., the FTS process can be intensified by a factor of up to 15 by using microchannel reactors [54]. Compared to a conventional tubular reactor with hot spots up to 30 K, the temperature deviation in the microchannel reactor (0.508 mm) was smaller than 1 K (483 K and 18000 h⁻¹ GHSV), which enables the protection of the catalyst from deactivation by local overheating [57]. Severe conditions could be operated in micro-structured reactors without large temperature gradients in the catalyst bed [27]. With 3 mm channel size the heat removal efficiency was still acceptable. High effectiveness factors were obtained with up to

350 μm catalyst particles [63]. Optimum productivity and stability could be achieved by flexible adjustment of the operating conditions in the micro-structured reactor [64].

Compared to bubble column, packed-bed and monolith reactors, the wall-coated microchannel reactor would possess the highest catalyst volumetric productivity. However, the reactor volumetric productivity would be lower due to the reduced catalyst loading [58]. Different support structures including microchannel block, micro-monolith, foam, etc. were investigated with the wall-coated $\text{Co}/\text{Al}_2\text{O}_3$ catalyst [62, 65-70]. Slightly lower activity compared to the powder catalyst (38-53 μm) was obtained for a 40-50 μm thick catalyst layer [65]. When increasing the layer thickness from 30 to 80 μm , slightly higher CH_4 selectivity was observed, which could be caused by the increased local H_2/CO ratio due to the larger diffusivity of H_2 [67, 70]. Both CO conversion and chain growth probability benefit from the microchannels with longer path and larger surface area [71]. Via computational analysis, pressure drop in microchannels with wall-coated catalysts was found to be strongly related to surface roughness [72]. Thickness of the liquid film would be determined by the shear stress of gas flow [73].

In order to fully utilize the benefits of micro-structured reactors, the catalyst has to be optimized. In a microchannel reactor with wall-coated catalysts, the highest CO conversion and resistance against deactivation were obtained on Co/SiO_2 , compared to Ru/SiO_2 and Fe/SiO_2 [74]. But addition of Ru as a promoter shows positive effects on CO conversion [75]. Hierarchically structured cobalt-based FTS catalysts supported on $\text{SiO}_2/\text{carbon nanofiber}/\text{carbon felt}$ were also developed, showing higher volumetric productivity than $\text{Co}/\text{Al}_2\text{O}_3$ in microchannel and monolith reactors [29]. The cobalt crystallite size, as well as its size distribution, was found to be related to the activity and stability of Co/SiO_2 catalysts [76]. With an optimum crystallite size of 9.8 nm and optimized size distribution, 0.08%/day decrease of CO conversion was observed in a microchannel reactor with an activity of 0.25 $\text{mol}_{\text{CO}} \cdot \text{g}_{\text{Co}}^{-1} \cdot \text{h}^{-1}$. The organic matrix combustion method proved to be an advanced catalyst preparation method with flexible control of the cobalt crystallite size, which was adopted to prepare a very stable and well performing catalyst by Velocys [30, 77]. Complete activity recovery was obtained after an in-situ regeneration. Enclosed oxidation was adopted to remove carbonaceous deposits and to convert the active metallic phase back into the oxide before the reactivation with H_2 .

The straightforward numbering-up by adding more units is an additional advantage of micro-structured reactors, owing to the unaffected catalyst performance [78]. In a microchannel

reactor with a capacity of 500 bpd (128867 channels, channel: $\Phi \times L = 1.5 \times 365$ mm), the temperature deviation could be limited to only 4 K (with 100 μ m catalyst particles, at 497 K, 21 bar, H₂/CO ratio of 2) [59]. Moderate pressure drop (< 3 bar/m) could be attained by choosing proper size and shape of the catalyst particles [63]. 3% liquid holdup, which is independent of CO conversion and reaction temperature, was observed in a micro packed-bed reactor.

Combined with highly active and stable catalysts, micro structured reactors hold promise for increased volumetric productivity, which enables more compact and lighter units and therefore attracts the interest from industry [28, 30, 32, 78-80]. In last 20 years a number of companies have been developing gas conversion technologies which are applicable to the challenges of small-scale gas supply, steep catalyst activity decline, and isolated locations with limited infrastructure. CompactGTL and Velocys have moved beyond the technology demonstration and are offering commercial solutions (Table 1-1) [79].

Table 1-1 Small-scale gas-to-liquid solutions [79]

	CompactGTL	Velocys
Footprint	0.5 acre	< 0.5 acre
Capex	\$ 125-180 MM	\$ 115 MM
Opex (w/o gas)	\$ 8 MM	\$ 5.5 MM
Product marketability	1250 bpd syncrude & FTS wax	1250-1750 bpd diesel
Energy efficiency	55-63%	55-63%
Carbon efficiency	70-75%	70-75%

CompactGTL, established in 2006, has put intensive efforts in the utilization of associated gas from remote oil fields. Modular plant design, incorporating multiple reactors in parallel, provides a flexible, operable solution to accommodate gas feed variation and declines over the life of the oil field. The world's first fully integrated small-scale gas-to-liquid demonstration plant was built in Brazil with a capacity of 20 bpd syncrude production [80]. The modular facility (Figure 1-5) includes gas pretreatment, pre-reforming, reforming, waste heat recovery, process steam generation, syngas compression, FTS, FTS cooling water system, and tail gas recycling. The mini-channel FTS unit is shown in Figure 1-6a, where the reaction channels are separated by coolant channels. In cooperation with Johnson Matthey, corrugated structured catalysts were developed (Figure 1-6b), making loading and unloading of the

catalyst easier [81]. FTS was operated in two-stage reactors with a per pass conversion of 30-50% (overall conversion up to 75%), which enables better control of catalyst deactivation. After approximate 3-5 years' lifetime without regeneration, the catalyst would be recycled.

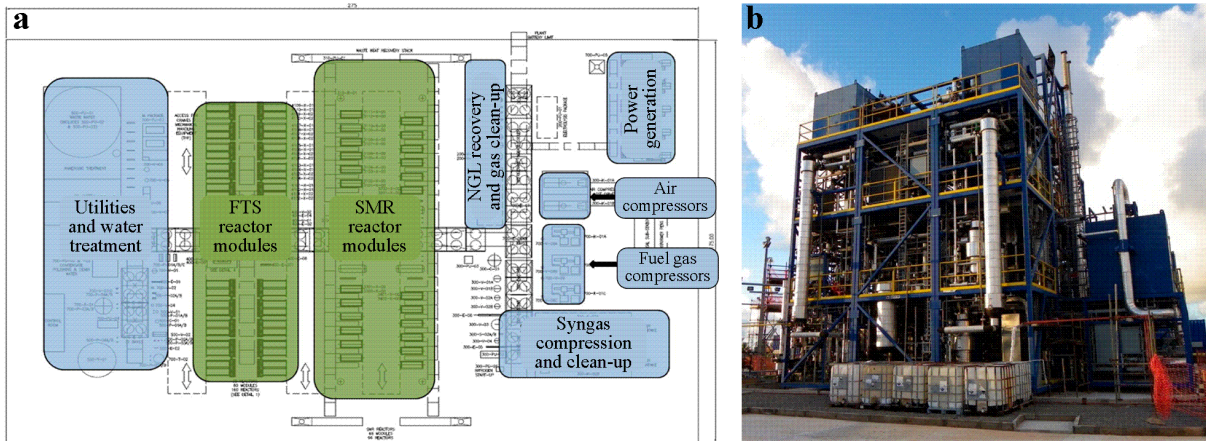


Figure 1-5 Modular gas-to-liquid plant (a. conceptual layout; b. demonstration plant) [80]

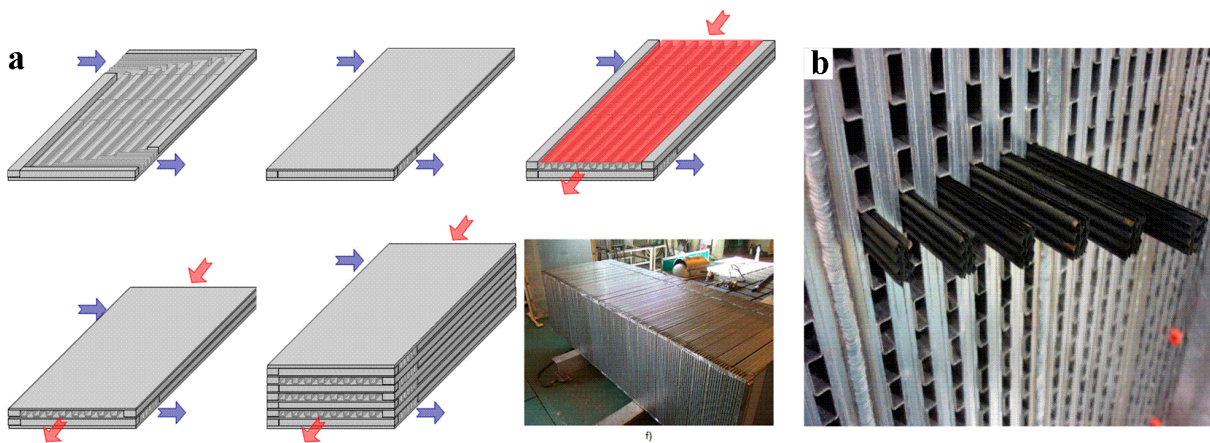


Figure 1-6 CompactGTL reactor technology (a. assembly of a FTS unit; b. catalyst insert) [80]

Velocys offers alternative solutions for gas-to-liquid and biomass-to-liquid processes. Microchannel reactors have been developed for high degree of process intensification (Figure 1-7a). With characteristic dimensions 1-2 orders of magnitude smaller, up to 10 times higher catalyst productivity ($\text{kg}/\text{m}^3/\text{h}$) and 4 times higher reactor productivity (bpd per ton) were achieved (Figure 1-7b) [28]. Based on the 44 bpd reactor core, larger systems for 175 bpd (4-core), 350 bpd (8-core) and 700 bpd (16-core) were developed (Figure 1-8). The microchannel reactor realizes attractive economics at much smaller size (500 bpd) than conventional technology (10,000 bpd). Velocys' full-scale FTS reactors were deployed in the ENVIA Energy's Oklahoma City GTL plant, which was designed to convert landfill gas into high value hydrocarbons [82]. Moreover, a biomass-to-liquid plant capable of producing 1100 bpd fuel was proposed for the Red Rock Biofuels project. Via the organic matrix combustion method Velocys has developed a highly active and stable FTS catalyst. Applying the

proprietary cobalt-based FTS catalyst in the microchannel reactor, sound stability was observed over 2 years' time-on-stream at single pass conversion near 80% [30]. The slow loss of catalyst performance could be completely reversed using an oxidative regeneration approach.

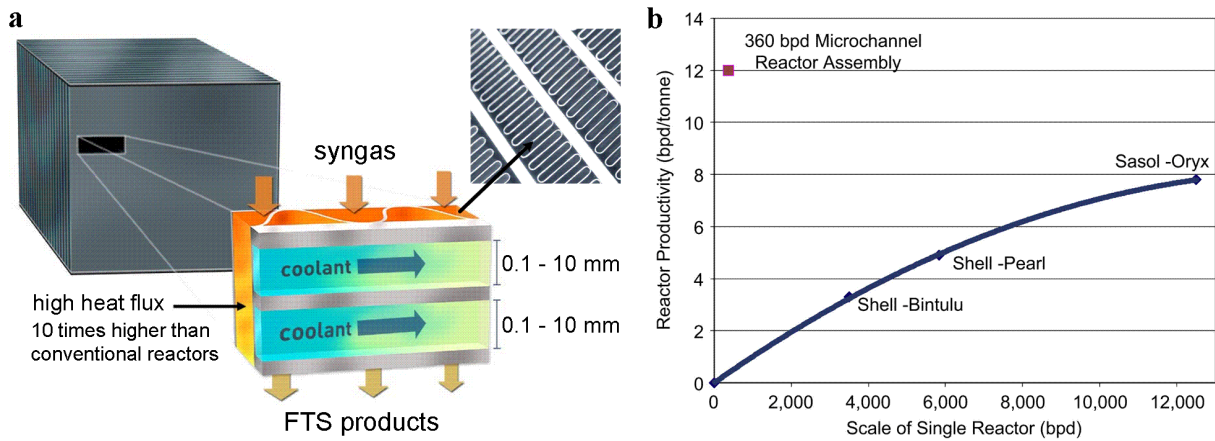


Figure 1-7 Velocys microchannel reactor technology (a. reactor core; b. comparison of reactor productivity between conventional and microchannel reactors) [28, 77]

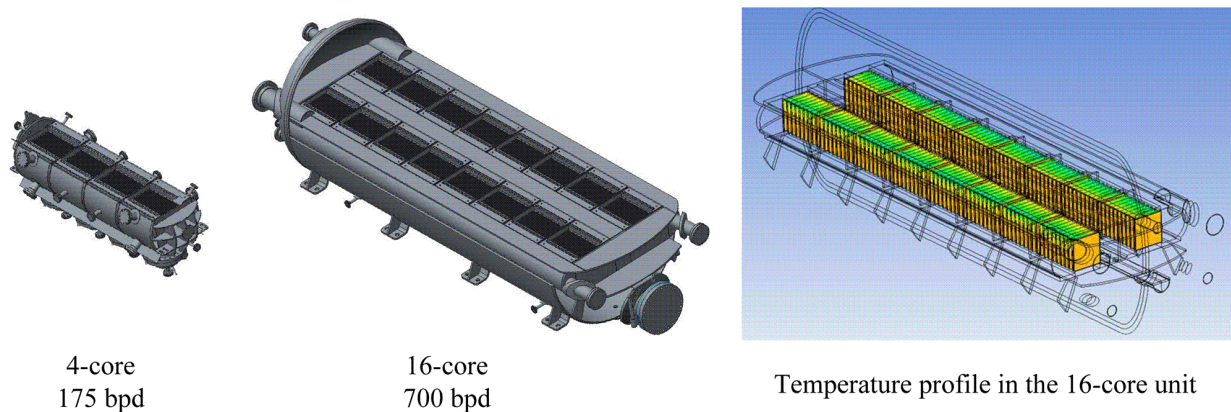


Figure 1-8 Microchannel reactor numbering-up [83]

The Institute for Micro Process Engineering (IMVT) at the Karlsruhe Institute of Technology (KIT) is developing micro-structured devices with more than two decades of experience in the design, fabrication and use of micro-reactors, -heat exchangers, -mixers, and more recently also separators. A sandwiched reactor for catalyst testing and process development was developed to cope with the highly exothermic FTS reaction [27]. As shown in Figure 1-9a, the catalyst and cooling plates are stacked one after the other to guarantee efficient heat-exchange. Each catalyst plate is composed of two foils placed in the face-to-face pattern. On the catalyst foil 400 μm high pillars are hexagonally placed with 800 μm distance between each other to create a large contact area with catalyst particles (Figure 1-9b). Eight parallel catalyst plates are diffusion-bonded in the micro-structured reactor to give 2 cm^3 bed volume. Reaction

temperature is controlled by thermal oil in cross-flow. Compared to a conventional tubular packed-bed reactor ($\Phi = 10$ mm) with diluted catalysts (1:20 dilution with SiC), better FTS performance (conversion, selectivity, stability), as well as isothermal operation, was obtained in the micro-structured reactor with undiluted catalysts. 2 g/h C_{5+} productivity (488 K, 20 bar, H_2/CO ratio of 2.1) was achieved, which translates to a reactor productivity of 16.7 bpd per ton. Influence of the catalyst foil geometry was also investigated [32]. In the reactor with larger slit size (Figure 1-9c, 750 μm pillar height, 1200 μm pillar distance, 2.7 cm^3 bed volume), identical CO conversion was obtained, which indicates the heat removal is still efficient with the 1.5 mm slit size. However, a lower chain growth probability was observed, which was attributed to the slight deviation from isothermality caused by the enlarged slit size (estimated mean difference of 3 K).

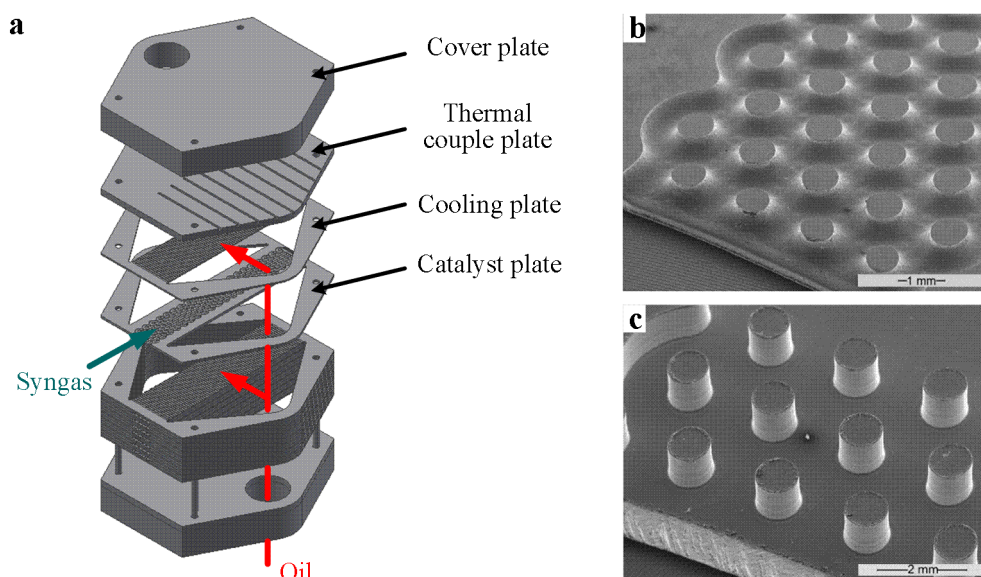


Figure 1-9 IMVT micro-structured reactor technology (a. scheme of the reactor structure; b. geometry of slit with 400 μm pillars; c. geometry of slit with 750 μm pillars) [27, 32]

INERATEC, a spin-off company of KIT, has transferred the IMVT reactor technology to commercial solutions of small-scale gas-to-liquid and power-to-liquid processes. Different reactor modules were developed based on the structured plates scaled up from the lab reactor (Figure 1-10) [84]. Identical space-time yield with the lab system was obtained for the 0.2 bpd pilot plant. Stable catalyst performance was observed over more than 3000 h time-on-stream. Process integration with an upstream reverse water-gas-shift unit to generate syngas was studied. Different from CompactGTL (associated and stranded gas) or Velocys (landfill gas and biomass), INERATEC offers particular solutions for the much smaller-scale renewable power sources — PtL. A first containerized 0.6 bpd FTS plant built for VTT Technical Research Center of Finland (Figure 1-11) is under operation since 2016, which is used for the

Finnish SOLETAIR project aiming at converting solar energy and CO₂ captured from air into liquid fuels [85, 86].

The energy transition to a system largely relying on renewables is targeted for the low-carbon future. Considering the highly unsteady and distributed properties of renewables, the PtL process has been proposed to stabilize the electrical grid in terms of surplus energy utilization and security of power supply. Micro-structured reactors with high space time yield and dynamic operability would be technically and economically the most feasible option for the decentralized small-scale PtL plants. Understanding of the possible process intensification and integration in the micro-structured reactors is of great importance for the practical application of the compact PtL plants.

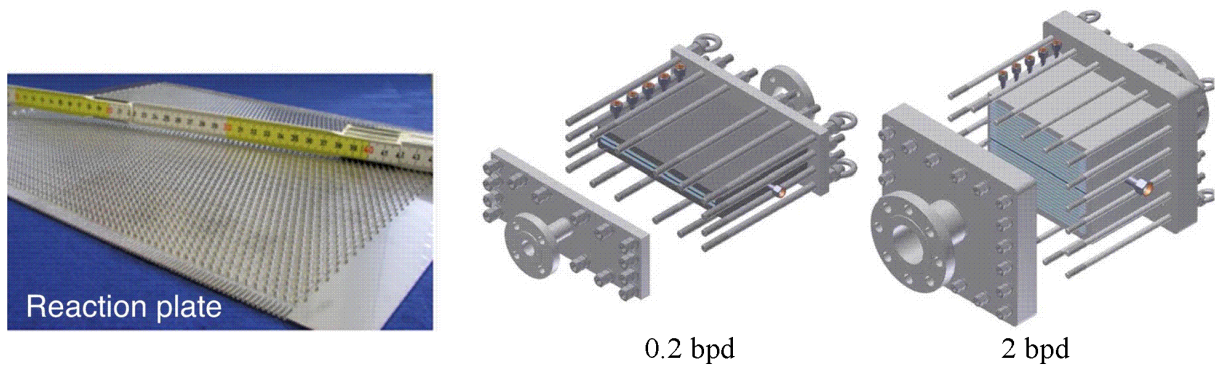


Figure 1–10 INERATEC micro-reactor modules [84]



Figure 1–11 Containerized FTS plants (14 kg/d) built by INERATEC for VTT Technical Research Center of Finland [85, 86]

1.3 Objectives of this dissertation

Process simplification by integrating FTS with HC in micro-structured reactors was targeted in this dissertation with a view to the feasibility of one-stage syngas-to-fuel application for decentralized small-scale PtL plants.

The integration was achieved by arranging FTS and HC catalysts in different patterns. Both experimental studies and computational analysis were carried out to understand the implications of the integrated process. Detailed analysis of the combined FTS-HC processes should be performed with a view to optimum catalyst configuration and operating conditions for maximizing the selectivity and productivity of liquid fuels. An overview of this work is shown in Figure 1-12.

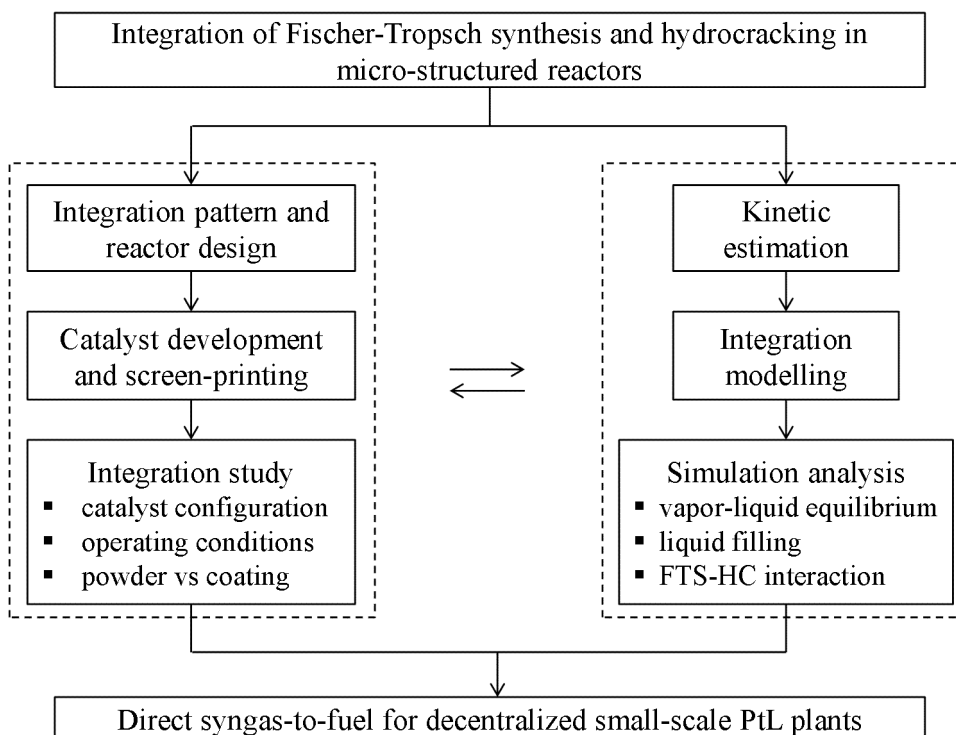


Figure 1–12 Outline of the study on one-stage integrated FTS-HC process

Configurations with catalysts in powder-form and as wall-coatings were developed for the integration of FTS with HC (Figure 1-13). Sequential and hybrid patterns were adopted for the powder catalyst. Sequential, face-to-face, dual-layer and hybrid patterns were studied for the wall-coated catalyst. Lab scale micro packed-bed (for powder catalyst) and microchannel (for wall-coated catalyst) reactors were developed for the targeted process simplification. An experimental setup able to accommodate the different reactor types was constructed. FTS and

HC catalysts were developed to meet the requirements of both reactor types. Screen-printing was selected and optimized to obtain uniform catalyst layers in the microchannels.

A two-stage reactor system with the FTS effluent directly fed upon HC catalyst was established to verify the possibility of process integration under FTS conditions [45]. Effects of temperature, residual syngas and wax content on the HC performance were studied, which could offer important learnings with a view to adjusting the HC performance by FTS control.

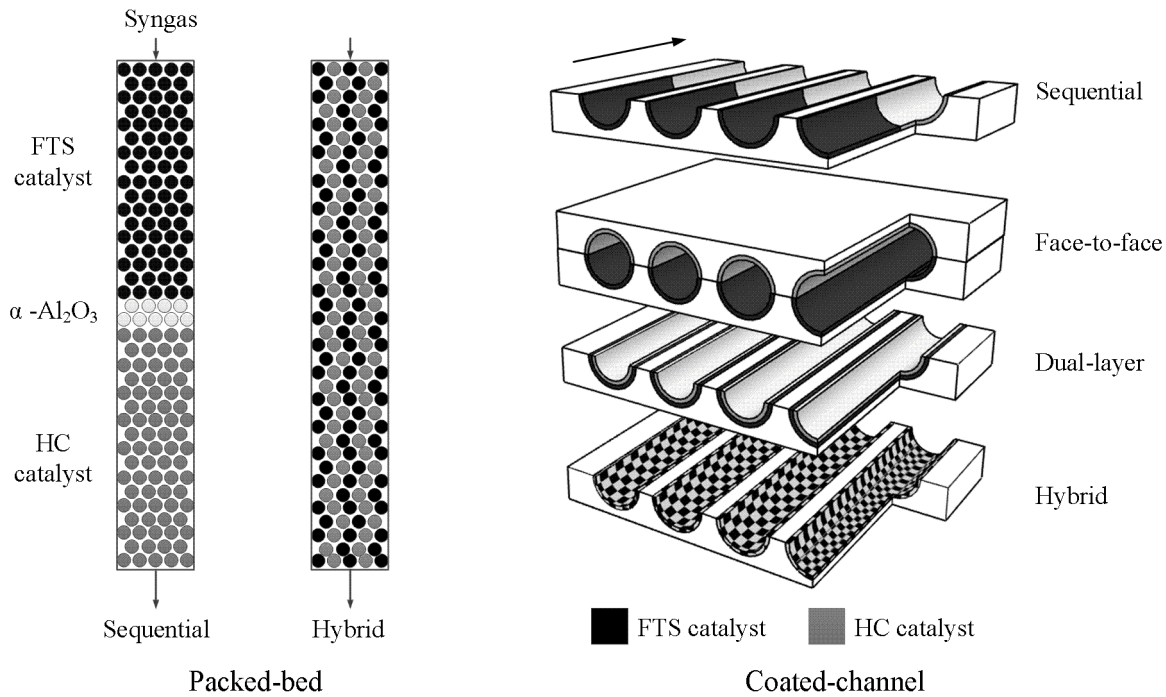


Figure 1–13 Catalyst configurations to integrate FTS with HC in micro packed-bed and microchannel reactors [87, 88]

One-stage FTS-HC integration in both micro packed-bed and microchannel reactors was implemented [87, 88]. The performance of different catalyst configurations, as well as different reactor types, was compared. The influence of temperature, pressure, H_2/CO ratio and syngas space velocity was investigated to figure out the optimum conditions for fuel synthesis and the reliability with unstable syngas supply. Interaction between FTS and HC in the integrated system was also analyzed.

Based on the experimental work, computational analysis by modelling and simulation was carried out [89]. Kinetic parameters for literature kinetic models were estimated with data from the micro packed-bed reactor. Different integration patterns were modelled with consideration of the vapor-liquid equilibrium (VLE). The influence of the condensed hydrocarbons was analyzed by simulation. Experimental and simulation results were compared to better understand the integrated process.

2. Experimental procedures and catalyst characterization results

2.1 Lab-scale micro-structured reactors

Micro-structured reactors play an important role for compact decentralized PtL plants. Instead of large pipes and vessels, micro-structured reactors have characteristic dimensions in the range of 50-2000 μm [90, 91], which generally lead to large wall area per volume and excellent heat transfer. The dramatically small passages in micro-structured reactors could narrow the residence time distribution and lead to precise fluid control (mixing, distribution, etc.). Application of super-active catalysts becomes possible. The advanced control could significantly improve safety, efficiency, etc. and reduce byproducts. The high space time yield of micro-structured reactors enables an overall volume reduction of 10 fold or more compared to conventional reactors. Higher efficiency, effectiveness and productivity of chemical processes have been achieved in micro-structured reactors [26-28, 69, 92-96]. All these features make micro-structured reactors an attractive option for decentralized small-scale PtL plants, where the highly exothermic FTS reaction is included.

To study process simplification by combing FTS with HC for decentralized small-scale PtL plants, integration configurations with catalyst in both powder-type and coated-layer were developed. Micro packed-bed and microchannel reactors were designed for each catalyst type, respectively.

2.1.1 Annular micro packed-bed reactor

For study of the integration of FTS and HC with powder-type catalyst configurations in the lab, an annular micro packed-bed reactor was developed (Figure 2-1). The catalyst bed was designed to be a 1.5 mm thick annular gap between two stainless steel tubes. Like in planar micro-structured reactors, good heat transfer performance is achieved due to the 1.5 mm narrow annular gap. The circulating thermal oil enables efficient removal of the heat generated from the FTS reaction. Near-isothermal operation can be assumed based on previous experience in planar micro packed beds with comparable slit size [27, 64]. Wall temperatures at the upper, middle and lower part of the reactor, as well as the oil temperature leaving the reactor, were measured.

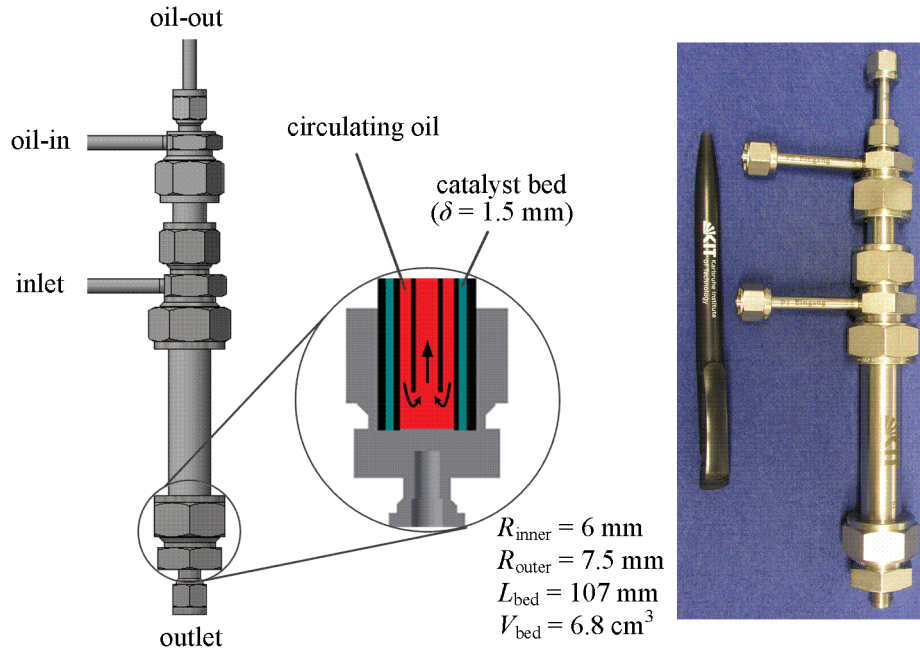


Figure 2–1 Annular micro packed-bed reactor [88]

Axial dispersion was neglected and plug flow behavior was assumed for the annular micro packed-bed reactor based on the Mears' criterion [97] (Eq. 2-1).

$$\frac{L_{bed}}{d_{particle}} > \frac{8}{Bo} \cdot n \cdot \ln\left(\frac{1}{1-X}\right) \quad \text{Eq. 2-1}$$

where n is the reaction order; X is the reactant conversion; Bo is the Bodenstein number (Eq. 2-2) [98].

$$\frac{1}{Bo} = \frac{\varepsilon \cdot D}{\tau \cdot d_{particle} \cdot u} + 0.5 \quad \text{Eq. 2-2}$$

where ε is the catalyst bed porosity; D is the bulk phase diffusion coefficient; τ is the catalyst bed tortuosity ($\tau = 1/\varepsilon^{0.5}$ [99]); u is the superficial velocity.

For a catalyst particle size of 100 μm , $L_{bed}/d_{particle}$ would be 1070. Assuming 60% H_2 conversion with 1st reaction order [100], a gas phase H_2 diffusion coefficient of $10^{-5} \text{ m}^2/\text{s}$, a bed porosity of 0.5 and a superficial velocity of 0.005 m/s, $8 \cdot n \cdot \ln(1/(1-X))/Bo$ would be around 55. The Mears' criterion is well satisfied.

Since the ratio $d_{bed}/d_{particle}$ was larger than 10, radial concentration gradients were also ignored [101]. Isobaric operation was assumed for the annular micro packed-bed reactor (Eq. 2-3) [102].

$$\frac{0.2 \cdot P}{n} > \Delta P \quad \text{Eq. 2-3}$$

where P is the reaction pressure; ΔP is pressure drop (Eq. 2-4).

$$\Delta P = \frac{1-\varepsilon}{\varepsilon^3} \cdot (1.75 + 150 \cdot \frac{1-\varepsilon}{Re}) \cdot \frac{\rho_{gas} \cdot u^2 \cdot L_{bed}}{d_{particle}} \quad \text{Eq. 2-4}$$

where Re is the Reynolds number ($Re = \rho_{gas} \cdot u \cdot d_{particle} / \mu_{gas}$); ρ_{gas} is the gas density; μ_{gas} is the gas dynamic viscosity.

With a gas density of 1.39 kg/m³ at 245 °C and 30 bar, and a hydrogen dynamic viscosity of 10⁻⁵ Pa s, a pressure drop of 161 Pa was estimated, which is far smaller than 0.2* P .

For tests in the annular micro packed-bed reactor, the FTS and HC catalysts were controlled to 1 g (weight ratio of 1:1 for the integration study) and the particle size was confined to 50-100 μ m. The catalysts were diluted with α -Al₂O₃ (50-100 μ m, Sigma-Aldrich) and carefully loaded into the reactor to guarantee a homogeneous packing.

2.1.2 Wall coated microchannel reactor

For study of the integration of FTS and HC with coated catalyst layers in the lab, microchannel reactors were developed (Figure 2-2&3). FTS and HC catalysts would be coated on stainless steel microchannel foils to generate catalytic foils, which would then be installed into microchannel reactors with different configurations.

Figure 2-2 shows the first microchannel reactor (MCR-I). Catalytic foils would be stacked in the reactor chamber with adapters to fill the entire space. According to the desired integration configuration, the foil stack could be adjusted to represent a single catalytic zone ($L_{foil} = 149.5$ mm) or two subsequent catalytic zones I and II ($L_{foil} = 73$ mm) (Figure 2-2a&b). For the case of two catalytic zones, two foil stacks are separated by a 4 mm thick frame in between. Sequential, face-to-face, dual-layer and hybrid integration configurations could be obtained by applying different catalytic foils.

The catalytic foil stack comprises 20 parallel foils arranged face-to-face to generate 10 layers of circular channels (Figure 2-2c). In each foil ($W \cdot H = 25 \cdot 0.3$ mm, Figure 2-2b), there are 22 etched semicircular channels ($\Phi = 500$ μ m).

The reaction temperature is controlled by circulating thermal oil or electric heating cartridge through the holes above and below the catalytic foil stack (Figure 2-2a). Temperature profile was measured by thermal couples inside and outside the reactor. A multipoint thermal couple was used to measure the temperature along the flow direction inside the reactor (Figure 2-2a, red points).

Via using circulating thermal oil for catalytic zone I (flowing through the holes) and electric heating cartridge for catalytic zone II (inserted in the holes), different temperatures could be applied in the two zones, which gives MCR-I a distinct additional feature for reaction control over conventional reactors. With independent FTS and HC reaction temperature, performance of the sequential integration could be flexibly controlled.

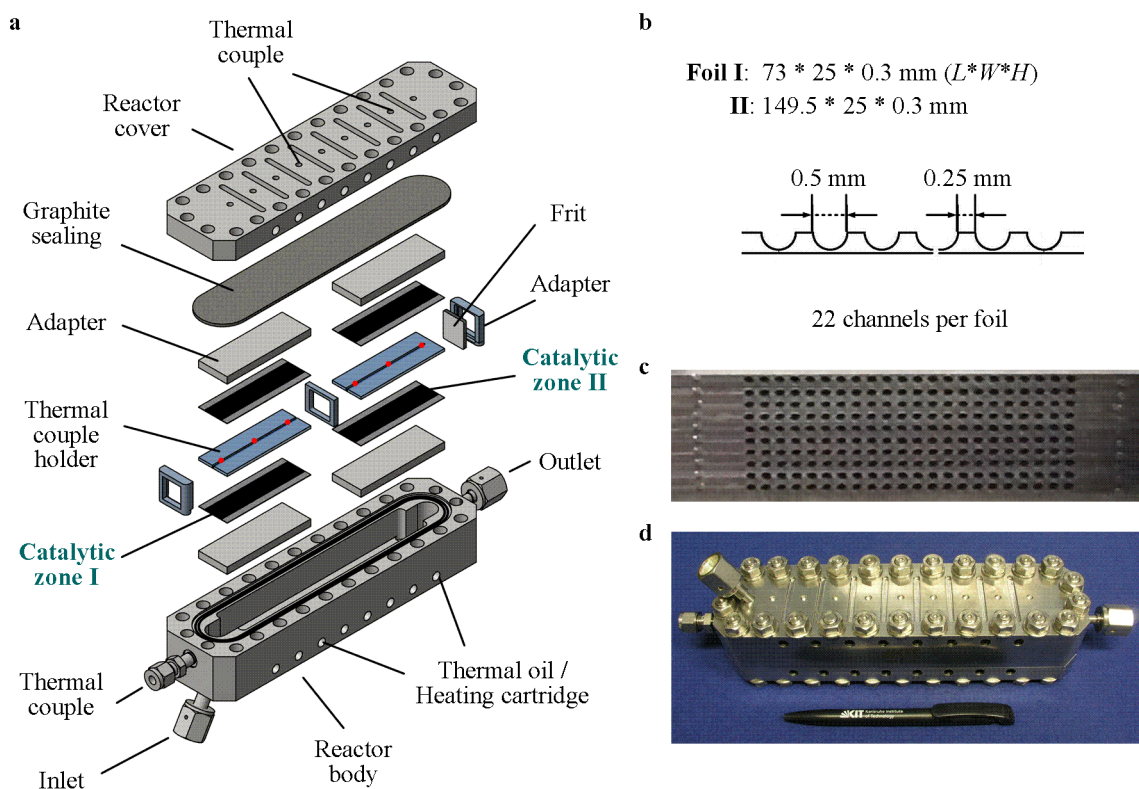


Figure 2–2 Microchannel reactor type I [87]

The second microchannel reactor (MCR-II) was designed for the face-to-face configuration (Figure 2-3), where the FTS temperature is controlled by circulating thermal oil and the HC temperature is controlled by electric heating cartridge. Flexible FTS and HC adjustment is also available due to the independent temperature control.

FTS and HC catalytic foils are inserted into the reactor body in the face-to-face pattern as a foil pair. Other than for the MCR-I, the temperature of each catalytic foil in one pair in the MCR-II is individually controlled. FTS and HC temperature inside the reactor was measured. A gas distributor was designed to ensure uniform syngas distribution in each foil pair.

8 foil pairs were used in the MCR-II. In each foil ($L*W*H = 150*50*3$ mm, Figure 2-3b), there are 44 milled rectangular channels ($W*H = 500*250$ μm). To ensure the independent FTS and HC temperature, the foil edge was designed to be 0.25 mm thicker than the channel

(Figure 2-3b), which generates a 0.5 mm gap between FTS and HC channels to reduce the direct contact.

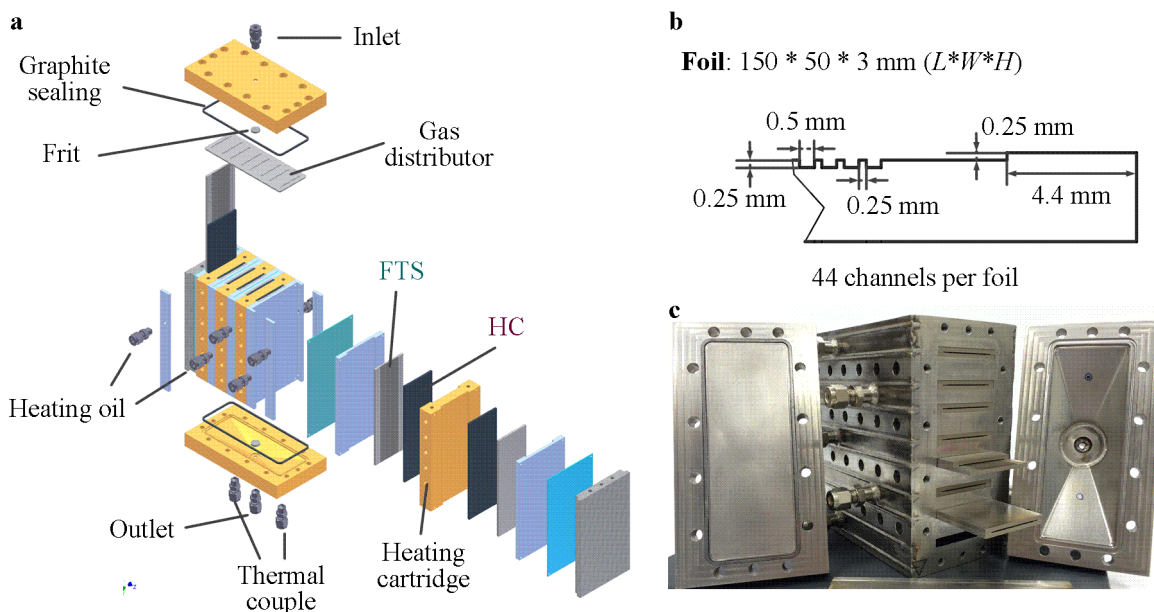


Figure 2–3 Microchannel reactor type II [87]

Every component of the reactor was fabricated precisely ($\pm 20 \mu\text{m}$) to avoid bypass.

Important reactor parameters of the different micro-structured reactors have been assessed and are compared in Table 2-1. Compared with a conventional multi-tubular reactor, the specific surface-to-volume ratio (S/V) of the micro-structured reactors is much higher (8.5 times for the annular micro packed-bed reactor, 51 times for the MCR-I and 18 times for the MCR-II), which indicates an increased contact between catalyst and reactor surface. The enlarged heat exchanging area per volume could significantly enhance the heat transfer performance, which is especially important for the highly exothermic FTS reaction. The small hydraulic diameter (d_h) of the micro-structured reactors indicates a short distance for heat and mass transport.

As mentioned in section 2.1.1, 1 g FTS catalyst and 1 g HC catalyst were determined for the integration study in the annular micro packed-bed reactor. With the same catalyst amount (2 g), layer thicknesses (δ_{cat}) of 48 and 24 μm would be obtained in MCR-I ($L_{\text{foil}} = 149.5 \text{ mm}$) and MCR-II, respectively. The large length-to-diameter ratio rules out the back-mixing effect. Compared to the micro packed-bed, much smaller pressure drop (ΔP) was obtained in wall-coated microchannels. To eliminate the influence between FTS and HC temperature, a 0.5 mm gap between FTS and HC channels was designed in MCR-II. Compared with MCR-I, a larger cross-sectional area and a lower gas velocity would be obtained. Accordingly, a lower Bodenstein number was estimated for MCR-II. Even so, axial dispersion has only limited influence ($10 < Bo < 100$). Radial concentration gradients could be ignored according to the

Péclet number ($Pe_{\text{rad}} < 0.01$). Plug flow behavior could be assumed for the micro-structured reactors.

Table 2-1 Comparison of the different micro-structured reactors

Reactor	S/V [m ⁻¹]	d_h [μm]	L/d_h	δ_{cat} [μm]	$u_{\text{superficial}}$ [m/s]	3Re	${}^4\Delta P$ [Pa]	5Bo	${}^6Pe_{\text{rad}}$
MCR-I	8000	500	300	48	5.1×10^{-3}	0.35	1	76	2.1×10^{-4}
MCR-II	2785	2993	151	24	8.7×10^{-4}	0.12	0.04	13	1.4×10^{-4}
Annular	1334	3000	36	50-100	3.4×10^{-3}	0.09	115	0.1	
¹ Gulf	157	25400	480						

$\rho_{\text{apparent}} = 1.6 \text{ g/cm}^3$, $\varepsilon_{\text{bed}} = 0.5$, at 245 °C, 30 bar and GHSV 10000 h⁻¹, if applicable;

¹ Gulf multi-tubular reactor with a 2.54 cm diameter and a 12.2 m length [103];

² $d_h = 4 * s_{\text{cross}} / L_{\text{perimeter}}$;

³ $\rho_{\text{gas}} = 1.39 \text{ kg/m}^3$, $\mu_{\text{gas}} = 10^{-5} \text{ Pa s}$, $d_{\text{particle}} = 100 \text{ μm}$;

⁴ $\Delta P = 32 * \mu * u * L / d_h^2$ [104], packed-bed see Eq. 2-2;

⁵ $Bo = u * L / D_{\text{ax}}$, $D_{\text{ax}} = D + u^2 * d_h^2 / 192 / D$, $D = 10^{-5} \text{ m}^2/\text{s}$ [104], packed-bed see Eq. 2-4;

⁶ Péclet number: $Pe_{\text{rad}} = u * d_h^2 / 4 / D / L$ [104]

2.2 Material preparation and characterization

Two types of micro-structured reactor, i.e. packed-bed and open-channel, were applied for study of the integration of FTS and HC. In the packed-bed reactor, a powder catalyst is required. Whereas in the open-channel reactor, the catalyst has to be coated on the channel wall. The catalysts were selected to meet the requirements of both reactor types. In this section, the preparation and characterization of FTS and HC catalysts, as well as the development of the screen-printing method, are described.

2.2.1 Preparation of FTS and HC catalysts

2.2.1.1 FTS catalyst

Most of group VIII metals (Fe, Co, Ni, Ru) were proved to have noticeable activity in the hydrogenation of carbon monoxide to hydrocarbons [53, 105, 106]. The high cost and low reserves of Ru and the high CH₄ selectivity of Ni make them less favorable for practical applications. Therefore, only Fe and Co based FTS catalysts are widely studied and used in academia and industry. Compared to Fe based catalysts, the negligible water-gas-shift (WGS) and oxygenate activity, lower olefin selectivity, higher hydrocarbon productivity and better

stability make the Co based catalysts the optimal option for the low-temperature Fischer Tropsch (LTFT) process.

Co-Re/Al₂O₃ was applied as the FTS catalyst in this work [45]. Re was added to improve the reducibility of the cobalt oxide particles, resulting from the faster hydrogen activation and subsequent H₂ spillover induced by Re [107]. To obtain a well adherent catalyst layer on the channel wall after coating, a particle size smaller than 10 μm is preferred [62, 108]. 20 wt.% Co and 0.5 wt.% Re were co-impregnated on a 3 μm γ-Al₂O₃ support (80-120 m²/g, Alfa Aesar). The γ-Al₂O₃ particles were stirred in a slurry containing Co(NO₃)₂·6H₂O and HReO₄ for 6 h to ensure a homogeneous Co and Re distribution throughout the support particles. After drying overnight at 120 °C, the catalyst was milled to break agglomerates and calcined at 400 °C for 2 h.

2.2.1.2 HC catalyst

Bifunctional catalysts with hydrogenation/dehydrogenation sites and acidic sites are the primary option for HC of FTS products [20, 39, 109-113]. Pt, Pd, and Ni are the generally used hydrogenation/dehydrogenation species in HC catalysts, among which Pt exhibits the highest activity. To obtain a high conversion of wax (C₂₁₊) while suppressing the formation of gas hydrocarbons (C₁-C₄), the acidic strength and the hydrogenation/dehydrogenation activity should be balanced [46, 113]. An increasing conversion of model hydrocarbons was observed until the Pt loading raises to 0.5 wt.% [112-115]. Silica-alumina and zeolites (ZSM-5 and β) are widely adopted as acidic supports in the HC of both model hydrocarbons [20, 21, 109, 116-121] and real FTS products (combined FTS-HC) [33-36, 38, 39, 45].

Pt-ZSM-5 was selected as the HC catalyst in this work [45]. NH₄-ZSM-5 (1.5 μm, 425 m²/g, SiO₂:Al₂O₃ mole ratio 80:1, Alfa Aesar) was calcined at 550 °C for 6 h to produce the H-ZSM-5. 0.5 wt.% Pt was impregnated by stirring the H-ZSM-5 in a precursor solution containing tetraamineplatinum(II) hydroxide (Pt 8-11 wt.%, Alfa Aesar) for 6 h. After drying overnight at 120 °C, the catalyst was calcined at 550 °C for 6 h.

2.2.2 Optimization of catalyst pastes for screen-printing

Compared to the catalyst packed-bed, a thin catalyst layer attached to the channel wall offers even better heat transfer and low pressure drop. Several methods, such as deposition (thin film) [122, 123], in-situ growth (zeolite) [124-127] and coating [128-133], are available to generate a catalyst layer on the channel surface, among which coating (wash-coating, screen-printing, etc.) is the most common way to prepare thick and porous catalyst layers. Screen-printing, due

to its automatic, reproducible and precise masking features, was selected to produce catalyst layers in microchannel foils [87].

A good catalyst layer should have uniform distribution, stable adhesion and good catalytic performance, which are all determined by the catalyst paste, as well as the drying and calcination procedure. The catalyst particle size and calcination process could influence the adhesion strength. The layer thickness is affected by solid concentration and viscosity of the paste. In addition, the shear thinning behavior is required for a screen-printable paste. The paste should stay static without being sheared by the squeegee (high viscosity, Figure 2-4a&c) and be able to flow through the screen when printing (low viscosity, Figure 2-4b).

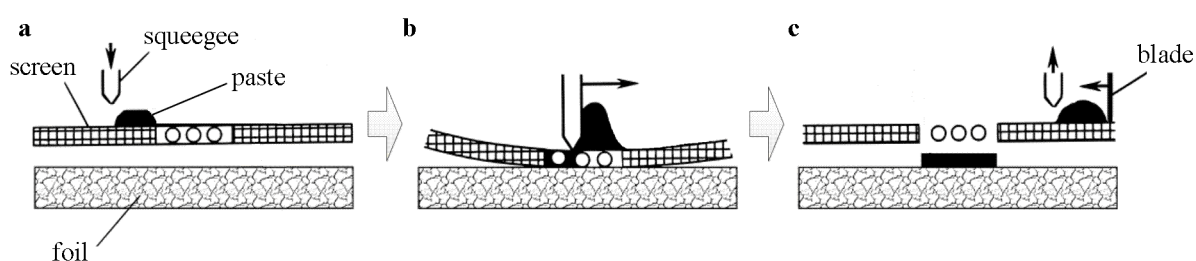


Figure 2–4 Schematic diagram of the screen-printing process

Terpineol (anhydrous, boiling point 213-218 °C, Sigma-Aldrich) was used as the solvent and ethyl cellulose (auto-ignition temperature 370 °C, Sigma-Aldrich) was used as the thickener. The composition of the paste was adjusted regarding rheological properties of the paste and mechanical stability of the coating layer. Details of the paste optimization are described in Appendix A1. The FTS catalyst paste was determined to be 4 vol.% Al_2O_3 (4.65 vol.% Co-Re/ Al_2O_3) and 4 vol.% cellulose. Whereas, the HC catalyst paste was determined to be 7 vol.% Pt-ZSM-5 and 6 vol.% cellulose.

The paste was homogenized in a three-roll-mill (EXAKT 50, EXAKT Technologies) for 30 min. Rheological properties of both pastes were measured as shown in Figure 2-5. For a screen-printable paste, the viscosity at 100 s^{-1} shear rate is preferred to be 10-20 Pa·s to obtain a good penetration through the screen [134]. The shear rate was kept at 0.1 s^{-1} in the first 50 s to represent the static state before printing. The viscosity remains constant at around 1000 and 90 Pa·s for FTS and HC catalyst pastes, respectively. Flow is obstructed by the high viscosity. Then the shear rate was set to 100 s^{-1} to simulate the squeegee movement in the printing process. The viscosity directly drops without any transition to around 12 and 17 Pa·s for FTS and HC catalyst pastes, respectively. During this period, the paste would flow into microchannels under the effect of gravity. After 50 s the shear rate was set back to 0.1 s^{-1} to indicate the end of the printing. The pastes quickly recover high viscosity and stop flowing.

The increasing curve in Figure 2-5 does not mean the viscosity recovery would be slow, but is because the rheometer cannot directly reach the 0.1 s^{-1} shear rate. Suitable rheological properties were obtained for both catalyst pastes.

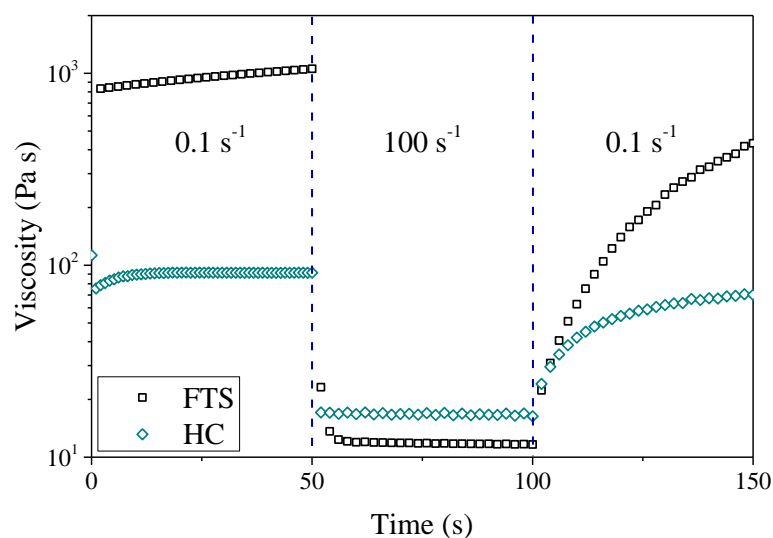


Figure 2–5 Viscosity change of FTS and HC catalyst pastes during screen-printing

Printing tests were carried out for both pastes. A screen with the same microchannel layout as the foil was designed (Figure 2-6a). To obtain a suitable amount of paste flowing through the screen, an opening with 72 mm length and 250 μm width was determined. The catalyst pastes were printed with a squeegee speed of 30 mm/s (EKRA M2, ASYS, Figure 2-6b). After drying at 120 $^{\circ}\text{C}$ for 8 h, the coated foils were calcined at 450 $^{\circ}\text{C}$ for 2 h to remove the cellulose. The weight loss was calculated after dropping three times from 1.2 m height. As listed in Table 2-2, the weight loss is less than 5%, indicating that the coated catalyst layer has reasonable mechanical stability. The screen-printing was carried out at the Institute for Applied Materials – Ceramic Materials and Technologies (IAM-KWT) at the Karlsruhe Institute of Technology.

Table 2-2 Viscosity and mechanical stability performance of FTS and HC catalyst pastes

paste	¹ viscosity (0.1 s^{-1})	¹ viscosity (100 s^{-1})	$m_{\text{single/foil}}$	$m_{\text{double/foil}}$	² weight loss
	[Pa·s]	[Pa·s]			
FTS	1.05e3	11.84	0.0246	0.0501	2.36
HC	91.39	16.75	0.0124	0.0250	4.03

¹ at 25 $^{\circ}\text{C}$ in HAAKE RheoStress 1 Rheometer (Thermo Scientific) with the C60/1 $^{\circ}$ -Ti cone;

² of double coating

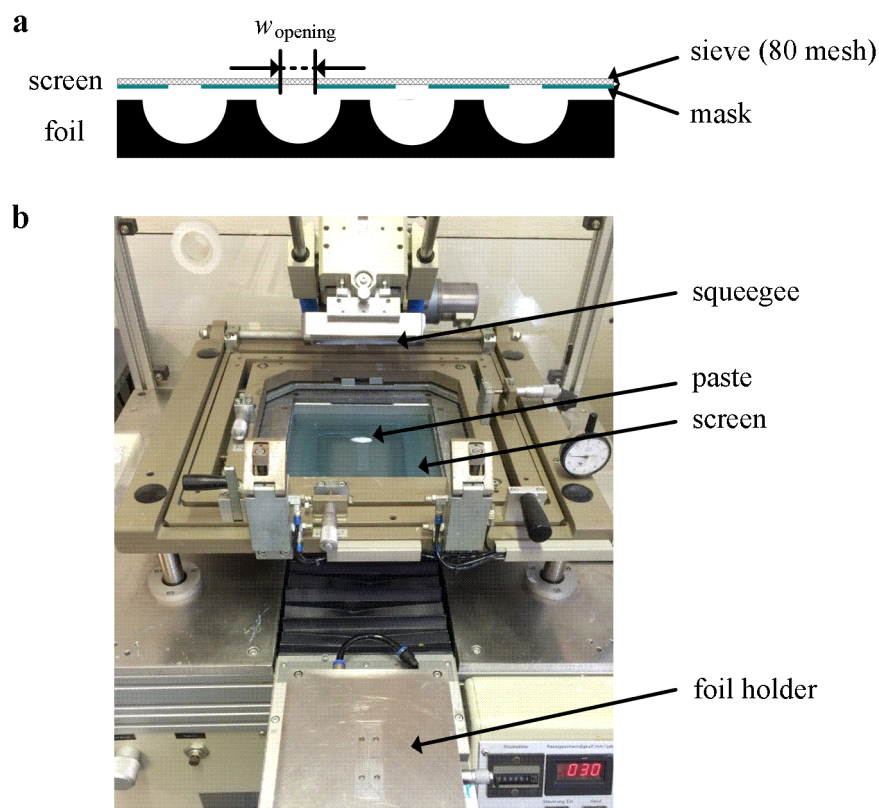


Figure 2–6 Schematic diagram of the screen (a) and the screen-printer (b)

2.2.3 Physical properties of original and coated catalysts

Properties of both catalyst supports and active metals were characterized for the home-made FTS and HC catalysts. Comparison between original catalyst particles and wall-coated catalyst layers was carried out to analyze the influence of the printing process. For characterization of the coated layer, catalysts were scraped off from the substrate.

2.2.3.1 Characterization methods

The morphology of the catalyst particles was characterized by transmission electron microscopy (TEM). Bright-field (BF) images of the HC catalyst were recorded in a Philips CM200FEG microscope at 200 kV with parallel illumination. For the FTS catalyst, high-angle annular dark-field scanning TEM (HAADF-STEM) images were recorded and the chemical composition was analyzed by energy dispersive X-ray spectroscopy (EDX) (FEI OSIRIS ChemiSTEM, 200 kV). The data was analyzed using the software ESPRIT (Bruker). The measurement was carried out at the Laboratory for Electron Microscopy (LEM) at the Karlsruhe Institute of Technology.

X-ray diffraction (XRD) patterns were recorded for both FTS and HC catalysts. A Bruker D8 Advance instrument equipped with a position-sensitive detector (PSD) Lynxeye[®] in θ - θ geometry, a variable divergence slit, and a 2.3° Soller-slit on the secondary side was used. Cu

anodes which utilize Cu K α _{1,2} radiation ($\lambda = 0.154$ nm) were used in the instrument. The XRD data was acquired over a 2θ range of 5-90°, with 336.04 s per 0.024° 2θ -step at 40 kV and 40 mA. The measurement was carried out at the Institute of Functional Interfaces (IFG) at the Karlsruhe Institute of Technology.

Catalyst surface area and pore volume were obtained from the N₂-adsorption/desorption isotherms measured at 77 K using an AUTOSORB-1 unit (Quantachrome Instruments). Before the measurement, the sample was outgassed at 300 °C for 2 h under vacuum. The specific surface area was obtained by applying the Brunauer-Emmett-Teller (BET) model [135] for adsorption at a relative pressure of 0.05-0.30. The total pore volume was calculated from the amount of N₂ adsorbed at a relative pressure of 0.99.

The Co dispersion was analyzed by H₂-chemisorption using an AUTOSORB-1 unit (Quantachrome Instruments). The catalyst was reduced online at 350 °C for 15 h in 5% H₂/Ar before the measurement. The amount of hydrogen chemisorbed on the catalyst was determined by interpolating the straight line portion of the isotherm to zero pressure (Langmuir method). The dispersion, surface area and average crystallite size of Co were calculated [136].

The total active metal content (Co and Re for the FTS catalyst and Pt for the HC catalyst) was analyzed by inductively coupled plasma optical emission spectrometry (ICP-OES) on an Optima 4300DV instrument (PerkinElmer). Before the measurement, all samples were digested with acid in the DAB-2 pressure digestion system (Berghof). The measurement was carried out at the Institute for Applied Materials – Applied Materials Physics (IAM-AWP) at the Karlsruhe Institute of Technology.

2.2.3.2 Analysis and comparison between original and printed catalysts

TEM images were recorded for both FTS and HC catalysts to study the catalyst morphology (Figure 2-7). According to HAADF images of the FTS catalyst, the particle size of the Al₂O₃ support is about 50-100 nm. Agglomerates were observed. The nano-sized particles are positive for both paste viscosity and coating adhesion. Relatively homogeneous Co dispersion in the FTS catalyst was observed in the EDX image (green color). No apparent difference was observed between the original and the scraped FTS catalyst. According to BF images of the HC catalyst, ZSM-5 has a much larger particle size (about 500-1000 nm) than Al₂O₃ in the FTS catalyst. No agglomeration was observed for the HC catalyst.

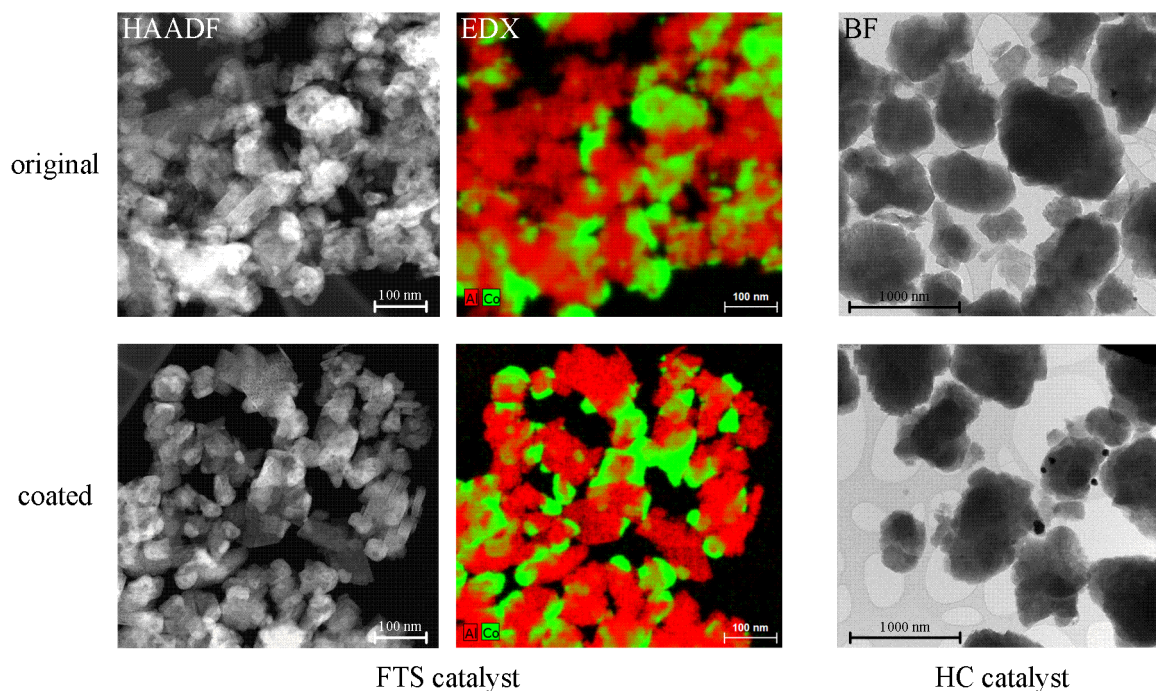


Figure 2–7 TEM images of the original and coated FTS and HC catalysts

Typical diffraction peaks of Co_3O_4 and Pt(111) crystallites were obtained in XRD patterns of FTS and HC catalysts, respectively. As illustrated in Figure 2-8, no difference was observed in qualitative comparison of original and printed samples.

The catalyst surface area and porosity data measured by N_2 physisorption are listed in Table 2-3. A lower surface area was observed for the scraped FTS catalyst (61 vs 51 $\text{m}^2/\text{g}_{\text{cat.}}$), which could be caused by the binding of nanoparticles in the coated layer. The scraped HC catalyst seems to have similar structural properties with the original one.

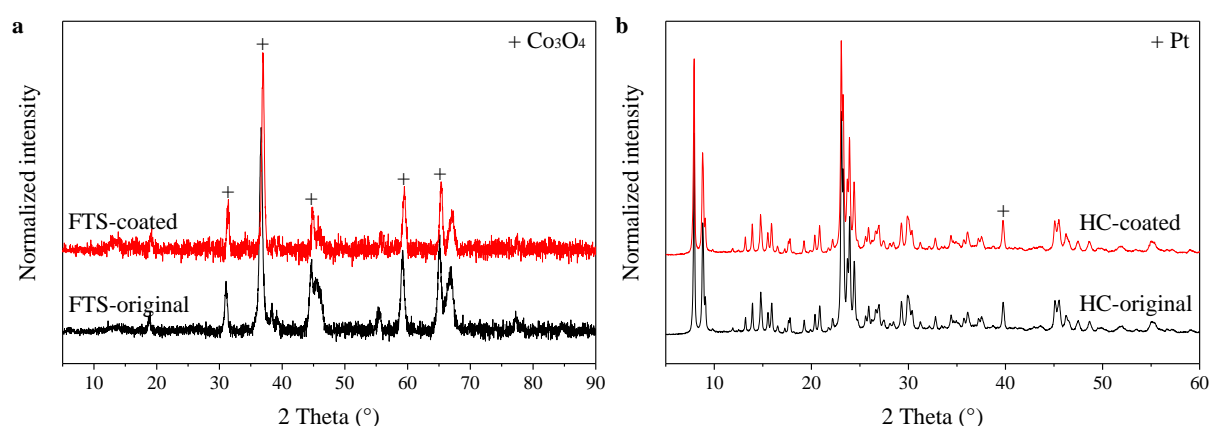


Figure 2–8 XRD patterns for FTS (a) and HC (b) catalysts [45]

No loss of active species (Co, Re, and Pt) was observed after coating (Table 2-3, ICP-OES). Co dispersion was characterized by H_2 -chemisorption. The number of Co surface sites depends on size, morphology, extent of reduction and stability of Co crystallite [107]. To improve the reducibility and dispersion of Co, 0.5 wt.% Re was added into the FTS catalyst as

a promoter. According to the temperature-programmed reduction (TPR), no peak was observed for the online-reduced sample. Co was assumed to be completely reduced under the chosen conditions. An average Co crystallite size of 20 nm was obtained for the home-made FTS catalyst. No apparent difference in average crystallite size and dispersion of Co was observed for the original and the scraped FTS catalyst.

Table 2-3 Physical properties of the original and coated FTS and HC catalysts [45]

sample	¹ S _{BET} [m ² /g _{cat.}]	¹ V _{pore} [cm ³ /g _{cat.}]	² d _{Co} [nm]	² s _{Co} [m ² /g _{cat.}]	² dispersion [%]	³ total [wt.%]
FTS-original	61	0.47	19.63	6.87	5.07	20.52
FTS-printed	51	0.50	20.34	6.19	4.90	20.63
HC-original	412	0.30 (⁴ 0.18)				0.53
HC-printed	408	0.30 (⁴ 0.18)				0.53

¹ from N₂ physisorption; ² from H₂-chemisorption; ³ from ICP-OES;

⁴ micro-pore volume calculated by the Horvath-Kawazoe method

2.2.4 Different configurations of wall-coated catalyst layers

As stated, different coating configurations were proposed for one-stage FTS-HC integration in micro-channel reactors. For sequential and face-to-face patterns, FTS and HC catalysts were printed independently and the combination was achieved via foil arrangement. For the dual-layer pattern, FTS catalyst was printed first and subsequently covered by a layer of the HC catalyst. A paste containing both FTS and HC catalysts was prepared for the hybrid pattern.

Back-scattered electron (BSE) and wavelength-dispersive spectroscopy (WDS) images were recorded for the cross-section of coated channels in an Electron Probe Microanalyzer (EPMA, JXA-8530FPlus, JEOL) to analyze the element distribution and thickness of the catalyst layers. The morphology of each coating was obtained from the top-view images.

As shown in Figure 2-9, catalyst layers are well distributed in the channel with uniform thickness. Cracks were observed in the FTS catalyst layers. Due to the larger particle size compared to the FTS catalyst, a larger void size was observed in the HC catalyst layer (Figure 2-9, dual-layer). After a second printing, the layer thickness increased from 20 to 40 and 20 to 37 μm for FTS and HC, respectively. In the triple-printed HC layer, a thickness of 54 μm was obtained. For sequential and face-to-face integration configurations, double-printed FTS and triple-printed HC layers were adopted to achieve a catalyst weigh ratio of 1.

For the dual-layer pattern, the FTS layer is completely covered by the HC layer with a clear boundary between each other. Both FTS and HC layers have a thickness of about 20 μm

(Table 2-4). Due to the difference in density, the weight ratio between the FTS and HC catalysts is 1.74.

Table 2-4 Properties of different catalyst layers

coating	¹ thickness [μm]	$m_{\text{FTS/foil}}$ [g]	$m_{\text{HC/foil}}$ [g]	$m_{\text{FTS}/m_{\text{HC}}}$
FTS-single	20	0.0267		
FTS-double	40	0.0516		
HC-single	20		0.0179	
HC-double	37		0.0352	
HC-triple	54		0.0523	
dual-layer	19 (FTS) + 20 (HC)	0.0262	0.0151	1/0.58
hybrid	50	0.0266	0.0247	1/0.93

¹ as marked by the white arrow in Figure 2-9

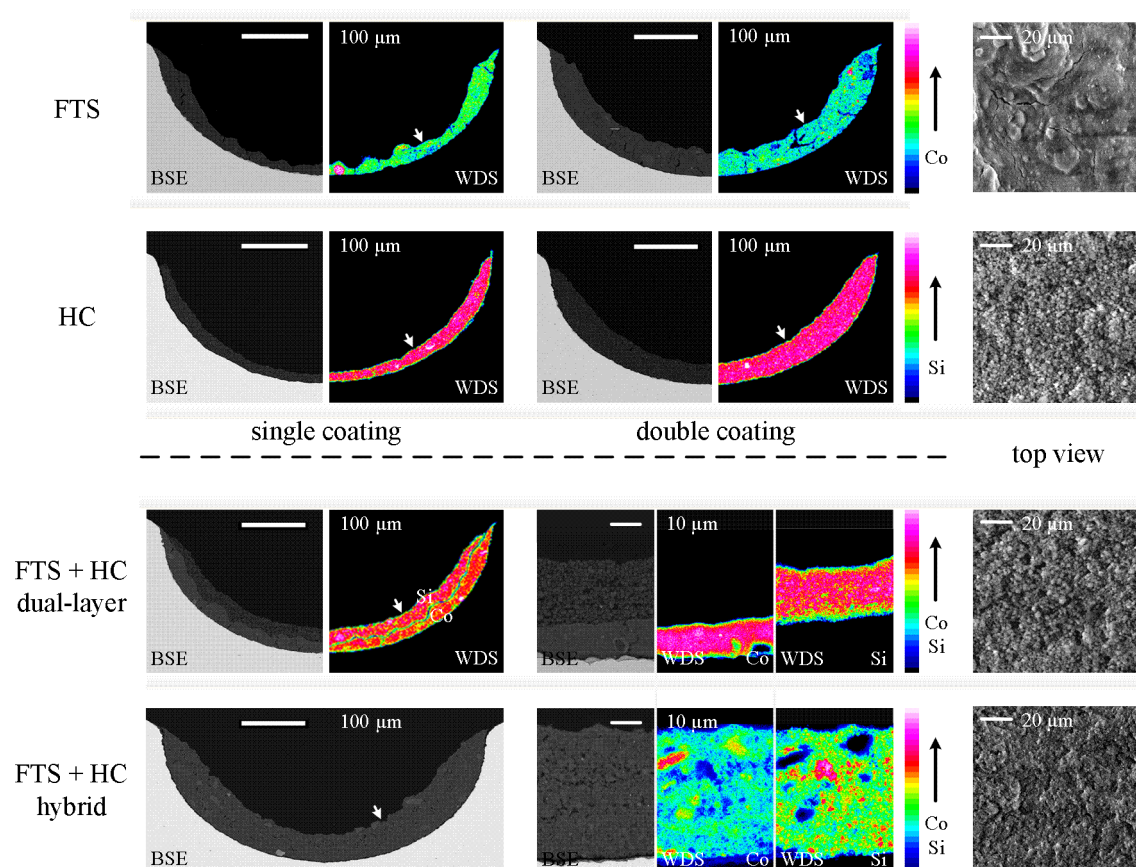


Figure 2-9 Characterization of different catalyst layers

The hybrid pattern was printed 3 times ($\sim 50 \mu\text{m}$) to achieve a certain catalyst amount. H-ZSM-5 has an apparent density of $\sim 1.5 \text{ g/cm}^3$ (terpineol and cellulose cannot enter the pores). The true density of Al_2O_3 is 3.95 g/cm^3 . In the hybrid paste with catalyst weight ratio of 1, the volumetric fraction of the HC catalyst is about 3 times larger than that of the FTS catalyst.

Accordingly, similar porosity and morphology like for the HC layer were observed in the hybrid layer (Figure 2-9).

2.3 Experimental setup

A lab-scale setup was built for the FTS-HC integration study (Figure 2-10&11). As shown in the flow diagram, the gases coming from the central gas network are filtered before entering the experimental setup. The gas flow rates are adjusted by mass flow controllers (MFC, Brooks Instrument), which are calibrated for the individual gases with the applied pressure and flow rate. Before mixing, all gases have to pass a ball valve and a non-return valve to secure the gas supply. After mixing, the gas flow is separated into two paths: one goes to the reactor and the other goes to the ventilation (Bypass 1).

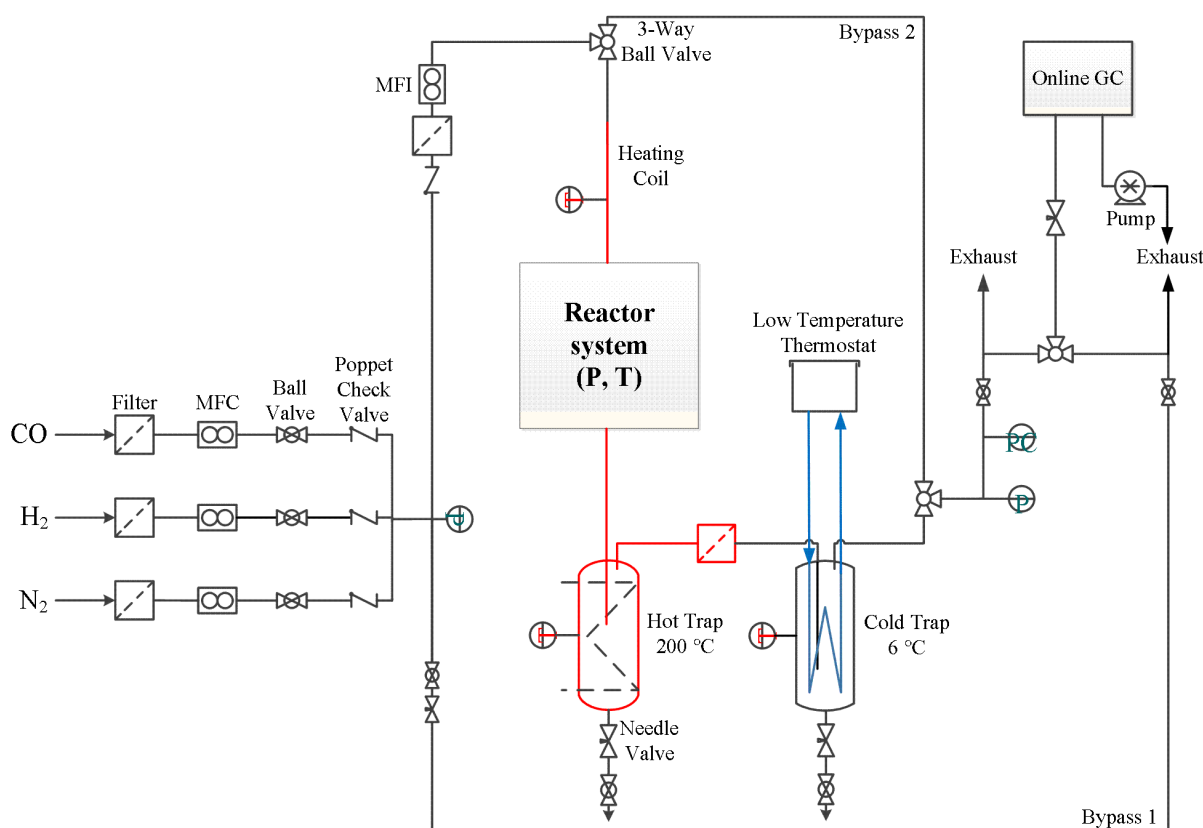


Figure 2–10 Flow diagram of the experimental setup for the FTS-HC integration study

The reactant flow is monitored by a mass flow meter (Brooks Instrument) and pre-heated to 150 °C before entering the reactor system, where different reactors would be installed according to the requirement. All components leaving the reactor system are first separated in a 200 °C hot trap, where the wax fraction (C_{10+}) is condensed. The leftover components then pass a 6 °C cold trap, where the liquid product fraction (C_5 - C_{30}) is condensed. At the end, the

residual gas is injected into an online gas chromatography (GC, 6890N, Agilent Technologies).

The reaction pressure is controlled by a back pressure regulator (Swagelok) installed after the cold trap. Both inlet and outlet pressure of the reactor system are measured to obtain the pressure drop. A second bypass (Bypass 2) was built to bypass the reactor system for security reasons. Since the system would be operated at high pressure and high temperature, a leak check was carried out at 30 bar with H₂ before each experiment.

The path connected to the online GC could be switched between the reactor system and Bypass 1. Bypass 1 is adjusted by a needle valve to 10-12 ml/min at 30 bar for the measurement of the feed composition.



Figure 2–11 Picture of the lab-scale setup

The experimental setup was operated in down flow mode. For each experiment, the catalyst was reduced online in 300 ml/min H₂ flow at 350 °C for 15 h with a temperature ramp of 1 °C/min at ambient pressure. After catalyst reduction the reactor temperature was set to 170 °C. The system was pressurized to 30 bar with H₂ and N₂ at the required flow rate. Then, CO was supplied to obtain the required feed composition. The reaction was started with a temperature ramp of 0.5 °C/min to the required value. The condensed samples were collected

by carefully controlling the valves below the cold and hot trap. After test, the reactor was flushed overnight with 300 ml/min N₂ at the working temperature and pressure before reduced to ambient pressure and cooled down.

2.4 Analysis methods

2.4.1 Product analysis

Product analysis was performed by gas chromatography (GC).

Residual gas leaving the cold trap, including inorganic components (H₂, CO, and N₂) and C₁-C₇ hydrocarbons, was analyzed in the online GC (6890N, Agilent Technologies, Figure 2-12).

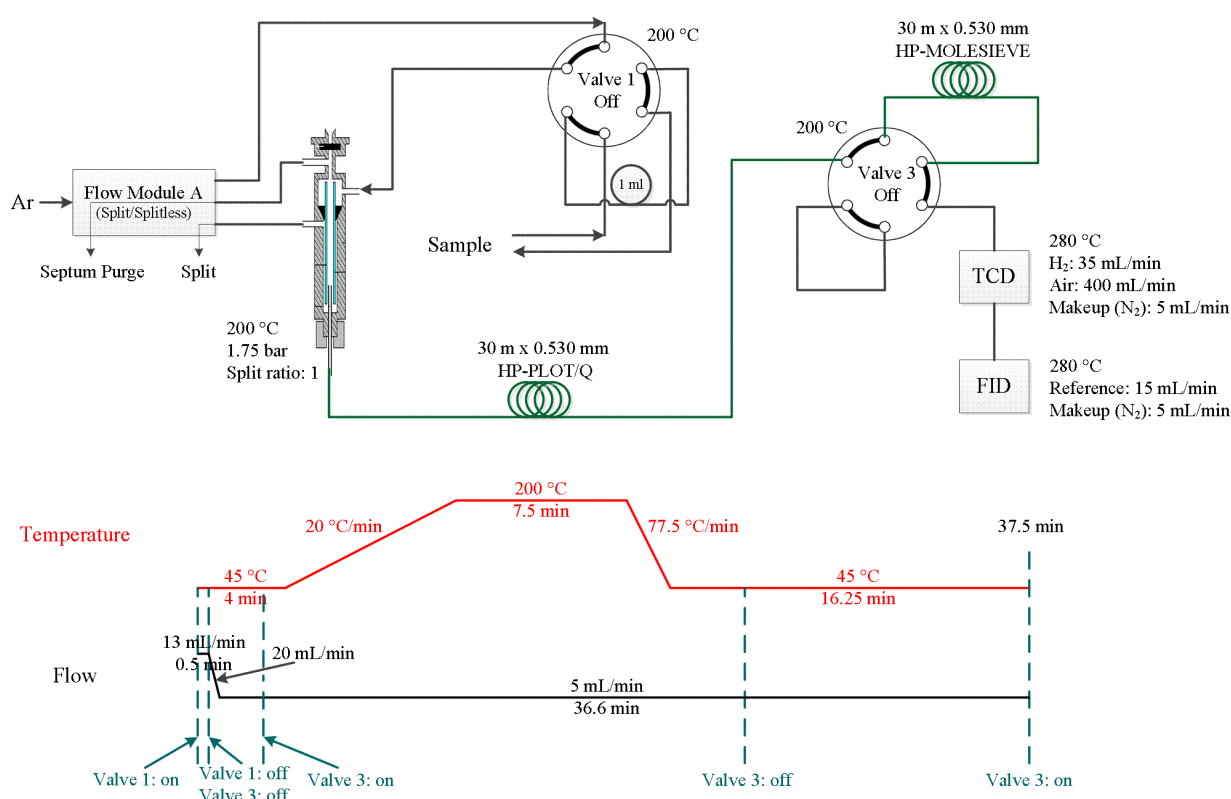


Figure 2–12 Flow diagram of the online gas chromatograph

The online GC is equipped with two columns and two detectors. H₂, CO, N₂ and CH₄ are separated in the HP-Molesieve 19095P-MS6 column ($L = 30$ m, $d = 0.53$ mm). C₂-C₇ hydrocarbons are separated in the HP-Plot/Q 19095P-Q04 column ($L = 30$ m, $d = 0.53$ mm). After injection from the sampling loop (valve 1: on), components are carried by Ar to the inlet, where the sample would be split with a ratio of 1. First, the two columns are connected (valve 3: off). H₂, CO, N₂ and CH₄ can hardly adsorb on the HP-Plot/Q column and therefore quickly get into the HP-Molesieve column. Then, the HP-Molesieve column will be bypassed (valve 3: on) to trap H₂, CO, N₂ and CH₄ in. After the C₂-C₇ hydrocarbons are separated using a

2. Experimental procedures and catalyst characterization results

temperature program and have left the HP-Plot/Q column, the HP-Molesieve column will be connected again to the system to separate H₂, CO, N₂ and CH₄.

The online GC was calibrated with standard gas mixtures (basi Schöberl) to obtain the retention time and the relation between signal and concentration. The peak area from the thermal conductivity detector (TCD) was used to obtain the content of H₂, CO, N₂ and CH₄. The peak area from the flame ionization detector (FID) was applied to obtain the content of the hydrocarbons (C₁-C₇). To analyze the composition of the sample, 3% N₂ was mixed with syngas as the internal standard.

The condensed hydrocarbons were analyzed in an offline GC (7820A, Agilent Technologies). As shown in Figure 2-13, the offline GC is equipped with a HP-5 19091J-413 column ($L = 30$ m, $d = 0.32$ mm) and a FID detector.

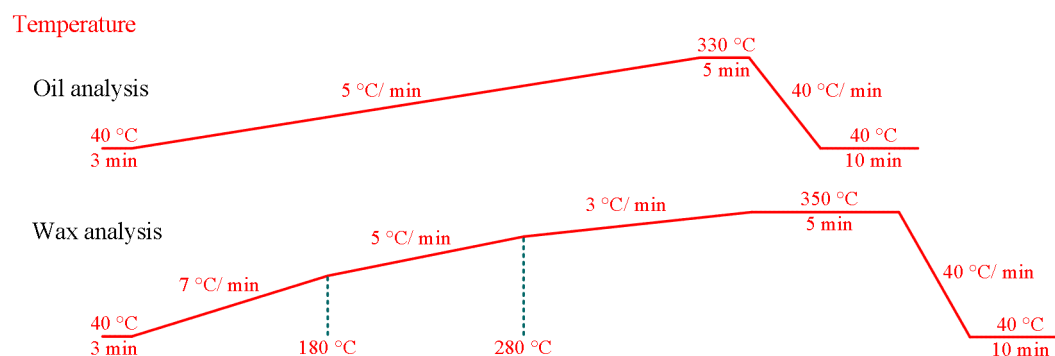
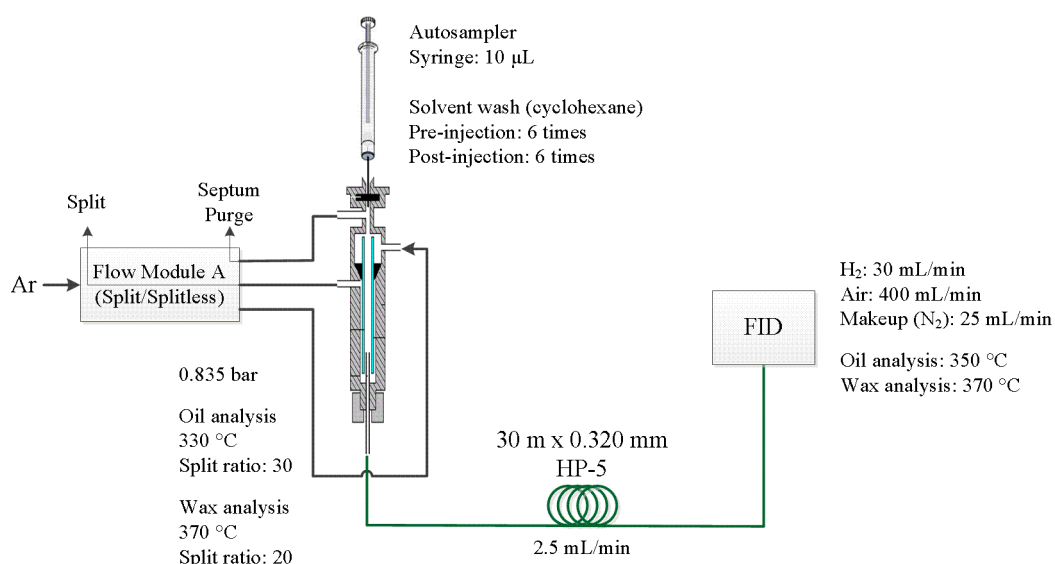


Figure 2–13 Flow diagram of the offline gas chromatograph

An autosampler was installed to inject samples into the GC. After being evaporated in the inlet, hydrocarbons are separated in the HP-5 column with a temperature program (Figure 2-13). The offline GC was calibrated with a standard hydrocarbon mixture (ASTM D2887 Quantitative Calibration Mix, Supelco). The mass fraction of each component was calculated

according to the peak area from the FID analysis. 1 μL sample was injected for each measurement. Before analysis, the solid hydrocarbons were dissolved in xylene using a weight ratio of 1:50 and kept at 60 $^{\circ}\text{C}$.

The syngas conversion and the selectivity of $\text{C}_1\text{-C}_4$ hydrocarbons were quasi-continuously measured in the online GC. The productivity of the condensed hydrocarbons was calculated according to the collected samples within a time of 14-16 h from hot and cold trap in steady state. Together with the mass fraction measured in the offline GC, the entire product distribution could so be obtained.

2.4.2 Data analysis

The conversion of a reactant i is defined as:

$$X_i = (\dot{n}_{i,in} - \dot{n}_{i,out}) / \dot{n}_{i,in} \quad \text{Eq. 2-5}$$

where \dot{n}_i is the molar flow rate of reactant i .

The FTS selectivity of a hydrocarbon species j was defined based on the amount of CO converted:

$$S_j = (\dot{n}_{j,out} - \dot{n}_{j,in}) \cdot j / (\dot{n}_{\text{CO},in} - \dot{n}_{\text{CO},out}) \quad \text{Eq. 2-6}$$

where j is the carbon number of hydrocarbon species j .

The mass fraction of a hydrocarbon species i is defined as:

$$w_i = m_i / \sum m_j \quad \text{Eq. 2-7}$$

where m_i is the mass of component i in g.

The reactor averaged consumption rate of H_2 and CO in FTS is defined as:

$$r_{\text{H}_2} = (\dot{n}_{\text{H}_2,in} - \dot{n}_{\text{H}_2,out}) / m_{\text{FTS-cat.}} \quad \text{Eq. 2-8}$$

$$r_{\text{CO}} = (\dot{n}_{\text{CO},in} - \dot{n}_{\text{CO},out}) / m_{\text{FTS-cat.}} \quad \text{Eq. 2-9}$$

where r_{H_2} and r_{CO} are in $\text{mol}/(\text{g}_{\text{cat.}} \cdot \text{h})$; $m_{\text{FTS-cat.}}$ is the FTS catalyst mass in g.

The reactor average reaction rate of a hydrocarbon species i is defined as:

$$r_i = (\dot{n}_{i,in} - \dot{n}_{i,out}) / m_{\text{cat.}} \quad \text{Eq. 2-10}$$

where r_i is in $\text{g}/(\text{g}_{\text{cat.}} \cdot \text{h})$; $m_{\text{cat.}}$ is the FTS or HC catalyst mass in g.

2.5 Experimental conditions

The experiments discussed in this dissertation were implemented at conditions of $T = 215$ - 280 °C, $P = 20$ - 30 bar, H_2/CO ratio = 1.6 - 2.0 and $WHSV = 6$ - 12 g/(g_{FTS-cat.}·h). For the integration study, the weight ratio between FTS and HC catalysts was controlled to 1, except the dual-layer configuration with wall-coated catalysts ($m_{FTS}/m_{HC} = 1.7$). The detailed operating conditions are listed in the Appendix A4.

3. FTS-HC integration in micro-structured reactors

To investigate the feasibility of different catalyst configurations, i.e. sequential and hybrid for catalyst powder, sequential, face-to-face, dual-layer and hybrid for printed catalyst layer, for process integration at different operating conditions (temperature, pressure, H₂/CO ratio and syngas space velocity), experiments and simulations were performed in different reactor types with a view to selectivity and productivity of the targeted liquid fuel fraction. Since heavy hydrocarbons are involved in the integrated FTS-HC system, the condensation of big molecules would generate a liquid phase in the catalyst bed, which may in turn affect the reaction performance owing to mass transport limitations, solvent effect, etc. Experiments designed to detect and quantify the formation of a liquid phase under typical FTS process conditions are extremely challenging, if possible at all. Therefore, a digital twin of the system was generated by setting up an appropriate computational model. This model was adopted to study the development and the influence of the liquid in the integrated system. The relation between FTS and HC in the integrated process was analyzed to derive deeper understanding of the implications of the process integration, which could help further tailoring and optimizing the integrated FTS-HC process.

3.1 Computational analysis

Computational analysis was applied to aid the study of the integrated FTS-HC process. The kinetics of the FTS and HC reactions was analyzed based on kinetic models from literature for which parameter estimates were derived by non-linear regression using the experimental data. Different integration configurations were modeled and simulated. Special attention was paid to the influence of the liquid phase, including mass transport and pore filling.

In this dissertation, H₂, CO, N₂, H₂O and hydrocarbons from C₁ to C₅₀ were considered. It was assumed the n-paraffin and iso-paraffin with the same carbon number have the same thermodynamic properties (density, vapor pressure, viscosity, etc.).

3.1.1 FTS and HC reaction kinetics

3.1.1.1 FTS kinetics

The complicated nature of the FTS reaction is reflected by its complex product spectrum. Even though discovered nearly a century ago, the mechanism of FTS is still under debate [17, 100, 137-154]. Being a catalyzed polymerization reaction taking place on the catalyst surface,

the elementary steps of FTS can be divided into reactant adsorption, chain initiation, chain growth, chain termination and product desorption. According to the difference in nature of the monomer incorporated into the growing carbon chain, the proposed mechanisms could be divided into three categories: carbide [17], CO insertion [139, 155] and oxygenate (enol) [138, 156, 157] mechanism (Table 3-1). The carbide mechanism by CH₂ insertion, which was first formulated by Fischer and Tropsch in 1926 [17], is the most accepted mechanism for the hydrocarbon formation on cobalt and iron. The CH₂ monomer is formed via hydrogenation of the carbon atom generated from CO dissociation. The hydrocarbon chain growth happens by the addition of one monomer at a time. Before leaving the catalyst surface, the growing intermediate would be terminated in different ways, giving rise to alkane, alkene or oxygenate.

Table 3-1 Overview of FTS mechanisms

	Carbide mechanism [17]	CO insertion mechanism [139]	Enol mechanism [138]
Initiation	CO → C + O C + 2H → CH ₂ O + 2H → H ₂ O	CO + H → HCO HCO + H → H ₂ CO H ₂ CO + 3H → CH ₃ + H ₂ O	CO + 2H → HCOH
Growth	R + CH ₂ → RCH ₂	R + CO → RCO RCO + H → RHCO RHCO + 3H → RCH ₂ + H ₂ O	RCOH + HCOH → RCCOH + H ₂ O RCCOH + 2H → RCH ₂ COH
Termination	RCH ₂ + H → RCH ₃ RCH ₂ CH ₂ → RCH=CH ₂ + H RCH ₂ + CO → oxygenates	RCH ₂ + H → RCH ₃ RCO + nH → oxygenates	RCOH + 4H → RCH ₃ + H ₂ O RCH ₂ COH + nH → oxygenates

R = H, alkyl

Based on the FTS mechanism, different kinetic models were developed to simulate, design and optimize the FTS process. However, detailed models that can predict the entire distribution of hydrocarbons are difficult to establish owing to the great number of possible chain lengths. Many kinetic models, therefore, lump products into groups [158-160] for simplification. Empirical macro-kinetic models, where the reactant consumption and the product distribution are separately considered, were derived [18, 100, 161, 162], but are only applicable if there is a rate-determining step in the formation of the monomer and the hydrocarbon products can be assumed not to affect the monomer formation. In addition, to

predict the entire product distribution, detailed micro-kinetic models were proposed [141, 145, 149, 150, 163-165].

The micro-kinetic model reported by Kwack et al. was applied in this dissertation to simulate the reaction system of FTS [149]. The carbide mechanism with CH₂ insertion was adopted to set up the kinetic model (Table 3-2). Since only limited amount of olefins and oxygenates were produced by the Co catalyst, the production of oxygenates and olefins was neglected. Reversible dissociative adsorption of H₂ was assumed. The adsorption of CO was assumed to be reversible as well, while the dissociation of adsorbed CO was assumed to be irreversible.

Table 3-2 Reaction mechanism for Co-catalyzed FTS [149]

No.	Elementary steps		
1	$H_2 + 2* \rightleftharpoons 2H^*$	$K_{H_2}^{ad} = \theta_{H^*}^2 \cdot c_{H_2}^{-1} \cdot \theta_*^{-2}$	
2	$CO + * \rightleftharpoons CO^*$	$K_{CO}^{ad} = \theta_{CO^*} \cdot c_{CO}^{-1} \cdot \theta_*^{-1}$	
3	$H_2O + * \rightleftharpoons H_2O^*$	$K_{H_2O}^{ad} = \theta_{H_2O^*} \cdot c_{H_2O}^{-1} \cdot \theta_*^{-1}$	Adsorption
4	$CO^* + * \rightarrow C^* + O^*$	$r_{CO} = k_{CO} \cdot \theta_{CO^*} \cdot \theta_*$	
5	$C^* + H^* \rightarrow CH^* + *$	$r_C = k_C \cdot \theta_{C^*} \cdot \theta_{H^*}$	
6	$CH^* + H^* \rightarrow CH_2^* + *$	$r_{CH} = k_{CH} \cdot \theta_{CH^*} \cdot \theta_{H^*}$	
7	$O^* + H^* \rightarrow OH^* + *$	$r_{OH} = k_{OH} \cdot \theta_{O^*} \cdot \theta_{H^*}$	
8	$OH^* + H^* \rightarrow H_2O + 2*$	$r_{H_2O} = k_{H_2O} \cdot \theta_{OH^*} \cdot \theta_{H^*}$	
9	$CH_2^* + H^* \rightarrow CH_3^* + *$	$r_{IN} = k_{IN} \cdot \theta_{CH_2^*} \cdot \theta_{H^*}$	initiation
10	$R_i^* + CH_2^* \rightarrow R_{i+1}^* + *$	$r_{G,i} = k_G \cdot \theta_{R_i^*} \cdot \theta_{CH_2^*}$	($i \geq 1$) growth
11	$CH_3^* + H^* \rightarrow CH_4^* + *$	$r_{CH_4} = k_{CH_4} \cdot \theta_{CH_3^*} \cdot \theta_{H^*}$	termination
12	$CH_3CH_2^* + H^* \rightarrow C_2H_6 + 2*$	$r_{C_2H_6} = k_2 \cdot \theta_{R_2^*} \cdot \theta_{H^*}$	
13	$R_i^* + H^* \rightarrow C_iH_{2i+2} + 2*$	$r_i = k_i \cdot \theta_{R_i^*} \cdot \theta_{H^*}$	($i \geq 3$)

R = alkyl; i indicates the carbon number of paraffin.

The reaction rate expressions developed from the elementary steps are listed as follows:

$$r_{CH_4} = k_{CH_4} \cdot A_1 / DEN \quad \text{Eq. 3-1}$$

$$r_{C_2H_6} = k_2 \cdot k_G \cdot A_{CH_2} / (k_G \cdot A_{CH_2} + k_2 \cdot A_H) \cdot A_1 / DEN \quad \text{Eq. 3-2}$$

$$r_i = k_i \cdot \left(\frac{k_G \cdot A_{CH_2}}{k_G \cdot A_{CH_2} + k_i \cdot A_H} \right)^{i-2} \cdot \frac{k_G \cdot A_{CH_2}}{k_G \cdot A_{CH_2} + k_2 \cdot A_H} \cdot A_1 / DEN \quad (i \geq 3) \quad \text{Eq. 3-3}$$

$$r_{CO} = -\sum_{i=1}^{50} i \cdot r_i \quad \text{Eq. 3-4}$$

$$r_{H_2} = r_{CO} - \sum_{i=1}^{50} (i+1) \cdot r_i \quad \text{Eq. 3-5}$$

$$DEN = \left(1 + A_H + A_{CH_2} + \frac{A_1}{A_H} \cdot \left(1 + \sum_{i=2}^{50} \left(\frac{k_G \cdot A_{CH_2}}{k_G \cdot A_{CH_2} + k_i \cdot A_H} \right)^{i-2} \cdot \frac{k_G \cdot A_{CH_2}}{(k_G \cdot A_{CH_2} + k_2 \cdot A_H)} \right) \right)^2 \quad \text{Eq. 3-6}$$

$$A_1 = k_{IN} \cdot A_{CH_2} \cdot A_H^2 / (k_G \cdot A_{CH_2} + k_{CH_4} \cdot A_H) \quad \text{Eq. 3-7}$$

$$A_H = (K_{H_2}^{ad} \cdot c_{H_2})^{0.5} \quad \text{Eq. 3-8}$$

$$A_{CH_2} = \frac{-k_{IN} \cdot A_H + \sqrt{(k_{IN} \cdot A_H)^2 + 4 \cdot k_{IN} \cdot k_G / k_i \cdot k_{CO} \cdot K_{CO}^{ad} \cdot c_{CO}}}{2 \cdot k_{IN} \cdot k_G / k_i} \quad \text{Eq. 3-9}$$

where k is the reaction rate constant; K^{ad} is the adsorption equilibrium constant; c is the concentration; subscript i denotes the carbon number of the respective paraffin; subscript IN and G denote chain initiation and chain growth, respectively.

3.1.1.2 HC kinetics

HC of a hydrocarbon denotes a reaction stoichiometry in which one or more carbon-carbon bonds are broken, and the created free valencies are saturated by hydrogen [46]. Bifunctional catalysts comprised of both hydrogenation/dehydrogenation and acidic active sites are generally applied [20, 21, 45, 109, 110, 112, 113, 115, 116, 118, 121, 166-190]. HC of an n-alkane starts from the dehydrogenation at the hydrogenation/dehydrogenation site (often a noble metal) to form the corresponding n-alkene (Figure 3-1). The n-alkene then desorbs from the metal site and migrates to the acidic site where it would be protonated to the carbenium ion ($n\text{-C}_i\text{H}_{2i+1}^+$). The carbenium ion $n\text{-C}_i\text{H}_{2i+1}^+$ would rearrange to the iso- $\text{C}_i\text{H}_{2i+1}^+$, which would either be deprotonated to the iso-alkene, or undergo β -scission, i.e. cracking, to form a smaller carbenium ion and an alkene. The generated alkenes could diffuse to the metal site and be hydrogenated to alkanes.

The first HC kinetic model was reported in the 1980s [191, 192]. The reaction products were lumped as n-paraffin, iso-paraffin and cracked products as shown in the simplified scheme:

n-paraffin \rightleftharpoons iso-paraffin \rightarrow cracked products

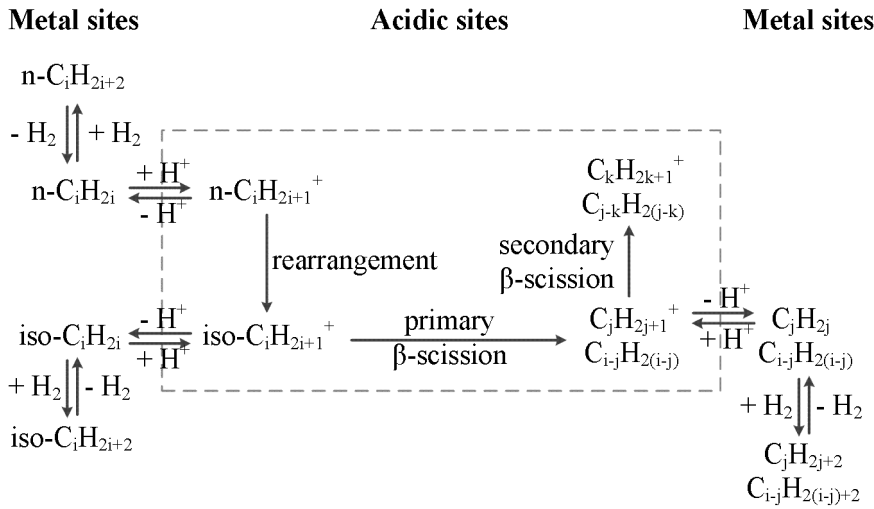


Figure 3–1 Mechanism of HC on a bifunctional catalyst [46]

The HC of long-chain hydrocarbons is mainly considered as an ideal form of HC, where the primary β -scission is dominant [45, 185]. The Langmuir-Hinshelwood-Hougen-Watson (LHHW) approach was widely used to develop kinetic equations for HC [193-200], where the adsorption/desorption and the hydrogenation/dehydrogenation were assumed to be in quasi-equilibrium. Rearrangement of the carbenium ion was verified to be the rate limiting step [192, 201], which indicates the acid function of the catalyst determines the kinetics.

An “all-component” kinetic model from literature was adopted in this dissertation [200]. Yet due to the numerous possibilities of isomers for long-chain hydrocarbons, a pseudo-component “iso-paraffin”, which represents all isomers with the same carbon number, was applied. In this model, it was assumed that hydrocarbons with a carbon number smaller than 6 would not be further cracked. Methane and ethane are only generated from the cracking of iso-hexane. n-butane does not undergo isomerization and iso-butane is only formed from cracking of heavier hydrocarbons. iso-heptane would be cracked into equal amounts of pentane and iso-butane. The cracking of an aliphatic chain with eight or more carbon atoms would follow a probability function (Figure 3-2) to resemble the bell-like cracking product distribution: the C-C bonds between C_4 and C_{i-3} would be cracked with the same probability (p); the 3rd terminal C-C bonds would be cracked with a probability of p/2; the 1st and 2nd terminal C-C bonds would not be cracked.

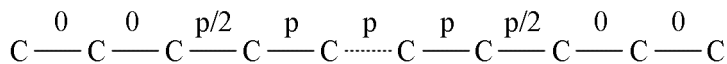


Figure 3–2 Cracking probability of different C-C bonds [200]

The overall rate expression for hydrocarbon component i is calculated as a combination of three items: isomerization (R_{iso-r} , k_{iso-r}), cracking (R_{cr-r} , k_{cr-r}), and formation from the cracking of longer molecules ($R_{form} = f(R_{cr-r})$).

$$R_{iso-r,i} = k_{iso-r,i} \cdot (c_{n,i} - c_{iso,i} / K_{eq,i}) / ADS \quad \text{Eq. 3-10}$$

$$R_{cr-r,i} = k_{cr-r,i} \cdot c_{iso,i} / ADS \quad \text{Eq. 3-11}$$

$$R_{form,iso,i} = 0.903 \sum_{j=i+4}^{50} (2 \cdot R_{cr-r,j} / (j-6)) + R_{cr-r,i+3} / (i-3) \quad (i = 4 \sim 46) \quad \text{Eq. 3-12}$$

$$R_{form,iso,47} = R_{cr-r,50} / (i-3) \quad \text{Eq. 3-13}$$

$$R_{form,n,i} = 0.097 \cdot \sum_{j=i+4}^{50} (2 \cdot R_{cr-r,j} / (j-6)) \quad (i = 4 \sim 46) \quad \text{Eq. 3-14}$$

$$R_{form,3} = \sum_{j=7}^{50} (R_{cr-r,j} / (j-6)) \quad \text{Eq. 3-15}$$

$$ADS = c_{H_2} \cdot (1 + \sum_1^{50} c_{n,i} \cdot K_{n,i}^{ad} + \sum_4^{50} c_{iso,i} \cdot K_{iso,i}^{ad}) \quad \text{Eq. 3-16}$$

where k is the reaction rate constant; K_{eq} is the equilibrium constant of isomerization; K^{ad} is the Langmuir adsorption equilibrium constant; c is the concentration; subscript i and j denote the carbon number of the paraffins; subscript n and iso indicate n-paraffin and iso-paraffin, respectively; subscript $iso-r$ and $cr-r$ denote isomerization and cracking reaction, respectively.

The reaction rate expressions for each hydrocarbon component are listed as follows:

$$r_{iso,i} = R_{iso-r,i} + R_{form,iso,i} - R_{cr-r,i} \quad (i = 6 \sim 50) \quad \text{Eq. 3-17}$$

$$r_{iso,5} = R_{iso-r,5} + R_{form,iso,5} \quad \text{Eq. 3-18}$$

$$r_{iso,4} = R_{form,iso,4} \quad \text{Eq. 3-19}$$

$$r_{n,i} = -R_{iso-r,i} + R_{form,n,i} \quad (i = 6 \sim 50) \quad \text{Eq. 3-20}$$

$$r_{n,5} = -R_{iso-r,5} + R_{form,n,5} + 0.4 \cdot R_{cr-r,6} \quad \text{Eq. 3-21}$$

$$r_{n,i} = R_{form,n,i} + 0.4 \cdot R_{cr-r,6} \quad (i = 3, 4) \quad \text{Eq. 3-22}$$

$$r_i = 0.4 \cdot R_{cr-r,6} \quad (i = 3, 4) \quad \text{Eq. 3-23}$$

$$r_{H_2} = \sum_6^{50} R_{cr-r,i} \quad \text{Eq. 3-24}$$

where subscript n and iso indicate n-paraffin and iso-paraffin, respectively.

3.1.2 Vapor-liquid equilibrium

Due to the existence of long-chain hydrocarbons (e.g. C₃₀, C₅₀, etc.) in the FTS product and HC feed, a liquid phase would appear in the reaction system. Possible influence of the liquid phase on the FTS and HC reactions is expected due to solvent effects, solubility difference, reduced diffusivity, etc., which would change the local composition, mass transport, etc. By adjusting vapor-liquid equilibrium (VLE) of the system, experimental observations confirmed effects of the liquid phase on both FTS and HC [88, 185, 202]. Caldwell and van Vuuren were the first to introduce VLE into the modelling of FTS [203]. The importance of the VLE has been more and more recognized in the last decade [198-200, 203-212]. Raoult's Law [75, 102, 203, 206], as well as Peng-Robinson and Soave-Redlich-Kwong equations of state [205, 207, 212, 213], were adopted for the VLE calculation of the FTS or HC system. Ideal behavior was proven to be a reasonable assumption for both the vapor and the liquid phase [204, 209, 214].

Raoult's Law (Eq. 3-25) was adopted in this dissertation to calculate the VLE in the FTS and HC system.

$$K_i = x_{V,i} / x_{L,i} = P_i^{vap} / P \quad \text{Eq. 3-25}$$

where $x_{V,i}$ and $x_{L,i}$ are the molar fractions of species i in the vapor and liquid phase, respectively; P_i^{vap} is the vapor pressure of species i [204]; P is the system pressure; K_i is the vapor-liquid distribution ratio of species i .

The Rachford-Rice flash equation (Figure 3-3, Eq. 3-26&27) [215] was used to calculate the composition of the vapor and the liquid phase.

$$\sum_i \frac{x_i \cdot (K_i - 1)}{1 + n_V / n \cdot (K_i - 1)} = 0 \quad \text{Eq. 3-26}$$

$$x_{L,i} = \frac{x_i}{1 + n_V / n \cdot (K_i - 1)} \quad \text{Eq. 3-27}$$

where x_i is the molar fraction of species i in the entire system; n_V and n represent the molar amounts of the vapor phase and the entire system, respectively.

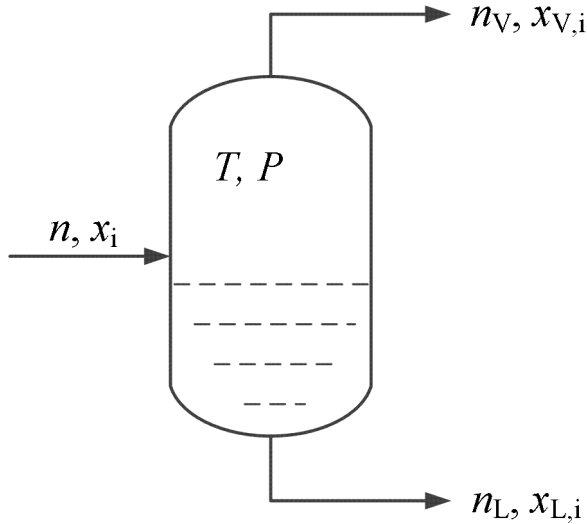


Figure 3–3 Scheme of a flash tank

The vapor pressure of C_{6+} hydrocarbons was calculated using the method reported by Marano and Holder (Eq. 3-28 to 3-30) [204].

$$P_i^{vap} = \exp(2.72709 + A \cdot (i - 1.126231) - B \cdot \exp(-0.619226 \cdot (i - 1.126231)^{0.416321})) \quad \text{Eq. 3-28}$$

$$A = 15.8059 - 1496.56 / T - 2.17342 \cdot \log(T) + 7.27763e - 7 \cdot T^2 + 37876.2 / T^2 \quad \text{Eq. 3-29}$$

$$B = -5.75509 - 7.56568 / T + 0.0857734 \cdot \log(T) - 1.41964e - 5 \cdot T^2 + 267209 / T^2 \quad \text{Eq. 3-30}$$

where P^{vap} is in bar; T is the temperature in K; i is the carbon number of the hydrocarbon.

A hypothetical vapor pressure was formulated for the non-condensable components (H_2 , CO , H_2O , N_2 , C_1 - C_5) based on data extracted from Aspen by calculating the VLE of a FTS output with the ideal model (Eq. 3-31&32).

$$P_{H_2}^{vap} = 14425.23882 \quad \text{Eq. 3-31}$$

$$P_i^{vap} = A + B \cdot \exp(-T / C) \quad \text{Eq. 3-32}$$

where P^{vap} is in bar; T is the temperature in K.

Being mainly composed of condensed heavy hydrocarbons, the liquid was represented by the hydrocarbon with the same carbon number ($M_{w,L} = \sum(M_{w,i} \cdot x_{L,i}) = 14 \cdot N_L + 2$, where N_L is the average carbon number of the liquid). Properties of the hydrocarbon $C_{N_L}H_{2N_L+2}$ were adopted for the liquid. The concentration of H_2 , CO , H_2O and N_2 in the liquid was calculated using Henry's Law (Eq. 3-33) [204]. The concentration of hydrocarbons in the liquid was calculated using the method reported by van Vuuren et al. (Eq. 3-34) [216].

$$H_i = 1000 \cdot \rho_L / M_{w,L} / \exp(A + B/T + C \cdot \ln(T) + D \cdot T^2 + E/T^2 - N_L \cdot F) \quad \text{Eq. 3-33}$$

$$S_i = 1000 \cdot \rho_L / M_{w,L} / P_i^{vap} \quad \text{Eq. 3-34}$$

where H_i is the Henry coefficient of species i in mol/m³/bar; ρ_L is the density of the liquid in kg/m³ [217]; $M_{w,L}$ is the average molecular weight of the liquid in g/mol; T is the temperature in K; S_i is the solubility of species i in mol/m³/bar; P_i^{vap} is the vapor pressure of species i in bar.

Table 3-3 Parameters for Eq. 3-32

	<i>A</i>	<i>B</i>	<i>C</i>
CO	11368.06	-14019.3	1054.485
H ₂ O	-11.862	0.06266	-77.93
N ₂	9755.494	-12367.56	895.5961
CH ₄	-32127.424	30363.027	-4720.7295
C ₂ H ₆	-774.753	282.085	-325.646
C ₃ H ₈	-213.7745	39.86443	-209.2483
C ₄ H ₁₀	-75.8279	7.03519	-154.819
C ₅ H ₁₂	-31.8087	1.4759	-124.011

Table 3-4 Parameters for Eq. 3-33 [204]

	<i>A</i>	<i>B</i>	<i>C</i>	<i>D</i> ×10 ⁶	<i>E</i>	<i>F</i> ×10 ⁻²
H ₂	12.9353	22.9058	-0.974709	-1.20408	2244.61	2.00959
CO	5.79833	19.5937	0.152199	-1.89733	2031.63	1.73238
N ₂	7.88232	14.4370	-0.0648305	0	-465952	6.05329
H ₂ O	8.44317	49.5974	-0.278896	-1.30377	4378.02	1.81705

3.1.3 Reaction-diffusion in the catalyst

With the accumulation of heavy hydrocarbons inside the catalyst, the catalyst pores could be filled with liquid. The reduced diffusivity in the liquid could lead to mass transfer limitation. To investigate influence of the mass transfer inside the catalyst (particle or coated-layer), the reaction-diffusion model was applied.

3.1.3.1 Reaction-diffusion in the particle

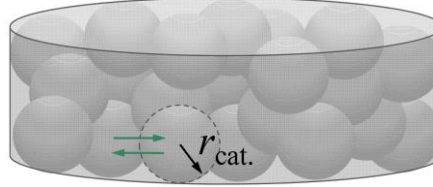
The material balance in the catalyst particle is given by Eq. 3-35.

$$D_{eff,i} \cdot \left(\frac{d^2 c_i}{dr^2} + \frac{2}{r} \cdot \frac{dc_i}{dr} \right) = R_i \quad \text{for spherical catalyst particle} \quad \text{Eq. 3-35}$$

with the boundary conditions:

$$\frac{dc_i}{dr} \Big|_{r=0} = 0 \quad \text{Eq. 3-36}$$

$$c_i \Big|_{r=r_{cat.}} = c_{s,i} \quad \text{Eq. 3-37}$$



where $D_{eff,i}$ is the effective diffusion coefficient of species i ($D_{eff,i} = D_i \cdot \varepsilon / \tau$, where ε is the catalyst porosity; τ is the catalyst tortuosity), R_i is the volumetric reaction rate of species i ; $r_{cat.}$ is the radius of catalyst particle; c_s is the concentration at the external catalyst surface.

3.1.3.2 Reaction-diffusion in the coated-layer

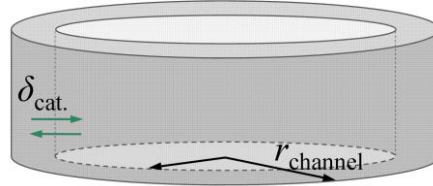
The material balance in the coated catalyst layer is given by Eq. 3-38.

$$D_{eff,i} \cdot \left(\frac{d^2 c_i}{dr^2} + \frac{1}{r} \cdot \frac{dc_i}{dr} \right) = R_i \quad \text{for cylindrical coated-layer} \quad \text{Eq. 3-38}$$

with the boundary conditions:

$$\frac{dc_i}{dr} \Big|_{r=r_{channel}} = 0 \quad \text{Eq. 3-39}$$

$$c_i \Big|_{r=(r_{channel}-\delta_{cat.})} = c_{s,i} \quad \text{Eq. 3-40}$$



where $r_{channel}$ is the radius of microchannel; $\delta_{cat.}$ is the thickness of coated catalyst layer.

The reaction-diffusion model was solved using the *bvp4c* function in Matlab (Release 2017a).

For diffusion in the gas phase, the binary molecular diffusion coefficient was calculated according to Fuller's method (Eq. 3-41) [218, 219]:

$$D_{i,j} = \frac{0.00143 \cdot T^{1.75} \cdot \sqrt{1/M_{w,i} + 1/M_{w,j}}}{P \cdot \sqrt{2} \cdot (\sqrt[3]{\sum \Delta_{V,i}} + \sqrt[3]{\sum \Delta_{V,j}})^2} \quad \text{Eq. 3-41}$$

where $D_{i,j}$ is the binary diffusion coefficient of species i in cm^2/s ; T is the temperature in K, M_w is the molecular weight in g/mol; P is the pressure in bar; Δ_v is the diffusion volume, which is determined with the group contributions from Table 3-5.

Table 3-5 Group contributions for the diffusion volumes in the Fuller method [219]

atom or molecule	C	H	H ₂	CO	H ₂ O	N ₂
contribution	15.9	2.31	6.12	18	13.1	18.5

The diffusion coefficient in multicomponent gas mixture was calculated according to Blanc's Law (Eq. 3-42) [220, 221]:

$$D_{mix,i} = \left(\sum_{j \neq i} \frac{x_j}{D_{i,j}} \right)^{-1} \quad \text{Eq. 3-42}$$

In case of the gas diffusion, the catalyst surface concentration equals to the bulk concentration.

For diffusion in the liquid phase, the diffusion coefficient was calculated according to Wilke's method (Eq. 3-43) [222]:

$$D_{L,i} = 7.4e - 11 \cdot \frac{T \cdot M_{w,L}^{0.5}}{\mu_L \cdot V_{m,i}^{0.6}} \quad \text{Eq. 3-43}$$

where $D_{L,i}$ is the liquid diffusion coefficient of species i in cm²/s; T is the temperature in K, $M_{w,L}$ is the average molecular weight of liquid in g/mol; μ_L is the dynamic viscosity of liquid in Pa·s [221]; $V_{m,i}$ is the molar volume of species i at normal boiling point in cm³/mol (H₂: 14.3, CO: 30.7, H₂O: 18.9, N₂: 31.2). The molar volume of hydrocarbons was calculated according to the Schroeder method with the group contribution of 7 for both H and C atoms [223].

In case of the liquid diffusion, the catalyst surface concentration was calculated from the bulk concentration using Henry's Law.

Effectiveness factor was calculated to analyze the possible mass transfer limitation inside the catalyst (Eq. 3-44).

$$\eta = \frac{D_{eff,i} \cdot \frac{dc_i}{dr} \cdot ds_{cat.}}{R_i \cdot dV_{cat.}} \quad \text{Eq. 3-44}$$

where dc_i/dr is the concentration gradient at the catalyst surface; R_i is the volumetric reaction rate calculated with the catalyst surface concentration; $ds_{cat.}$ and $dV_{cat.}$ are the catalyst external surface area and volume in each reactor cell, respectively.

3.1.4 Reactor modelling

Isothermal operation was achieved in all micro-structured reactors employed in this dissertation owing to the high heat transfer rates typical of these systems. Moreover, the pressure drop proved to be negligible both in the annular micro packed-bed reactor and in the wall-coated microchannel reactors. Plug flow behavior was assumed according to the estimation in section 2.1 based on Mear's criterion and Bodenstein number.

An isothermal, isobaric plug flow reactor model was adopted to simulate the integrated FTS-HC process in micro-structured reactors. Only the steady state behavior is treated by the model. Homogeneous bulk phase was applied in each cell of the cascade reactor model (Figure 3-4).

The material balance of species i in each cell is shown in Eq. 3-45.

$$u(x) \cdot c_i(x) \cdot s_{cross} = u(x+dx) \cdot c_i(x+dx) \cdot s_{cross} + d\dot{n}_{R,i} \quad \text{Eq. 3-45}$$

where $u(x)$ and $u(x+dx)$ are the axial linear velocity at reactor cell inlet and outlet, respectively; $c_i(x)$ and $c_i(x+dx)$ are the concentration of species i at reactor cell inlet and outlet, respectively; s_{cross} is the cross-section area of the reactor cell; dx is the length of the reactor cell; $d\dot{n}_{R,i}$ is the material change of species i caused by reaction in the reactor cell.

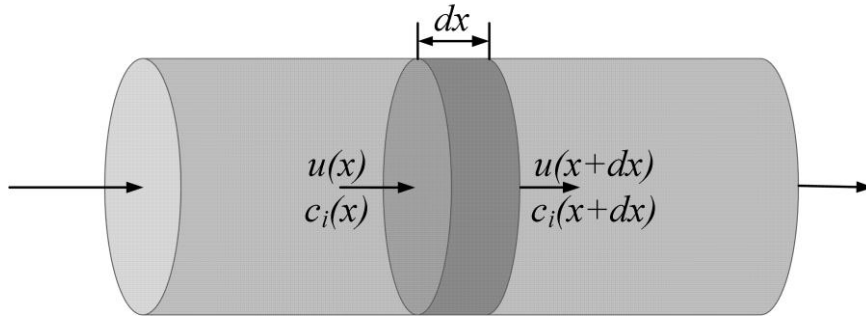


Figure 3–4 Schematic diagram of the cascade plug flow reactor model

For a homogeneous model, the material change of species i in each cell is given by Eq. 3-46.

$$\dot{n}_{R,i} = dV_{cat.} \cdot R_i(x+dx) \quad \text{Eq. 3-46}$$

where $dV_{cat.}$ is the catalyst volume in each reactor cell; $R_i(x+dx)$ is the volumetric reaction rate of species i calculated with the catalyst surface concentration.

For a heterogeneous model, the material change of species i in each cell is given by Eq. 3-47.

$$\dot{n}_{R,i} = ds_{cat.} \cdot j_i(x+dx) = ds_{cat.} \cdot D_{eff,i} \cdot \frac{dc_i}{dr} \quad \text{Eq. 3-47}$$

where $ds_{cat.}$ is the catalyst external surface area in each reactor cell; $j_i(x+dx)$ is the molar flux of species i between the catalyst and the bulk phase; dc_i/dr is the concentration gradient of species i at the catalyst surface.

3.1.5 Pore filling model

Liquid phase would appear in FTS or HC due to the condensation of heavy hydrocarbons. To investigate the local accumulation of hydrocarbons in FTS, the pore filling model reported by Pöhlmann et al. was adopted [224].

As shown in Figure 3-5, the accumulation rate of liquid hydrocarbon i in FTS ($dn_{L,i}/dt$) is given by the interplay of formation in the pore ($r_{reaction,i}$) and evaporation out of the pore ($r_{evaporation,i}$) (Eq. 3-48).

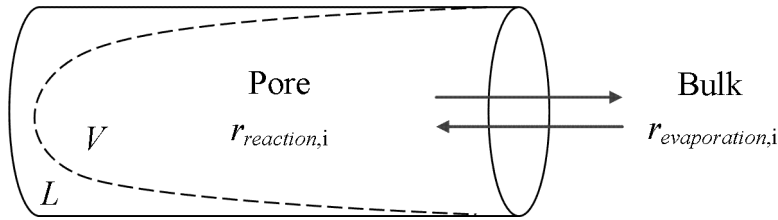


Figure 3–5 Schematic diagram of the mass balance of liquid hydrocarbons in the catalyst pore

$$\frac{dn_{L,i}}{dt} = r_{reaction,i} + r_{evaporation,i} \quad \text{Eq. 3-48}$$

Only hydrocarbons with a carbon number larger than 10 (C_{11+}) were assumed to be condensable. The liquid hydrocarbons in the pore was assumed to be in VLE. The evaporation was assumed to be only limited by external diffusion into the bulk gas phase. The accumulation of liquid hydrocarbon i in the pore takes place in accordance with the BET multilayer adsorption theory, where the vapor pressure ($P_i^{vap,BET}$) is determined by the pore filling degree (F) (Eq. 3-49).

$$F = \frac{V_L}{V_{cat.} \cdot \varepsilon} = \frac{F_{mono} \cdot 100 \cdot \frac{P_i^{vap,BET}}{P_i^{vap}} \cdot \left(1 - (n_{max} + 1) \cdot \left(\frac{P_i^{vap,BET}}{P_i^{vap}}\right)^{n_{max}} + n_{max} \cdot \left(\frac{P_i^{vap,BET}}{P_i^{vap}}\right)^{n_{max}+1}\right)}{\left(1 - \frac{P_i^{vap,BET}}{P_i^{vap}}\right) \cdot \left(1 + 99 \cdot \frac{P_i^{vap,BET}}{P_i^{vap}} - 100 \cdot \left(\frac{P_i^{vap,BET}}{P_i^{vap}}\right)^{n_{max}+1}\right)}$$

Eq. 3-49

where V_L is the liquid volume; $V_{cat.}$ is the catalyst volume; ε is the catalyst porosity; F_{mono} denotes the filling degree with monolayer adsorption ($F_{mono} = (r_{pore}^2 - (r_{pore} - \delta_i)^2)/r_{pore}^2$); n_{max} is the maximum molecule layers in a cylindrical pore ($n_{max} = r_{pore}/\delta_i$, where r_{pore} is the radius

of cylindrical pores; δ_i is the monolayer thickness of the adsorbed molecule i). The monolayer thickness of the adsorbed molecule was set to 0.3 nm.

The evaporation of liquid hydrocarbon i is defined in Eq. 3-50.

$$r_{evaporation,i} = -\beta_i \cdot \varepsilon \cdot S_{cat.} \cdot \frac{P_i^{vap,BET} \cdot x_{L,i}}{R \cdot T} \quad \text{Eq. 3-50}$$

The mass transfer coefficient was defined in Eq. 3-51.

$$\beta_i = Sh \cdot D_i / d_{cat.,char} \quad \text{Eq. 3-51}$$

where Sh is the Sherwood number; $d_{cat.,char}$ is the characteristic length of the catalyst particle.

The liquid volume was defined in Eq. 3-52.

$$V_L = m_L / \rho_L = (\sum n_{L,i} \cdot M_{w,i}) / \rho_L \quad (\text{with } n_{L,i} = n_{L,i} + dn_{L,i} \cdot dt) \quad \text{Eq. 3-52}$$

3.2 FTS reference of different catalyst configurations

Stand-alone FTS experiments were carried out as a reference for the integrated process. The FTS performance of the powder type catalyst in the micro packed-bed reactor and of the wall-coated catalyst in the microchannel reactor were both investigated. The FTS kinetics was estimated based on the derived experimental data. Complete filling with liquid in the catalyst was confirmed. The influence of the liquid hydrocarbons was studied using a heterogeneous model.

3.2.1 FTS reference with powder catalyst in the micro packed-bed reactor

As references for the FTS-HC integration in the annular micro packed-bed reactor, two catalyst configurations were studied, where the FTS Ref. I corresponds to the sequential bed and FTS Ref. II corresponds to the hybrid bed (Figure 3-6). To compare with the wall-coated catalyst layer, the powder catalyst was prepared from the FTS catalyst paste with the same procedure as for the screen-printing. After drying and calcination on a flat plate, the layer was scraped and the catalyst was pelletized, crushed and sieved to 50-100 μm . Near-isothermal operation ($\Delta T \leq 2 \text{ }^\circ\text{C}$) was obtained in the annular micro packed-bed reactor.

CO conversion for both reference cases is plotted in Figure 3-7a. Positive effects of higher temperature and lower syngas weight hourly space velocity (WHSV) were observed. CO conversion also benefits from higher H_2/CO ratio and pressure (Table 3-6). Increased C_{5+} selectivity was observed at higher pressure due to the improved chain growth probability (Table 3-6). However, a higher H_2/CO ratio is negative to the chain growth and leads to

increased CH₄ selectivity. Even though a higher WHSV leads to lower CO conversion and lower product yields when other conditions are unchanged, it still increases the productivity of hydrocarbons, which is the result of yield and throughput. Figure 3-8 shows the CO conversion over the 360 h experiment of the FTS-Ref. II. Clearly, CO conversion was stable for each set of conditions, which indicates a reasonable stability of the FTS catalyst.

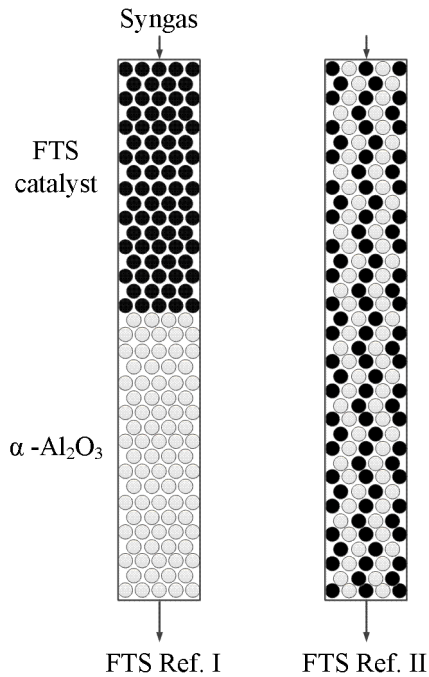


Figure 3–6 FTS reference with powder catalyst in the micro packed-bed reactor [88]

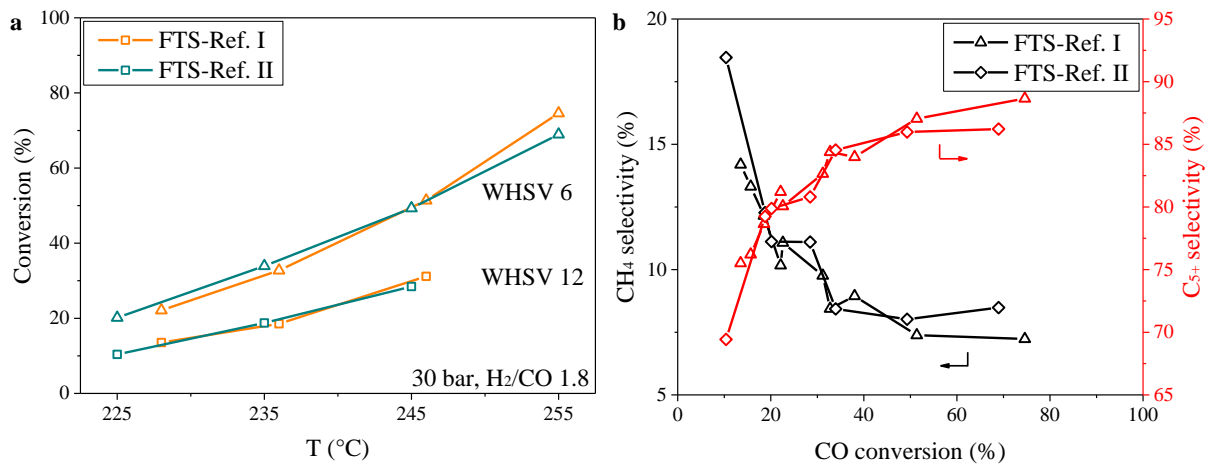


Figure 3–7 FTS performance with powder catalyst in the micro packed-bed reactor (a. CO conversion; b. CH₄ and C₅₊ selectivity)

With CO conversion rising from 10% to 50%, CH₄ selectivity was observed to decrease from about 18% to 8% (Figure 3-7b). Beyond 50% CO conversion, CH₄ selectivity remains more or less constant at around 8%. On the contrary, higher C₅₊ selectivity, i.e. higher chain growth probability, was obtained at higher CO conversion (Figure 3-7b). Since higher CO conversion

here is associated with a higher temperature, which is negative to chain growth, the change of CH₄ and C₅₊ selectivity with CO conversion is the joint result of both positive and negative effects.

As shown in Figure 3-7, the CO conversion, as well as the CH₄ and C₅₊ selectivity, were similar for both catalyst bed configurations, i.e. FTS-Ref. I and II, under the same operating conditions, which indicates that the influence of catalyst bed dilution is negligible.

Table 3-6 Results for FTS Ref. II at different pressure and H₂/CO ratio [88]

<i>P</i> [bar]	H ₂ /CO	Conversion / Selectivity [%]		
		CO	CH ₄	C ₅₊
30	1.6	43.40	7.70	86.38
30	2.0	51.65	8.52	85.26
25	1.8	46.71	8.57	85.26
20	1.8	46.43	9.08	84.61

245 °C, WHSV 6

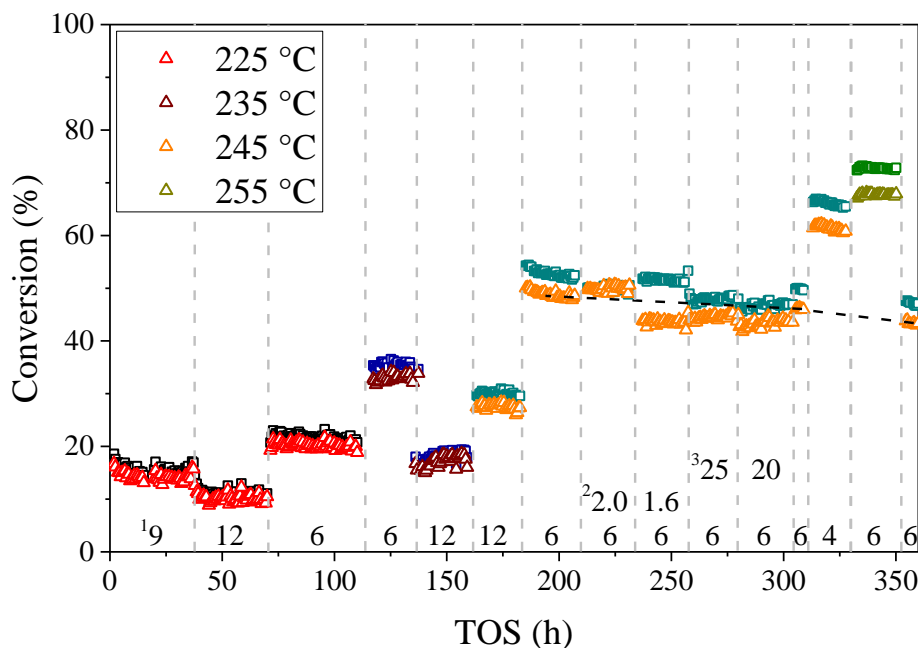


Figure 3–8 FTS catalyst stability (FTS-Ref. II; H₂ conversion in square symbol, CO conversion in triangular symbol; ¹ syngas WHSV in g/(g_{FTS-cat}·h); ² H₂/CO; ³ pressure in bar; if not specified: 30 bar, H₂/CO 1.8)

To compare with the wall-coated catalyst configuration, the powder catalyst was prepared by scraping the coated layer off the substrate. Yet an activity loss was observed for the scraped catalyst (FTS reference), compared with the original catalyst powder used for preparation of

the FTS catalyst paste. At 225 °C and WHSV 6, the original catalyst reached a CO conversion of about 50%, which is 2.5 times higher than for the FTS reference. At 245 °C and WHSV 6, 86% CO conversion was obtained for the original catalyst. Whereas CO conversion for the FTS reference was only 50%. According to the H₂-chemisorption data in section 2.2.3, there seems no apparent difference in average crystallite size and dispersion of Co between the original and the scraped catalyst. However, the ex-situ H₂-chemisorption was proved not an optimum method to correlate the Co active surface with the activity [225]. H₂-chemisorption only measures the available surface sites that are active for H₂ adsorption. When being exposed to syngas at FTS conditions, surface reconstruction caused by CO adsorption is likely to happen [226]. Based on an in-situ CO adsorption measurement, it was found the actual number of active sites would be less than that derived from H₂-chemisorption [225]. For the scraped catalyst, there must be some change occurred in the process of layer preparation to eventually lead to the reduced activity. One possibility could be the available actual active sites are reduced for the scraped catalyst, despite the similar average Co crystallite size (H₂-chemisorption). Further in-situ characterization is required to investigate the activity loss and finally solve it.

At 255 °C, 30 bar, H₂/CO ratio 1.8 and WHSV 6 an apparent activity (average rate for the integral reactor) of $18.4 \times 10^{-5} \text{ mol}_{\text{CO}}/(\text{g}_{\text{Co}} \cdot \text{s})$ was achieved in FTS Ref. I, which is comparable to the reported activity of $19.2 \times 10^{-5} \text{ mol}_{\text{CO}}/(\text{g}_{\text{Co}} \cdot \text{s})$ for a catalyst with an optimum Co crystallite size of 6.9 nm at similar conditions of 250 °C, 35 bar, H₂/CO ratio 2 [227]. Even though the Co crystallite size is larger here and the activity was reduced, obviously a reasonable activity was obtained for the scraped FTS catalyst, which ensures the validity of the results related to process integration.

3.2.2 FTS reference with wall-coated catalyst in the microchannel reactor I

The FTS reference case with wall-coated catalyst in MCR-I was also studied. The performance of layers with different thickness was compared (Figure 3-9). Near-isothermal operation ($\Delta T \leq 2 \text{ °C}$) was obtained in MCR-I. The FTS catalyst layer thickness was determined to be 20 and 40 μm, respectively.

The FTS performance of the wall-coated catalyst layer is shown in Figure 3-10. Identical conversion and selectivity were observed for both 20 and 40 μm thick layers, which indicates that within the studied range the layer thickness only has limited influence on the FTS performance.

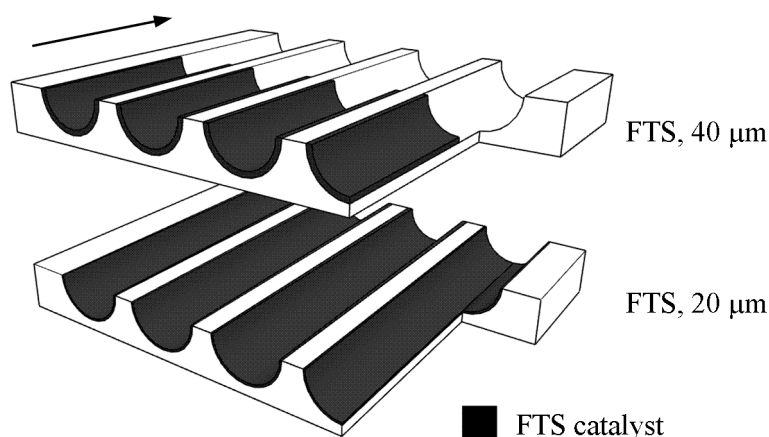
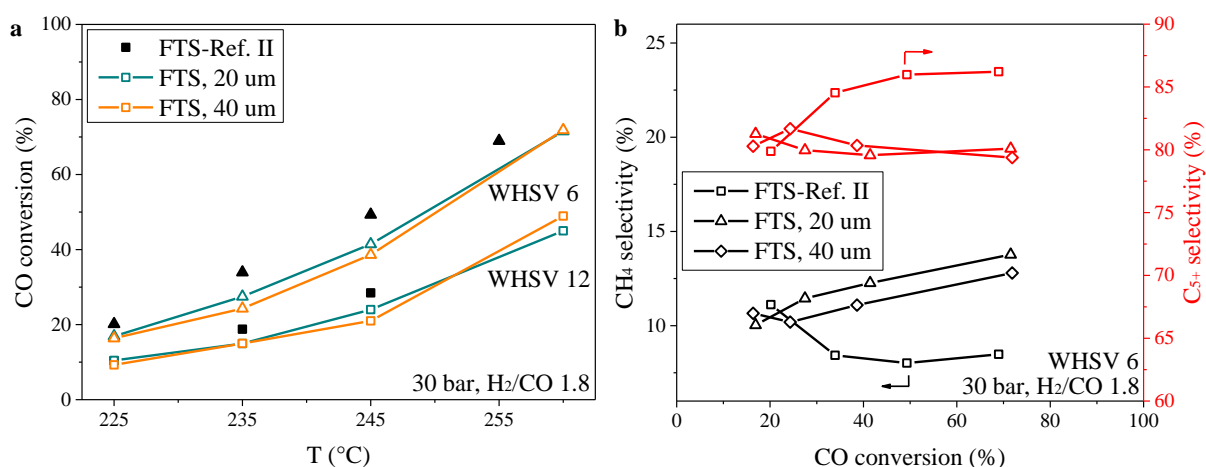


Figure 3–9 FTS reference with wall-coated catalyst in MCR-I

Compared to the powder catalyst in the micro packed-bed reactor, the wall-coated catalyst in the microchannel reactor showed a slightly lower CO conversion. The trend of the hydrocarbon selectivity versus CO conversion was also different. At low CO conversion (~20%), a similar CH₄ selectivity of about 10% was obtained for FTS in both systems. However, contrary to the decreasing CH₄ selectivity with increasing CO conversion in the micro packed-bed reactor, the CH₄ selectivity slightly increased with CO conversion in the microchannel reactor (Figure 3-10b).

Figure 3–10 FTS performance with wall-coated catalyst in MCR-I (a. CO conversion; b. CH₄ and C₅₊ selectivity)

The hydrocarbon selectivity is known to be affected by competitive adsorption of water and olefins [228-236]. α -olefins compete with surface methyl species for available active sites, which therefore leads to the reduced CH₄ selectivity. Water could inhibit the hydrogenation of growing chains (chain termination), which then leads to increased C₅₊ selectivity and reduced CH₄ selectivity. Higher CO conversion means a higher amount of water and α -olefins, which is favorable for the competitive adsorption. Since higher CO conversion here indicates not

only a higher amount of α -olefins and water, but also a higher temperature, the observed selectivity trend is the joint result of both positive and negative effects.

One possibility of the observed conversion-selectivity trend in the microchannel reactor could be that the competitive adsorption of water and α -olefins in the microchannel reactor is restrained. In the packed-bed reactor, the catalyst is mixed with the inert material to form a porous packing. Assuming a liquid phase would be generated owing to the production of long-chain hydrocarbons, the capillary effects in the porous particle (catalyst and inert material) and in the porous packing can lower the vapor pressure of reacting species, and therefore shift the VLE to a larger liquid amount. Since α -olefins are mainly light hydrocarbons and water is non-condensable at the studied conditions, their proportion in the vapor phase, i.e. partial pressure, would increase along the enlarged liquid amount, which is positive to the competitive adsorption. Compared to the compact porous catalyst packed-bed, the wall-coated microchannel with a thin catalyst layer (~ 400 μm diameter free space, no inert particles) would have limited capillary effects, indicating a reduced liquid holdup and a lower concentration of water and α -olefins. The positive effects of the higher CO conversion on the chain growth are restricted, which may explain the observed selectivity trend in the microchannel reactor.

FTS catalyst stability in MCR-I could be deduced from Figure 3-11. The CO conversion remained constant under each test condition over the 380 h experiment, which indicates a reasonable stability of the catalyst.

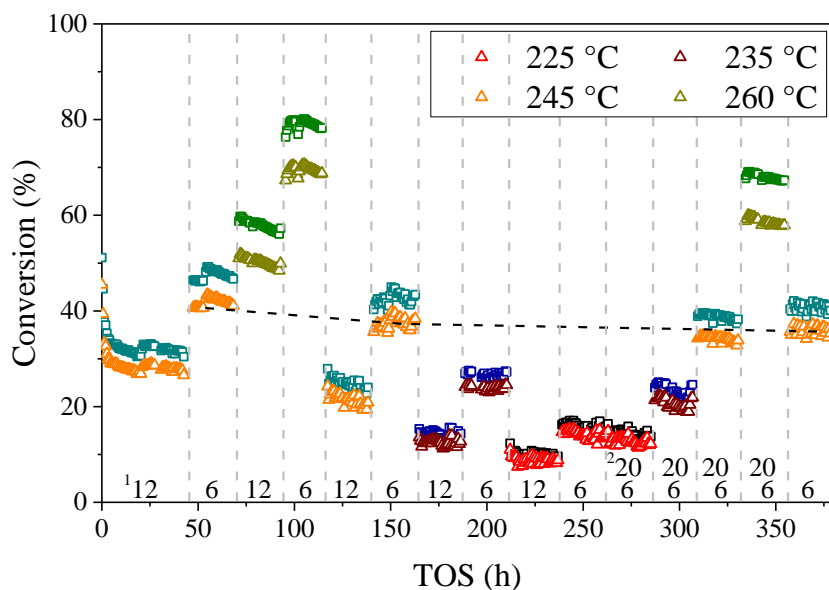


Figure 3–11 FTS catalyst stability (FTS, 40 μm ; H₂ conversion in square symbol, CO conversion in triangular symbol; ¹ syngas WHSV in g/(g_{FTS-cat}·h); ² pressure in bar; if not specified: 30 bar, H₂/CO 1.8)

3.2.3 Estimation of the FTS kinetics

Computational analysis was applied to aid the study of the integrated FTS-HC process. The kinetics of FTS was regressed based on the experimental data of FTS-Ref. II. For determining parameter estimates by regression, only results obtained at CO conversions below 50% were adopted to limit the potential influence of condensed hydrocarbons. The kinetic parameters were estimated with the least squares method using the *lsqnonlin* function in Matlab (Release 2017a). A homogeneous model without consideration of mass transport was adopted.

The obtained FTS kinetic parameter estimates are listed in Table 3-7. The simulated results using the homogeneous model were compared with the experimental data. As shown in Figure 3-12a, the simulated results could reasonably fit the experimental data at CO conversions lower than 50%. At 255 °C and WHSV 6 an overestimation of CO conversion was observed in the homogeneous model (77% vs 67%). For the product distribution, reasonable agreement was obtained between the experimental data and the simulated results, despite the chain growth probability (α) being a little overestimated with increasing temperature. Overall, the estimated kinetics could well predict the FTS experimental results.

Table 3-7 Estimated FTS kinetic parameters [89]

Parameter	Estimated value	95% Confidence interval	Units
$K_{H_2}^{ad}$	1.18e-4	2.18e-5	bar ⁻¹
$k_{CO} \cdot K_{CO}^{ad}$	^b 5.82e-2		mol/(kg·s·bar)
^a k_{IN}^0	6.03e-1	^c 8.25e-1	mol/(kg·s)
^a k_G^0	3.75e-1	2.53e-2	mol/(kg·s)
k_{CH_4}	^b 18.9		mol/(kg·s)
k_2	1.08	5.32e-1	mol/(kg·s)
k_i	3.75	3.55e-1	mol/(kg·s)
E_{IN}	7.99e4	5.6e3	J/mol
E_G	^b 9.95e4		J/mol

^a $k = k^0 \cdot \exp(-E_a/R \cdot (1/T - 1/T_{ref}))$, $T_{ref} = 518.15$ K;

^b adopted from literature [149];

^c the large confidence interval is due to correlation between the parameters.

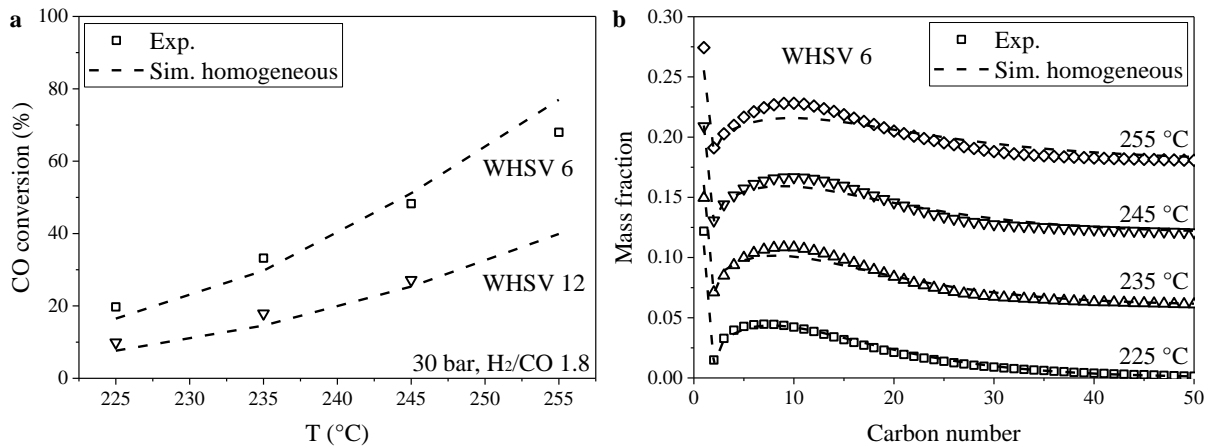


Figure 3–12 Comparison of the FTS experimental data with the simulated results (a. CO conversion, b. product distribution) [89]

3.2.4 Accumulation of liquid hydrocarbons

A liquid phase would be formed along with the accumulation of long-chain hydrocarbons in the FTS catalyst pores, as well as in the catalyst bed. The reduced diffusivity and different solubility of the syngas could probably influence both catalyst effectiveness and product selectivity. On the contrary, the liquid would be gradually consumed in HC. Figure 3-13 shows the hydrocarbon distribution of a typical FTS output in the vapor and the liquid phase, respectively. Nearly all C₁-C₁₀ hydrocarbons are in the vapor phase. Similarly, the non-condensable H₂, CO, N₂ and H₂O are also in the vapor phase. Almost all C₃₁₊ are in the liquid phase. With the reaction going on, the composition of the liquid phase would change, which therefore also affects the reaction.

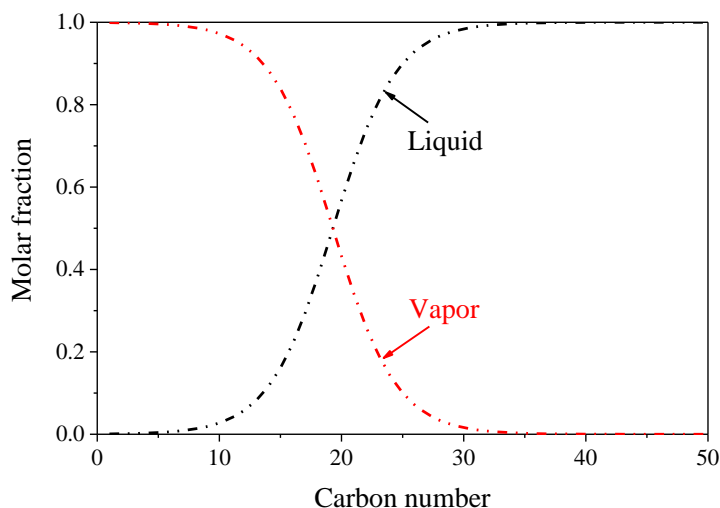


Figure 3–13 Hydrocarbon distribution in the vapor and the liquid phase for a typical FTS effluent (245 °C, 30 bar, 48 % CO conversion, liquid fraction 0.5 mol.%) [89]

The liquid increases or decreases gradually in the FTS or HC sections, respectively. At 255 °C the high CO conversion indicates a high liquid fraction in FTS, which could cause negative influence on the reaction and be responsible for the lower experimental conversion compared to the model.

The influence of the liquid depends on its amount (catalyst particle partially filled, completely filled, or even spilled) and composition (diffusivity, solubility). To study its effects, the local profile of the liquid should be figured out first.

The local accumulation of hydrocarbons in FTS catalyst particles was investigated using the pore filling model reported by Pöhlmann et al. [224]. The accumulation rate of liquid hydrocarbons in FTS is given by the interplay of formation in the pore and evaporation out of the pore. Pore filling of the 100 μm FTS catalyst particle at the bed inlet was analyzed. As shown in Figure 3-14, after a quick liquid filling at the beginning, the pore filling slows down. At 225 °C the catalyst pore is completely filled within 460 min. With an increase of temperature, the time required for complete pore filling reduces to around 80 and 40 min at 245 and 255 °C, respectively.

At the FTS inlet, i.e. with extremely low liquid fraction, the catalyst pores would still be filled within several hours, which indicates that for a small particle size of 100 μm the pores would be completely filled with liquid hydrocarbons all over the reactor. Even though HC consumes heavy hydrocarbons, complete pore filling of the HC catalyst could be assumed in analogy to the situation at the FTS inlet.

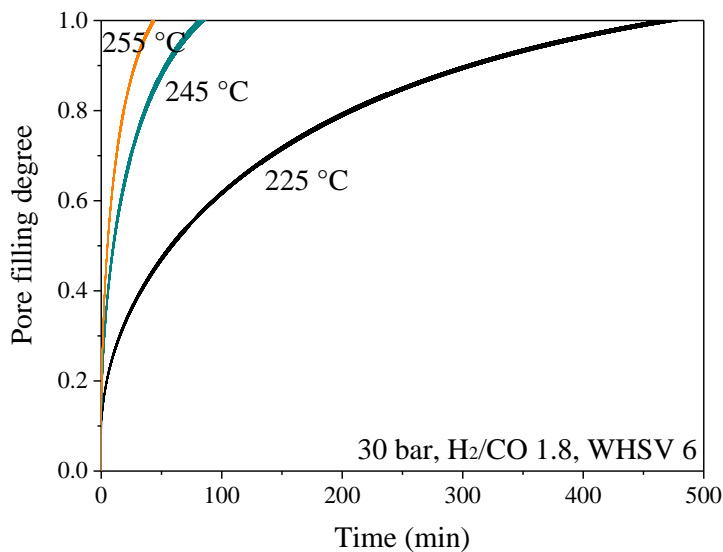


Figure 3–14 Pore filling at different temperatures at the FTS inlet [89]

To verify the liquid filling in the FTS catalyst experimentally, the used catalyst foil in MCR-I was tested. To trap the hydrocarbons inside the catalyst layer when shutting down, the

temperature was quickly reduced to restrain vaporization of the hydrocarbons inside the catalyst. Before that, the free hydrocarbons in the vapor were swept out with N₂ for 30 min to avoid condensation when reducing the temperature. The pressure was released after the reactor was completely cooled down (< 50 °C).

Inlet cross-sectional images of the used catalyst foil are shown in Figure 3-15. A uniform distribution of carbon (hydrocarbons) in the catalyst layer was observed (WDS image), which confirms complete filling of the pores in the catalyst layer. When zooming in, even a liquid film was observed above the catalyst layer. By comparison between top-view images of the fresh and the used catalysts, it was found that the catalyst layer was covered after use by some material, which also confirms existence of a liquid film.

Hence both experimentally and by simulation, complete filling in the catalyst with liquid (100 μm powder or 40 μm layer) over the entire catalyst bed could be verified.

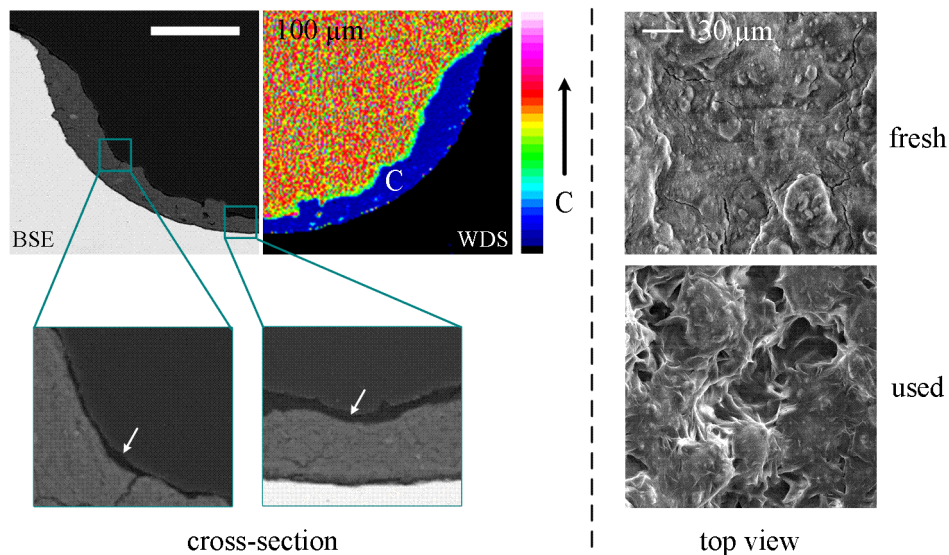


Figure 3–15 Accumulated wax in the wall-coated FTS catalyst layer (inlet)

3.2.5 Influence of the liquid hydrocarbons on FTS

To figure out whether the overestimation of CO conversion at 255 °C in FTS-Ref. II is caused by internal mass transfer limitation in the liquid, a heterogeneous model solving the reaction-diffusion equations for spherical particles with 100 μm diameter was established (see Table 3-8 for additional parameters used in these simulations). The catalyst pores were assumed to be fully liquid-filled. Liquid phase diffusion coefficients were adopted.

Table 3-8 Properties of the catalyst applied in the heterogeneous model [89]

catalyst	apparent density [kg/m ³]	particle size [μm]	porosity	tortuosity
FTS	1445	100	0.5	3

The influence of internal diffusion on FTS is shown in Figure 3-16. The liquid fraction (molar fraction of the liquid from VLE calculation) increases along with the CO conversion. The catalyst effectiveness factor for consumption of H₂ and CO along the FTS section is plotted in Figure 3-16a. At 255 °C and syngas WHSV 6, the effectiveness factor is about 0.985 at the inlet. With increase of CO conversion, it goes down and reaches a value around 0.957 at the end of the FTS section, which indicates that pore diffusion even in liquid-filled state would only have limited influence on the FTS performance.

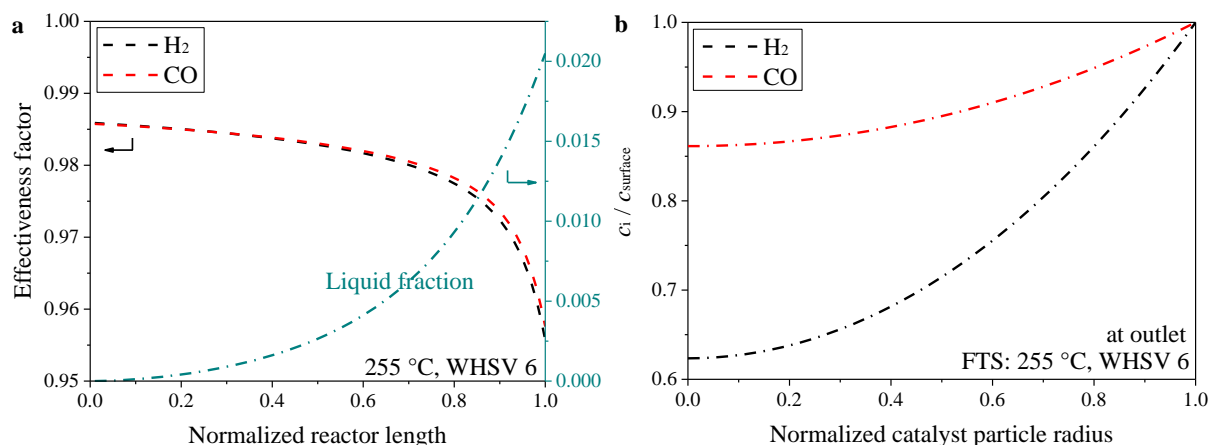


Figure 3–16 Influence of internal diffusion on FTS (a. effectiveness factor and liquid fraction along the FTS section; b. concentration profile across the catalyst particle at the FTS outlet) [89]

Normalized concentration profiles of H₂ and CO across the catalyst particle at the end of the FTS section are shown in Figure 3-16b. The CO concentration at the catalyst center reaches about 86% of the external surface concentration. Somewhat larger concentration gradients were obtained for H₂, where the concentration in the center is about 62% of the surface concentration. According to the reaction kinetics, the reaction order decreases at higher conversion, which then explains the still high effectiveness factor despite the already marked concentration gradients. CO conversion and hydrocarbon distribution for the heterogeneous model almost fall on the same curves as for the homogeneous model (Figure 3-17).

The analysis of the interplay of reaction and diffusion in a single catalyst particle shows that internal mass transport does not limit the performance of FTS within the studied range. The filling of liquid hydrocarbons in catalyst pores is probably not the reason of the experimentally observed lower CO conversion in FTS-Ref. II obtained at 255 °C. Hence, there must be other factors responsible for the reduced reaction performance.

For study in the annular micro packed-bed reactor, the home-made catalysts were pelletized and crushed to 50-100 μm, which indicates the shape of catalyst particle is irregular. A rather

wide size distribution of the void spaces between the catalyst particles in the bed would be formed in the 1.5 mm thick annular catalyst packing. With relatively high liquid fraction, the heavy hydrocarbons would also condense in the catalyst packing where they could block smaller spaces around the catalyst particles (Figure 3-18). Stagnant extra-particle liquid would lead to an increased diffusion resistance, as such regions would behave like larger particles filled with stagnant liquid. Eventually, part of the catalyst particles would even be inaccessible to the flow if channeling occurs. The annular gap geometry could be particularly critical regarding channeling caused by partial blocking by liquid. The net effect is a reduction of the catalyst effectiveness over the reactor cross-section, which could explain the inferior experimental performance of FTS compared to the simulation.

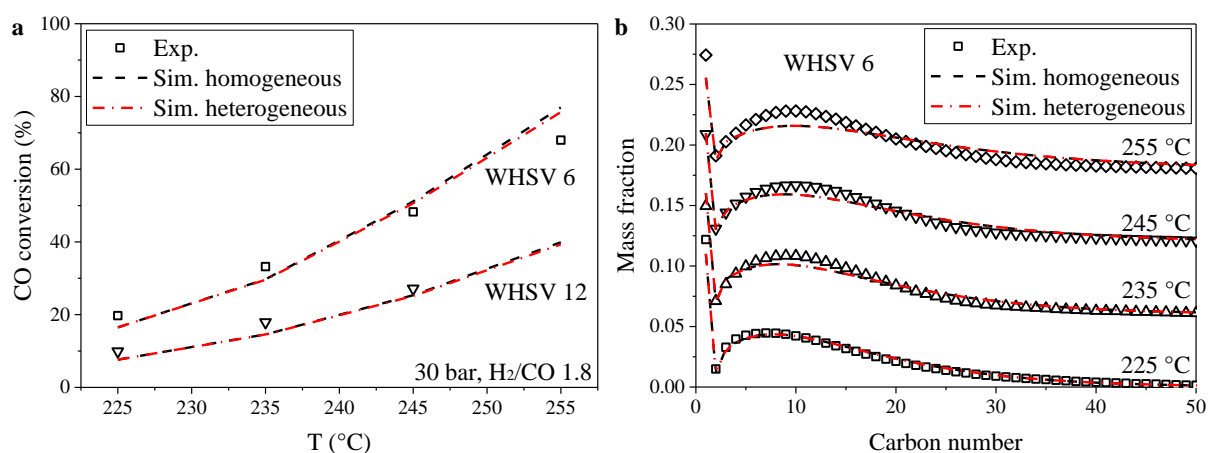


Figure 3–17 Comparison of the FTS experimental data with the simulated results (a. CO conversion, b. product distribution). Note that the simulation results for homogeneous and heterogeneous model basically fall on the same curves. [89]

As depicted in Figure 3-18, a transitional region would exist in FTS, where small void spaces in the catalyst bed would be gradually blocked by heavy hydrocarbons with the increase of CO conversion. HC would possess the opposite situation starting from blocking to gradual unblocking due to the consumption of heavy hydrocarbons.

To study the influence of local blocking by liquid, a simplified model was created. The blocked catalyst particles were treated as fictitious agglomerates with enlarged size to describe the increased diffusional distance. Instead of making a detailed description of the complicated transitional region, a simple step function was adopted in this model (Figure 3-18). Considering that the blocking depends on the local liquid fraction, a defined value was used to evaluate the amount of liquid along the reactor. If the local liquid fraction is above this value, blocking was assumed. For the case of mild blocking (agglomerates), the enlarged

diffusional distance was applied. For the case of severe blocking (channeling), the accessible amount of catalyst was reduced.

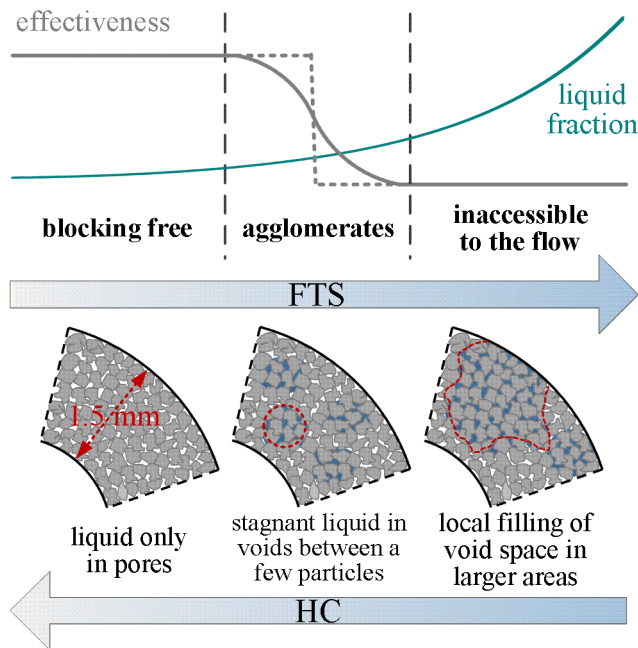


Figure 3–18 Scheme of the assumed catalyst particle blocking by liquid along the reactor [89]

As shown in Figure 3-17, at 245 °C the simulated results using the heterogeneous model are in good agreement with the experimental data, which indicates that catalyst blocking is negligible. With further increase of the liquid fraction, a deviation between experimental and simulation results was obtained at 255 °C. Therefore, the liquid fraction of the FTS effluent at 245 °C was adopted as a switching value to describe the liquid-phase blocking effect.

For FTS a liquid fraction of 0.31 mol.% was identified as being the threshold for liquid blocking. If the liquid fraction exceeds this threshold, hypothetical agglomerates generated by liquid filling of the small voids between the catalyst particles were assumed. With an agglomerate size of 500 μm (5 times of the catalyst particle), good agreement was obtained between the simulated CO conversion and the experimental data (Figure 3-19a).

Severe internal diffusion limitation was observed in these hypothetical agglomerates. At the outlet of the FTS section, both H_2 and CO exhibit large concentration gradient across the agglomerates (Figure 3-19c), where the H_2 concentration even drops to zero towards the center. An inner part of the agglomerate ($\sim 300 \mu\text{m}$ diameter) is not used for the reaction at all. The conversion and the liquid phase fraction profile along the FTS section are shown in Figure 3-19d. At the beginning of the FTS section, the CO effectiveness factor is close to 1. With an increase of CO conversion, more and more heavy hydrocarbons would be produced. At around 53% of the length of the FTS section, the liquid fraction exceeds the threshold and

the effectiveness factor drops to around 0.7. Beyond that point the increase of CO conversion and liquid fraction along the reactor is reduced due to the retarding effect of liquid blocking.

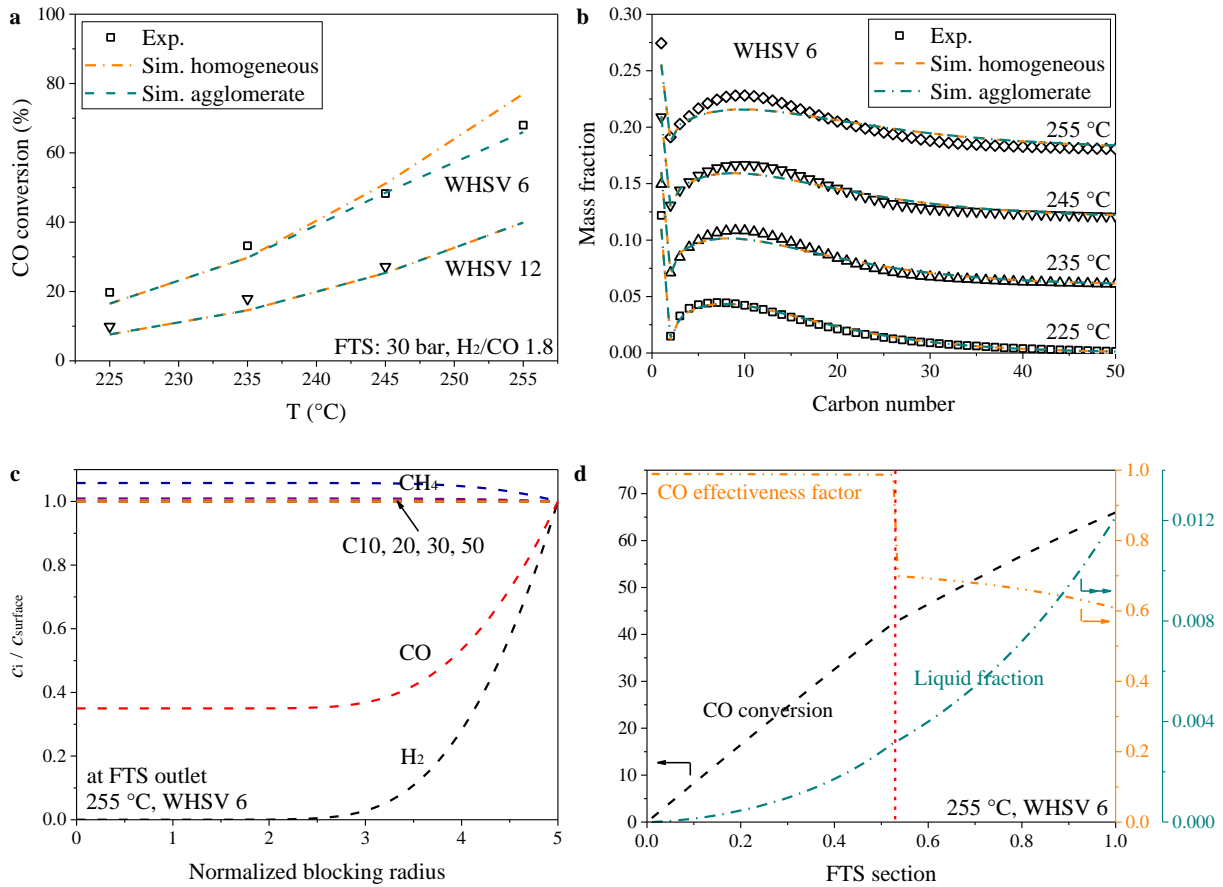


Figure 3–19 Influence of the liquid blocking on FTS performance (a. CO conversion; b. product distribution; c. concentration gradient in hypothetical agglomerates; d. development along FTS section) [89]

3.3 Two-stage FTS-HC integration with powder-type catalysts

Different from the conventional HC process, all components from FTS, including H_2 , CO, H_2O and light hydrocarbons (C_1 - C_{20}), are passed over the HC catalyst in the integrated system, among which CO and H_2O have been proven to inhibit cracking or facilitate migration of the hydrogenation site [237]. Since residual syngas cannot be avoided in the directly integrated system, it appears to be important to understand the influence of concentration changes in the residual syngas on the performance. A systematic study of the effects of temperature and FTS performance (concentration of residual H_2 and CO as well as amount of heavy hydrocarbons) on HC was carried out, and the overall performance of the integrated process was analyzed regarding the liquid fuel (C_5 - C_{20}) selectivity. This is expected to offer insight in how to adjust HC performance by FTS control and should provide basic information for further process development of small-scale PtL plants.

3.3.1 Two-stage reactor system

A two-stage reactor system was developed for the integration study (Figure 3-20a). The FTS catalyst and the HC catalyst, respectively, were loaded in two sequential reactors. Additional Ar was supplied to the HC stage to be able to adjust the inlet partial pressure for the HC reactor, and a bypass was built to enable switching of the HC reactor ON or OFF. 1 g FTS catalyst and 1 g HC catalyst were used.

The annular micro packed-bed reactor was used for the FTS stage. Whereas a tubular reactor (Figure 3-20b, $L_{bed} = 90$ mm, $d_{bed} = 6$ mm) was employed for HC, with temperature control by an electric heating jacket. Axial dispersion was neglected and plug flow behavior could be assumed for this reactor based on the Mears' criterion [97] (Eq. 2-1&2. Assuming a catalyst particle size of 100 μm , 90% hydrocarbon conversion with 1st reaction order [238], a gas phase H_2 diffusion coefficient of 10^{-5} m^2/s , a bed porosity of 0.5, a bed tortuosity of 1.4 and a superficial velocity of 0.001 m/s, $8 \cdot n \cdot \ln(1/(1-X))/Bo$ would be around 660, which is smaller than the $L_{bed}/d_{particle}$ ratio of 900). Since the ratio $d_{bed}/d_{particle}$ was larger than 10, radial concentration gradients were also ignored [101]. Radial heat transfer limitation was estimated based on Eq. 3-53 [239].

$$\Delta T = \frac{R_{obs} \cdot |\Delta_r H| \cdot (1 - \varepsilon) \cdot (1 - b) \cdot d_{bed}^2}{32 \cdot \lambda_{eff}} < \frac{0.05 \cdot R \cdot T_{wall}^2}{E_a} \quad \text{Eq. 3-53}$$

where R_{obs} is the observed reaction rate; $\Delta_r H$ is the reaction heat; b is the volumetric fraction of inert material; λ_{eff} is the effective thermal conductivity in the bed; R is the ideal gas constant; T_{wall} is the reactor wall temperature; E_a is the activation energy of cracking.

Assuming the HC reactor is fed from a FTS reactor with 60% CO conversion at WHSV 6 and all CO is converted into $\text{C}_{16}\text{H}_{34}$, the $\text{C}_{16}\text{H}_{34}$ entering the HC reactor would be around 0.007 mol/h. Taking a $\text{C}_{16}\text{H}_{34}$ to C_8H_{18} conversion of 90% at 245 °C and 30 bar, the observed reaction rate would be -2.46 mol/ $\text{m}^3_{cat.}/\text{s}$. With a reaction heat of -42 kJ/mol [240], a $\text{C}_{16}\text{H}_{34}$ cracking activation energy of 150 kJ/mol [238, 241], an inert material fraction of 0.44, an effective thermal conductivity of 0.1 W/m/K, the radial temperature difference would be 0.33 K, which is much smaller than the limiting value of $0.05 \cdot R \cdot T_{wall}^2 / E_a = 0.74$ K. Hence the assumption of isothermal operation is justified.

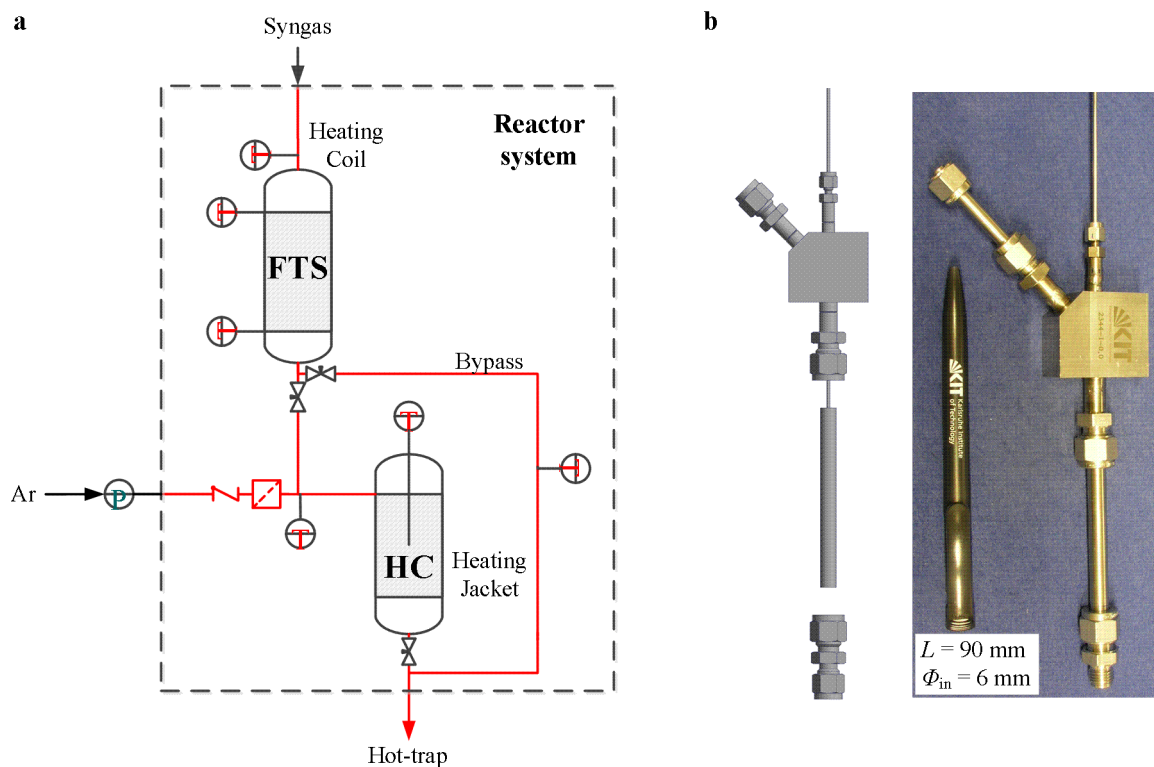


Figure 3–20 Two-stage reactor system (a. schematic diagram; b. tubular HC reactor)

FTS experiments were carried out with bypassing of the HC reactor before the process integration study to obtain the feed information for the HC catalyst. Since the temperature applied in the HC stage of the integrated process is relatively low ($< 300 \text{ }^\circ\text{C}$), hydrothermal deactivation of the HC catalyst caused by steam is negligible. The most possible influence of water, therefore, is the partial pressure contribution, especially at high CO conversion of FTS, which was, however, not in the focus of this study. The influence of temperature, H_2 and CO partial pressure, and wax feed amount were analyzed. To highlight the influence of the partial pressure of the residual syngas, and to limit the catalyst deactivation, the CO conversion of the FTS stage was controlled in a range between 15% and 30%. The system was kept as close as possible to the original integrated process to ensure that the information obtained would be meaningful for further process development. Additional feed or product removal between FTS and HC was avoided or limited to the addition of an inert gas (Ar) to adjust the level of the partial pressure.

3.3.2 Influence of the HC temperature

After the reference FTS test, the HC reactor was coupled into the system. Figure 3-21 shows the difference between the FTS product at operation conditions of 30 bar and $241 \text{ }^\circ\text{C}$ and the subsequent product effluent from the HC stage at different temperatures. From Figure 3-21a it can be observed that CO conversion and CH_4 as well as C_{5+} selectivity remain unchanged

when coupling FTS to the HC stage operating at 249 °C. The main reactant for HC, the mass fraction of C_{21+} is significantly reduced from 19% to 5% by HC at 249 °C, whereas the mass fraction of C_5-C_{20} (known as liquid fuels) increases from 53% to 64% and that of C_1-C_4 remains constant at 29% (Figure 3-21b). Note that by “mass fraction” it is referred to the mass fraction of the respective cuts in the mixture of hydrocarbons only. This indicates that the C_{21+} is preferentially cracked into liquid fuels already close to the temperature of FTS, even in presence of H_2O and CO , which have been reported to lower the HC performance [36].

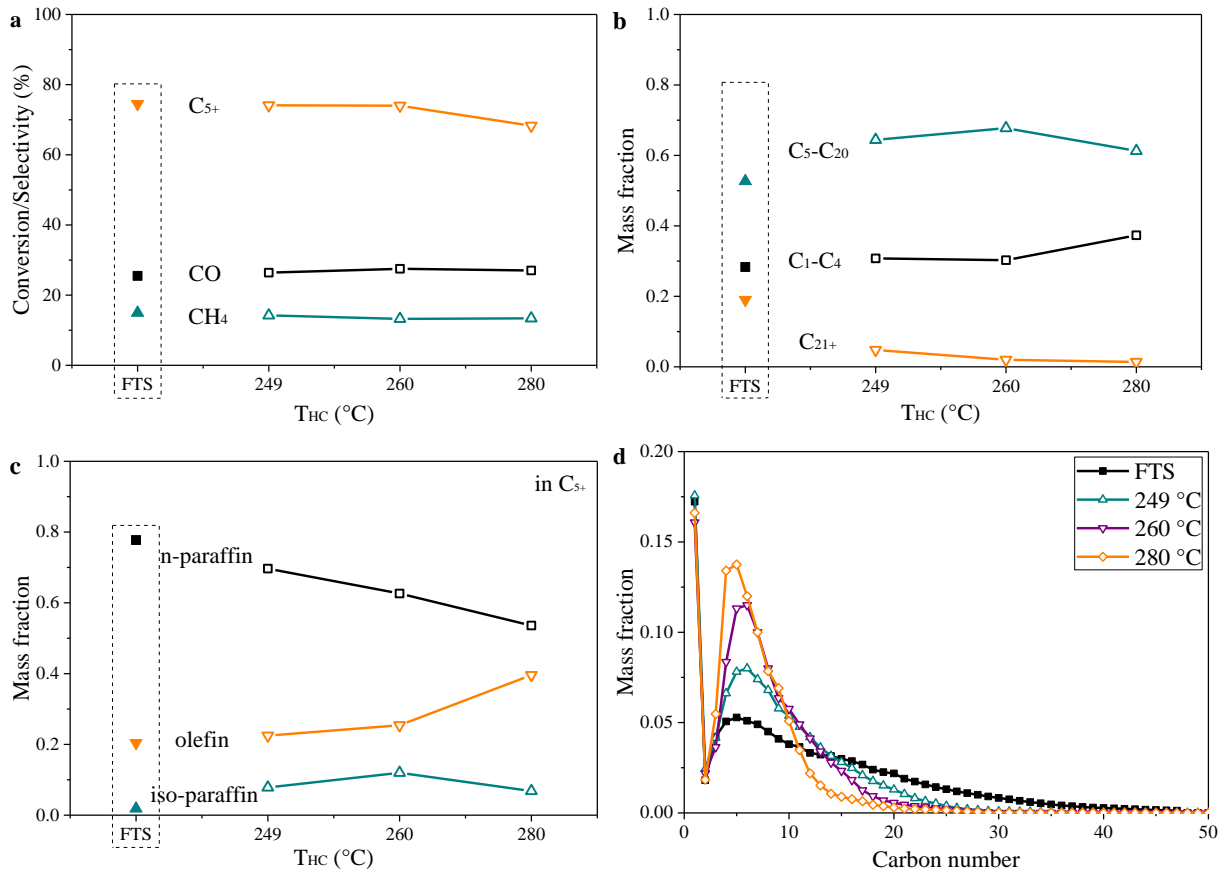


Figure 3–21 Influence of the HC temperature on the product spectrum of the coupled process (FTS: 241 °C, 30 bar, H_2/CO 1.8, 1WHSV 9.03 $g/(g_{cat} \cdot h)$, $\alpha = 0.87$) [45]

Since the cracking temperature (300-500 °C) is usually higher than for low-temperature FTS (200-240 °C), an increase of the HC temperature was tested while keeping the FTS conditions constant. The C_{21+} mass fraction then continuously decreased from 5% to 1% when the temperature was raised from 249 °C to 280 °C. At the same time, the C_5-C_{20} mass fraction increased to 68% at 260 °C. Beyond it started to drop upon further heating up to 280 °C, which indicates that the light hydrocarbons then start to be cracked and, correspondingly, an increase of C_1-C_4 products is observed. Higher temperature is favorable not only for cracking, but even more for hydrogenation, which is verified by a decrease of the olefin fraction in the

C_{5+} product mix when increasing the temperature from 260 °C to 280 °C (Figure 3-21c), considering the cracking produces more olefins.

Even though higher temperature has a positive effect on the HC reaction rate (Figure 3-21b&d), a limit to the liquid fuel production was observed with a maximum of about 70 wt.%. An intermediate temperature should therefore be adopted to maximize the selectivity of the C_5 - C_{20} fraction.

3.3.3 Influence of the H_2 partial pressure on HC

The residual H_2 from FTS, which also serves as a reactant for hydrogenation, plays an important role in the HC. Therefore, the influence of the H_2 partial pressure on the HC performance was evaluated. Based on the hydrocarbons detected in the hot-trap, the wax is supposed to be liquid under operating conditions. The partial pressure was calculated assuming that the components detected in the residual gas and in the cold trap would be in the vapor phase under operating conditions. Via carefully choosing the FTS operating conditions and adjusting the flow rate of supplementary Ar, different H_2 partial pressures at the HC reactor inlet were obtained while keeping the CO partial pressure and the wax flow rate constant (Table 3-9).

Table 3-9 FTS reference for the H_2 partial pressure study [45]

T_{FTS} [°C]	1WHSV	H_2/CO	X_{CO} [%]	$^2P_{CO}$ [bar]	$^2P_{H_2}$ [bar]	1wax [g/(g _{cat} ·h)]	FTS mass fraction		
							C_1 - C_4	C_5 - C_{20}	C_{21+}
235	5.9	1.8	29.90 (α 0.88)	8.5	14.6	0.31	0.247	0.512	0.241
241	8.9	1.6	24.37 (α 0.87)	8.6	12.7	0.29	0.264	0.532	0.204

at a total pressure of 30 bar; 1 related to FTS catalyst; 2 HC inlet

Table 3-9 shows the FTS reference (FTS operating conditions and resulting feed composition for HC) for the H_2 partial pressure study on HC. The mass fraction of C_{21+} detected for a residual H_2 partial pressure of 12.7 bar is 20.4%, which is lower than the value of 24.1% for the case of a higher H_2 partial pressure of 14.6 bar. At the same time, the C_1 - C_4 and C_5 - C_{20} mass fraction is higher. Theoretically, a lower syngas H_2/CO ratio should lead to a higher chain growth probability (due to reduced chain termination). The higher C_{21+} mass fraction for the case of higher H_2 partial pressure in Table 3-9 is caused by the concomitant changes of the larger contact time (CO conversion) and lower temperature, which have positive effects on the chain growth probability. Accordingly, since both selected cases have similar FTS C_{21+}

production rates (0.17 g/(g_{cat}·h) at P_{H_2} 12.7 bar and 0.15 g/(g_{cat}·h) at P_{H_2} 14.6 bar), there are more light hydrocarbons being fed into the HC reactor in the low H_2 partial pressure case.

The apparent conversion rates of different cuts are listed in Table 3-10. The C_{21+} apparent consumption rate at lower H_2 partial pressure is similar to that at higher H_2 partial pressure. However, a higher C_1-C_4 and a lower C_5-C_{20} apparent production rate have been detected in the lower H_2 partial pressure case, which indicates that the cracking is more efficient at lower H_2 partial pressure. A negative effect of higher H_2 partial pressure was also observed in the study of model hydrocarbons [109, 169, 237]. The steady-state concentration of alkenes formed at the Pt sites by dehydrogenation (the first step of HC) will be reduced with an increase of the H_2 partial pressure, which could therefore limit the cracking rate.

According to the “carbenium ion” mechanism of HC, one hydrocarbon molecule is cracked into one olefin molecule and one iso-paraffin molecule, and the C-C bond cleavage is more facile in the middle of the hydrocarbon chain [46]. When dividing the fuel fraction (C_5-C_{20}) into C_5-C_{10} and $C_{11}-C_{20}$, we found that the net reaction rate of $C_{11}-C_{20}$ is rather small (-0.0235 g/(g_{cat}·h) at H_2 partial pressure 12.7 bar), whereas C_5-C_{10} formation is clearly visible (0.1013 g/(g_{cat}·h)). This indicates that C_5-C_{10} is the main product at the studied conditions, and it can also be assumed that primary cracking still dominates under these conditions.

Table 3-10 Influence of the H_2 partial pressure on HC [45]

P_{H_2} [bar]	Apparent rate of formation or consumption [g/(g _{cat} ·h)]			Mass fraction		
	C_1-C_4	C_5-C_{20}	C_{21+}	C_1-C_4	C_5-C_{20}	C_{21+}
14.6	0.0177	0.0852	-0.1029	0.276	0.650	0.074
12.7	0.0286	0.0778	-0.1065	0.299	0.625	0.076

$T_{HC} = 249\text{ }^\circ\text{C}$

The product distribution at a H_2 partial pressure of 12.7 bar is shown in Figure 3-22. Compared to the total pressure of 30 bar, the H_2 partial pressure is rather high here (H_2 /hydrocarbon mole ratio of 19). However, there are still olefins present among the light hydrocarbons, reaching about 20 wt.% of the total products. This can be explained by the alkene/alkane equilibrium and by assuming that hydrogenation would be impeded by the presence of large amounts of n-paraffins and iso-paraffins [168].

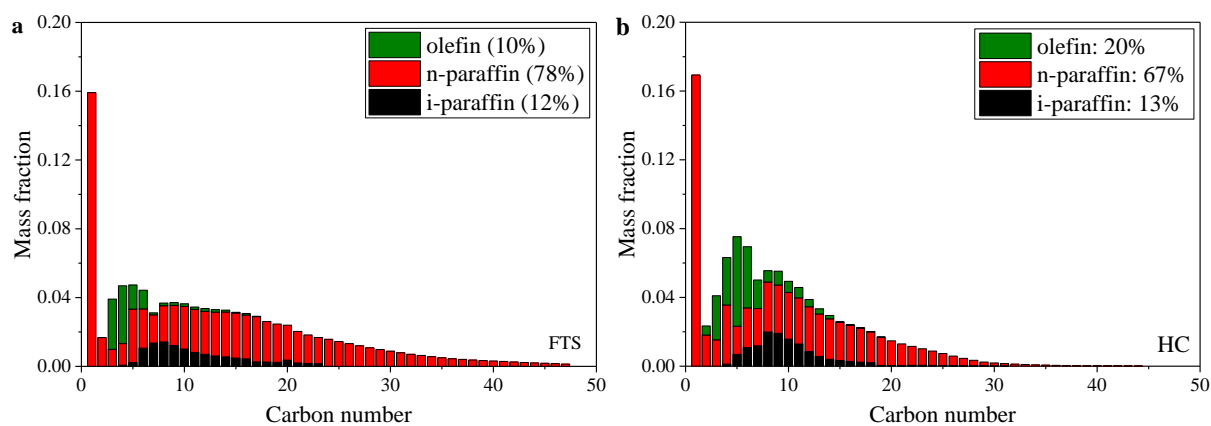


Figure 3–22 Product distribution for FTS only (a) and FTS followed by HC (b) at a H_2 partial pressure of 12.7 bar [45]

3.3.4 Influence of the CO partial pressure on HC

Generally, CO could poison the noble-metal HC catalyst. For example, Pt-MFI is reported to deactivate immediately upon exposure to CO [237]. However, the influence of the CO partial pressure is still not quantified and is important for the performance of the integrated process, since residual CO cannot be avoided in a directly coupled FTS-HC system.

A higher CO partial pressure (9.9 bar) at unchanged H_2 partial pressure (14.6 bar) was obtained by reducing the Ar flow rate of the lower H_2 partial pressure case in section 3.3.3. The resulting apparent reaction rates of the different cuts and lumped species for different CO partial pressure are listed in Table 3-11&12. The C_{21+} apparent consumption rate drops when the CO partial pressure is raised from 8.5 to 9.9 bar. Due to the reduction of the Ar flow rate, the partial pressure of H_2 and the hydrocarbons also increased compared to the experiment in the H_2 partial pressure study. Since a higher hydrocarbon partial pressure is favorable for the cracking, a negative effect of a higher CO partial pressure on the cracking rate is confirmed. The change of the hydrogenation behavior was also evaluated. The apparent olefin production rate is higher at higher CO partial pressure, even though the cracking reaction is increasingly inhibited, which demonstrates that the hydrogenation is also obstructed. Generally, it is widely accepted that the introduction of noble metals with hydrogenation/dehydrogenation function can noticeably improve the cracking activity by dehydrogenating saturated hydrocarbons to alkenes, which undergo easier cracking, and by hydrogenating olefin intermediates at acid sites [166]. CO could be competitively adsorbed at the Pt sites. With an increase of the CO partial pressure, the concentration of Pt sites accessible for H_2 and hydrocarbons would decrease, which would weaken the hydrogenation/dehydrogenation function of the catalyst and therefore suppress the cracking.

Table 3-11 Influence of the CO partial pressure on HC (Part 1) [45]

P_{CO} [bar]	Apparent rate of formation or consumption [g/(g _{cat} ·h)]			Mass fraction		
	C ₁ -C ₄	C ₅ -C ₂₀	C ₂₁₊	C ₁ -C ₄	C ₅ -C ₂₀	C ₂₁₊
8.5	0.0177	0.0852	-0.1029	0.276	0.650	0.074
9.9	0.0150	0.0685	-0.0835	0.283	0.617	0.100

$T_{HC} = 249$ °C, $P_{H_2} = 14.6$ bar, wax 0.30 g/(g_{cat}·h), at a total pressure of 30 bar;

Table 3-12 Influence of the CO partial pressure on HC (Part 2) [45]

P_{CO} [bar]	Apparent rate of formation or consumption [g/(g _{cat} ·h)]		
	¹ n-paraffin	¹ olefin	¹ iso-paraffin
8.5	-0.0492	0.0418	0.0073
9.9	-0.0490	0.0493	-0.0003

$T_{HC} = 249$ °C, $P_{H_2} = 14.6$ bar, wax 0.30 g/(g_{cat}·h)

at a total pressure of 30 bar; ¹ in C₅₊;

The final product distribution at different CO partial pressures is shown in Figure 3-23. In both cases, a similar percentage of n-paraffins, olefins and iso-paraffins, regardless of the H₂ or CO partial pressure, was obtained (compare also Figure 3-22&23), which further supports the assumption of an alkane/alkene reaction equilibrium.

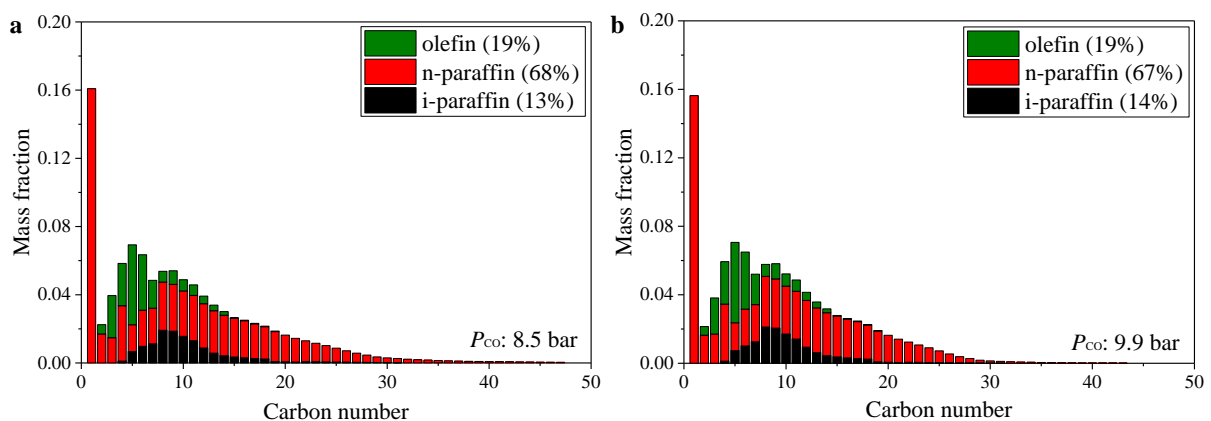


Figure 3–23 HC product distribution at CO partial pressures of 8.5 bar (a) and 9.9 bar (b) ($T_{HC} = 249$ °C, $P_{H_2} = 14.6$ bar, $P_{total} = 30$ bar, wax 0.30 g/(g_{cat}·h)) [45]

3.3.5 Influence of the wax space velocity on HC

In addition to the residual syngas from the FTS stage, also the amount of hydrocarbons, especially of the wax, should be important for the performance of the integrated process. With

a change of the reactant flow rate, the catalyst contact time will change, which affects conversion accordingly. The HC behavior was analyzed at different wax flow rates while keeping the inlet CO and H₂ partial pressures constant. As listed in Table 3-13, two wax weight hourly space velocities, i.e. 0.24 and 0.36 g/(g_{cat.}·h), were compared. Since the CO conversion in the lower wax feed case is lower than in the higher wax feed case, a larger Ar fraction was adopted to reach the same CO and H₂ partial pressure as the HC reactor inlet with the higher wax feed case, which results in a lower fraction of hydrocarbons in the gas phase in the feed to the HC stage.

Table 3-13 FTS reference for the wax feed amount study [45]

T_{FTS} [°C]	$^1\text{WHSV}$ [g/(g _{cat.} ·h)]	X_{CO} [%]	$^2P_{\text{CO}}$ [bar]	$^2P_{\text{H}_2}$ [bar]	^1Wax [g/(g _{cat.} ·h)]	FTS mass fraction		
						C ₁ -C ₄	C ₅ -C ₂₀	C ₂₁₊
235	9.0	17.95 (α 0.87)	8.7	15.2	0.24	0.293	0.511	0.196
241	12.2	19.82 (α 0.87)	8.9	15.5	0.36	0.283	0.517	0.200

at a total pressure of 30 bar; ¹ related to FTS catalyst; ² HC inlet

The apparent reaction rates of the different lumped species are shown in Table 3-14. The C₂₁₊, as the targeted cracking reactant, exists mainly in the wax and has a similar space velocity ratio ($0.20 / 0.13 = 1.54$) with the wax ($0.36 / 0.24 = 1.50$). The hydrocarbon distribution at the HC reactor inlet is similar. With an increase of the wax space velocity, i.e., higher liquid reactant flow rate, the apparent C₂₁₊ consumption rate also increases. Furthermore, the prolonged contact time for the lower wax space velocity does not enhance the cracking degree according to the final product distribution (Figure 3-24).

Table 3-14 Influence of the feed amount of wax on HC [45]

Wax [g/(g _{cat.} ·h)]	C ₂₁₊ feed [g/(g _{cat.} ·h)]	Apparent rate of formation or consumption [g/(g _{cat.} ·h)]			Mass fraction		
		C ₁ -C ₄	C ₅ -C ₂₀	C ₂₁₊	C ₁ -C ₄	C ₅ -C ₂₀	C ₂₁₊
0.24	0.13	0.0224	0.0591	-0.0815	0.327	0.599	0.074
0.36	0.20	0.0735	0.0762	-0.1497	0.357	0.593	0.050

T_{HC} 249 °C; hot-trap wax (C₁₀₊), cold-trap oil (C₅-C₃₀), gas (C₁-C₇)

The VLE plays an important role in wax cracking [19, 185, 189, 242]. Different adsorption behavior on the catalyst surface was observed for gas and liquid hydrocarbons [242]. Due to the preferential physisorption at high density, HC is dominated by the compounds present in the liquid phase [194]. Considering that the vapor is mainly composed of light hydrocarbons, the cracking of the light fraction would be limited. As mentioned above, the hydrocarbon

fraction under lower wax space velocity is lower than that under higher wax space velocity, which indicates the liquid fraction would be lower and the hydrocarbons in the liquid would be heavier on average. For the same reason, at constant temperature and pressure the larger hydrocarbon fraction could shift the VLE to increase the amount of liquid and maintain more heavy hydrocarbons in the liquid state. The C_{21+} are mainly in the liquid phase under operating conditions. The larger liquid fraction may explain the higher ratio of the C_{21+} apparent consumption rates (1.8) compared to the ratio of the wax flow rate (1.5).

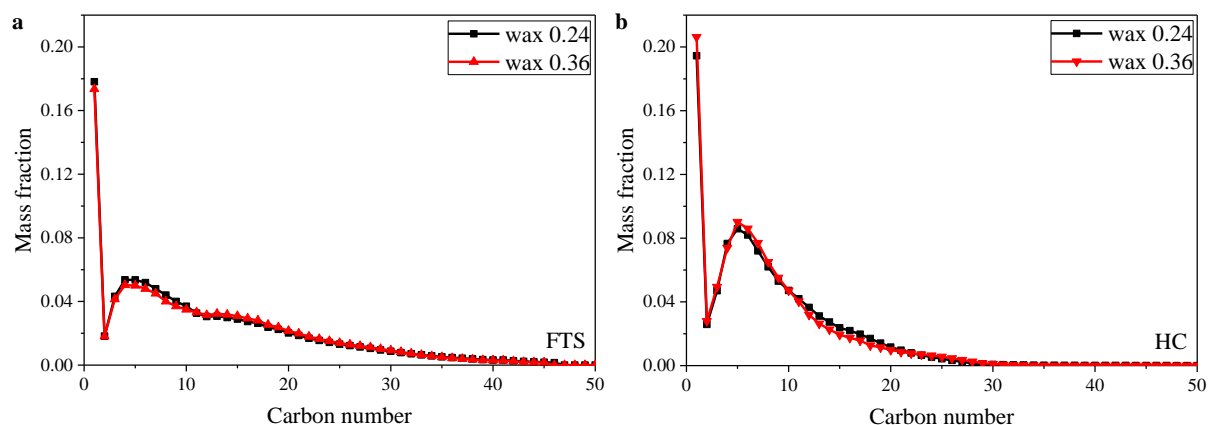


Figure 3–24 Hydrocarbon distribution for FTS only (a) and FTS followed by HC (b) with different wax flow rate [45]

3.3.6 Stability of the catalysts

The large life-time difference between FTS and HC catalysts indicated from industrial application is a challenge for the practical implementation of an integrated FTS-HC system. The long-term stability of both FTS and HC catalysts was therefore analyzed in the two-stage reactor system.

The CO apparent reaction rate at 241 °C, 30 bar and a H_2/CO ratio of 1.8 was selected for monitoring of the FTS catalyst stability and is plotted against time-on-stream in Figure 3-25 (black symbols). Over 1000 h, it slightly decreased from 0.080 mol/(g_{cat}·h) to 0.065 mol/(g_{cat}·h) with an average deactivation rate of 0.45% per day. From this we can conclude that the effects of the process parameters on catalyst performance investigated here are not significantly influenced by deactivation phenomena.

For the stability study of the HC catalyst, the apparent reaction rate of the C_5 - C_{20} and C_{21+} cuts at 249 °C and standard FTS conditions is also plotted in Figure 3-25 (red symbols). The HC reactor was connected to the FTS at TOS = 185 h (black dashed line in Figure 3-25). The C_{21+} apparent consumption rate drops from -0.17 g/(g_{cat}·h) at TOS = 250 h to -0.15 g/(g_{cat}·h) at TOS = 635 h. To better analyze the deactivation tendency, data were fitted to an

exponential decay curve. The HC catalyst activity declines quickly at the beginning and then the deactivation slows down and the reaction rates become almost stable. The HC results discussed here were all obtained after 350 h time-on stream (dark green dashed line in Figure 3-25), where the activity had already more or less stabilized.

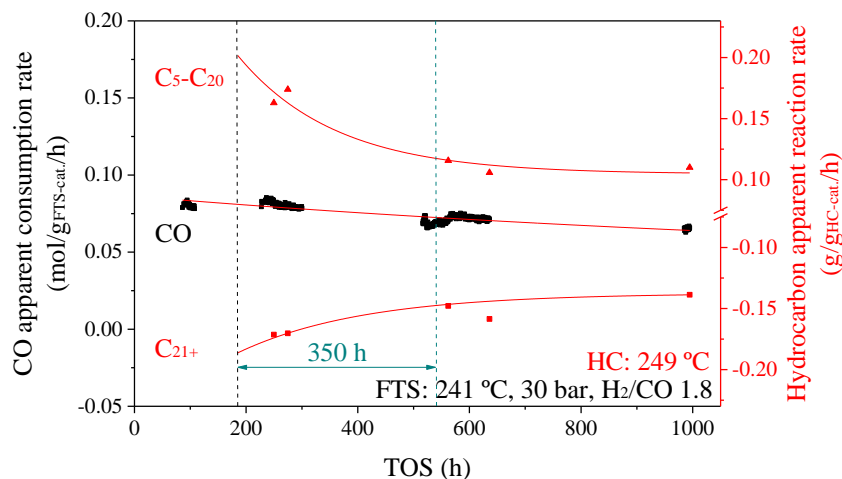


Figure 3–25 Long-term stability of FTS and HC catalysts in the two-stage integrated process [45]

Even though CO and water, which are poisonous to the HC catalyst, are fed into the HC stage together with H₂ and hydrocarbons, the HC catalyst still holds a reasonable long-term stability, which could be explained by the relatively mild operating conditions. The hydrothermal deactivation is slow under the applied low temperatures and also the hydrogenation function causes good coking resistance. Overall, both FTS and HC catalysts exhibited reasonable stability.

3.4 One-stage FTS-HC integration with powder-type catalysts

Fundamental studies in the two-stage system have revealed the feasibility of the integration of FTS with HC as well as the influence of temperature, residual syngas, contact wax flow rate, etc., on the product distribution. Targeting small-scale simplified and intensified PtL plants, it is interesting to study also more intimate options for the integration of FTS and HC for the relationship between liquid fuel synthesis and operating conditions, and also to maximize the production of liquid fuels in the integrated process by using advanced micro-structured reactor technology. Therefore, a systematic one-stage FTS-HC integration study was carried out in a micro packed-bed reactor. Different catalyst configurations (sequential and hybrid) are compared here regarding the effectiveness of the integration and the interaction mode between FTS and HC. Moreover, some practical information on the configuration of small-scale PtL plants is derived.

The study was performed with the annular micro packed-bed reactor shown in Figure 3-26. 1 g FTS catalyst and 1 g HC catalyst were used for each configuration, i.e. sequential and hybrid. In the sequential pattern, the FTS and HC catalysts were separated by a thin layer of inert α -Al₂O₃.

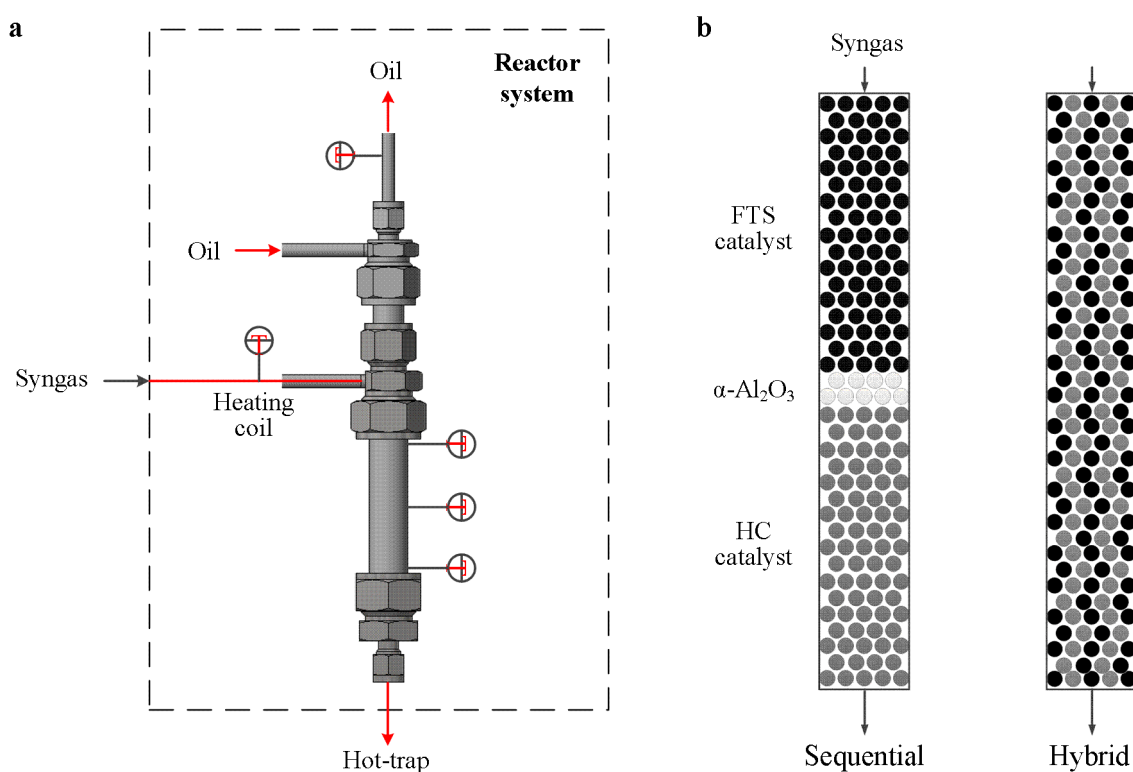


Figure 3–26 One-stage reactor system: a) schematic diagram and b) catalyst configurations [88]

3.4.1 Comparison of FTS performance

The FTS performance of both sequential and hybrid integration mode was compared with the reference test. As shown in Figure 3-27, very similar CO conversion was obtained in the sequential integration as compared to the FTS reference, which approves that incorporation of HC in the sequential mode, either in one stage or in separated stages, has no influence on the FTS performance.

Compared to the sequential system, the composition and concentration of the species in the hybrid system differ significantly due to the in-situ cracking of the hydrocarbons, which changes the VLE in the reactor. The CO conversion of the hybrid system is plotted in Figure 3-28a. At 225 °C and WHSV 12, the CO conversion is 20%, while that of the FTS Ref. II is only 10%. Higher CO conversion was also observed at WHSV 6 (30% vs 20%). Moreover, higher CO conversion was always obtained in the hybrid system for any set of studied

conditions, which indicates that the FTS in the hybrid system profits from the presence of the HC catalyst, at least regarding conversion, i.e. hydrocarbon productivity.

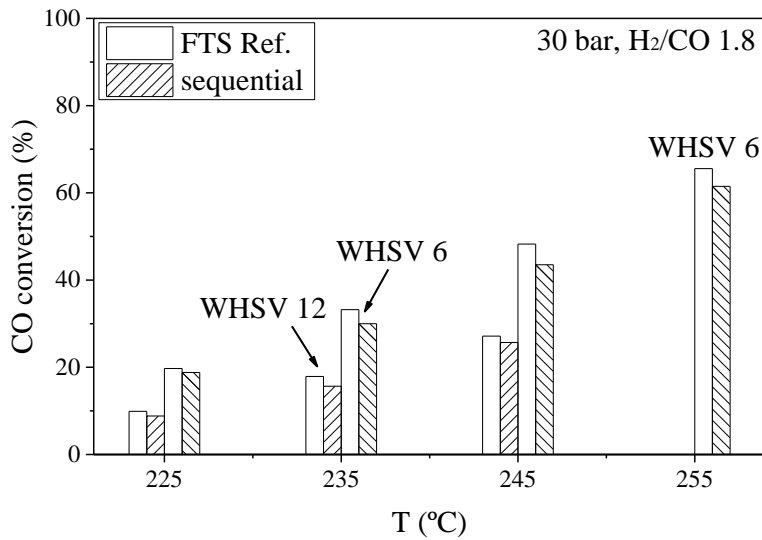


Figure 3–27 Comparison of the sequential-bed FTS performance with the FTS reference test

To better indicate the enhancement of the FTS in the hybrid system, the ratio of the CO conversion between the hybrid system and the FTS Ref. II is plotted against time-on-stream (Figure 3-28b). The FTS reference is indicated by the dashed line. At the beginning of the experiment, the CO conversion of the hybrid system is nearly twice as high as for the FTS reference. The ratio then sharply drops and reaches 1.63 at 60 h. From 150 h onwards, the FTS enhancement ratio tends to become stable at around 1.38. Note that due to the decline of the local reaction rate along the reactor, especially at high conversions, the CO conversion as a reactor-average may overlay the time-dependent changes.

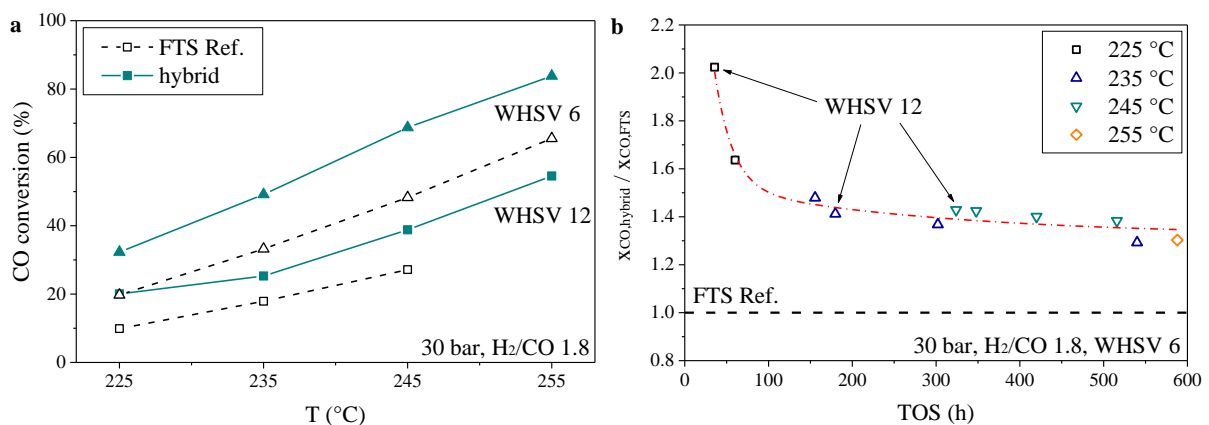


Figure 3–28 Comparison of the hybrid system FTS performance with the reference test (a. CO conversion; b. development of improved CO conversion against time-on-stream) [88]

3.4.2 Influence of temperature and syngas space velocity on fuel synthesis

The overall liquid fuel selectivity and productivity of the integrated system were studied in respect of the influence of temperature and syngas WHSV. As shown in Figure 3-29a, the hydrocarbon distribution in the sequential system shifts to lower carbon numbers with an increase of temperature. At low temperature, the HC catalyst activity is limited and the final product distribution mainly depends on the FTS stage. With temperature raised, the HC catalyst activity, as well as the CO conversion in the FTS, increase. Additional CH_4 produced from HC causes an increase of the CH_4 mass fraction when going from 245 °C to 255 °C, which is clearly different from FTS Ref. II. The ASF distribution also indicates an improved HC efficiency at high temperature, where the heavy hydrocarbons drop significantly from 225 °C to 255 °C. However, be aware that the low amount of heavy hydrocarbons is very difficult to measure accurately.

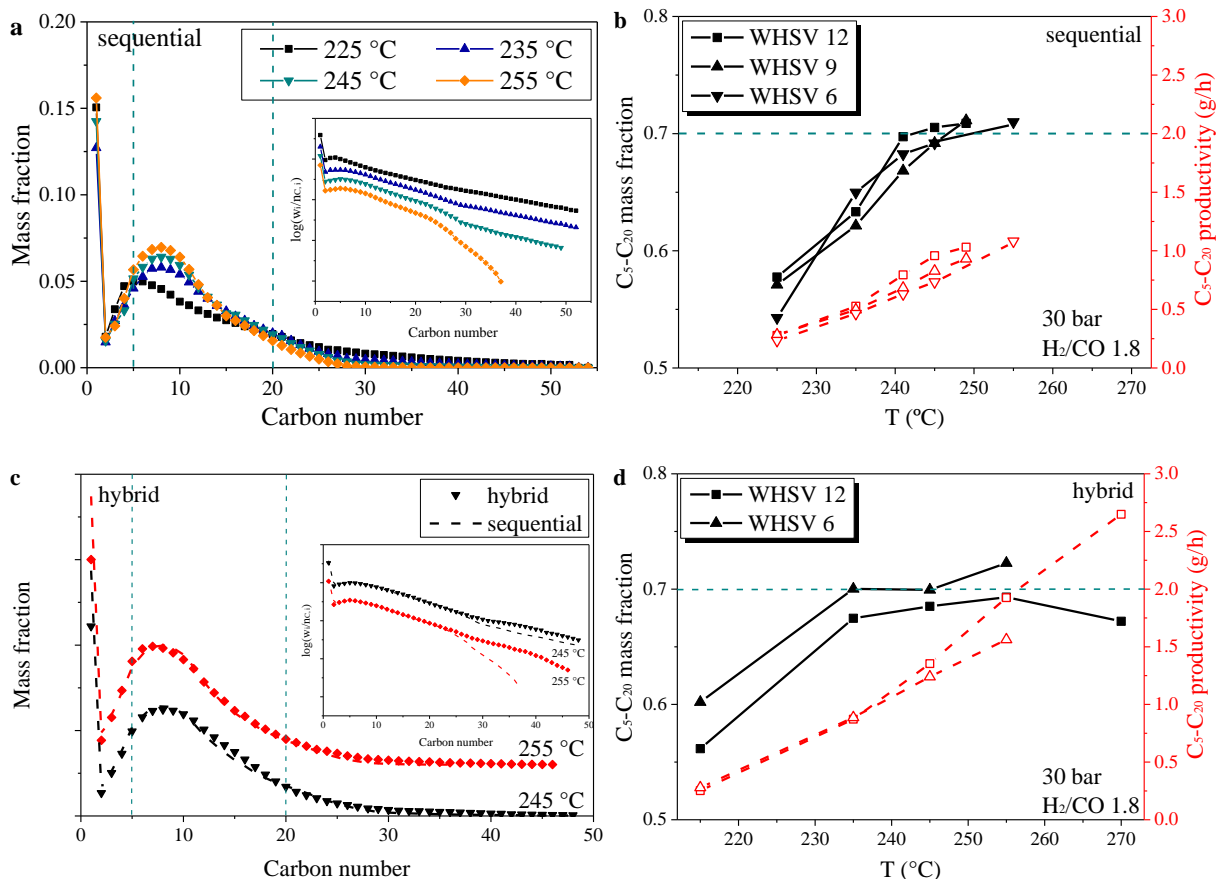


Figure 3–29 Influence of temperature and syngas WHSV on liquid fuel synthesis in the sequential (a&b) and hybrid (c&d) system (left. product distribution; right. selectivity and productivity of $\text{C}_5\text{-C}_{20}$) [88]

As shown in Figure 3-29b, the liquid fuel selectivity at WHSV 12 increases from 58% to 70% with temperature raised from 225 °C to 241 °C and levels off at around 70% upon further

increasing the temperature to 249 °C. Note that by “liquid fuel selectivity” it is referred to the mass fraction of the C₅-C₂₀ cut in the produced hydrocarbons. Due to the cracking of FTS hydrocarbons, the liquid fuel selectivity from the FTS has been changed. However, the C₂₁₊ fraction cannot be selectively cracked while keeping the C₅-C₂₀ intact. The C₅-C₂₀ would be cracked into C₁-C₄ at the same time. A balance exists between the cracking of C₂₁₊ and C₅-C₂₀ fractions. Therefore, there would be a limitation of the maximum C₅-C₂₀ mass fraction that can be achieved. According to literature results on a similar sequential bed FTS-HC configuration [39, 45], the maximum value that has been reached is around 70%. For the test at WHSV 9, selectivity was again close to 70%, i.e. 69% at 245 °C and 71% at 249 °C. A similar liquid fuel selectivity was achieved at 245 °C in the case of WHSV 6. It is notable that the increase of the liquid fuel selectivity slows down at higher temperature and ends at a final value around 70%, which then remains steady even upon further increase of temperature. Practically, it is therefore easy to operate at this highest possible selectivity in the integrated FTS-HC process.

Regarding the liquid fuel productivity, a positive effect of temperature was observed (Figure 3-29b). The higher the temperature, the higher the CO conversion. Increased conversion at increased or constant liquid fuel selectivity leads to an increased production of liquid fuels. Higher syngas WHSV appears to promote the liquid fuel synthesis (Figure 3-29b), which is consistent with an improved hydrocarbon production by the FTS, despite the lower single-pass CO conversion.

In the sequential integration, both higher temperature and syngas WHSV have positive effects on the production of liquid fuel, as they have on the hydrocarbon production by FTS. The same response was obtained for the production of total hydrocarbons and liquid fuels.

The hybrid integration was studied in comparison with the sequential system. The direct contact between the FTS and the HC catalyst, i.e. in-situ cracking of hydrocarbons, in the hybrid system creates a gradual change of the reactant and product concentrations along the catalyst bed, which leads to, compared to the sequential system, more uniform performance of all catalyst particles independent of their position relative to the bed entrance. According to Figure 3-28b, the hybrid system tends to become stable from 100 h time-on-stream on. Hence, the influence of the operating conditions on the liquid fuel synthesis in the hybrid system was investigated with taken data after 100 h time-on-stream.

Figure 3-29d shows the C₅-C₂₀ selectivity and productivity with a change of temperature. The maximum liquid fuel selectivity of 70% was achieved for WHSV 6 at 235 °C, which is lower

than the 245 °C needed in the sequential system. However, the selectivity at WHSV 12 is always lower than that at WHSV 6. Similar to the sequential system, the selectivity is rather constant within the studied range after reaching the plateau value. A positive effect of temperature on the liquid fuel production was also obtained, which is once more consistent with the trend of CO conversion.

As discussed above, the FTS is notably enhanced in the hybrid system, which means that there are more hydrocarbons being produced as reactants for the HC. However, the plateau value of the liquid fuel selectivity was achieved at even lower temperature. Moreover, a similar product distribution, once the selectivity was established at its plateau value, was obtained for both integration patterns (Figure 3-29c). A lower CH₄ mass fraction was observed in the hybrid system, which is assumed to be caused by the improved CO conversion. Be aware that in the hybrid system the HC catalyst near the micro-reactor inlet can probably not be fully utilized due to the low concentration of FTS hydrocarbons. And the heavy hydrocarbons near the micro-reactor outlet may probably not be fully cracked. Overall, all evidence points to the same conclusion, i.e. the efficiency of the HC catalyst in the hybrid system is higher than in the sequential bed. Even though the cracking of heavy hydrocarbons in the sequential integration seems to be more efficient (Figure 3-29c, ASF distribution).

3.4.3 Influence of the pressure on fuel synthesis

FTS is a polymerization reaction, while HC is a decomposition reaction. Higher pressure is favorable for FTS, but negative for HC. The influence of pressure on liquid fuel synthesis was investigated for the integrated process.

In the sequential bed, the conditions of 245 °C, 30 bar, H₂/CO 1.8 and WHSV 6 were selected as the standard considering the high single-pass CO conversion and the achieved maximum C₅-C₂₀ selectivity. The C₅-C₂₀ selectivity in the FTS slightly decreased from 65% to 64% with pressure increasing from 20 to 30 bar (Figure 3-30a). When combined with HC, the selectivity was improved to 70% and exhibited only a very weak response to pressure change (70%, 71% and 70% at 20, 25 and 30 bar, respectively). The increased FTS chain growth probability and decreased HC efficiency causes a slightly decreasing C₁-C₄ mass fraction when moving from 20 bar to 30 bar in the integrated process. Pressure did hardly influence the final product distribution (Figure 3-30b) of the integrated process but negative effects of higher pressure on the HC efficiency are visible in the heavy hydrocarbon range from the ASF distribution.

A positive effect of pressure on liquid fuel productivity was achieved in the sequential system (Figure 3-30a, dashed line). Considering the almost constant selectivity at different pressure, the increase of the productivity is consistent with the increase of CO conversion.

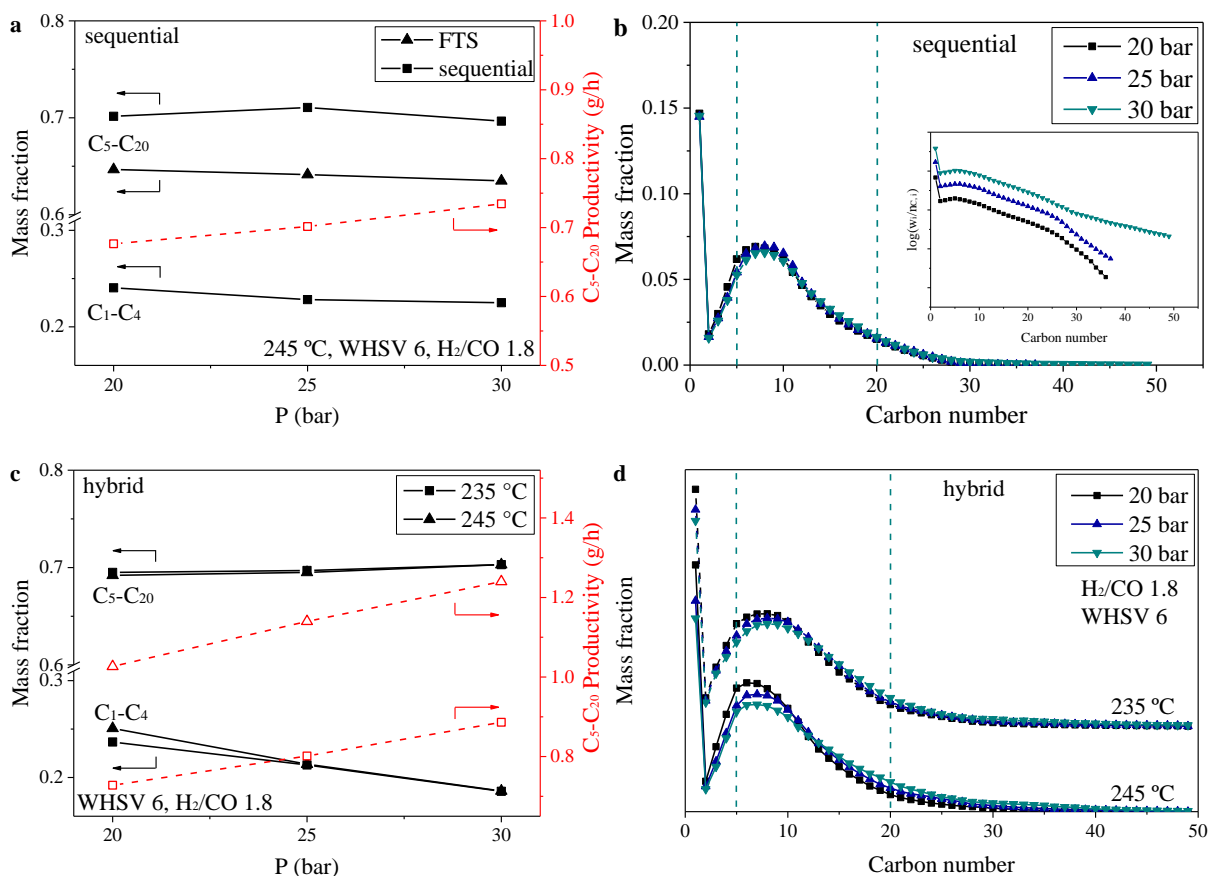


Figure 3–30 Influence of pressure on liquid fuel synthesis in the sequential (a&b) and hybrid (c&d) system (left. selectivity and productivity of C₅-C₂₀; right. product distribution) [88]

Regarding the hybrid system, the influence of pressure on the liquid fuel synthesis was studied at 235 °C and 245 °C, respectively (Figure 3-30c). Similar to the sequential pattern, the liquid fuel selectivity remained at its maximum value, and the C₁-C₄ mass fraction decreased between 20 and 30 bar at different temperatures. A much larger improvement of the liquid fuel output than for the sequential pattern was obtained in the hybrid system (Figure 3-30c, dashed line), which is caused by the improved CO conversion in the hybrid system. Compared to the sequential integration, the product distribution is more sensitive to pressure change in the hybrid system. As shown in Figure 3-30d, the product distribution shifts to lower carbon numbers with a decrease of pressure. And this trend becomes more obvious at 245 °C. In the hybrid system, both FTS and HC catalysts experience the same conditions where both reactions can influence and, at the same time, be influenced. The interaction between FTS and HC reactions caused by the change of composition and VLE in the hybrid system would be magnified at higher temperatures.

The coupling with HC exhibits a promising improvement of the liquid fuel synthesis, while the FTS is still the main contribution. Higher pressure is favorable for FTS and correspondingly positive for liquid fuel production. The quality of fuels produced in the integrated process exhibits reasonable tolerance against changing operating pressure.

3.4.4 Influence of the H₂/CO ratio on fuel synthesis

Considering that the syngas supply in decentralized small scale PtL plants may be unsteady, attention should be paid to the influence of temporal fluctuations on the fuel synthesis. To mimic the fluctuating syngas supply, not only space velocity, but also H₂/CO ratio were adjusted.

The H₂/CO ratio was varied from 1.6 to 2.0 to investigate possible effects of an unstable syngas composition. The CO conversion rises with higher H₂/CO ratio. Meanwhile, the FTS chain growth probability decreases, which consequently leads to an increased FTS C₅-C₂₀ selectivity from 62% to 65% when raising the H₂/CO ratio from 1.6 to 2.0 (Figure 3-31a). An increased CH₄ selectivity was observed owing to the same reason. Besides, the increased CO conversion reduces the partial pressure of the residual CO, which is favorable for HC.

In the sequential integration, a slightly negative influence was observed after the incorporation with HC on the C₅-C₂₀ selectivity, which decreased from 70% to 69% with an increase of the H₂/CO ratio from 1.6 to 2.0 (Figure 3-31a). The mass fraction of C₁-C₄ increases from 20% to 23% (Figure 3-31a). The interaction between FTS and HC finally leads to a similar product distribution (Figure 3-31b) and a slightly increased liquid fuel productivity (Figure 3-31a, dashed line).

Compared to the sequential bed, the same trend of the liquid fuel selectivity as a function of the H₂/CO ratio was observed at 245 °C in the hybrid system (Figure 3-31c): it decreases from 70% at H₂/CO = 1.6 to 67% at H₂/CO = 2.0. However, an opposite tendency was obtained at 235 °C, where the selectivity slightly increased from 68% to 69%. The C₁-C₄ mass fraction in the hybrid system is much lower than in the sequential bed, but also increases at higher H₂/CO ratio. A larger H₂/CO ratio is also favorable for the output of liquid fuels (Figure 3-31c, dashed line). Similar to the sequential bed, varying H₂/CO ratio between 1.6 and 2.0 only has limited influence on product distribution. However, a lower average carbon number of the hydrocarbon products was observed at 245 °C (Figure 3-31d). Considering the higher CO conversion, a higher HC efficiency is thus obtained at higher temperature.

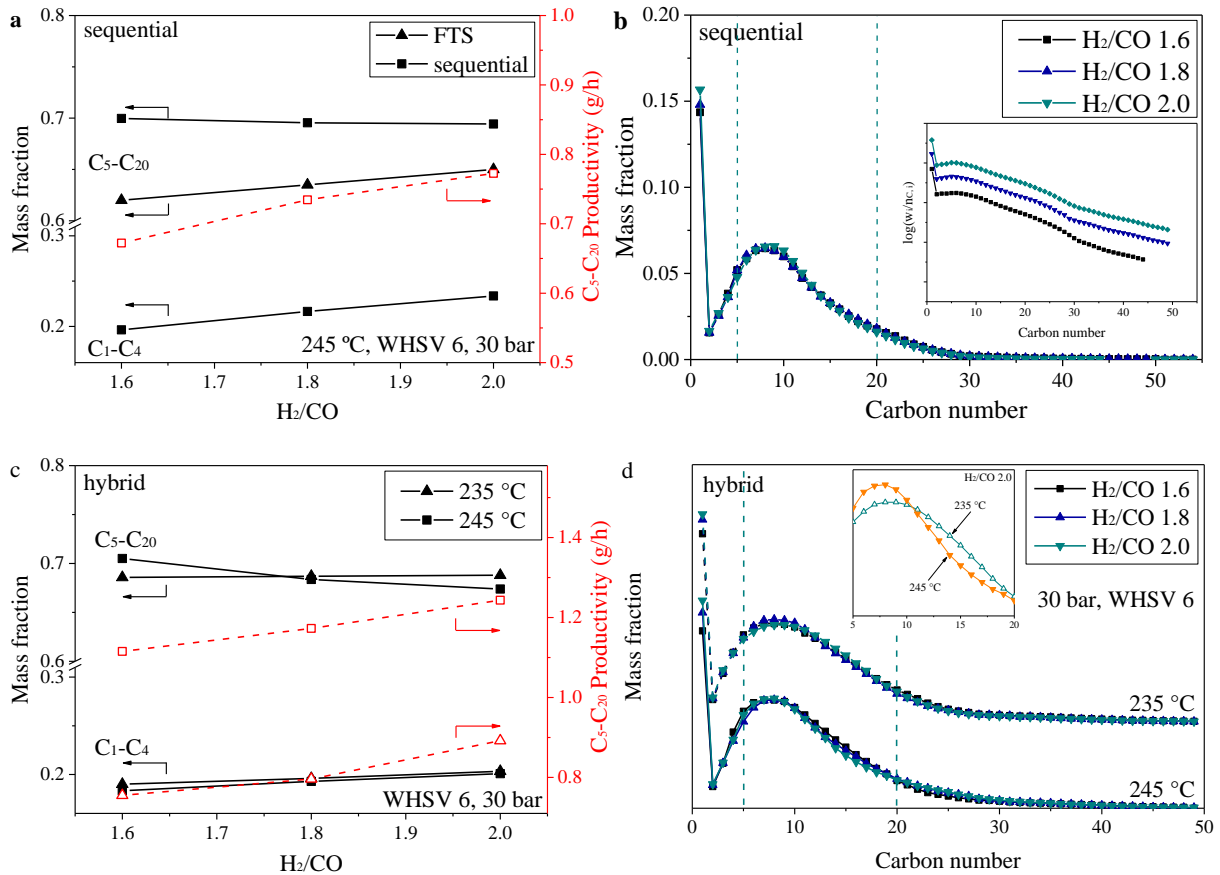


Figure 3–31 Influence of H_2/CO ratio on liquid fuel synthesis in the sequential (a&b) and hybrid (c&d) system (left. selectivity and productivity of C_5-C_{20} ; right. product distribution) [88]

The independence of the liquid fuel selectivity and final product distribution on the H_2/CO ratio, within the limited range covered, indicates that the selectivity and the product quality of the liquid fuel would be stable against small variations of the syngas composition.

Obviously, higher temperature, pressure, H_2/CO ratio and syngas WHSV are all beneficial for the productivity of liquid fuels in the integrated FTS-HC system, and also for the productivity of FTS hydrocarbons. FTS lays the foundation of the liquid fuel synthesis in the integrated process, whereas HC promotes the selectivity towards the maximum possibility.

3.4.5 Stability of the catalysts

The long-term stability of the FTS and HC catalysts is another determining parameter for practical implementation of the integrated process. Numerous concerns have been reported given the large life-time difference between industrial FTS and HC catalysts. Even though the two-stage FTS-HC integration revealed stable long-term performance, long-term catalyst stability of the one-stage sequential and hybrid integration in the annular micro packed-bed reactor was also studied.

Figure 3-32 shows the reactor average CO consumption rate over the 580 h experiment in the sequential system. It is obvious that the CO apparent reaction rate remains stable during each test, which indicates a reasonable stability of the FTS catalyst. 245 °C, 30 bar, H₂/CO 1.8 and syngas WHSV 6 were selected as standard conditions, where the reactor average CO consumption rate of FTS and the reactor average C₂₁₊ consumption rate of HC were monitored (Figure 3-32). The standard test was first carried out at 300 h time-on-stream after the tests at lower temperatures. Over 270 h of further testing, the CO apparent reaction rate slightly decreased from 0.074 to 0.068 mol/(g_{FTS-cat.}·h), and the C₂₁₊ apparent consumption rate decreased from -0.14 to -0.13 g/(g_{HC-cat.}·h).

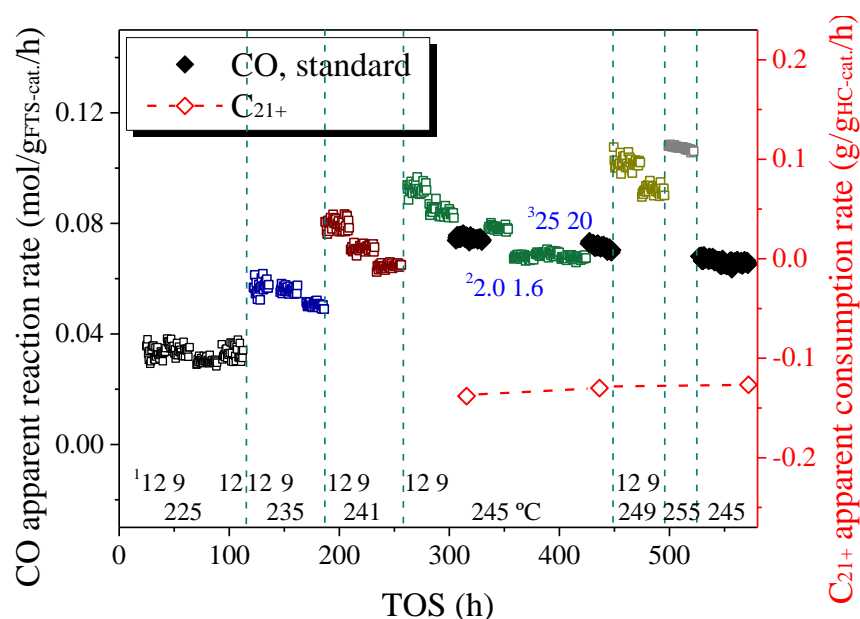


Figure 3–32 Catalyst stability in the sequential bed (¹ syngas WHSV in g/(g_{FTS-cat.}·h); ² H₂/CO; ³ pressure in bar; if not specified: 30 bar, H₂/CO 1.8, WHSV 6) [88]

As discussed in section 3.4.1, improved CO conversion was obtained in the hybrid bed. The FTS enhancement is the joint effect of the FTS and HC catalysts. The enhancement ratio plotted in Figure 3-28b reveals not only the improvement of the FTS, but also the effects of catalyst stability. As indicated in Figure 3-32, the FTS catalyst stabilizes quickly at the start of an experiment. Therefore, the stability of the HC catalyst in the hybrid system can be deduced from the change of the enhancement ratio. If the HC catalyst deactivates, the enhancement ratio would decrease. If the enhancement ratio remains at a constant value above unity, it would indicate the HC catalyst is stable. The effect of temperature on the FTS enhancement ratio appears to be moderate, because both the hybrid system and the FTS reference CO conversion is influenced by temperature in a similar way (Figure 3-28b, from 150 h onwards). At 225 °C, the enhancement ratio decreases from 1.94 at WHSV 12 to 1.63 at WHSV 6. Opposite to this, at 235 and 245 °C, the ratio is a bit larger at the lower WHSV. This seems to

indicate that in the steady state (Figure 3-28b, from 150 h onwards) the space velocity has only little effect on the FTS enhancement ratio. Therefore, the initial decline of the FTS enhancement ratio observed at 225 °C must be due to another reason. Most likely a quick deactivation of the HC catalyst during the first 100 h diminishes the positive effect of the HC catalyst in the hybrid system. Yet the HC catalyst does not lose its activity completely, as to be seen from the fact that the FTS enhancement ratio remains at a value around 1.38 over the following 500 h time-on-stream.

Consistent with the earlier study for a two-stage system [45], reasonable long-term stability of both catalysts are demonstrated also in the one-stage sequential and hybrid integration mode.

3.4.6 Interaction between FTS and HC in the integrated process

In the sequential bed, the HC catalyst was loaded below the FTS catalyst without contact. The FTS is independent from the HC and affects the HC only by controlling its feed supply, which then yields an unaffected CO conversion and a modified hydrocarbon distribution.

Whereas in the hybrid bed the FTS and HC catalysts are mixed together. Both CO conversion and hydrocarbon distribution differ from those in the FTS reference, which indicates that the FTS and HC in the hybrid system could influence each other in some way.

When taking a deeper look into the hybrid system, both integration patterns yield the same species, and the only difference is the composition change caused by the in-situ cracking of the hydrocarbons. For the FTS, the liquid in the catalyst packing would increase with accumulation of heavy hydrocarbons. The influence becomes significant at high CO conversion, where the liquid could even block small spaces around the catalyst particles. As described in section 3.2.5, stagnant extra-particle liquid would lead to an increased diffusion resistance, which is negative for the FTS. Different diffusivity and solubility of H₂ and CO may also change the local H₂/CO ratio, which would affect the product selectivity. The importance of the VLE has been more and more recognized in FTS [203, 205-207, 212, 243]. The direct contact of the FTS and the HC catalyst in the hybrid system renders the newly-born hydrocarbons, especially the heavy ones, subject to immediate cracking, which shifts the VLE and reduces the amount of liquid. The decrease of the liquid phase leads to an improved contact of the syngas with the FTS catalyst and accordingly increases the CO conversion. Moreover, the local cracking of hydrocarbons also indicates a higher fraction of olefins, which is favorable for the competitive adsorption and thus improves the FTS chain growth probability and CO conversion.

The interaction between FTS and HC caused by the change of the reaction circumstance in the hybrid bed not only offers the potential of improved fuel synthesis for decentralized small-scale PtL plants. It also indicates that further research on the influence of liquid hydrocarbons on the FTS should be undertaken to provide more detailed information for further catalyst and process optimization. Modelling and simulation were used to analyze these phenomena, for which the reaction kinetics for HC was also estimated.

3.4.7 Estimation of HC kinetics

The HC kinetic parameters (Table 3-15) were estimated based on the results of one-stage sequential FTS-HC integration experiments with the FTS effluent obtained at the same conditions as input. Again, only results obtained at CO conversions below 50% in the FTS stage were adopted. Due to the correlation between different kinetic parameters and the limited experimental data, large confidence intervals were obtained for some estimates.

Table 3-15 Estimated HC kinetic parameters [89]

Parameter	Estimated value	95% Confidence interval	Units
$K_{n,i}^{ad}$	^b $8.43 \cdot (B_{n,i} + 1)$		MPa ⁻¹
$K_{iso,i}^{ad}$	^b $4.61 \cdot (B_{iso,i} + 1)$		MPa ⁻¹
^a $k_{iso-r,i}^0$, m	1.34e-5	^c 3.93e-4	mol/(g·h)
^a $k_{iso-r,i}^0$, n	3.29	^c 8.99	
^a $k_{cr-r,i}^0$, m	1.02e-9	^c 4.36e-9	
^a $k_{cr-r,i}^0$, n	10.57	1.22	mol/(g·h)
$K_{eq,i}$	^b $104 \cdot (i^2 - 9) + 1530 \cdot (i - 3)$		
^a $E_{iso-r,i}$, m	2.26e4	^c 6.99e5	
^a $E_{iso-r,i}$, n	4.57e-3	^c 9.35	
^a $E_{cr-r,i}$, m	3.50e4	^c 2.62e4	J/mol
^a $E_{cr-r,i}$, n	0.621	1.30e-1	J/mol

$$k = k^0 \cdot \exp(-E_a/R \cdot (1/T - 1/T_{ref})), T_{ref} = 632.15 \text{ K}, k = k_{iso}; k_{cr};$$

$$B_{n,i} = (e^{i \cdot 0.251 - 2} - e^{-i \cdot 0.251 + 2}) / (e^{i \cdot 0.251 - 2} + e^{-i \cdot 0.251 + 2})$$

$$B_{iso,i} = (e^{i \cdot 0.11 - 2} - e^{-i \cdot 0.11 + 2}) / (e^{i \cdot 0.11 - 2} + e^{-i \cdot 0.11 + 2})$$

$$^a y = m \cdot i^n; y = k_{iso-r,i}^0, k_{cr-r,i}^0, E_{iso-r,i}, E_{cr-r,i}$$

^b adopted from the literature [200]

^c the large confidence intervals are due to correlation between the parameters

The validation using a pseudo-homogeneous model is shown in Figure 3-33. At 225 °C a slight deviation from the experimental data is observed, where the cracking is a little underestimated in the homogeneous model. At 235 and 245 °C good agreement is obtained between the experimental data and the simulated results. The regressed kinetics can reasonably well predict the experimental data from 225 to 245 °C. However, a significant deviation was observed at 255 °C, where the cracking is overestimated in the simulation and more light hydrocarbons were predicted. Overall, the estimated kinetic parameters can reasonably capture the information of the experimental data, which ensures the validity of the following simulation study.

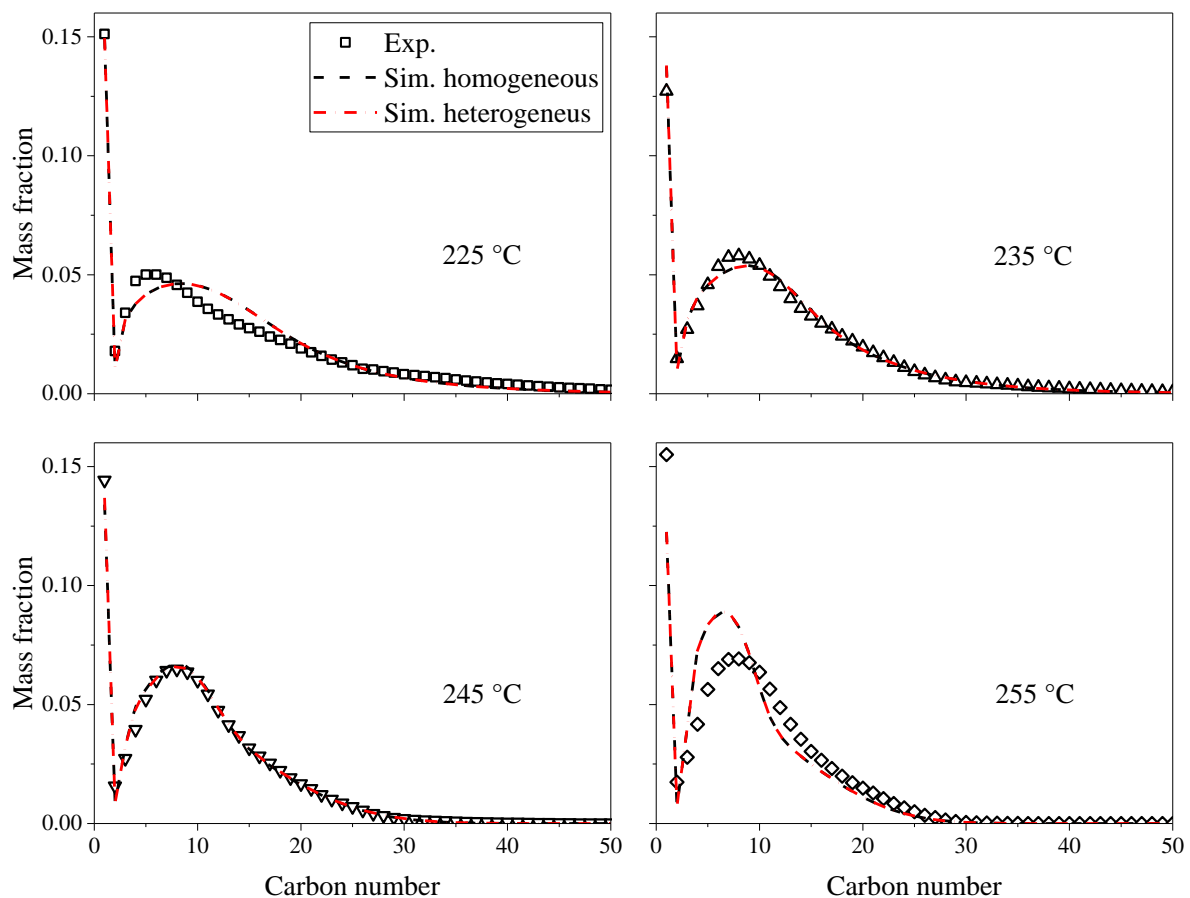


Figure 3–33 HC product distribution at different temperatures (feed from the FTS at 30 bar, H_2/CO 1.8 and WHSV 6). Note that the simulation results for homogeneous and heterogeneous model basically fall on the same curves [89]

3.4.8 Influence of the liquid hydrocarbons on HC

To figure out whether the overestimation at 255 °C in HC is caused by internal mass transfer limitation in the liquid, a heterogeneous model solving the reaction-diffusion equations for

spherical particles with 100 μm diameter was established (see Table 3-16 for additional parameters used in these simulations).

Table 3-16 Properties of the catalyst applied in the heterogeneous model [89]

catalyst	apparent density [kg/m^3]	particle size [μm]	porosity	tortuosity
HC	1500	100	0.5	3

The interaction of reaction and diffusion was studied for the HC catalyst particles at the conditions where an overestimation was obtained. Heavy hydrocarbons from FTS would be cracked into lighter ones. The effectiveness factors for consumption of the main cracking reactants (C_{20} , C_{30} and C_{50}) are plotted in Figure 3-34a. Identical effectiveness factors are obtained for C_{20} , C_{30} and C_{50} . The values slightly larger than unity reflect the negative reaction order of hydrocracking. With a decrease of the liquid fraction along the HC section, the effectiveness factor decreases. However, given the values very close to unity, the effect of internal diffusion on the rate of HC can be ignored. Normalized concentration profiles of different hydrocarbons across the catalyst particle at the HC outlet are plotted in Figure 3-34b. Negligible concentration gradients were predicted across the catalyst particle for all hydrocarbons. An identical product distribution was obtained from the heterogeneous and the pseudo-homogeneous model (Figure 3-33).

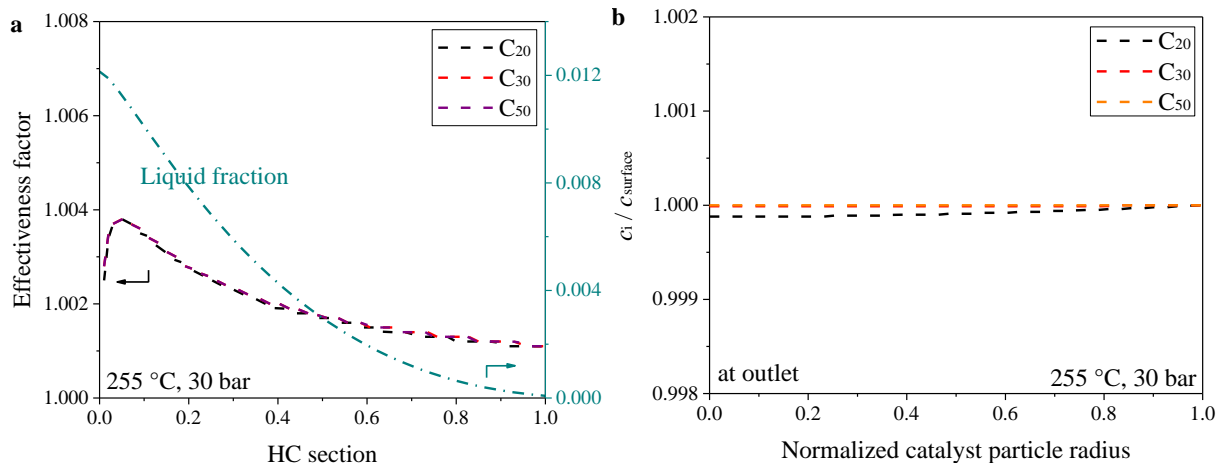


Figure 3–34 Influence of internal diffusion on HC assuming fully liquid-filled pores (a. Effectiveness factor and liquid fraction along the HC section; b. concentration profile across the catalyst particle at the HC outlet) [89]

Similar to the case of FTS, internal mass transport in a single catalyst particle does not limit the performance of HC within the studied range. As described in section 3.2.5, with relatively high liquid fraction, the smaller spaces around the catalyst particles would be blocked.

Stagnant extra-particle liquid would lead to an increased diffusion resistance. Eventually, part of the catalyst particles would even be inaccessible to the flow if channeling occurs.

Liquid blocking can explain the inferior FTS experimental performance compared to the simulation at high CO conversion. The influence of hypothetical agglomerates created by liquid-filled voids on HC was analyzed accordingly.

The same agglomerate size of 500 μm like for FTS was adopted first to investigate the effects of an enlarged diffusional distance on HC. However, similar results were still obtained as for the pseudo-homogeneous model (Figure 3-35a), where the fraction of light hydrocarbons is much higher than detected experimentally. The effectiveness factor is even higher than for the case without liquid blocking (Figure 3-35b). Increasing the diffusional distance 5 times has no negative influence on the HC performance, which is apparently caused by the slow reaction rate combined with the negative reaction order under the studied conditions. The same behavior was observed with further increasing the agglomerate size to 800 μm .

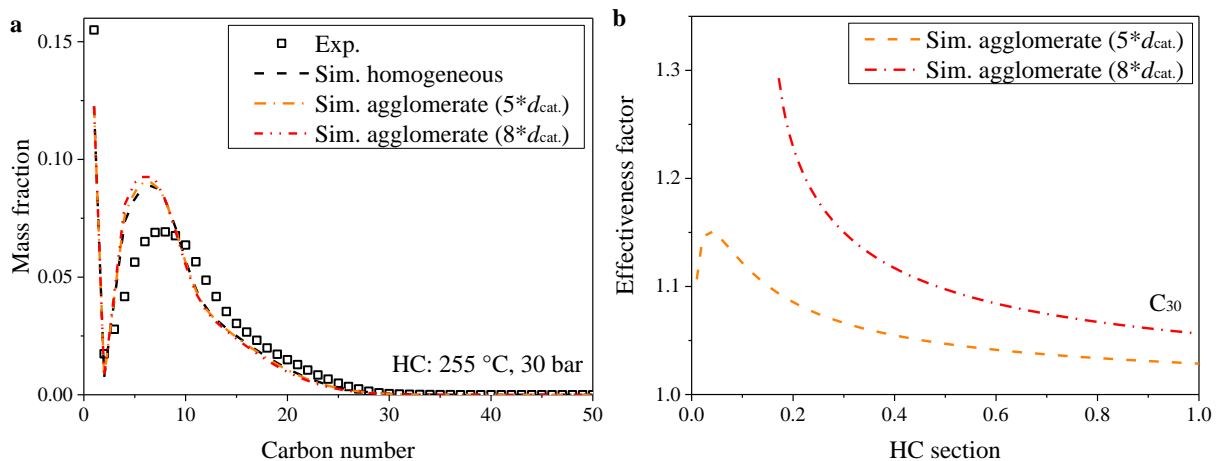


Figure 3–35 HC performance at hypothetical agglomerates of different size (a. production distribution; b. effectiveness factor) [89]

Consequently, an enlarged internal diffusion resistance in hypothetical catalyst particle agglomerates is not the reason for the inferior HC performance at 255 °C. However, if liquid-filled void space would block certain regions of the cross-section of the annular packed bed completely, channeling would be the result and, as depicted in Figure 3-18, part of the catalyst would be bypassed and thus inaccessible to the reactants. It is assumed that such phenomenon could particularly happen in flat wide channels where the large width-to-height ratio of the cross-section makes the distribution of the flow more difficult.

To analyze the influence of liquid-induced channeling in the HC catalyst packing, a factor describing the inaccessible area was introduced into the heterogeneous model. A liquid

fraction threshold value of 0.50 mol.% was determined together with a blocking factor of 0.6 (indicating that 40% of the catalyst are not accessible due to channeling). At the inlet of the HC section the liquid amount is above the threshold and hence it is assumed that only 60% of the catalyst is accessible to the reactants. Along with cracking of the heavy hydrocarbons, the liquid fraction is reduced and the catalyst packing would recover to blocking-free. As shown in Figure 3-36b, a turning-point was obtained at around 73% of the HC section. Beyond this point the decrease of the liquid fraction would accelerate and a C₅-C₂₀ (liquid fuel) mass fraction of 72% is achieved at the end. Good agreement with the experimental product distribution was observed based on these assumptions (Figure 3-36a).

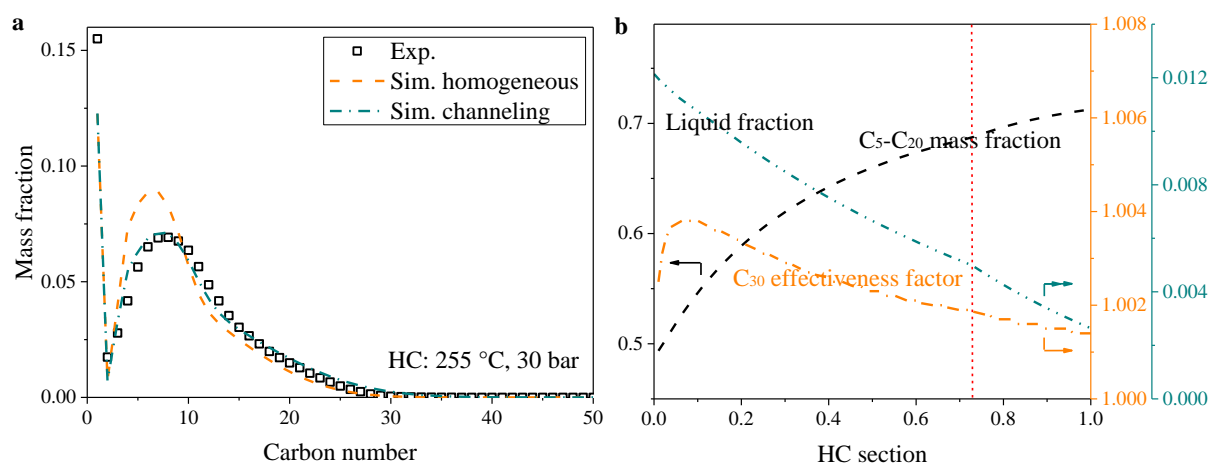


Figure 3–36 Influence of the liquid blocking on HC performance (a. product distribution; b. development along HC section) [89]

Even though different forms of liquid blocking are assumed for FTS (liquid leads to hypothetical agglomerates) and HC (liquid leads to channeling), and it is not obvious why channeling should not occur in the FTS section as well, the negative influence of the presence of liquid hydrocarbons on both reactions was confirmed and similar cross-section averaged effectiveness factors (0.6-0.7) were obtained for the liquid-affected regions, which indicates that the assumption of liquid blocking is reasonable.

3.5 One-stage FTS-HC integration with printed catalyst layers

Promising potential was observed for FTS-HC integration in the micro packed-bed reactor. Compared to the powder catalyst, more options for integration (sequential, face-to-face, dual-layer and hybrid) are available for wall-coated catalysts in microchannel reactors. Despite suffering from limited catalyst loading, better heat transfer and lower pressure drop can be achieved in the microchannel reactor. Moreover, stagnant liquid zones could be avoided. And the possibility of setting independent FTS and HC temperatures represents another advantage

for fundamental studies on process integration. The performance of different catalyst configurations in the microchannel reactor was analyzed.

3.5.1 Interaction between FTS and HC in different catalyst configurations

Interaction between FTS and HC via the change of the local reaction circumstance was observed in the hybrid system. Complete catalyst pore filling with liquid was verified for FTS. HC of FTS hydrocarbons would change the local VLE and consequently affect the FTS, which would then change the concentration and composition of the HC reactants.

The arrangement of FTS and HC catalysts in different integration configurations is shown in Figure 3-37. In the sequential configuration, FTS is independent of HC, which is identical with the integration using powder catalysts.

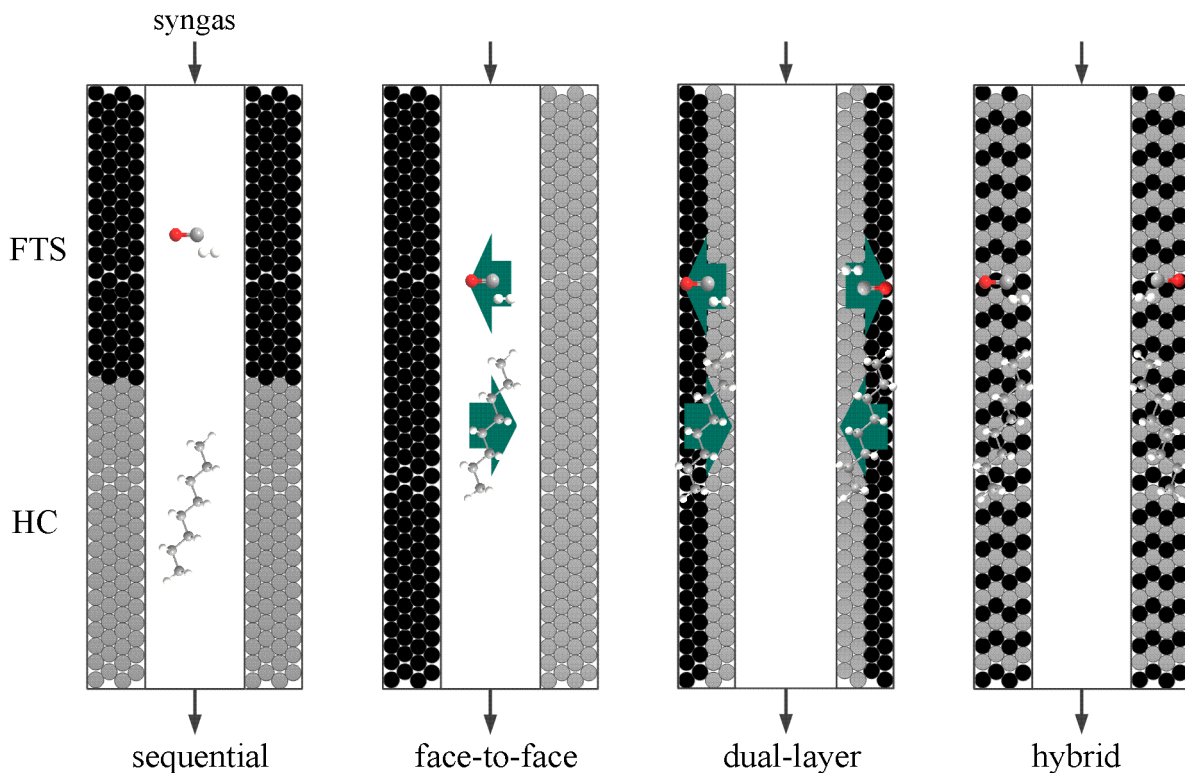


Figure 3–37 Interaction between FTS and HC in different catalyst configurations

In the face-to-face configuration, bridged via transverse diffusion, communication between FTS and HC is also available. Assuming the bulk vapor phase boundary is in equilibrium with the liquid boundary of the FTS catalyst layer, hydrocarbons would leave the FTS catalyst layer and enter the bulk space owing to concentration gradient at the top of the FTS catalyst layer. HC of hydrocarbons creates another concentration gradient in the HC catalyst layer. From FTS to HC catalyst a hydrocarbon flux would be generated. The overall transverse concentration gradient depends on VLE, mass transport, and activity of both FTS and HC

catalysts. HC could indirectly influence the composition of the liquid in FTS, but can hardly affect the concentration and diffusion of the syngas, which indicates that only limited interaction between FTS and HC would be expected.

In the dual-layer configuration, a FTS catalyst layer is covered by a HC catalyst layer. Both reactants and products of FTS have to pass through the HC catalyst layer to exchange material with the bulk space. Instead of liquid-vapor-liquid transport of hydrocarbons from FTS catalyst to HC catalyst in the face-to-face configuration, single liquid phase material transport would prevail between FTS and HC catalyst layers based on the direct contact, indicating more efficient mass transfer and higher concentration of hydrocarbons for HC (no concentration gradient in the bulk gas phase). An escape of FTS hydrocarbons via the free space is avoided owing to the complete coverage by the HC catalyst layer, which suggests a higher HC efficiency. Accordingly, the changed VLE would lead to different liquid amount (liquid filling) and vapor composition (syngas partial pressure). Moreover, consumption of H₂ (H₂/CO ratio) and change of the hydrocarbon distribution (olefin adsorption) in HC could also affect the FTS performance.

In the hybrid configuration, the intimate contact between FTS and HC catalysts represents the strongest interaction. Immediate cracking of FTS hydrocarbons, especially the heavy ones, would directly change the FTS reaction circumstance. The transport distance from FTS to HC active sites is negligible. Compared to the “group-born, group-cracking” in other configurations, the “individual-born, individual-cracking” in the hybrid system would enable more efficient hydrocarbon removal from FTS and even higher HC efficiency. After coating, FTS and HC catalysts would bind together, which could probably create a new multi-functional catalyst and bring in catalyst level interaction (e.g. hydrogenation/dehydrogenation).

The properties of the screen-printed FTS and HC catalyst layers for different integration configurations are listed in Table 3-17. In all systems, the layer thickness was controlled to 40-54 μm to achieve a comparable diffusion distance. Identical with the integration using powder catalyst, the weight ratio of FTS and HC catalysts was adjusted to be one in sequential, face-to-face and hybrid configurations. In the dual-layer pattern, less HC catalyst was used.

Table 3-17 Catalyst layer properties of different configurations in MCR-I

configuration	layer thickness [μm]		$m_{\text{FTS}} / m_{\text{HC}}$
	FTS	HC	
sequential	40	54	1 / 1
face-to-face	40	54	1 / 1
dual-layer	20	20	1 / 0.58
hybrid	50	50	1 / 1

3.5.2 Performance at 30 bar

The performance of different catalyst configurations was tested at 30 bar. The influence of the interaction between FTS and HC was analyzed in terms of CO conversion and hydrocarbon distribution. The selectivity and productivity of liquid fuels for different integration configurations was compared.

Figure 3-38a shows the CO conversion at different temperatures. Independence of FTS from HC in the sequential configuration leads to the same FTS performance as for the FTS reference. Similar CO conversion was observed. For the face-to-face integration, the CO conversion also stayed identical with the FTS reference, which is an indicator of the limited interaction between FTS and HC. Higher CO conversion was observed for dual-layer and hybrid configurations. At low temperature, the difference is limited. With temperature increasing, the difference becomes more obvious with 28% vs. 24% at 235 °C, 49% vs. 40% at 245 °C, and 82% vs. 73% at 260 °C. An improvement ratio of about 1.2 was obtained at 235 and 245 °C. At 260 °C the improvement ratio is a bit lower (1.12), which could be caused by the limit of high conversion. The improved CO conversion suggests that the interaction between FTS and HC is stronger in dual-layer and hybrid configurations. Higher productivity at constant temperature or constant productivity at lower temperature could be achieved in the dual-layer and hybrid system. Even though the interaction between FTS and HC in the dual-layer configuration would differ from that in the hybrid configuration, the overall effects on CO conversion are similar.

As discussed in section 3.2.2, compared to the catalyst packed-bed, slightly lower CO conversion and higher CH₄ selectivity were observed for the wall-coated FTS catalyst, which could be explained by the restricted effects of water and olefin adsorption owing to the limited capillary effects in the wall-coated microchannel (~400 μm diameter free space, no inert particles). Compared to the improvement ratio of 1.4 for the hybrid catalyst packed-bed, the

lower improvement ratio for the wall-coated catalysts could be another indirect evidence for the confined effects of water and olefin adsorption in the wall-coated microchannel.

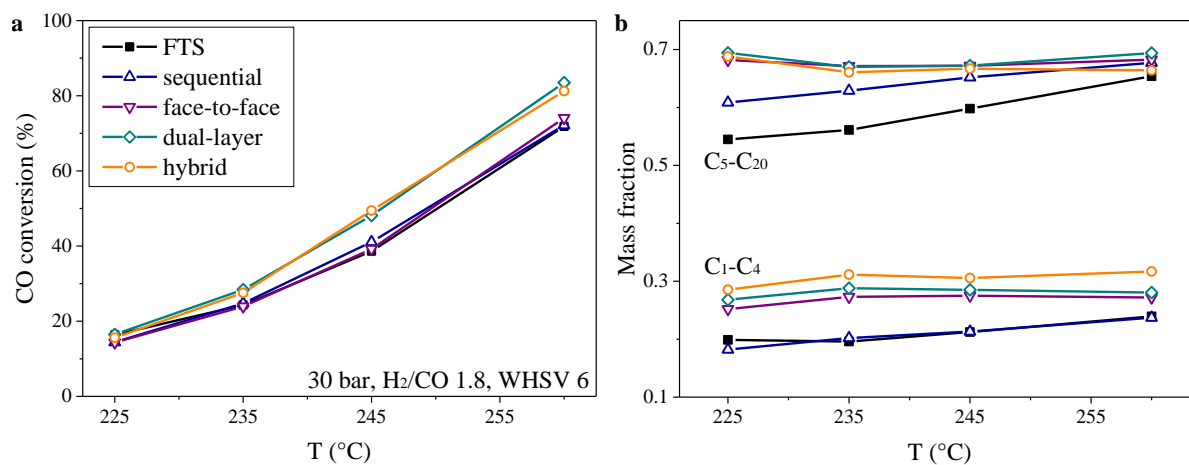


Figure 3–38 Integration performance of different catalyst configurations at 30 bar (a. CO conversion; b. mass fraction of C₁-C₄ and C₅-C₂₀)

The selectivity of the liquid fuel fraction (C₅-C₂₀) and of the gaseous hydrocarbons (C₁-C₄) is shown in Figure 3-38b. From 225 to 260 °C, the mass fraction of C₁-C₄ and C₅-C₂₀ in the FTS reference increases from 20% and 54% to 24% and 65%, respectively, which indicates a decreasing chain growth probability. In the sequential integration, an identical C₁-C₄ mass fraction like for the FTS reference was observed. The C₅-C₂₀ mass fraction was improved to 61% at 225 °C and continuously increased to 68% at 260 °C, suggesting that cracking of C₂₁₊ to C₅-C₂₀ is dominant. The sequential combination of FTS with HC enables an adjustment of the selectivity of the final products (Figure 3-38b and 3-39).

Compared to the sequential integration, a higher C₁-C₄ mass fraction was observed in the face-to-face arrangement (Figure 3-38b and 3-39), which varies between 25% and 27% over 225 to 260 °C. At the same time, a relatively stable C₅-C₂₀ mass fraction of 67-68% was obtained, which is identical with the maximum liquid fuel mass fraction that has been reached for the integrated system with powder catalysts. Similar CO conversion but higher mass fraction of C₁-C₄ and C₅-C₂₀ indicate that a higher degree of HC was achieved in the face-to-face configuration, which means that parallel FTS-HC is more efficient than consecutive FTS-HC.

Similar to the face-to-face configuration, dual-layer and hybrid configurations could also be categorized as parallel FTS-HC, but with enhanced interaction. As shown in Figure 3-39, hydrocarbons with a carbon number larger than 30 are almost eliminated in the parallel FTS-HC system. A stable C₅-C₂₀ mass fraction of 67-69% in the investigated temperature range of 225 to 260 °C was also observed for the dual-layer and hybrid systems. From face-to-face to

dual-layer and then to hybrid, an increasing C_1 - C_4 mass fraction was obtained. A clear shift to lighter hydrocarbons is visible in the product distribution (Figure 3-39). Since dual-layer and hybrid integration led to increased CO conversion, a higher HC efficiency with increasing interaction strength can be concluded. As listed in Table 3-17, a lower amount of HC catalyst was applied in the dual-layer configuration. The entire coverage of the FTS catalyst layer by the HC catalyst layer not only ensures the efficient cracking of FTS hydrocarbons, but also enables a similar FTS improvement like for the hybrid integration mode.

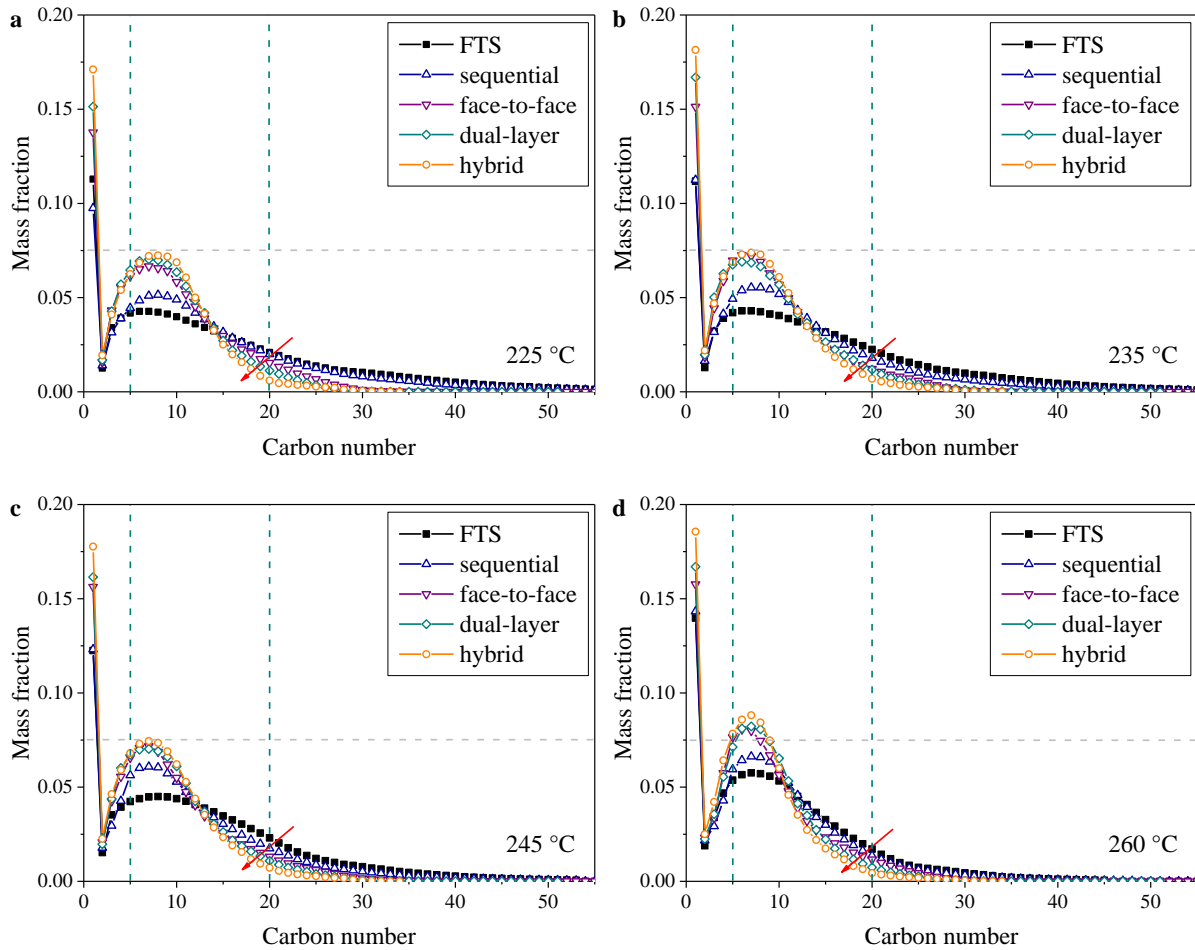


Figure 3–39 Hydrocarbon distribution at 30 bar (a. 225 °C; b. 235 °C; c. 245 °C; d. 260 °C)

Even though the same selectivity for C_5 - C_{20} was obtained in face-to-face, dual-layer and hybrid integration, the quality of the liquid fuels would be different. A higher gasoline fraction would be produced with stronger interaction between FTS and HC (Figure 3-39). From 225 to 260 °C the mass fraction of C_1 - C_4 and C_5 - C_{20} is roughly constant, which indicates the net production or consumption of the liquid fuel fraction is negligible. As implied by the grey dashed line in Figure 3-39, at 30 bar, temperature only has limited influence on the carbon number composition of the liquid fuels produced.

At 30 bar, the change of the reaction circumstance caused by the interaction between FTS and HC is beneficial for both FTS and HC. Higher HC efficiency, as well as higher CO conversion, was obtained for the parallel FTS-HC integration (face-to-face, dual-layer and hybrid).

Compared to the integration using powder catalysts, the mass fraction of C₅-C₂₀ reached its maximum value of around 70% at much lower temperature in the parallel FTS-HC integration scheme with wall-coated catalysts. However, a much higher selectivity of gaseous hydrocarbons (C₁-C₄) was obtained, which is clearly undesired from the perspective of PtL.

3.5.3 Performance at 20 bar

The performance of the wall-coated catalyst systems was also investigated at 20 bar. The VLE would be significantly affected by the lower pressure. The lower liquid fraction and different composition, accordingly, would influence both FTS and HC reactions.

CO conversion for different catalyst configurations is plotted against temperature in Figure 3-40a. As expected, identical CO conversion as for the FTS reference was obtained for the sequential integration.

Compared to the observation at 30 bar, different behavior was obtained for the parallel FTS-HC integration at 20 bar. The face-to-face integration exhibits higher CO conversion than the FTS reference under the same operating conditions. Whereas CO conversion for the dual-layer configuration was lower and close to the FTS reference. The lowest CO conversion was obtained for the hybrid integration. It seems like with an increase of the interaction strength between FTS and HC at 20 bar, the overall effects on CO conversion varies from positive to faint and ends to be negative. According to the VLE calculation of the effluent for the FTS reference, no liquid would exist at 20 bar. Counting in the capillary effects caused by the pores inside the catalyst layer, it is possible that the catalyst still can be, to some extent, filled with liquid. With synchronized cracking of heavy molecules in the parallel FTS-HC integration, at some point along the reactor the liquid cannot survive at 20 bar and both FTS and HC turn to be gas-solid two phase reactions. The molar fraction of hydrocarbons would further increase with progressive cracking of hydrocarbons into smaller molecules. Consequently, the partial pressure of the syngas would be limited, which may surpass the positive effects of olefin adsorption and therefore restrict the CO conversion.

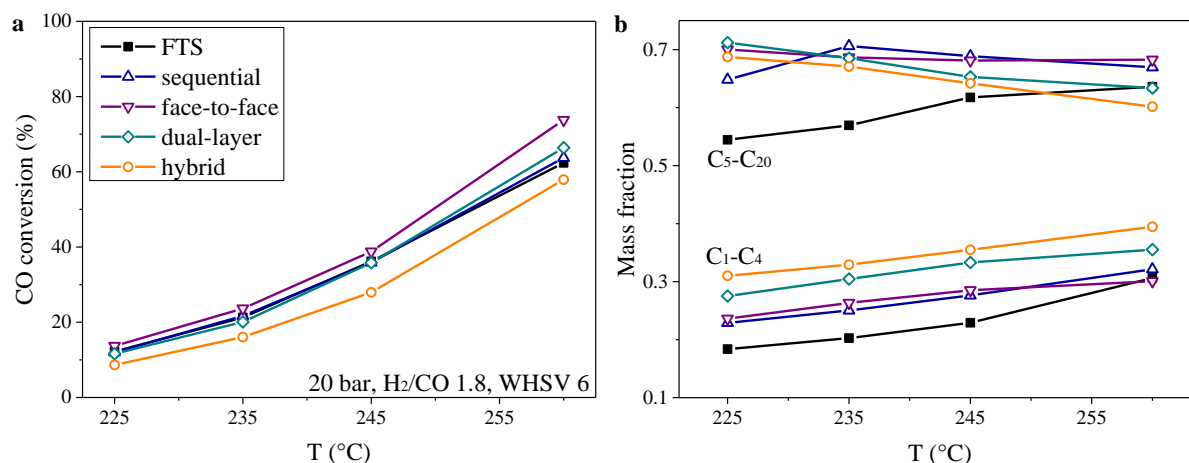


Figure 3-40 Integration performance of different catalyst configurations at 20 bar (a. CO conversion; b. mass fraction of C₁-C₄ and C₅-C₂₀)

From 225 to 260 °C, the mass fraction of C₁-C₄ and C₅-C₂₀ for the FTS reference increases from 18% and 54% to 31% and 64%, respectively (Figure 3-40b). Compared to FTS at 30 bar, a similar C₅-C₂₀ mass fraction, but a higher C₁-C₄ mass fraction was obtained, indicating a reduced chain growth probability at 20 bar. For the FTS-HC integration, a clear increase of the C₁-C₄ mass fraction was observed from sequential to face-to-face, dual-layer, and hybrid. Whereas a clear decrease was observed with the same order for the mass fraction of C₅-C₂₀. An improved HC efficiency was observed with enhanced FTS-HC interaction. Accordingly, the increased mass fraction of light hydrocarbons from face-to-face to dual-layer and hybrid system indicates a decreased fraction of the syngas, which may explain the decreased CO conversion.

Compared to the study at 30 bar, higher C₁-C₄ and C₅-C₂₀ mass fraction for the sequential integration was observed at 20 bar. For the parallel FTS-HC integration, hydrocarbons heavier than C₂₀ are almost completely missing (Figure 3-41). An increasing C₁-C₄ mass fraction and a decreasing C₅-C₂₀ mass fraction were obtained with increase of the temperature at 20 bar, which is different from the temperature-invariant mass fraction of C₁-C₄ and C₅-C₂₀ at 30 bar. The reduced pressure leads to a clear shift of the product distribution towards smaller carbon numbers. An increasing gasoline fraction (C₅-C₁₀) was observed with an increase of both temperature and interaction strength.

As an overall consequence, close to 70% C₅-C₂₀ mass fraction was obtained for the sequential integration at 20 bar. Whereas the “over-cracking” caused by the FTS-HC interaction leads to a reduced selectivity of liquid fuels and increased selectivity of gaseous hydrocarbons in the dual-layer and hybrid systems. The face-to-face integration, which offers the weakest FTS-

HC interaction, is the only one that preserves the positive effects for both productivity and selectivity of liquid fuels at 20 bar.

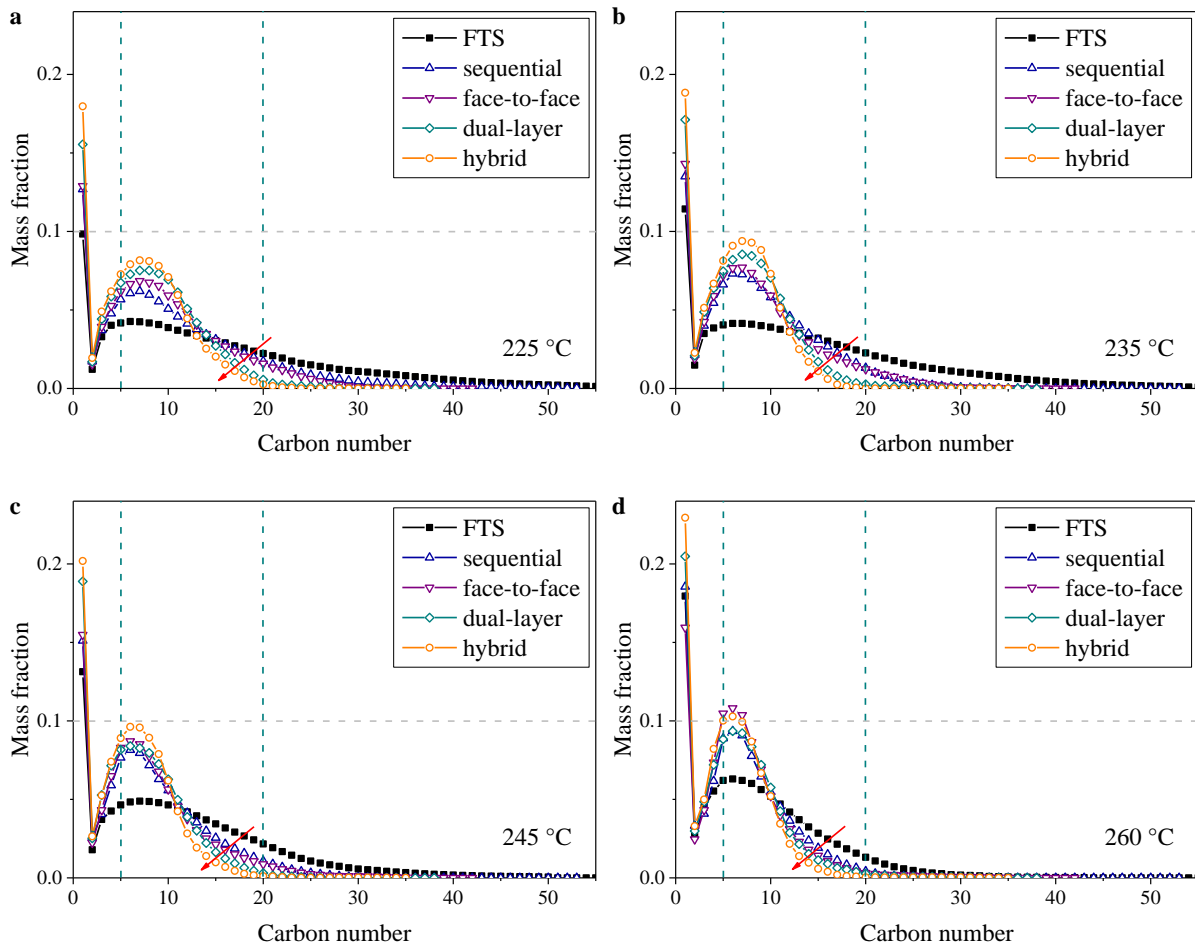


Figure 3–41 Hydrocarbon distribution at 20 bar (a. 225 °C; b. 235 °C; c. 245 °C; d. 260 °C)

Pressure only has a limited influence on the C₅-C₂₀ selectivity for the integration with powder catalysts. Opposite to this, an obvious influence of pressure was obtained for the integration with wall-coated catalysts. Compared to the wall-coated microchannel (400 μm diameter free space), the packing of catalyst particles (diluted with inert materials) would create stronger capillary effects to shift the VLE and hold more liquid, which could then explain the resistance to pressure change.

The FTS-HC integration with wall-coated catalysts offers more options for a flexible control of the desired product spectrum. At different operating conditions, the interaction between FTS and HC in the parallel FTS-HC integration system is significantly different. It is therefore important to figure out the optimum operating conditions for a given integration configuration or the optimum integration configuration for given operating conditions to ensure that both CO conversion and C₅-C₂₀ selectivity would benefit from the integrated FTS-HC system.

3.5.4 Stability of the catalysts

The stability of the wall-coated FTS and HC catalysts was also studied. The time-on-stream performance of all configurations is plotted in Figure 3-42.

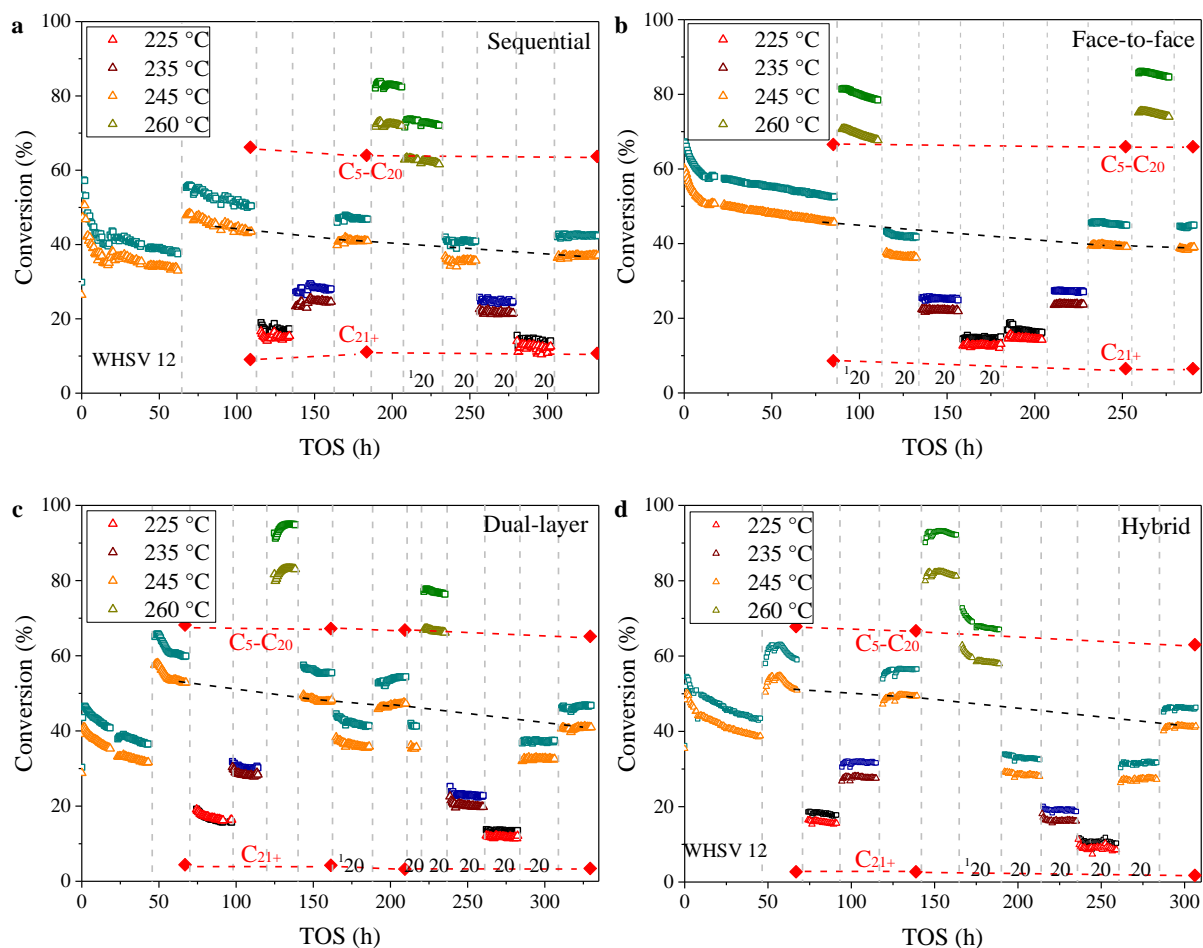


Figure 3–42 Catalyst stability in (a) sequential, (b) face-to-face, (c) dual-layer and (d) hybrid integration (¹ pressure in bar; if not specified: 30 bar, H₂/CO 1.8, WHSV 6)

In sequential integration, identical behavior as for the FTS reference is expected. Stable CO conversion was observed under each test, indicating a reasonable stability of the FTS catalyst layer. 245 °C, 30 bar, H₂/CO 1.8 and syngas WHSV 6 were selected as standard conditions to monitor the FTS and HC performance. From 100 to 175 h time-on-stream CO conversion dropped from 44% to 41% (1% per day). In the following a 0.5% per day conversion drop was observed until 350 h time-on-stream (37%). The stable FTS performance indicates a stable feeding for the HC. The mass fraction of C₅-C₂₀ and C₂₁₊ was followed as an indicator of the HC catalyst stability. From 100 to 175 h, and then to 350 h time-on-stream, the C₅-C₂₀ mass fraction varied from 66.2% to 64.0% (0.7% per day), and then to 63.7% (0.04% per day). Correspondingly, the C₂₁₊ mass fraction changed from 9.1% to 11.1% (0.6% per day), and

then to 10.7% (0.05% per day). Both FTS and HC catalysts in the sequential integration exhibited reasonable stability.

In the parallel FTS-HC integration, both CO conversion and hydrocarbon mass fractions are caused by joint effects of the interaction between FTS and HC. Similar to the sequential integration, a reasonable FTS and HC catalyst stability was observed in the face-to-face (Figure 3-42b), dual-layer (Figure 3-42c) and hybrid (Figure 3-42d) configurations.

Hence, a reasonable stability was obtained for all wall-coated FTS and HC catalysts.

3.5.5 Integration performance with independent temperature control of FTS and HC

The intrinsic difference between FTS and HC makes the integration complicated. As a polymerization reaction, FTS would benefit from high pressure, which is, however, negative for HC. CO and water from FTS are also unfavorable for HC. Compared to HC (260-320 °C), a lower temperature is preferred for LTFT (200-250 °C). Intensive efforts are required to achieve the optimal performance for the integrated system. It would be interesting to figure out the difference if the temperature is different for the FTS and the HC. The microchannel reactors capable of flexible temperature control may offer a suitable solution. Via using circulating thermal oil for the FTS zone and electric heating cartridges for the HC zone, independent temperatures could be applied for the sequential configuration in MCR-I and for the face-to-face configuration in MCR-II. The influence of independent temperature control on the performance of the integrated systems was investigated.

3.5.5.1 Sequential integration in MCR-I

Independent FTS and HC temperatures were achieved in MCR-I for sequential integration. The performance at constant FTS (HC) temperature and different HC (FTS) temperatures was compared. While keeping the FTS (HC) temperature at 245 °C, the HC (FTS) temperature was varied from 235 to 260 °C. The temperature profiles in the MCR-I are shown in Figure 3-43. The FTS temperature was well isolated from the HC temperature. In between the FTS and the HC section a narrow transition region with intermediate temperature was observed, which would have limited influence on both reactions.

Figure 3-44 shows the performance at constant HC temperature but different FTS temperatures. With FTS temperature increasing from 235 to 260 °C, CO conversion increases from 29% to 70%. The conversion difference caused by the transition region is no larger than 1.5%. The C₅-C₂₀ mass fraction decreases from 70% to 65%, which is caused by the increased feeding for HC. Correspondingly, more heavy hydrocarbons were observed due to the

insufficient HC. Dominated by FTS, an increasing C_1 - C_4 mass fraction was obtained, which is consistent with the FTS reference. Even though the selectivity went down, a higher productivity was observed for the liquid fuel fraction due to the increased CO conversion.

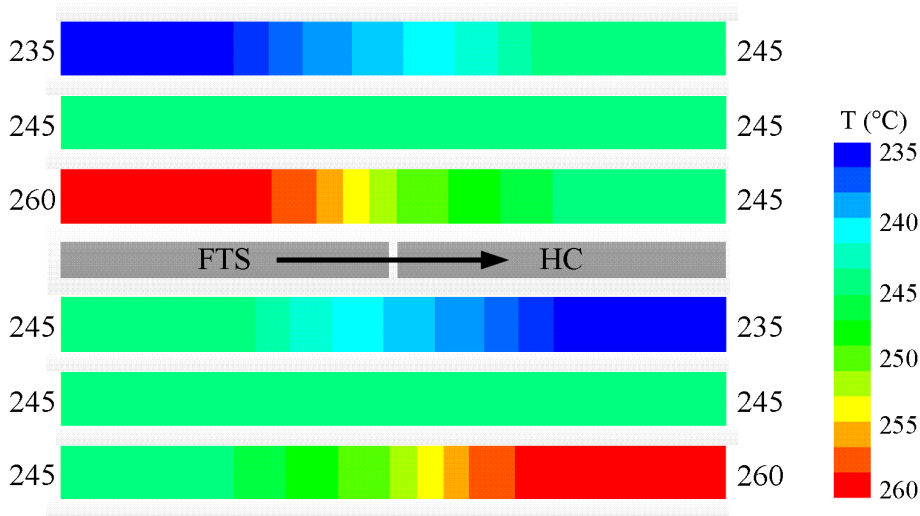


Figure 3–43 Temperature profiles in MCR-I for independent FTS and HC temperatures

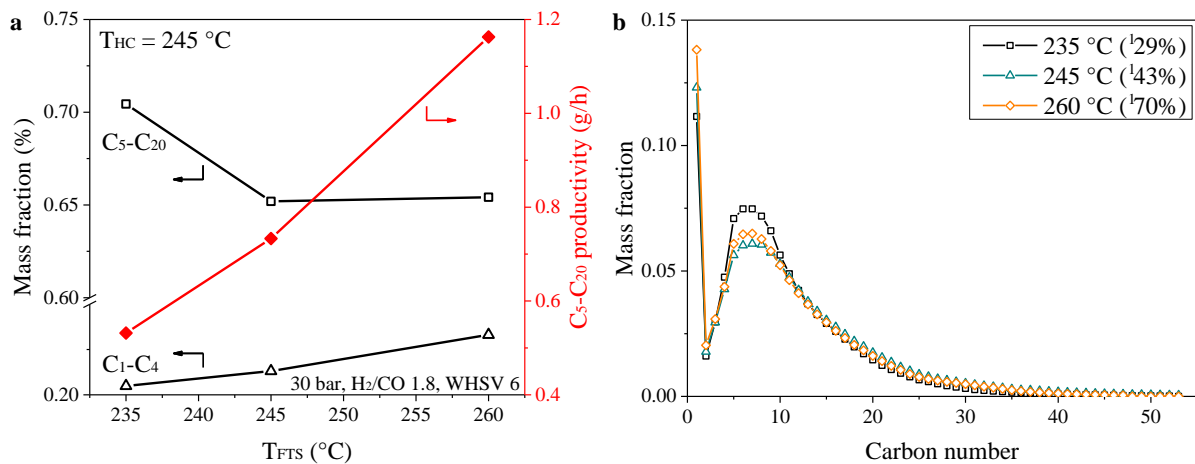


Figure 3–44 Performance of the sequential FTS-HC system at constant HC temperature but different FTS temperatures (1 CO conversion)

The performance at constant FTS temperature but different HC temperatures is depicted in Figure 3-45. Stable CO conversion was obtained when increasing the HC temperature from 235 to 260 °C. With the enhanced HC activity, more hydrocarbons get cracked. The mass fraction of C_5 - C_{20} raises from 61% to 72%, which indicates a significant improvement of the liquid fuel selectivity via the independent temperature adjustment. Accordingly, a higher C_5 - C_{20} productivity was obtained. The relatively stable C_1 - C_4 mass fraction suggests that further cracking of the liquid fuel fraction was limited.

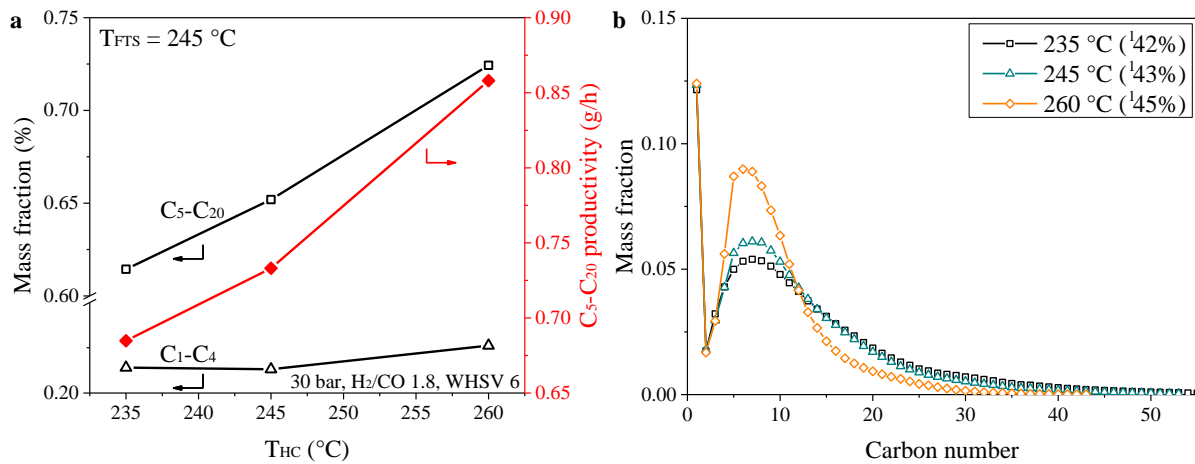


Figure 3–45 Performance of the sequential FTS-HC system at constant FTS temperature but different HC temperatures (¹ CO conversion)

3.5.5.2 Face-to-face integration in MCR-II

MCR-II enables independent FTS and HC temperatures for the face-to-face integration. Temperature profile derived by simulation with the FEM method is shown in Figure 3-46 [244]. Assuming a thermal oil temperature (FTS) of 220 °C, a heating cartridge temperature (HC) of 350 °C and no flow between FTS and HC foils, a uniform FTS layer and HC layer temperature is predicted, indicating sufficient thermal insulation by the 0.5 mm gap and the controlling systems for FTS and HC foils.

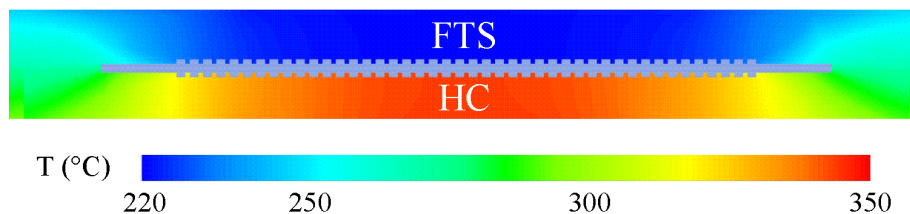


Figure 3–46 Temperature profile in MCR-II for independent FTS and HC temperatures

To study the influence on the performance of the face-to-face system, FTS temperature was kept at 245 °C and HC temperature was increased from 245 to 280 °C. Different from the increasing C₅-C₂₀ mass fraction in the sequential integration (Figure 3-45a), the selectivity of the liquid fuel fraction did not change much in the face-to-face integration (Figure 3-47a). At 245 °C 71% C₅-C₂₀ was achieved. A further increase of the HC temperature had only limited influence on the C₅-C₂₀ mass fraction, while the mass fraction of C₁-C₄ slightly increased from 24% to 28%. Even though the HC temperature did hardly affect the liquid fuel selectivity within the studied range, it changed the quality of the liquid fuel fraction (Figure 3-47b). More C₁₁-C₂₀ hydrocarbons were cracked into C₅-C₁₀ with increasing HC temperature.

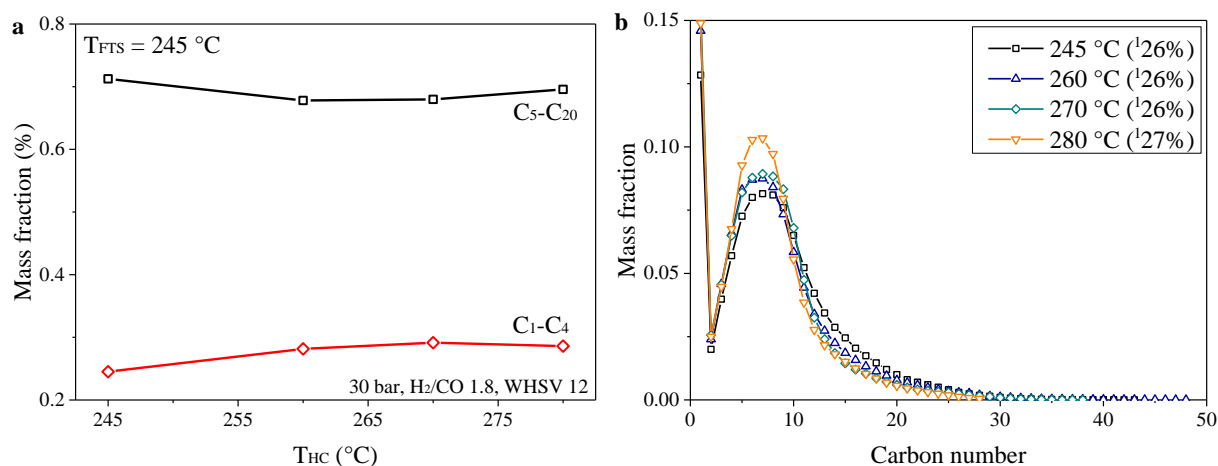


Figure 3-47 Performance of the face-to-face FTS-HC system at constant FTS temperature but different HC temperatures (¹ CO conversion)

3.5.6 Computational analysis of the wall-coated FTS-HC integration system

The experimental investigation of the integrated FTS-HC system with wall-coated catalysts showed the performance of the different configurations and the influence of the operating conditions with a view to liquid fuel synthesis. However, there are still open questions which are very challenging to be answered experimentally. As discussed in section 3.2.2, compared to the catalyst packed-bed, slightly lower CO conversion and different conversion-selectivity relationships were observed for the FTS with wall-coated catalysts. To be able to understand these observations, detailed information on the interaction between FTS and HC is required, for which computational analysis of the wall-coated system was carried out. The same reaction kinetics as for the powder catalysts were applied. Plug flow behavior was assumed for the free space of the channel according to the estimation of the Bodenstein number (section 2.1.2).

The influence of catalyst layer thickness on FTS was investigated. As elaborated in section 3.2.4, the entire catalyst layer would be filled with liquid hydrocarbons. A heterogeneous model solving the reaction-diffusion equations for the cylindrical catalyst layer was established assuming annular geometry. 245 °C, 30 bar, H₂/CO 1.8 and syngas WHSV 6 were selected as standard conditions.

The effectiveness factors for the consumption of H₂ and CO are plotted in Figure 3-48a. With increase of the layer thickness from 20 to 80 μm, the effectiveness factor of H₂ and CO decreases from 1 to 0.94. Larger descent of the effectiveness factors along the reactor length was predicted at larger thickness. Concentration gradients of H₂ and CO inside the catalyst layer are shown in Figure 3-48b. In the 20 μm thick layer, the concentration gradients are negligible. In the 80 μm thick layer, the H₂ concentration close to the channel wall is only 65%

of concentration on the surface of the coating. Owing to the increased catalyst layer thickness, a slight reduction of CO conversion is predicted. From 20 to 80 μm , CO conversion decreases by 6% (50.6% to 47.6%). Within the studied range, the mass transport inside the catalyst layer has only limited influence on the overall CO conversion. The increasing difference between the H_2 and CO concentration gradients with increasing layer thickness indicates a decreasing local H_2/CO ratio inside the catalyst layer, which could affect the hydrocarbon selectivity. Overall, both experimentally and by simulation similar CO conversion and hydrocarbon selectivity were obtained for the 20 and 40 μm FTS catalyst layers.

However, the simulated CO conversion (50%) and CH_4 selectivity (8%) failed to match the experimental values (40% CO conversion and 12% CH_4 selectivity) of the wall-coated catalyst system, whereas they are in good agreement with the experimental data for the catalyst packed-bed (50% CO conversion and 8% CH_4 selectivity). As discussed in section 3.2.2, compared to the catalyst packed-bed, the lower CO conversion and higher CH_4 selectivity for the wall-coated FTS catalyst could be caused by the suppressed effects of water and olefin adsorption owing to the reduced capillary condensation in the wall-coated channel compared to the packed-bed, which changes the VLE and leads to lower partial pressures of water and olefins. Note that in the simplified FTS kinetics neither olefin production, nor water adsorption are included. Hence, the associated effects on the reaction kinetics cannot be reproduced by the model. Considering that an influence of the diffusion of the syngas in the catalyst layer can be excluded, the simulation results suggest, indirectly, that the difference in the adsorption of water and olefins would be responsible for the different behavior between the packed-bed and the wall-coated catalyst.

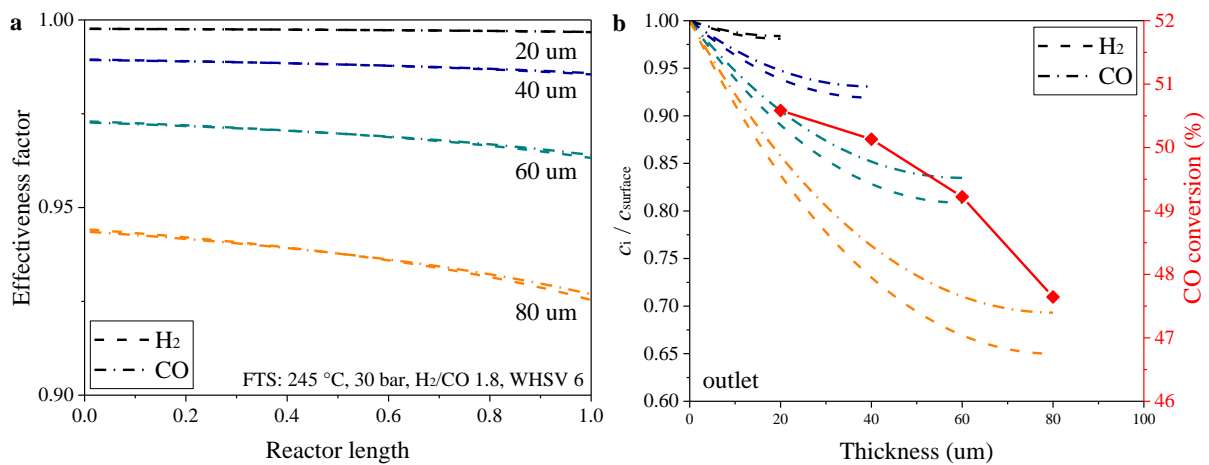


Figure 3–48 Influence of catalyst layer thickness on the FTS performance (note that the effectiveness factors for H_2 and CO basically fall on the same curves)

Based on the experimental data, an interaction between FTS and HC can be expected in parallel FTS-HC integration. From face-to-face to dual-layer and then to hybrid configuration, the interaction strength increases. Even though the simplified kinetics cannot predict the water and olefin adsorption for FTS and also not the CO adsorption and olefin reactions (consumption and production) for HC, they were nevertheless used to study the influence of the composition change caused by the local hydrocarbon cracking in the parallel FTS-HC system. The hybrid system at 245 °C, 30 bar, H₂/CO 1.8 and syngas WHSV 6 was simulated and compared to the FTS reference.

As shown in Figure 3-49, different profiles of the C₅-C₂₀ mass fraction along the reactor are predicted for the FTS reference (red dashed line) and the hybrid system (red dashed-dotted line). For the FTS reference, the mass fraction of C₅-C₂₀ slightly decreases from 56.3% to 55.3%. On the contrary, an increasing C₅-C₂₀ mass fraction from 56.3% to 66.3% was predicted for the hybrid integration, indicating sufficient HC of heavy hydrocarbons. Correspondingly, a slower increase of the liquid fraction was predicted for the hybrid system (green dashed-dotted line). The local hydrocarbon cracking in the hybrid system not only lowers the syngas molar fraction and produces more olefins, but also consumes additional H₂. The composition change could be well reproduced by the simulation. However, the CO conversion for the FTS reference and the hybrid system basically fall on the same curves (black dashed and dashed-dotted lines), which stands against the experimentally observed higher CO conversion for the hybrid system. According to the simulated results here, the changed syngas concentration and H₂/CO ratio are expected to have only limited influence on the FTS. Hence, there must be other effects that influence the CO conversion in the parallel FTS-HC integration system. Considering that the HC of FTS hydrocarbons can also consume and produce olefins, indirect evidence again points to the adsorption of water and olefins, which could explain higher CO conversion for the hybrid system as a consequence of the increased olefin concentration, i.e. adsorption, owing to the local hydrocarbon cracking.

To conclude, the computational analysis of the wall-coated system suggests that, within the studied range, the diffusion in the catalyst layer has only limited influence on the reaction performance. Indirect evidence exists indicating that the adsorption of water and olefins may not only be responsible for the conversion-selectivity relation in the FTS reference, but also contribute to the interaction between FTS and HC in the parallel FTS-HC. A more detailed kinetic model including olefin formation and consumption as well as the effects of water adsorption on the reaction rates is required though to better analyze the possible effects.

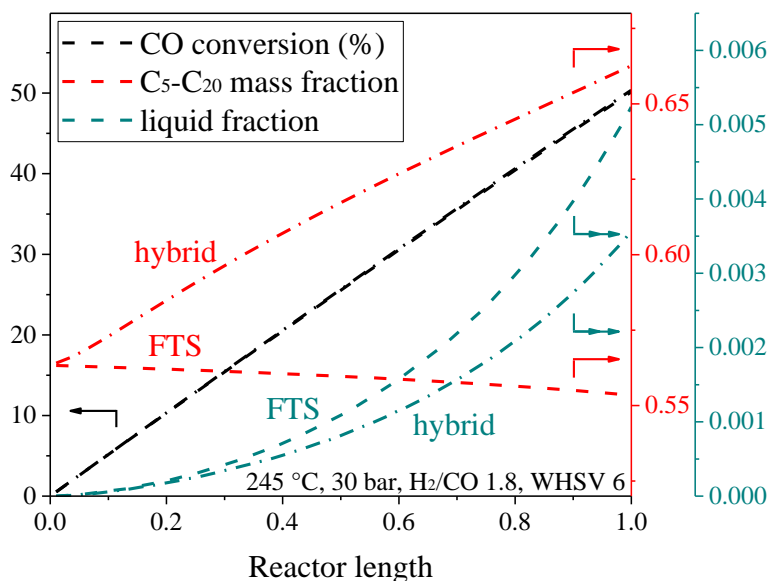


Figure 3-49 Comparison between FTS reference and hybrid integration

3.6 Discussion of the different integration options

The integration of FTS and HC in micro-structured reactors was investigated with a view to selectivity and productivity of liquid fuels. Both sequential and parallel modes were proposed to achieve a one-stage combination of FTS with HC. For the packed-bed catalyst, sequential and hybrid configurations were analyzed. For the wall-coated catalyst, sequential, face-to-face, dual-layer and hybrid configurations were studied. The influence of the operating conditions was also investigated. The liquid fuel production in the integrated system is the joint effect of FTS and HC. FTS determines the productivity of all hydrocarbons (CO conversion and chain growth probability). Whereas HC, then, promotes the selectivity and productivity of the liquid fuels. A brief summary of different integrated systems is listed in Table 3-18. All integrated systems reached a maximum C₅-C₂₀ mass fraction of around 70 wt.%.

For the sequential mode, FTS is independent of HC. Identical CO conversion as for the FTS reference was observed with the packed-bed catalyst and with the wall-coated catalyst. Compared to the packed-bed, the wall-coated catalyst showed a lower CO conversion, indicating a lower hydrocarbon productivity. At 245 °C the C₅-C₂₀ mass fraction reached its maximum value both for the sequential packed-bed and wall-coated catalyst systems, which was furthermore maintained constant over the pressure range of 20-30 bar.

For the parallel mode, the local cracking of hydrocarbons changes the FTS reaction environment and therefore affects the FTS performance. More parallel options are available for the wall-coated catalyst than for the packed-bed. Compared to the sequential integration, superior hydrocarbon productivity, i.e. higher CO conversion, was obtained at 30 bar for the

parallel FTS-HC scheme. From face-to-face over dual-layer to hybrid, the interaction between FTS and HC increased, leading to an increased CO conversion. Lower temperature was sufficient for the parallel integration compared to the sequential integration to reach the maximum C₅-C₂₀ mass fraction. Accordingly, at 30 bar a higher yield of liquid fuels was obtained for parallel integration compared to the sequential integration, among which the hybrid packed-bed catalyst gave even higher yields than the hybrid wall-coated catalyst. When reducing the pressure to 20 bar, the hybrid packed-bed catalyst kept the improved CO conversion and the maximum C₅-C₂₀ mass fraction. On the contrary, the hybrid wall-coated catalyst produced lower CO conversion than the FTS reference and reduced C₅-C₂₀ mass fraction. Hence, better resistance against pressure changes was obtained for the hybrid packed-bed catalyst than for the hybrid wall-coated catalyst. Moreover, a larger fraction of undesired C₁-C₄ was obtained for the parallel integration using the wall-coated catalyst.

Overall, regarding selectivity and productivity, the hybrid packed-bed catalyst achieved the best performance in terms of liquid fuel synthesis within the studied range. The larger volumetric productivity could be another advantage of the packed-bed over the coating. Considering that the FTS and HC catalysts are loaded in one reactor but have a different lifetime, a detailed study of catalyst regeneration appears to be necessary.

3. FTS-HC integration in micro-structured reactors

Table 3-18 Summary of different integration options

integration option	CO conversion	¹ C ₅ -C ₂₀ mass fraction	
packed-bed catalyst (larger catalyst loading)	sequential	identical with FTS reference	reached 70 wt.% at 245 °C; constant at 70 wt.% over 20-30 bar at 245 °C; constant at 70 wt.% over H ₂ /CO 1.6-2.0 at 245 °C
	hybrid	higher than FTS reference	reached 70 wt.% at 235 °C; constant at 70 wt.% over 20-30 bar at 235 and 245 °C; constant at 70 wt.% over H ₂ /CO 1.6-2.0 at 235 and 245 °C
wall-coated catalyst layer (lower pressure drop)	sequential	identical with FTS reference; slightly lower than catalyst packed-bed	30 bar: reached 70 wt.% at 245 °C; 20 bar: constant at 70 wt.% over 225-260 °C
	face-to-face	30 bar: similar to FTS reference; 20 bar: higher than FTS reference	30 and 20 bar: constant at 70 wt.% over 225-260 °C
	dual-layer (less HC catalyst)	30 bar: higher than FTS reference; 20 bar: similar to FTS reference	30 bar: constant at 70 wt.% over 225-260 °C; 20 bar: decreasing from 70 to 63 wt.% over 225-260 °C
	hybrid	30 bar: higher than FTS reference; lower than catalyst packed-bed 20 bar: lower than FTS reference	30 bar: constant at 70 wt.% over 225-260 °C; 20 bar: decreasing from 70 to 60 wt.% over 225-260 °C

¹ WHSV 6, H₂/CO 1.8 and 30 bar, if applicable

4. Summary and conclusions

Direct syngas-to-fuel conversion via integration of Fischer-Tropsch synthesis (FTS) and hydrocracking (HC) in micro-structured reactors has been investigated in this dissertation with a view to selectivity and productivity of liquid fuels (C₅-C₂₀). The feasibility of this integration was verified with a two-stage sequential system using powder catalysts. Significant improvement of the C₅-C₂₀ mass fraction was obtained via the incorporation of HC. Moreover, a reasonable stability of the FTS and HC catalysts was observed.

Targeting small-scale simplified power-to-liquid (PtL) plants, the integration of FTS and HC in one stage was also implemented. For powder catalysts, an annular micro packed-bed reactor was developed and sequential and hybrid integration options were tested. The influence of the operating conditions on the performance was analyzed. The sequential FTS-HC system exhibits the same CO conversion as the FTS reference, whereas improved CO conversion was observed for the hybrid integration. A maximum C₅-C₂₀ mass fraction of 70 wt.% was achieved in both sequential and hybrid systems. In case of the hybrid system, lower temperature was required to reach the maximum fuel selectivity. Limited effects of pressure and H₂/CO ratio on the selectivity of liquid fuels were observed for both sequential and hybrid integration. The hybrid configuration showed superior capability regarding fuel synthesis. Sufficient evidence points out that the FTS lays the foundation of the fuel synthesis and HC just promotes it. In the sequential configuration, FTS is independent from HC. HC only changes the product distribution. In the hybrid system, the local cracking of hydrocarbons changes the reaction environment and therefore also affects the FTS.

To compare with the FTS-HC integration using packed-bed catalysts, wall-coated catalyst layers were also applied, for which microchannel reactors were developed and screen-printing was adopted to prepare the different catalyst layers. Identical performance was observed for 20 and 40 μm thick FTS catalyst layers, indicating the absence of diffusion limitation. Compared to the FTS packed-bed, slightly lower CO conversion was observed for the wall-coated FTS catalyst. For the FTS-HC integration, sequential and parallel (face-to-face, dual-layer and hybrid) arrangements were tested. The sequential integration gave identical CO conversion like the FTS reference. At 30 bar, increasing CO conversion and HC efficiency were observed from face-to-face over dual-layer to hybrid integration, indicating an increased interaction between FTS and HC in the parallel system. However, at 20 bar, decreasing CO conversion was found from face-to-face over dual-layer to hybrid integration, which was

tentatively explained by the reduced syngas partial pressure owing to increased hydrocarbon fraction caused by the local cracking. Compared to the hybrid packed-bed catalyst, fuel synthesis was less effective and the tolerance against pressure change was reduced for the hybrid wall-coated catalyst. This was explained tentatively by the reduced effects of water and olefin adsorption owing to the reduced water and olefin concentration caused by the reduced capillary condensation in the wall-coated channel compared to the packed-bed. The independent FTS and HC temperature control in the microchannel reactor offers a distinct advantage for the study of the integrated process. In a practical system, attention must be paid to the FTS-HC interaction to ensure that the positive effects on both the CO conversion and the C₅-C₂₀ mass fraction can be achieved.

For investigation of liquid filling along with the accumulation of heavy hydrocarbons in the catalyst particles and in the voids of the packed-bed, both experimental and simulation studies were carried out. FTS and HC kinetic parameters were estimated based on the data from the packed-bed experiments. Via characterization of the used FTS catalyst layer as well as modelling and simulation, at 30 bar complete liquid filling of the pores in the catalyst particles and catalyst layers over the entire reactor length was confirmed. The influence of the liquid on the reaction performance was analyzed using a heterogeneous model solving the reaction-diffusion equations. Neither FTS nor HC are significantly affected by the mass transport inside the catalyst particles and the catalyst layers. However, in the packed-bed system, the simulation showed evidence for local blocking of void spaces for both FTS and HC at relatively high liquid fraction. A reduced catalyst effectiveness factor of around 0.6-0.7 was predicted for the blocked sections. The annular gap geometry of the micro packed-bed reactor, where the large width-to-height ratio of the cross-section makes the distribution of the flow more difficult, could be particularly critical regarding liquid blocking.

To find out the difference between the packed-bed and the wall-coated catalyst, and to understand the implications of the FTS-HC interaction in the parallel integration mode, the wall-coated catalyst system was also simulated. The experimentally observed absence of transport limitations in the studied range was confirmed by the simulation results. The change of the syngas concentration and H₂/CO ratio caused by the local hydrocarbon cracking in the hybrid FTS-HC system was well predicted. The simulation results rule out the influence of the syngas concentration change on the CO conversion at the selected conditions. Indirect evidence again points tentatively to the adsorption of water and olefins, which was reported to be positive to the FTS chain growth. Compared to the packed-bed catalyst, the lower CO conversion and chain growth probability for the wall-coated FTS catalyst were explained by

the reduced partial pressures of water and olefins owing to the reduced capillary condensation in the wall-coated channel. The improved CO conversion for the parallel FTS-HC system was explained by the increased olefin partial pressure owing to the local cracking of hydrocarbons.

5. Outlook

Integration of FTS and HC in micro-structured reactors exhibits promising potential for process simplification in decentralized small-scale PtL plants. To better understand and practically better apply the integrated FTS-HC process, further efforts should be focused on:

1) Effects of water and olefin adsorption on FTS. Indirect evidence indicates the adsorption of water and olefins would be responsible for both the relation between CO conversion and hydrocarbon selectivity and the interaction between FTS and HC. An experimental study with additional feeding of water or olefins could be implemented to provide direct evidence for the influence of water and olefin adsorption. Computational analysis with more detailed kinetic model including olefin and water adsorption could be performed. The change of VLE caused by capillary effects could be studied by detailed simulation.

2) Catalyst development. Activity loss of the FTS catalyst was observed after undergoing the coating procedure, which would lower the efficiency of the microchannel reactor with wall-coated catalysts. To take full advantage of the micro-structured reactors, more active and stable catalysts could be developed. Considering the difficulty of catalyst replacement and the different lifetime of FTS and HC catalysts, regeneration must also be investigated.

3) Integration with CO₂ activation. The combined FTS and HC in micro-structured reactors appears promising with a view to process simplification for small-scale PtL plants. Extra benefits could be achieved due to interactions between the different reactions. The possibility of directly converting CO₂ into a gasoline fuel was also verified. Further simplification by including the CO₂ activation into micro-structured reactors could be tested. One-stage CO₂-to-fuel would be a new milestone for decentralized power-to-fuel conversion.

Nomenclature

Symbols

ΔH	reaction enthalpy
L	length
r or R	radius or reaction rate
V	volume
X	conversion
n	reaction order
D	diffusivity
u	velocity
ΔP	pressure drop
ΔT	temperature difference
m	mass
W	width
H	height
S/V	surface-to-volume ratio
s	area
P	pressure
T	temperature
\dot{n}	molar flow rate
S	selectivity or solubility
w	mass fraction
K	equilibrium constant
k	reaction rate constant
c	concentration
x	molar fraction
n	molar amount
M_w	molecular weight
N_L	average carbon number of the liquid

Nomenclature

H	Henry coefficient
j_i	material flux of component i
F	filling degree
R	ideal gas constant
Δ_V	diffusion volume
V_m	molar volume
E_a	activation energy
Exp.	experiment
Sim.	simulation
Ref.	reference
Eq.	equation
α	chain growth probability
d or Φ	diameter
δ	thickness
ε	porosity
τ	tortuosity
ρ	density
μ	dynamic viscosity
λ	wavelength length or thermal conductivity
θ	angle
β	mass transfer coefficient
η	effectiveness factor
Bo	Bodenstein number
Re	Reynolds number
Pe	Péclet number
Sh	Sherwood number

Subscripts and superscripts

cat.	catalyst
h	hydraulic

rad	radial
ax	axial
<i>i</i> or <i>j</i>	component or carbon number
ad	adsorption
IN	chain initiation
G	chain growth
iso-r	isomerization
cr-r	cracking
iso	iso-paraffin
n	n-paraffin
form	formation
V	vapor phase
L	liquid phase
0	initial value
max	maximum
mono	monolayer
char	characteristic length
eff	effective
mix	mixture
obs	observed

Abbreviations

PtG	power-to-gas
PtL	power-to-liquid
FTS	Fischer-Tropsch synthesis
ASF	Anderson-Schulz-Flory
LTFT	low-temperature Fischer-Tropsch synthesis
HC	hydrocracking
VLE	vapor-liquid equilibrium
MCR	microchannel reactor
GHSV	gas hourly space velocity
WGS	water-gas-shift

Nomenclature

TEM	transmission electron microscope
BF	bright-field
HAADF-STEM	high-angle annular dark-field scanning TEM
EDX	energy dispersive X-ray
XRD	X-ray diffraction
PSD	position-sensitive detector
BET	Brunauer-Emmett-Teller
ICP-OES	inductively coupled plasma optical emission spectrometry
TPR	temperature-programmed reduction
BSE	back-scattered electron
WDS	wavelength-dispersive spectroscopy
EPMA	electron probe microanalyzer
MFC	mass flow controller
GC	gas chromatography
TCD	thermal conductivity detector
FID	flame ionization detector
WHSV	weight hourly space velocity

References

- [1] BP, BP statistical review of world energy 2016. <<http://www.bp.com/en/global/corporate/energy-economics/statistical-review-of-world-energy.html>>, 2017.
- [2] B. Jager, R. Espinoza, Advances in low temperature Fischer-Tropsch synthesis, Catal. Today 23 (1995) 17-28.
- [3] D. Pimentel, M.A. Moran, S. Fast, G. Weber, R. Bukantis, L. Balliett, P. Boveng, C. Cleveland, S. Hindman, M. Young, Biomass energy from crop and forest residues, Science 212 (1981) 1110-1115.
- [4] G. Schaub, R. Edzang, Synthetic fuels from natural gas and biomass - status and perspectives, Chem. Ing. Tech. 83 (2011) 1912-1924.
- [5] S. Chu, A. Majumdar, Opportunities and challenges for a sustainable energy future, Nature 488 (2012) 294-303.
- [6] W.M. Verdegaal, S. Becker, C. von Olshausen, Power-to-liquids: synthetic crude oil from CO₂, water, and sunshine, Chem. Ing. Tech. 87 (2015) 340-346.
- [7] European Commission, Energy strategy: secure, competitive, and sustainable energy. <<https://ec.europa.eu/energy/en/topics/energy-strategy>>, 2016
- [8] T. Klaus, C. Vollmer, K. Werner, H. Lehmann, K. Müschen, Energieziel 2050: 100% Strom aus erneuerbaren Quellen. <https://www.umweltbundesamt.de/sites/default/files/medien/378/publikationen/energieziel_2050.pdf>, Umweltbundesamt, 2010.
- [9] German Federal Ministry for Economic Affairs and Energy, Erneuerbare Energien in Zahlen: Nationale und internationale Entwicklung im Jahr 2015. <http://www.erneuerbare-energien.de/EE/Redaktion/DE/Downloads/erneuerbare-energien-in-zahlen-2015.pdf?__blob=publicationFile&v=6>, 2016.
- [10] German Federal Ministry for Economic Affairs and Energy, For a future of green energy. <<http://www.bmwi.de/Redaktion/EN/Dossier/renewable-energy.html>>, 2017.
- [11] German Federal Ministry for Economic Affairs and Energy, Ready for the next phase of the energy transition. <<http://www.bmwi.de/Redaktion/EN/Dossier/energy-transition.html>>, 2017.

- [12] German Association of Energy and Water Industries, Erneuerbare Energien und das EEG: Zahlen, Fakten, Grafiken. <[https://www.bdew.de/internet.nsf/res/4A5D437AB754A529C125817C00323A64/\\$file/Awh_20170710_Erneuerbare-Energien-EEG_2017.pdf](https://www.bdew.de/internet.nsf/res/4A5D437AB754A529C125817C00323A64/$file/Awh_20170710_Erneuerbare-Energien-EEG_2017.pdf)>, 2017.
- [13] G. Maschio, A. Lucchesi, G. Stoppato, Production of syngas from biomass, *Bioresour. Technol.* 48 (1994) 119-126.
- [14] V. Kirubakaran, V. Sivaramakrishnan, R. Nalini, T. Sekar, M. Premalatha, P. Subramanian, A review on gasification of biomass, *Renewable Sustainable Energy Rev.* 13 (2009) 179-186.
- [15] G. Centi, S. Perathoner, Opportunities and prospects in the chemical recycling of carbon dioxide to fuels, *Catal. Today* 148 (2009) 191-205.
- [16] W.M. Verdegaal, S. Becker, C. von Olshausen, Power-to-liquids: synthetic crude oil from CO₂, water, and sunshine, *Chem. Ing. Tech.* 87 (2015) 340-346.
- [17] F. Fischer, H. Tropsch, The synthesis of petroleum at atmospheric pressures from the gasification products of coal, *Brennst. Chem.* 7 (1926) 97-104.
- [18] R.B. Anderson, H. Kölbel, M. Rálek, *The Fischer-Tropsch synthesis*, Academic Press 1984.
- [19] V. Calemma, S. Corraera, C. Perego, P. Pollesel, L. Pellegrini, Hydroconversion of Fischer-Tropsch waxes: assessment of the operating conditions effect by factorial design experiments, *Catal. Today* 106 (2005) 282-287.
- [20] D. Leckel, M. Liwanga-Ehumbu, Diesel-selective hydrocracking of an iron-based Fischer-Tropsch wax fraction (C₁₅-C₄₅) using a MoO₃-modified noble metal catalyst, *Energy Fuels* 20 (2006) 2330-2336.
- [21] Y.Y. Liu, T. Hanaoka, K. Murata, K. Okabe, M. Inaba, I. Takahara, K. Sakanishi, Hydrocracking of Fischer-Tropsch wax to diesel-range hydrocarbons over bifunctional catalysts containing Pt and polyoxocation-pillared montmorillonite, *Chem. Lett.* 36 (2007) 1470-1471.
- [22] V. Calemma, C. Gambaro, W.O. Parker, R. Carbone, R. Giardino, P. Scorletti, Middle distillates from hydrocracking of FT waxes: composition, characteristics and emission properties, *Catal. Today* 149 (2010) 40-46.

- [23] G. Polczmann, J. Valyon, A. Szegedi, R.M. Mihalyi, J. Hancsok, Hydroisomerization of Fischer-Tropsch wax on Pt/AlSBA-15 and Pt/SAPO-11 Catalysts, *Top. Catal.* 54 (2011) 1079-1083.
- [24] R.S. Paris, M.E. L'Abbate, L.F. Liotta, V. Montes, J. Barrientos, F. Regali, A. Aho, M. Boutonnet, S. Jaras, Hydroconversion of paraffinic wax over platinum and palladium catalysts supported on silica-alumina, *Catal. Today* 275 (2016) 141-148.
- [25] S.T. Sie, M.M.G. Senden, H.M.H. Van Wechem, Conversion of natural gas to transportation fuels via the shell middle distillate synthesis process (SMDS), *Catal. Today* 8 (1991) 371-394.
- [26] G. Kolb, V. Hessel, Micro-structured reactors for gas phase reactions, *Chem. Eng. J.* 98 (2004) 1-38.
- [27] R. Myrstad, S. Eri, P. Pfeifer, E. Rytter, A. Holmen, Fischer-Tropsch synthesis in a microstructured reactor, *Catal. Today* 147 (2009) S301-S304.
- [28] J.J. Lerou, A.L. Tonkovich, L. Silva, S. Perry, J. McDaniel, Microchannel reactor architecture enables greener processes, *Chem. Eng. Sci.* 65 (2010) 380-385.
- [29] A. Holmen, H.J. Venvik, R. Myrstad, J. Zhu, D. Chen, Monolithic, microchannel and carbon nanofibers/carbon felt reactors for syngas conversion by Fischer-Tropsch synthesis, *Catal. Today* 216 (2013) 150-157.
- [30] S. LeViness, S.R. Deshmukh, L.A. Richard, H.J. Robota, Velocys Fischer-Tropsch synthesis technology - new advances on state-of-the-art, *Top. Catal.* 57 (2014) 518-525.
- [31] M. Gotz, J. Lefebvre, F. Mors, A.M. Koch, F. Graf, S. Bajohr, R. Reimert, T. Kolb, Renewable power-to-gas: a technological and economic review, *Renewable Energy* 85 (2016) 1371-1390.
- [32] P. Piermartini, T. Boeltken, M. Selinsek, P. Pfeifer, Influence of channel geometry on Fischer-Tropsch synthesis in microstructured reactors, *Chem. Eng. J.* 313 (2017) 328-335.
- [33] C.D. Chang, W.H. Lang, A.J. Silvestri, Synthesis gas conversion to aromatic hydrocarbons, *J. Catal.* 56 (1979) 268-273.
- [34] N. Tsubaki, Y. Yoneyama, K. Michiki, K. Fujimoto, Three-component hybrid catalyst for direct synthesis of isoparaffin via modified Fischer-Tropsch synthesis, *Catal. Commun.* 4 (2003) 108-111.

- [35] X.H. Li, M.F. Luo, K. Asami, Direct synthesis of middle iso-paraffins from synthesis gas on hybrid catalysts, *Catal. Today* 89 (2004) 439-446.
- [36] A. Freitez, K. Pabst, B. Kraushaar-Czarnetzki, G. Schaub, Single-stage Fischer-Tropsch synthesis and hydroprocessing: the hydroprocessing performance of Ni/ZSM-5/ γ -Al₂O₃ under Fischer-Tropsch conditions, *Ind. Eng. Chem. Res.* 50 (2011) 13732-13741.
- [37] J. Bao, G.H. Yang, C. Okada, Y. Yoneyama, N. Tsubaki, H-type zeolite coated iron-based multiple-functional catalyst for direct synthesis of middle isoparaffins from syngas, *Appl. Catal., A* 394 (2011) 195-200.
- [38] K. Pabst, M.I. Gonzalez, B. Kraushaar-Czarnetzki, G. Schaub, Combination of Fischer-Tropsch synthesis and hydroprocessing in a single-stage reactor. part I. mathematical modeling of the reaction kinetics, *Ind. Eng. Chem. Res.* 52 (2013) 8978-8987.
- [39] K. Pabst, B. Kraushaar-Czarnetzki, G. Schaub, Combination of Fischer-Tropsch synthesis and hydroprocessing in a single-stage reactor. part II. effect of catalyst combinations, *Ind. Eng. Chem. Res.* 52 (2013) 8988-8995.
- [40] S. Sartipi, K. Parashar, M. Makkee, J. Gascon, F. Kapteijn, Breaking the Fischer-Tropsch synthesis selectivity: direct conversion of syngas to gasoline over hierarchical Co/H-ZSM-5 catalysts, *Catal. Sci. Technol.* 3 (2013) 572-575.
- [41] S. Sartipi, K. Parashar, M.J. Valero-Romero, V.P. Santos, B. van der Linden, M. Makkee, F. Kapteijn, J. Gascon, Hierarchical H-ZSM-5-supported cobalt for the direct synthesis of gasoline-range hydrocarbons from syngas: Advantages, limitations, and mechanistic insight, *J. Catal.* 305 (2013) 179-190.
- [42] Y.Z. Jin, R.Q. Yang, Y. Mori, J. Sun, A. Taguchi, Y. Yoneyama, T. Abe, N. Tsubaki, Preparation and performance of Co based capsule catalyst with the zeolite shell sputtered by Pd for direct isoparaffin synthesis from syngas, *Appl. Catal., A* 456 (2013) 75-81.
- [43] J. Bao, N. Tsubaki, Core-shell catalysts and bimodal catalysts for Fischer-Tropsch synthesis, *Catalysis: Volume 25*, The Royal Society of Chemistry 2013, pp. 216-245.
- [44] S. Sartipi, M. Alberts, V.P. Santos, M. Nasalevich, J. Gascon, F. Kapteijn, Insights into the catalytic performance of mesoporous H-ZSM-5-supported cobalt in Fischer-Tropsch synthesis, *ChemCatChem* 6 (2014) 142-151.

- [45] C. Sun, T. Zhan, P. Pfeifer, R. Dittmeyer, Influence of Fischer-Tropsch synthesis (FTS) and hydrocracking (HC) conditions on the product distribution of an integrated FTS-HC process, *Chem. Eng. J.* 310, Part 1 (2017) 272-281.
- [46] J. Weitkamp, Catalytic hydrocracking - mechanisms and versatility of the process, *ChemCatChem* 4 (2012) 292-306.
- [47] J.J. He, B.L. Xu, Y. Yoneyama, N. Nishiyama, N. Tsubaki, Designing a new kind of capsule catalyst and its application for direct synthesis of middle isoparaffins from synthesis gas, *Chem. Lett.* 34 (2005) 148-149.
- [48] G.H. Yang, J.J. He, Y. Yoneyama, Y.S. Tan, Y.Z. Han, N. Tsubaki, Preparation, characterization and reaction performance of H-ZSM-5/cobalt/silica capsule catalysts with different sizes for direct synthesis of isoparaffins, *Appl. Catal., A* 329 (2007) 99-105.
- [49] S. Sartipi, M. Alberts, M.J. Meijerink, T.C. Keller, J. Pérez-Ramírez, J. Gascon, F. Kapteijn, Towards Liquid Fuels from Biosyngas: Effect of Zeolite Structure in Hierarchical-Zeolite-Supported Cobalt Catalysts, *ChemSusChem* (2013) n/a-n/a.
- [50] N. Tsubaki, K. Michiki, Y. Yoneyama, K. Fujimoto, Hybrid catalyst for direct synthesis of isoparaffin through modified Fischer-Tropsch synthesis, *Sekiyu Gakkaishi* 44 (2001) 338-339.
- [51] Y. Yoneyama, J.J. He, Y. Morii, S. Azuma, N. Tsubaki, Direct synthesis of isoparaffin by modified Fischer-Tropsch synthesis using hybrid catalyst of iron catalyst and zeolite, *Catal. Today* 104 (2005) 37-40.
- [52] T.S. Zhao, J. Chang, Y. Yoneyama, N. Tsubaki, Selective synthesis of middle isoparaffins via a two-stage Fischer-Tropsch reaction: Activity investigation for a hybrid catalyst, *Ind. Eng. Chem. Res.* 44 (2005) 769-775.
- [53] M.E. Dry, The Fischer-Tropsch process: 1950-2000, *Catal. Today* 71 (2002) 227-241.
- [54] C.S. Cao, Y. Wang, S.B. Jones, J.L. Hu, X.S. Li, D.C. Elliott, D.J. Stevens, Microchannel catalytic processes for converting biomass-derived syngas to transportation fuels, *ACS Symp. Ser.* 914 (2005) 273-284.
- [55] C.S. Cao, D.R. Palo, A.L.Y. Tonkovich, Y. Wang, Catalyst screening and kinetic studies using microchannel reactors, *Catal. Today* 125 (2007) 29-33.

- [56] L. Guillou, D. Balloy, P. Supiot, V. Le Courtois, Preparation of a multilayered composite catalyst for Fischer-Tropsch synthesis in a micro-chamber reactor, *Appl. Catal., A* 324 (2007) 42-51.
- [57] C.S. Cao, J.L. Hu, S.R. Li, W. Wilcox, Y. Wang, Intensified Fischer-Tropsch synthesis process with microchannel catalytic reactors, *Catal. Today* 140 (2009) 149-156.
- [58] R. Guettel, T. Turek, Comparison of different reactor types for low temperature Fischer-Tropsch synthesis: a simulation study, *Chem. Eng. Sci.* 64 (2009) 955-964.
- [59] J. Knochen, R. Guettel, C. Knobloch, T. Turek, Fischer-Tropsch synthesis in milli-structured fixed-bed reactors: experimental study and scale-up considerations, *Chem. Eng. Process.* 49 (2010) 958-964.
- [60] S. Chambrey, P. Fongarland, H. Karaca, S. Piche, A. Griboval-Constant, D. Schweich, F. Luck, S. Savin, A.Y. Khodakov, Fischer-Tropsch synthesis in milli-fixed bed reactor: comparison with centimetric fixed bed and slurry stirred tank reactors, *Catal. Today* 171 (2011) 201-206.
- [61] X. Ying, L. Zhang, H. Xu, Y. Ren, J. Xuan, An experimental study on a microchannel reactor for Fischer-tropsch synthesis, *Energy Procedia* 61 (2014) 1394-1397.
- [62] L.C. Almeida, F.J. Echave, O. Sanz, M.A. Centeno, G. Arzamendi, L.M. Gandía, E.F. Sousa-Aguar, J.A. Odriozola, M. Montes, Fischer-Tropsch synthesis in microchannels, *Chem. Eng. J.* 167 (2011) 536-544.
- [63] C. Knobloch, R. Guettel, T. Turek, Holdup and pressure drop in micro packed-bed reactors for Fischer-Tropsch synthesis, *Chem. Ing. Tech.* 85 (2013) 455-460.
- [64] J. Yang, S. Boullosa-Eiras, R. Myrstad, H. Venvik, P. Pfeifer, A. Holmen, Fischer-Tropsch synthesis on Co-based catalysts in a microchannel reactor. effect of temperature and pressure on selectivity and stability, in: B.H. Davis, M.L. Occelli (Eds.) *Fischer-Tropsch synthesis, catalysts and catalysis: advances and applications*, CRC Press 2016, pp. 223-242.
- [65] A.M. Hilmen, E. Bergene, O.A. Lindvåg, D. Schanke, S. Eri, A. Holmen, Fischer-Tropsch synthesis on monolithic catalysts of different materials, *Catal. Today* 69 (2001) 227-232.
- [66] A.M. Hilmen, E. Bergene, O.A. Lindvag, D. Schanke, S. Eri, A. Holmen, Fischer-Tropsch synthesis on monolithic catalysts with oil circulation, *Catal. Today* 105 (2005) 357-361.

- [67] F. Kapteijn, R.M. de Deugd, J.A. Moulijn, Fischer-Tropsch synthesis using monolithic catalysts, *Catal. Today* 105 (2005) 350-356.
- [68] C.G. Visconti, E. Tronconi, L. Lietti, G. Groppi, P. Forzatti, C. Cristiani, R. Zennaro, S. Rossini, An experimental investigation of Fischer-Tropsch synthesis over washcoated metallic structured supports, *Appl. Catal., A* 370 (2009) 93-101.
- [69] L.C. Almeida, O. Sanz, J. D'olhaberriague, S. Yunes, M. Montes, Microchannel reactor for Fischer-Tropsch synthesis: adaptation of a commercial unit for testing microchannel blocks, *Fuel* 110 (2013) 171-177.
- [70] L.C. Almeida, O. Sanz, D. Merino, G. Arzamendi, L.M. Gandia, M. Montes, Kinetic analysis and microstructured reactors modeling for the Fischer-Tropsch synthesis over a Co-Re/Al₂O₃ catalyst, *Catal. Today* 215 (2013) 103-111.
- [71] L. Yu, R. Nassar, J. Fang, D. Kuila, K. Varahramyan, Investigation of a novel microreactor for enhancing mixing and conversion, *Chem. Eng. Commun.* 195 (2008) 745-757.
- [72] I.V. Derevich, V.S. Ermolaev, V.Z. Mordkovich, Modeling of hydrodynamics in microchannel reactor for Fischer-Tropsch synthesis, *Int. J. Heat Mass Transfer* 55 (2012) 1695-1708.
- [73] I.V. Derevich, V.S. Ermolaev, V.Z. Mordkovich, D.D. Galdina, Simulation of fluid dynamics in a microchannel Fischer-Tropsch reactor, *Theor. Found. Chem. Eng.* 46 (2012) 8-19.
- [74] S. Mehta, V. Deshmane, S.H. Zhao, D. Kuila, Comparative studies of silica-encapsulated iron, cobalt, and ruthenium nanocatalysts for Fischer-Tropsch synthesis in silicon-microchannel microreactors, *Ind. Eng. Chem. Res.* 53 (2014) 16245-16253.
- [75] A.P. Raje, B.H. Davis, Effect of vapor-liquid equilibrium on Fischer-Tropsch hydrocarbon selectivity for a deactivating catalyst in a slurry reactor, *Energy Fuels* 10 (1996) 552-560.
- [76] L.A. Richard, P. Moreau, S. Rugmini, F. Daly, Fischer-Tropsch performance correlated to catalyst structure: trends in activity and stability for a silica-supported cobalt catalyst, *Appl. Catal., A* 464 (2013) 200-206.

- [77] H.J. Robota, L.A. Richard, S. Deshmukh, S. LeViness, D. Leonarduzzi, D. Roberts, High activity and selective Fischer-Tropsch catalysts for use in a microchannel reactor, *Catal. Surv. Asia* 18 (2014) 177-182.
- [78] S.R. Deshmukh, A.L.Y. Tonkovich, K.T. Jarosch, L. Schrader, S.P. Fitzgerald, D.R. Kilanowski, J.J. Lerou, T.J. Mazanec, Scale-up of microchannel reactors for Fischer-Tropsch synthesis, *Ind. Eng. Chem. Res.* 49 (2010) 10883-10888.
- [79] T. Fleisch, Associated gas utilization via miniGTL. <<https://openknowledge.worldbank.org/handle/10986/21976>>, World Bank, 2012.
- [80] J.G. Koortzen, S. Bains, L.L. Kocher, I.K. Baxter, R.A. Morgan, Modular gas-to-liquid: converting a liability into economic value, *Ind. Eng. Chem. Res.* 53 (2014) 1720-1726.
- [81] M.J. Bowe, Plate-type reactor with a removable catalytic structure, Google Patents, 2005.
- [82] Velocys, Our biorefineries: ENVIA Energy. <<http://www.velocys.com/our-biorefineries>>, 2017.
- [83] P. Schubert, Development of larger FT reactors & progress at ENVIA Energy's GTL plant. <http://www.velocys.com/media_presentations.php>, Velocys, 2016.
- [84] R. Dittmeyer, T. Boeltken, P. Piermartini, M. Selinsek, M. Loewert, F. Dallmann, H. Kreuder, M. Cholewa, A. Wunsch, M. Belimov, S. Farsi, P. Pfeifer, Micro and micro membrane reactors for advanced applications in chemical energy conversion, *Curr. Opin. Chem. Eng.* 17 (2017) 108-125.
- [85] INERATEC, Compact containerized chemical plants. <<http://inratec.de/technologien/?lang=en>>, 2017.
- [86] INERATEC, Power-to-liquid: 200 liters of fuel from solar power and the air's carbon dioxide. <<http://inratec.de/power-to-liquid-200-liters-of-fuel-from-solar-power-and-the-air-carbon-dioxide/?lang=en>>, 2017.
- [87] C. Sun, M. Klumpp, J. Binder, P. Pfeifer, R. Dittmeyer, One-stage syngas-to-fuel conversion with printed catalyst layers in microstructured reactors, *Chem. Ing. Tech.* 89 (2017) 894-902.
- [88] C. Sun, P. Pfeifer, R. Dittmeyer, One-stage syngas-to-fuel in a micro-structured reactor: investigation of integration pattern and operating conditions on the selectivity and productivity of the liquid fuel, *Chem. Eng. J.* 326 (2017) 37-46.

- [89] C. Sun, Z. Luo, A. Choudhary, P. Pfeifer, R. Dittmeyer, Influence of the condensable hydrocarbons on an integrated Fischer-Tropsch synthesis and hydrocracking process: simulation and experimental validation, *Ind. Eng. Chem. Res.* (2017).
- [90] H. Löwe, W. Ehrfeld, State-of-the-art in microreaction technology: concepts, manufacturing and applications, *Electrochim. Acta* 44 (1999) 3679-3689.
- [91] V. Hessel, J.C. Schouten, A. Renken, *Micro process engineering: a comprehensive handbook*, Wiley 2009.
- [92] V. Hessel, H. Löwe, Organic synthesis with microstructured reactors, *Chem. Eng. Technol.* 28 (2005) 267-284.
- [93] O. Gorke, P. Pfeifer, K. Schubert, Controlled hydrogen oxidation in a microstructures blender reactor module, *Chem. Ing. Tech.* 78 (2006) 581-587.
- [94] E. Klemm, H. Doring, A. Geisselmann, S. Schirrmeister, Microstructured reactors in heterogeneous catalysis, *Chem. Eng. Technol.* 30 (2007) 1615-1621.
- [95] G. Kolb, Review: Microstructured reactors for distributed and renewable production of fuels and electrical energy, *Chem. Eng. Process.* 65 (2013) 1-44.
- [96] H.J. Venvik, J. Yang, Catalysis in microstructured reactors: Short review on small-scale syngas production and further conversion into methanol, DME and Fischer-Tropsch products, *Catal. Today* 285 (2017) 135-146.
- [97] D.E. Mears, Tests for transport limitations in experimental catalytic reactors, *Ind. Eng. Chem. Process Des. Dev.* 10 (1971) 541-547.
- [98] N. Wakao, S. Kaguei, T. Funazkri, Effect of fluid dispersion coefficients on particle-to-fluid heat-transfer coefficients in packed-beds - correlation of Nusselt numbers, *Chem. Eng. Sci.* 34 (1979) 325-336.
- [99] M. Punčochář, J. Drahoš, The tortuosity concept in fixed and fluidized bed, *Chem. Eng. Sci.* 48 (1993) 2173-2175.
- [100] I.C. Yates, C.N. Satterfield, Intrinsic kinetics of the Fischer-Tropsch synthesis on a cobalt catalyst, *Energy Fuels* 5 (1991) 168-173.
- [101] C.F. Chu, K.M. Ng, Flow in packed tubes with a small tube to particle diameter ratio, *AIChE J.* 35 (1989) 148-158.
- [102] X.D. Zhan, B.H. Davis, Two alpha Fischer-Tropsch product distribution. a role for vapor-liquid equilibrium?, *Petrol. Sci. Technol.* 18 (2000) 1037-1053.

- [103] B.H. Davis, Fischer-Tropsch synthesis: overview of reactor development and future potentialities, *Top. Catal.* 32 (2005) 143-168.
- [104] N. Kockmann, *Transport phenomena in micro process engineering*, 1 ed., Springer Berlin Heidelberg 2008.
- [105] M.E. Dry, J.C. Hoogendoorn, Technology of the Fischer-Tropsch process, *Catal. Rev.* 23 (1981) 265-278.
- [106] A.Y. Khodakov, W. Chu, P. Fongarland, Advances in the development of novel cobalt Fischer-Tropsch catalysts for synthesis of long-chain hydrocarbons and clean fuels, *Chem. Rev.* 107 (2007) 1692-1744.
- [107] F. Diehl, A.Y. Khodakov, Promotion of cobalt Fischer-Tropsch catalysts with noble metals: a review, *Oil Gas Sci. Technol.* 64 (2009) 11-24.
- [108] A. Stefanescu, A.C. van Veen, C. Mirodatos, J.C. Beziat, E. Duval-Brunel, Wall coating optimization for microchannel reactors, *Catal. Today* 125 (2007) 16-23.
- [109] V. Calemma, S. Peratello, C. Perego, Hydroisomerization and hydrocracking of long chain n-alkanes on Pt/amorphous SiO₂-Al₂O₃ catalyst, *Appl. Catal., A* 190 (2000) 207-218.
- [110] U.M. Teles, F.A.N. Fernandes, Hydrocracking of Fischer-Tropsch products. optimization of diesel and naphtha cuts, *Chem. Biochem. Eng. Q.* 22 (2008) 227-231.
- [111] I. Nam, K.M. Cho, J.G. Seo, S. Hwang, K.W. Jun, I.K. Song, Production of middle distillate from synthesis gas in a dual-bed reactor through hydrocracking of wax over mesoporous Pd-Al₂O₃ composite catalyst, *Catal. Lett.* 130 (2009) 192-197.
- [112] Y.Y. Liu, K. Murata, K. Okabe, M. Inaba, I. Takahara, T. Hanaoka, K. Sakanishi, Selective hydrocracking of Fischer-Tropsch waxes to high-quality diesel fuel over Pt-promoted polyoxocation-pillared montmorillonites, *Top. Catal.* 52 (2009) 597-608.
- [113] M.G. Seo, D.W. Lee, K.Y. Lee, D.J. Moon, Pt/Al-SBA-15 catalysts for hydrocracking of C₂₁-C₃₄ n-paraffin mixture into gasoline and diesel fractions, *Fuel* 143 (2015) 63-71.
- [114] T. Hanaoka, T. Miyazawa, K. Shimura, S. Hirata, Effect of Pt particle density on the hydrocracking of Fischer-Tropsch products over Pt-loaded zeolite catalysts prepared using water-in-oil microemulsions, *Chem. Eng. J.* 274 (2015) 256-264.
- [115] T. Hanaoka, T. Miyazawa, K. Shimura, S. Hirata, Effects of catalyst preparation on hydrocarbon product distribution in hydrocracking of the Fischer-Tropsch product with low Pt-loaded catalysts, *Catalysts* 5 (2015) 1983-2000.

- [116] M. Steijns, G. Froment, P. Jacobs, J. Uytterhoeven, J. Weitkamp, Hydroisomerization and hydrocracking .2. product distributions from normal-decane and normal-dodecane, *Ind. Eng. Chem. Prod. Res. Dev.* 20 (1981) 654-660.
- [117] M. Kobayashi, S. Togawa, K. Ishida, Properties and molecular structures of fuel fractions obtained from hydrocracking/isomerization of Fischer-Tropsch waxes, *Sekiyu Gakkaishi* 49 (2006) 194-201.
- [118] C. Bouchy, G. Hastoy, E. Guillon, J.A. Martens, Fischer-Tropsch waxes upgrading via hydrocracking and selective hydroisomerization, *Oil Gas Sci. Technol.* 64 (2009) 91-112.
- [119] G.Z. Liu, G.L. Zhao, F.X. Meng, S.D. Qu, L. Wang, X.W. Zhang, Catalytic cracking of supercritical n-dodecane over wall-coated H-ZSM-5 zeolites with micro- and nanocrystal sizes, *Energy Fuels* 26 (2012) 1220-1229.
- [120] F. Regali, R.S. Paris, A. Aho, M. Boutonnet, S. Jaras, Deactivation of a Pt/Silica-Alumina catalyst and effect on selectivity in the hydrocracking of n-hexadecane, *Top. Catal.* 56 (2013) 594-601.
- [121] T. Hanaoka, T. Miyazawa, K. Shimura, S. Hirata, Jet fuel synthesis from Fischer-Tropsch product under mild hydrocracking conditions using Pt-loaded catalysts, *Chem. Eng. J.* 263 (2015) 178-185.
- [122] M.A. Liauw, M. Baerns, R. Broucek, O.V. Buyevskaya, J.-M. Commenge, J.-P. Corriou, L. Falk, K. Gebauer, H.J. Hefter, O.-U. Langer, H. Löwe, M. Matlosz, A. Renken, A. Rouge, R. Schenk, N. Steinfeldt, S. Walter, Periodic operation in microchannel reactors, in: W. Ehrfeld (Ed.) *Microreaction Technology: Industrial Prospects: IMRET 3: Proceedings of the Third International Conference on Microreaction Technology*, Springer Berlin Heidelberg, Berlin, Heidelberg, 2000, pp. 224-234.
- [123] A.J. Franz, K.F. Jensen, M.A. Schmidt, Palladium membrane microreactors, in: W. Ehrfeld (Ed.) *Microreaction Technology: Industrial Prospects: IMRET 3: Proceedings of the Third International Conference on Microreaction Technology*, Springer Berlin Heidelberg, Berlin, Heidelberg, 2000, pp. 267-276.
- [124] M.A. Ulla, R. Mallada, J. Coronas, L. Gutierrez, E. Miro, J. Santamaria, Synthesis and characterization of ZSM-5 coatings onto cordierite honeycomb supports, *Appl. Catal., A* 253 (2003) 257-269.

- [125] X.F. Zhang, H.O. Liu, K.L. Yeung, Influence of seed size on the formation and microstructure of zeolite silicalite-1 membranes by seeded growth, *Mater. Chem. Phys.* 96 (2006) 42-50.
- [126] A. Eleta, P. Navarro, L. Costa, M. Montes, Deposition of zeolitic coatings onto FeCrAlloy microchannels: washcoating vs. in situ growing, *Microporous Mesoporous Mater.* 123 (2009) 113-122.
- [127] L. Wang, Y. Wang, J.G. Hao, G.Z. Liu, X.S. Ma, S.L. Hu, Synthesis of H-ZSM-5 coatings on the inner surface of stainless steel tubes and their catalytic performance in n-dodecane cracking, *Appl. Catal., A* 462 (2013) 271-277.
- [128] R. Zapf, C. Becker-Willinger, K. Berresheim, H. Bolz, H. Gnaser, V. Hessel, G. Kolb, P. Lob, A.K. Pannwitt, A. Ziogas, Detailed characterization of various porous alumina-based catalyst coatings within microchannels and their testing for methanol steam reforming, *Chem. Eng. Res. Des.* 81 (2003) 721-729.
- [129] G. Germani, A. Stefanescu, Y. Schuurman, A.C. van Veen, Preparation and characterization of porous alumina-based catalyst coatings in microchannels, *Chem. Eng. Sci.* 62 (2007) 5084-5091.
- [130] R. Guettel, J. Knochen, U. Kunz, M. Kassing, T. Turek, Preparation and catalytic evaluation of cobalt-based monolithic and powder catalysts for Fischer-Tropsch synthesis, *Ind. Eng. Chem. Res.* 47 (2008) 6589-6597.
- [131] N.R. Peela, A. Mubayi, D. Kunzru, Washcoating of gamma-alumina on stainless steel microchannels, *Catal. Today* 147 (2009) S17-S23.
- [132] H. Pennemann, M. Dobra, M. Wichert, G. Kolb, Optimization of wash-coating slurries as catalyst carrier for screen printing into microstructured reactors, *Chem. Eng. Technol.* 36 (2013) 1033-1041.
- [133] X. Ying, L. Zhang, H. Xu, Y.L. Ren, Q. Luo, H.W. Zhu, H. Qu, J. Xuan, Efficient Fischer-Tropsch microreactor with innovative aluminizing pretreatment on stainless steel substrate for Co/Al₂O₃ catalyst coating, *Fuel Process. Technol.* 143 (2016) 51-59.
- [134] H.-W. Lin, C.-P. Chang, W.-H. Hwu, M.-D. Ger, The rheological behaviors of screen-printing pastes, *J. Mater. Process. Technol.* 197 (2008) 284-291.
- [135] S. Brunauer, P.H. Emmett, E. Teller, Adsorption of gases in multimolecular layers, *J. Am. Chem. Soc.* 60 (1938) 309-319.

- [136] R.C. Reuel, C.H. Bartholomew, The stoichiometries of H₂ and Co adsorptions on cobalt - effects of support and preparation, *J. Catal.* 85 (1984) 63-77.
- [137] J.T. Kummer, H.H. Podgurski, W.B. Spencer, P.H. Emmett, Mechanism studies of the Fischer-Tropsch synthesis - the addition of radioactive alcohol, *J. Am. Chem. Soc.* 73 (1951) 564-569.
- [138] H. Storch, N. Golumbic, R.B. Anderson, *The Fischer-Tropsch and related synthesis*, Wiley, New York, 1951.
- [139] H. Pichler, H. Schulz, Neuere Erkenntnisse auf dem Gebiet der Synthese von Kohlenwasserstoffen aus CO und H₂, *Chem. Ing. Tech.* 42 (1970) 1162-1174.
- [140] V. Ponc, Some aspects of the mechanism of methanation and Fischer-Tropsch synthesis, *Catal. Rev.* 18 (1978) 151-171.
- [141] G.P. Van der Laan, A.A.C.M. Beenackers, Kinetics and selectivity of the Fischer-Tropsch synthesis: a literature review, *Catal. Rev.* 41 (1999) 255-318.
- [142] B.H. Davis, Fischer-Tropsch synthesis: current mechanism and futuristic needs, *Fuel Process. Technol.* 71 (2001) 157-166.
- [143] N.O. Elbashir, C.B. Roberts, Reaction pathway and kinetic modeling of Fischer-Tropsch synthesis over an alumina supported cobalt catalyst in supercritical-hexane, *Abstr. Pap. Am. Chem. Soc.* 227 (2004) U235-U235.
- [144] G. Lozano-Blanco, J.W. Thybaut, K. Surla, P. Galtier, G.B. Marin, Fischer-Tropsch synthesis: development of a microkinetic model for metal catalysis, *Oil Gas Sci. Technol.* 61 (2006) 489-496.
- [145] C.G. Visconti, E. Tronconi, L. Lietti, R. Zennaro, P. Forzatti, Development of a complete kinetic model for the Fischer-Tropsch synthesis over Co/Al₂O₃ catalysts, *Chem. Eng. Sci.* 62 (2007) 5338-5343.
- [146] O.R. Inderwildi, S.J. Jenkins, D.A. King, Fischer-tropsch mechanism revisited: alternative pathways for the production of higher hydrocarbons from synthesis gas, *J. Phys. Chem. C* 112 (2008) 1305-1307.
- [147] B.H. Davis, Fischer-Tropsch synthesis: reaction mechanisms for iron catalysts, *Catal. Today* 141 (2009) 25-33.

- [148] M. Ojeda, R. Nabar, A.U. Nilekar, A. Ishikawa, M. Mavrikakis, E. Iglesia, CO activation pathways and the mechanism of Fischer-Tropsch synthesis, *J. Catal.* 272 (2010) 287-297.
- [149] S.H. Kwack, M.J. Park, J.W. Bae, K.S. Ha, K.W. Jun, Development of a kinetic model of the Fischer-Tropsch synthesis reaction with a cobalt-based catalyst, *React. Kinet. Mech. Catal.* 104 (2011) 483-502.
- [150] C. Visconti, E. Tronconi, L. Lietti, P. Forzatti, S. Rossini, R. Zennaro, Detailed kinetics of the Fischer-Tropsch synthesis on cobalt catalysts based on H-assisted CO activation, *Top. Catal.* 54 (2011) 786-800.
- [151] R.A. van Santen, A.J. Markvoort, I.A.W. Filot, M.M. Ghouri, E.J.M. Hensen, Mechanism and microkinetics of the Fischer-Tropsch reaction, *Phys. Chem. Chem. Phys.* 15 (2013) 17038-17063.
- [152] P. Kaiser, F. Pohlmann, A. Jess, Intrinsic and effective kinetics of cobalt-catalyzed Fischer-Tropsch synthesis in view of a power-to-liquid process based on renewable energy, *Chem. Eng. Technol.* 37 (2014) 964-972.
- [153] B. Todic, W.P. Ma, G. Jacobs, B.H. Davis, D.B. Bukur, CO-insertion mechanism based kinetic model of the Fischer-Tropsch synthesis reaction over Re-promoted Co catalyst, *Catal. Today* 228 (2014) 32-39.
- [154] P. Azadi, G. Brownbridge, I. Kemp, S. Mosbach, J.S. Dennis, M. Kraft, Microkinetic modeling of the Fischer-Tropsch synthesis over cobalt catalysts, *ChemCatChem* 7 (2015) 137-143.
- [155] P.M. Maitlis, A new view of the Fischer-Tropsch polymerisation reaction, *Pure Appl. Chem.* 61 (1989) 1747-1754.
- [156] W.K. Hall, R.J. Kokes, P.H. Emmett, Mechanism studies of the Fischer-Tropsch synthesis. the addition of radioactive methanol, carbon dioxide and gaseous formaldehyde, *J. Am. Chem. Soc.* 79 (1957) 2983-2989.
- [157] L.M. Tau, H.A. Dabbagh, B.H. Davis, Fischer-Tropsch synthesis: comparison of carbon-14 distributions when labeled alcohol is added to the synthesis gas, *Energy Fuels* 5 (1991) 174-179.
- [158] R.A. Dictor, A.T. Bell, Fischer-Tropsch synthesis over reduced and unreduced iron oxide catalysts, *J. Catal.* 97 (1986) 121-136.

- [159] M.E. Dry, Advances in Fischer-Tropsch chemistry, *Ind. Eng. Chem. Prod. Res. Dev.* 15 (1976) 282-286.
- [160] G.A. Huff, C.N. Satterfield, Intrinsic kinetics of the Fischer-Tropsch synthesis on a reduced fused-magnetite catalyst, *Ind. Eng. Chem. Process Des. Dev.* 23 (1984) 696-705.
- [161] F.G. Botes, B.B. Breman, Development and testing of a new macro kinetic expression for the iron-based low-temperature Fischer-Tropsch reaction, *Ind. Eng. Chem. Res.* 45 (2006) 7415-7426.
- [162] F.G. Botes, B. van Dyk, C. McGregor, The development of a macro kinetic model for a commercial Co/Pt/Al₂O₃ Fischer-Tropsch catalyst, *Ind. Eng. Chem. Res.* 48 (2009) 10439-10447.
- [163] E.S. Lox, G.F. Froment, Kinetics of the Fischer-Tropsch reaction on a precipitated promoted iron catalyst .2. kinetic modeling, *Ind. Eng. Chem. Res.* 32 (1993) 71-82.
- [164] Y.N. Wang, W.P. Ma, Y.J. Lu, J. Yang, Y.Y. Xu, H.W. Xiang, Y.W. Li, Y.L. Zhao, B.J. Zhang, Kinetics modelling of Fischer-Tropsch synthesis over an industrial Fe-Cu-K catalyst, *Fuel* 82 (2003) 195-213.
- [165] C.G. Visconti, L. Lietti, E. Tronconi, P. Forzatti, R. Zennaro, S. Rossini, Detailed kinetics of the Fischer-Tropsch synthesis over Co-based catalysts containing sulphur, *Catal. Today* 154 (2010) 202-209.
- [166] H.L. Coonradt, W.E. Garwood, Mechanism of hydrocracking - reactions of paraffins + olefins, *Ind. Eng. Chem. Process Des. Dev.* 3 (1964) 38-45.
- [167] H.F. Schulz, J.H. Weitkamp, Zeolite catalysts. hydrocracking and hydroisomerization of n-dodecane, *Ind. Eng. Chem. Prod. Res. Dev.* 11 (1972) 46-53.
- [168] J. Weitkamp, H. Schulz, Olefinic intermediates in catalytic hydrocracking of paraffins, *J. Catal.* 29 (1973) 361-366.
- [169] J. Weitkamp, P.A. Jacobs, J.A. Martens, Isomerization and hydrocracking of C₉ through C₁₆ n-alkanes on Pt/HZSM-5 zeolite, *Appl. Catal.* 8 (1983) 123-141.
- [170] G.E. Giannetto, G.R. Perot, M.R. Guisnet, Hydroisomerization and hydrocracking of normal-alkanes .1. ideal hydroisomerization pthy catalysts, *Ind. Eng. Chem. Prod. Res. Dev.* 25 (1986) 481-490.

- [171] F. Alvarez, G. Giannetto, M. Guisnet, G. Perot, Hydroisomerization and hydrocracking of n-alkanes .2. n-heptane transformation on a Pt-dealuminated Y-zeolite - comparison with a Pt-Y-zeolite, *Appl. Catal.* 34 (1987) 353-365.
- [172] F. Alvarez, F.R. Ribeiro, G. Perot, C. Thomazeau, M. Guisnet, Hydroisomerization and hydrocracking of alkanes - Influence of the balance between acid and hydrogenating functions on the transformation of n-decane on PtHY catalysts, *J. Catal.* 162 (1996) 179-189.
- [173] R.A. Keogh, R. Srinivasan, B.H. Davis, The effect of Pt concentration on the activity and selectivity of SO_4^{2-} -ZrO₂ catalysts for the hydrocracking and hydroisomerization of n-hexadecane, *Appl. Catal., A* 140 (1996) 47-57.
- [174] K.R. Venkatesh, J. Hu, W. Wang, G.D. Holder, J.W. Tierney, I. Wender, Hydrocracking and hydroisomerization of long-chain alkanes and polyolefins over metal-promoted anion-modified zirconium oxides, *Energy Fuels* 10 (1996) 1163-1170.
- [175] A. Corma, A. Martinez, S. Pergher, S. Peratello, C. Perego, G. Bellusi, Hydrocracking-hydroisomerization of n-decane on amorphous silica-alumina with uniform pore diameter, *Appl. Catal., A* 152 (1997) 107-125.
- [176] B. Debrabandere, G.F. Froment, Influence of the hydrocarbon chain length on the kinetics of the hydroisomerization and hydrocracking of n-paraffins, *Stud. Surf. Sci. Catal.* 106 (1997) 379-389.
- [177] J.F. Denayer, G.V. Baron, G. Vanbutsele, P.A. Jacobs, J.A. Martens, Evidence for alkylcarbenium ion reaction intermediates from intrinsic reaction kinetics of C₆-C₉ n-alkane hydroisomerization and hydrocracking on Pt/H-Y and Pt/USY zeolites, *J. Catal.* 190 (2000) 469-473.
- [178] P.N. Kuznetsov, Study of n-octane hydrocracking and hydroisomerization over Pt/HY zeolites using the reactors of different configurations, *J. Catal.* 218 (2003) 12-23.
- [179] V. Calemma, S. Peratello, F. Stroppa, R. Giardino, C. Perego, Hydrocracking and hydroisomerization of long-chain n-paraffins. reactivity and reaction pathway for base oil formation, *Ind. Eng. Chem. Res.* 43 (2004) 934-940.
- [180] Y. Rezgui, M. Guemini, Effect of acidity and metal content on the activity and product selectivity for n-decane hydroisomerization and hydrocracking over nickel-tungsten supported on silica-alumina catalysts, *Appl. Catal., A* 282 (2005) 45-53.

- [181] D. Leckel, Low-pressure hydrocracking of coal-derived Fischer-Tropsch waxes to diesel, *Energy Fuels* 21 (2007) 1425-1431.
- [182] D. Leckel, Noble metal wax hydrocracking catalysts supported on high-siliceous alumina, *Ind. Eng. Chem. Res.* 46 (2007) 3505-3512.
- [183] M. Olschar, M. Endisch, T. Dimmig, T. Kuchling, Investigation of catalytic hydrocracking of Fischer-Tropsch wax for the production of transportation fuels, *Oil Gas Eur. Mag.* 33 (2007) 187-193.
- [184] H. Ling, Q. Wang, B.X. Shen, Hydroisomerization and hydrocracking of hydrocracker bottom for producing lube base oil, *Fuel Process. Technol.* 90 (2009) 531-535.
- [185] I. Rossetti, C. Gambaro, V. Calemma, Hydrocracking of long chain linear paraffins, *Chem. Eng. J.* 154 (2009) 295-301.
- [186] V. Calemma, C. Gambaro, Hydrocracking of Fischer-Tropsch wax: effect of feed composition, *Abstr. Pap. Am. Chem. Soc.* 240 (2010).
- [187] J. Lee, S. Hwang, J.G. Seo, U.G. Hong, J.C. Jung, I.K. Song, Pd catalyst supported on SiO₂-Al₂O₃ xerogel for hydrocracking of paraffin wax to middle distillate, *J. Ind. Eng. Chem.* 17 (2011) 310-315.
- [188] F. Regali, M. Boutonnet, S. Jaras, Hydrocracking of Fischer-Tropsch waxes over Pt/Pd catalysts supported on amorphous silica-alumina, *Abstr. Pap. Am. Chem. Soc.* 242 (2011).
- [189] J. Kang, W.P. Ma, R.A. Keogh, W.D. Shafer, G. Jacobs, B.H. Davis, Hydrocracking and hydroisomerization of n-hexadecane, n-octacosane and Fischer-Tropsch wax over a Pt/SiO₂-Al₂O₃ catalyst, *Catal. Lett.* 142 (2012) 1295-1305.
- [190] J.A. Martens, D. Verboekend, K. Thomas, G. Vanbutsele, J. Perez-Ramirez, J.P. Gilson, Hydroisomerization and hydrocracking of linear and multibranched long model alkanes on hierarchical Pt/ZSM-22 zeolite, *Catal. Today* 218 (2013) 135-142.
- [191] M. Steijns, G.F. Froment, Hydroisomerization and hydrocracking .3. kinetic-analysis of rate data for normal-decane and normal-dodecane, *Ind. Eng. Chem. Prod. Res. Dev.* 20 (1981) 660-668.
- [192] M.A. Baltanas, H. Vansina, G.F. Froment, Hydroisomerization and hydrocracking .5. kinetic-analysis of rate data for n-octane, *Ind. Eng. Chem. Prod. Res. Dev.* 22 (1983) 531-539.

- [193] J.W. Thybaut, C.S. Laxmi Narasimhan, J.F. Denayer, G.V. Baron, P.A. Jacobs, J.A. Martens, G.B. Marin, Acid-metal balance of a hydrocracking catalyst: ideal versus nonideal behavior, *Ind. Eng. Chem. Res.* 44 (2005) 5159-5169.
- [194] J.W. Thybaut, C.S.L. Narasimhan, G.B. Marin, Bridging the gap between liquid and vapor phase hydrocracking, *Catal. Today* 111 (2006) 94-102.
- [195] L. Pellegrini, S. Locatelli, S. Rasella, S. Bonomi, V. Calemma, Modeling of Fischer-Tropsch products hydrocracking, *Chem. Eng. Sci.* 59 (2004) 4781-4787.
- [196] L. Pellegrini, S. Bonomi, S. Gamba, V. Calemma, D. Molinari, The "all components hydrocracking model", *Chem. Eng. Sci.* 62 (2007) 5013-5020.
- [197] L.A. Pellegrini, S. Gamba, S. Bonomi, V. Calemma, Equilibrium constants for isomerization of n-paraffins, *Ind. Eng. Chem. Res.* 46 (2007) 5446-5452.
- [198] L.A. Pellegrini, S. Gamba, V. Calemma, S. Bonomi, Modelling of hydrocracking with vapour-liquid equilibrium, *Chem. Eng. Sci.* 63 (2008) 4285-4291.
- [199] S. Gamba, L.A. Pellegrini, V. Calemma, C. Gambaro, Introduction of a breakage probability function in the hydrocracking reactor model, *Ind. Eng. Chem. Res.* 48 (2009) 5656-5665.
- [200] C. Gambaro, V. Calemma, D. Molinari, J. Denayer, Hydrocracking of Fischer-Tropsch waxes: kinetic modeling via LHHW approach, *AIChE J.* 57 (2011) 711-723.
- [201] H. Kumar, G.F. Froment, A generalized mechanistic kinetic model for the hydroisomerization and hydrocracking of long-chain paraffins, *Ind. Eng. Chem. Res.* 46 (2007) 4075-4090.
- [202] B. Browning, R. Henry, P. Afanasiev, G. Lapisardi, G. Pirngruber, M. Tayakout-Fayolle, Vapor-liquid equilibrium of hydrogen, vacuum gas oil, and middle distillate fractions, *Ind. Eng. Chem. Res.* 53 (2014) 8311-8320.
- [203] L. Caldwell, D.S. Van Vuuren, On the formation and composition of the liquid phase in Fischer-Tropsch reactors, *Chem. Eng. Sci.* 41 (1986) 89-96.
- [204] J.J. Marano, G.D. Holder, Characterization of Fischer-Tropsch liquids for vapor-liquid equilibria calculations, *Fluid Phase Equilib.* 138 (1997) 1-21.
- [205] Y.N. Wang, Y.Y. Xu, H.W. Xiang, Y.W. Li, B.J. Zhang, Modeling of catalyst pellets for Fischer-Tropsch synthesis, *Ind. Eng. Chem. Res.* 40 (2001) 4324-4335.

- [206] X.D. Zhan, B.H. Davis, Assessment of internal diffusion limitation on Fischer-Tropsch product distribution, *Appl. Catal., A* 236 (2002) 149-161.
- [207] I.V. Derevich, V.S. Ermolaev, V.Z. Mordkovich, Liquid-vapor thermodynamic equilibrium in Fischer-Tropsch synthesis products, *Theor. Found. Chem. Eng.* 42 (2008) 216-219.
- [208] K. Moller, P. le Grange, C. Accolla, A two-phase reactor model for the hydrocracking of Fischer-Tropsch-derived wax, *Ind. Eng. Chem. Res.* 48 (2009) 3791-3801.
- [209] C.M. Masuku, W.P. Ma, D. Hildebrandt, D. Glasser, B.H. Davis, A vapor-liquid equilibrium thermodynamic model for a Fischer-Tropsch reactor, *Fluid Phase Equilib.* 314 (2012) 38-45.
- [210] Z. Karimi, M. Rahmani, M. Moqadam, A study on vapour-liquid equilibria in Fischer-Tropsch synthesis, *Procedia Eng.* 42 (2012) 25-33.
- [211] C.G. Visconti, M. Mascellaro, Calculating the product yields and the vapor-liquid equilibrium in the low-temperature Fischer-Tropsch synthesis, *Catal. Today* 214 (2013) 61-73.
- [212] C.G. Visconti, Vapor-liquid equilibria in the low-temperature Fischer-Tropsch synthesis, *Ind. Eng. Chem. Res.* 53 (2014) 1727-1734.
- [213] S. Srinivas, R.K. Malik, S.M. Mahajani, Feasibility of reactive distillation for Fischer-Tropsch synthesis, *Ind. Eng. Chem. Res.* 47 (2008) 889-899.
- [214] J.J. Birtill, Measurement and modeling of the kinetics of catalyst decay in fixed beds: the eurokin survey, *Ind. Eng. Chem. Res.* 46 (2007) 2392-2398.
- [215] H.H. Rachford, J.D. Rice, Procedure for use of electronic digital computers in calculating flash vaporization hydrocarbon equilibrium, *Trans. Am. Inst. Min., Metall. Pet. Eng.* 195 (1952) 327-328.
- [216] D.S. van Vuuren, J.R. Hunter, M.D. Heydenrych, The solubility of various gases in Fischer-Tropsch reactor wax, *Chem. Eng. Sci.* 43 (1988) 1291-1296.
- [217] M. Ramos-Estrada, G.A. Iglesias-Silva, K.R. Hall, Experimental measurements and prediction of liquid densities for n-alkane mixtures, *J. Chem. Thermodyn.* 38 (2006) 337-347.
- [218] E.N. Fuller, K. Ensley, J.C. Giddings, Diffusion of halogenated hydrocarbons in helium. the effect of structure on collision cross sections, *J. Phys. Chem.* 73 (1969) 3679-3685.
- [219] VDI Heat Atlas, 2 ed., Springer-Verlag Berlin Heidelberg 2010.

- [220] A. Blanc, Recherches sur les mobilités des ions dans les gaz, *J. Phys. Theor. Appl.* 7 (1908) 825-839.
- [221] B. Poling, J. Prausnitz, J.O. Connell, *The properties of gases and liquids*, McGraw-Hill Education 2000.
- [222] C.R. Wilke, P. Chang, Correlation of diffusion coefficients in dilute solutions, *AIChE J.* 1 (1955) 264-270.
- [223] J.R. Partington, *An advanced treatise on physical chemistry: fundamental principles. the properties of gases*, Longmans, Green 1949.
- [224] F. Pöhlmann, C. Kern, S. Rossler, A. Jess, Accumulation of liquid hydrocarbons in catalyst pores during cobalt-catalyzed Fischer-Tropsch synthesis, *Catal. Sci. Technol.* 6 (2016) 6593-6604.
- [225] J. Yang, V. Froseth, D. Chen, A. Holmen, Particle size effect for cobalt Fischer-Tropsch catalysts based on in situ CO chemisorption, *Surf. Sci.* 648 (2016) 67-73.
- [226] G. Prieto, A. Martinez, P. Concepcion, R. Moreno-Tost, Cobalt particle size effects in Fischer-Tropsch synthesis: structural and in situ spectroscopic characterisation on reverse micelle-synthesised Co/ITQ-2 model catalysts, *J. Catal.* 266 (2009) 129-144.
- [227] G.L. Bezemer, J.H. Bitter, H.P.C.E. Kuipers, H. Oosterbeek, J.E. Holewijn, X.D. Xu, F. Kapteijn, A.J. van Dillen, K.P. de Jong, Cobalt particle size effects in the Fischer-Tropsch reaction studied with carbon nanofiber supported catalysts, *J. Am. Chem. Soc.* 128 (2006) 3956-3964.
- [228] H. Schulz, K. Beck, E. Erich, Kinetics of Fischer-Tropsch selectivity, *Fuel Process. Technol.* 18 (1988) 293-304.
- [229] E. Iglesia, S.C. Reyes, R.J. Madon, Transport-enhanced α -olefin readsorption pathways in Ru-catalyzed hydrocarbon synthesis, *J. Catal.* 129 (1991) 238-256.
- [230] E. Iglesia, S.C. Reyes, R.J. Madon, S.L. Soled, Selectivity control and catalyst design in the Fischer-Tropsch synthesis: sites, pellets, and reactors, *Adv. Catal.* 39 (1993) 221-302.
- [231] E.W. Kuipers, I.H. Vinkenburg, H. Oosterbeek, Chain length dependence of α -olefin readsorption in Fischer-Tropsch synthesis, *J. Catal.* 152 (1995) 137-146.
- [232] F.G. Botes, Influences of water and syngas partial pressure on the kinetics of a commercial alumina-supported cobalt Fischer-Tropsch catalyst, *Ind. Eng. Chem. Res.* 48 (2009) 1859-1865.

- [233] O. Borg, Z.X. Yu, D. Chen, E.A. Blekkan, E. Rytter, A. Holmen, The effect of water on the activity and selectivity for carbon nanofiber supported cobalt Fischer-Tropsch catalysts, *Top. Catal.* 57 (2014) 491-499.
- [234] W.P. Ma, G. Jacobs, D.E. Sparks, R.L. Spicer, B.H. Davis, J.L.S. Klettlinger, C.H. Yen, Fischer-Tropsch synthesis: kinetics and water effect study over 25%Co/Al₂O₃ catalysts, *Catal. Today* 228 (2014) 158-166.
- [235] J. Yang, W.P. Ma, D. Chen, A. Holmen, B.H. Davis, Fischer-Tropsch synthesis: A review of the effect of CO conversion on methane selectivity, *Appl. Catal., A* 470 (2014) 250-260.
- [236] N. Fischer, B. Clapham, T. Feltes, M. Claeys, Cobalt-based Fischer-Tropsch activity and selectivity as a function of crystallite size and water partial pressure, *ACS Catal.* 5 (2015) 113-121.
- [237] R. Brosius, J.C.Q. Fletcher, Hydrocracking under Fischer-Tropsch conditions; the effect of CO on the mass transfer resistance by metal clusters, *J. Catal.* 317 (2014) 318-325.
- [238] R. Brosius, P.J. Kooyman, J.C.Q. Fletcher, Selective formation of linear alkanes from n-hexadecane primary hydrocracking in shape-selective MFI zeolites by competitive adsorption of water, *ACS Catal.* 6 (2016) 7710-7715.
- [239] D.E. Mears, Diagnostic criteria for heat transport limitations in fixed bed reactors, *J. Catal.* 20 (1971) 127-&.
- [240] V.M. Kurganov, A.B. Gorshtein, G.Y. Starodubskaya, Calculation of heats of reaction in hydrocracking, *Chem. Technol. Fuels Oils* 16 (1980) 612-616.
- [241] M.I. Hosukoglu, M. Karakaya, A.K. Avci, Modeling and simulation of hydrocracking of Fischer-Tropsch hydrocarbons in a catalytic microchannel reactor, *Ind. Eng. Chem. Res.* 51 (2012) 8913-8921.
- [242] B. Li, V. Calemme, C. Gambaro, G.V. Baron, J.F.M. Denayer, Competitive adsorption of C₂₀-C₃₆ linear paraffins on the amorphous microporous silica-alumina ERS-8 in vapor phase and liquid phase, *Ind. Eng. Chem. Res.* 49 (2010) 7541-7549.
- [243] N. Kruse, A.G. Machoke, W. Schwieger, R. Guettel, Nanostructured encapsulated catalysts for combination of Fischer-Tropsch synthesis and hydroprocessing, *ChemCatChem* 7 (2015) 1018-1022.

- [244] R. Dürschnabel, Konstruktion und Wärmeberechnung eines 2-Zonen FT-Reaktors, Hochschule RheinMain, Wiesbaden, 2014.

Appendix

A1 Optimization of screen-printing pastes

Considering the cost and availability of the catalysts, the catalyst supports, i.e. Al₂O₃ and H-ZSM-5, were used for the paste optimization. For a screen-printable paste, the viscosity at 100 s⁻¹ shear rate is preferred to be 10-20 Pa·s to obtain a good penetration through the screen [134]. The weight loss after the drop test was controlled within 5% to obtain a good mechanical stability.

A1.1 Optimization of Al₂O₃ paste

Different concentrations of Al₂O₃ and cellulose were adjusted as listed in Table A1.

Table A1 Viscosity and mechanical stability performance of different Al₂O₃ pastes

Al ₂ O ₃ [vol.%]	cellulose [vol.%]	¹ viscosity (0.1 s ⁻¹) [Pa·s]	viscosity (100 s ⁻¹) [Pa·s]	<i>m</i> _{coating/foil} [g]	weight loss [wt.%]
3	3	13.32	3.25	0.0187	0.20
3	4	66.10	6.95	0.0185	1.03
4	3	212.70	4.07	0.0248	1.96
4	4	2.68e5	8.24	0.0244	2.45
5		30.99	0.22	0.0335	>10
5	1	81.40	0.76	0.0326	>10
5	2	500.12	2.13	0.0308	>10
5	3	2.43e3	5.01	0.0300	>10
7.5		63.22	1.06	0.0442	>10
7.5	1	7.17e3	1.98	0.0440	>10
10		158.73	2.53	0.0549	>10

¹ deviation would exist since the rheometer cannot stabilize at 0.1 s⁻¹ for some pastes

With the increase of Al₂O₃ content (5, 7.5, 10 vol.%), the paste viscosity at 100 s⁻¹ shear rate increases to 2.53 Pa·s. Besides, a high weight loss of the coating layer was observed. To increase the viscosity and decrease the weight loss, cellulose was added and Al₂O₃ amount was reduced at the same time. A viscosity of 5.01 Pa·s at 100 s⁻¹ shear rate was obtained for the paste containing 5 vol.% Al₂O₃ and 3 vol.% cellulose. A linear relation was observed between the coating mass and the Al₂O₃ concentration. By reducing Al₂O₃ amount to 3 and 4 vol.% an acceptable weigh loss was obtained (< 5%). With 4 vol.% Al₂O₃ and 4 vol.%

cellulose, a viscosity of 8.24 Pa·s at 100 s⁻¹ shear rate was observed, which is close to the required range. Based on the optimization above, the FTS catalyst paste was determined to be 4 vol.% Al₂O₃ support (4.65 vol.% FTS catalyst) and 4 vol.% cellulose in terpineol.

A1.2 Optimization of H-ZSM-5 paste

Different concentrations of H-ZSM-5 and cellulose were adjusted as listed in Table A2.

Table A2 Viscosity and mechanical stability performance of different H-ZSM-5 pastes

H-ZSM-5 [vol.%]	cellulose [vol.%]	¹ viscosity (0.1 s ⁻¹) [Pa·s]	viscosity (100 s ⁻¹) [Pa·s]	<i>m</i> _{coating/foil} [g]	weight loss [wt.%]
5	4	12.51	6.38	0.0099	0.88
7	4	15.32	7.28	0.0129	2.01
7	5	33.24	12.04		
7	6	62.31	17.13	0.0124	1.73
7	7	141.84	² n.a.		
10	4	20.79	9.02	0.0185	3.24
15	4	32.35	12.44	0.0277	>10
20	4	60.38	17.27	0.0365	>10

¹ deviation would exist since the rheometer cannot stabilize at 0.1 s⁻¹ for some pastes;

² not able to be measured by the rheometer

Optimization of the HC catalyst paste started with 4 vol.% cellulose. The amount of H-ZSM-5 was varied from 5 to 20 vol.%, which leads to an increased viscosity at 100 s⁻¹ shear rate from 6.38 to 17.27 Pa·s. The pastes containing 10, 15 and 20 vol.% H-ZSM-5 could meet the viscosity requirement. But, a high weight loss was observed. 7 vol.% H-ZSM-5 was determined for the HC catalyst paste. To meet the rheological requirements, the content of cellulose was increased. With 5 and 6 vol.% cellulose the paste viscosity at 100 s⁻¹ shear rate increased to 12.04 and 17.13 Pa·s, respectively. Considering the viscosity at 0.1 s⁻¹ shear rate is too low for the paste containing 5 vol.% cellulose, the HC catalyst paste was determined to have 6 vol.% cellulose.

A2 Gas chromatography

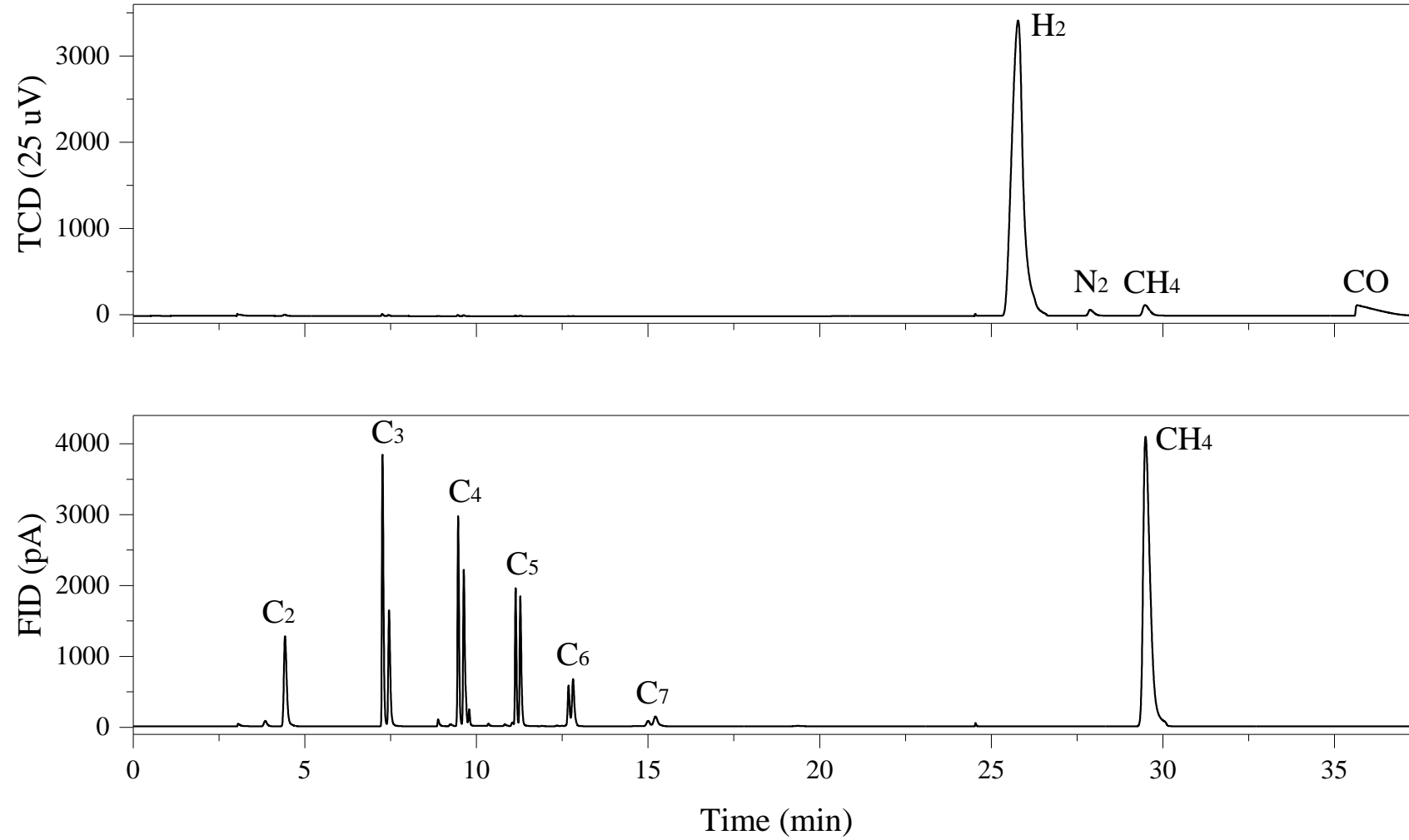


Figure A1 Example gas chromatogram for residual gas (online-GC)

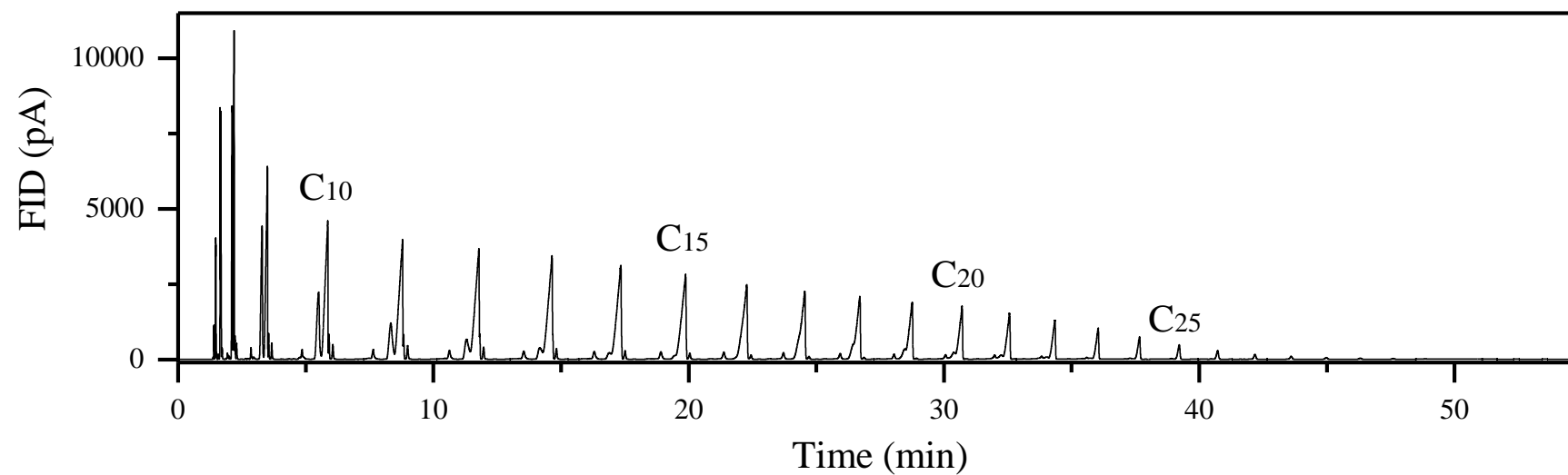


Figure A2 Example gas chromatogram for oil (offline-GC)

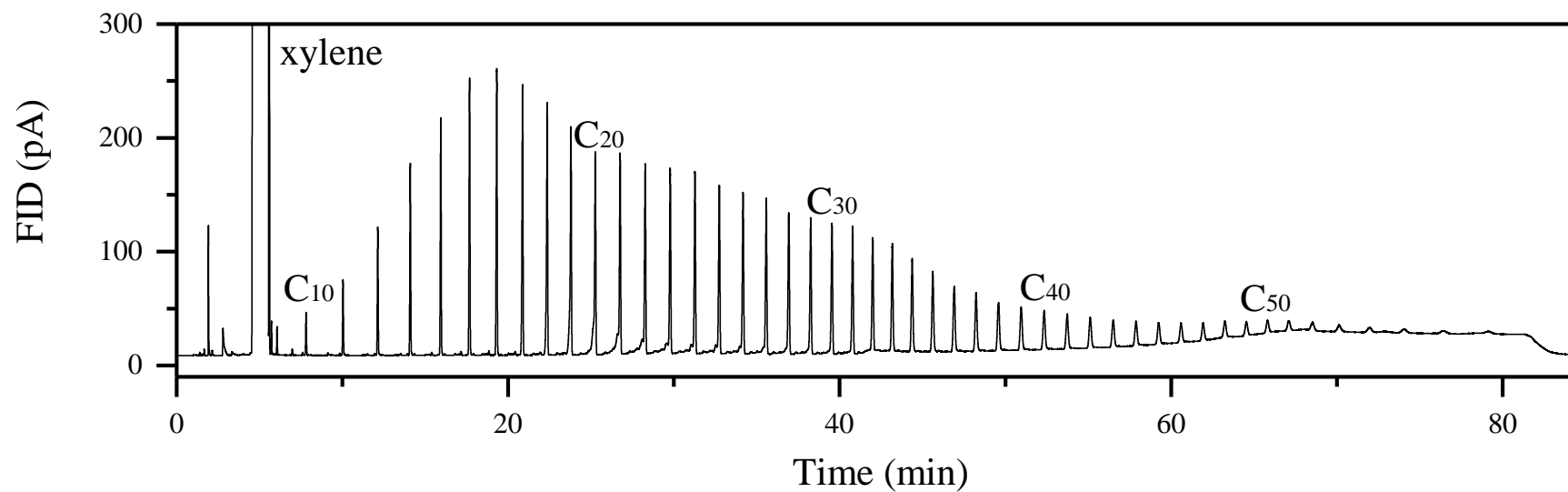


Figure A3 Example gas chromatogram for wax (offline-GC)

A3 Blank test of syngas activity of Pt-ZSM-5

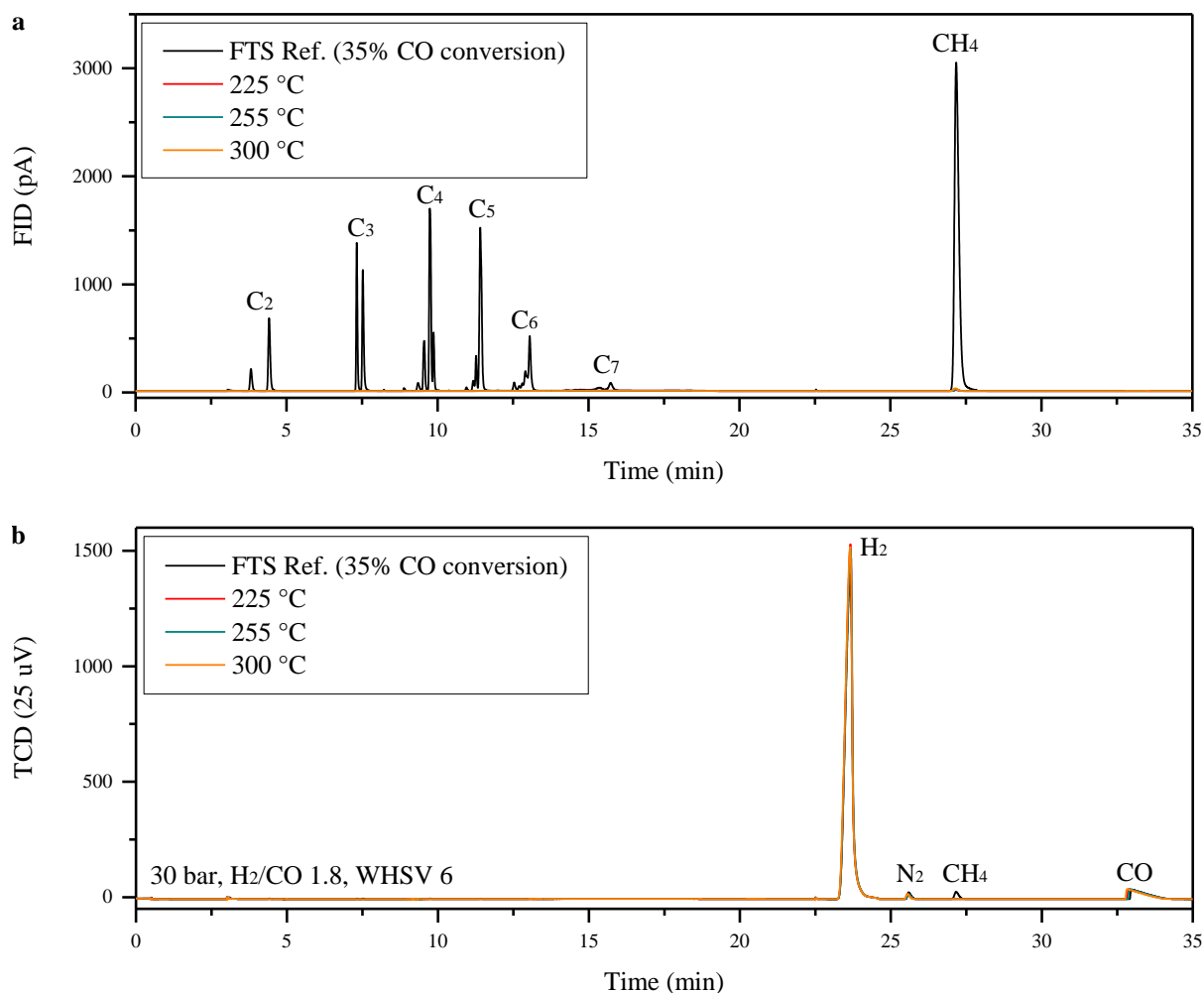


Figure A4 Gas chromatogram for residual gas (a. FID; b. TCD)

Syngas activity for the Pt-ZSM-5 catalyst at typical FTS conditions were tested. Gas chromatogram is shown in Figure A4. From 225 to 300 °C, no hydrocarbon signal was observed on FID. TCD signal of H₂ and CO for each case basically fall on the same curves. Pt-ZSM-5 was proven to be syngas-inert.

A4 Experimental conditions

Operating conditions for experiments discussed in this dissertation are summarized as follows:

Table A3 Reaction conditions for FTS tests with powder catalysts

test	$m_{\text{cat.}}$ [g]	T [°C]	P [bar]	H ₂ /CO ratio	¹ WHSV
FTS-original	1	215	30	1.8	12 / 6
		225	30	1.8	12 / 6
		235	30	1.8	12 / 6

Appendix

		245	30	1.8	12 / 6
FTS-Ref. I	1	225	30	1.8	12 / 9 / 6
		235	30	1.8	12 / 9 / 6
		245	30	1.8	12 / 9 / 6
		255	30	1.8	12 / 9 / 6
FTS-Ref. II	1	225	30	1.8	12 / 9 / 6
		235	30	1.8	12 / 6
		245	30	1.8	12 / 6 / 4
			30	1.6 / 2.0	6
			25 / 20	1.8	6
		255	30	1.8	6

¹ syngas weight hourly space velocity related to the FTS catalyst

Table A4 Reaction conditions for two-stage sequential integration with powder catalysts

$m_{\text{cat.}}$ [g]	T_{FTS} [°C]	T_{HC} [°C]	P [bar]	H ₂ /CO ratio	WHSV
FTS: 1 g	235		30	1.8	9 / 6
	241		30	1.8	12 / 9 / 6
	241		25 / 20	1.8	9
			30	1.6 / 2.0	9
	246		20	1.8	9
	249		30	1.8	12 / 9
HC: 1 g	235	243	30	1.8	9
		249	30	1.8	9 / 6
	241	249	30	1.8	12 / 9
		249	30	1.6 / 2.0	9
		260 / 280	30	1.8	9
	246	249	20	1.8	9
	249	249	30	1.8	12 / 9
	260	30	1.8	9	

Table A5 Reaction conditions for one-stage integration with powder catalysts

test	$m_{\text{cat.}}$ [g]	T [°C]	P [bar]	H ₂ /CO ratio	WHSV
sequential	FTS: 1 g	225	30	1.8	12 / 9 / 6

Appendix

	HC: 1 g	235	30	1.8	12 / 9 / 6
		241	30	1.8	12 / 9 / 6
		245	30	1.8	12 / 9 / 6
			30	1.6 / 2.0	6
			25 / 20	1.8	6
		249	30	1.8	12 / 9
		255	30	1.8	6
hybrid	FTS: 1 g	215	30	1.8	12 / 6
	HC: 1 g	225	30	1.8	12 / 6
		235	30	1.8	12 / 6
			30	1.6 / 2.0	6
			25 / 20	1.8	6
		245	30	1.8	12 / 6
			30	1.6 / 2.0	6
			25 / 20	1.8	6
		255	30	1.8	12 / 6
		270	30	1.8	12

Table A6 Reaction conditions for FTS tests with wall-coated catalysts

$m_{\text{cat.}}$ [g]	Thickness [μm]	T [$^{\circ}\text{C}$]	P [bar]	H ₂ /CO ratio	WHSV
1	20	225	30	1.8	12 / 6
		235	30	1.8	12 / 6
		245	30	1.8	12 / 9 / 6
		260	30	1.8	12 / 6
		280	30	1.8	12
1	40	225	30	1.8	12 / 6
		235	30	1.8	12 / 6
		245	30	1.8	12 / 6
		260	30	1.8	12 / 6
		225	20	1.8	6
		235	20	1.8	6
		245	20	1.8	6
		260	20	1.8	6

Table A7 Reaction conditions for integration with wall-coated catalysts in MCR-I

test	$m_{\text{cat.}}$ [g]	thickness [μm]	T [$^{\circ}\text{C}$]	P [bar]	H ₂ /CO ratio	WHSV
sequential	FTS: 1 g	40	225	30 / 20	1.8	6
			235	30 / 20	1.8	6
	HC: 1 g	50	245	30	1.8	12
			245	30 / 20	1.8	6
			260	30 / 20	1.8	6
face-to-face	FTS: 1 g	40	225	30 / 20	1.8	6
			235	30 / 20	1.8	6
	HC: 1 g	50	245	30 / 20	1.8	6
			245	30 / 20	1.8	6
			260	30 / 20	1.8	6
dual-layer	FTS: 1 g	20	225	30 / 20	1.8	6
			235	30 / 20	1.8	6
	HC: 0.58 g	20	245	30	1.8	12
			245	30 / 20	1.8	6
			260	30 / 20	1.8	6
hybrid	FTS: 1 g	50	225	30 / 20	1.8	6
			235	30 / 20	1.8	6
	HC: 1 g	50	245	30	1.8	12
			245	30 / 20	1.8	6
			260	30 / 20	1.8	6

Table A8 Reaction conditions for integration with wall-coated catalyst and independent temperature control of the FTS and HC

test	$m_{\text{cat.}}$ [g]	thickness [μm]	T _{FTS} [$^{\circ}\text{C}$]	T _{HC} [$^{\circ}\text{C}$]	WHSV
sequential	FTS: 1 g	40	245	235 / 245 / 260	6
MCR-I	HC: 1 g	50	235	245	6
			260	245	6
face-to-face	FTS: 1 g	20	245	245 / 260 / 270 /	12

Appendix

				280	
MCR-II	HC: 1 g	37	225	225	6
			235	235	6
			245	245	6

30 bar, H₂/CO 1.8

Curriculum Vitae

Chenghao Sun

Date of birth: 06.04.1988
Place of birth: Shandong, PR China

Education

09.2013 – 12.2017 Doctoral research
Chemical Engineering
Institute for Micro Process Engineering (IMVT)
Karlsruhe Institute of Technology (KIT)

09.2010 – 07.2013 Master study
Chemical Engineering and Technology
China University of Petroleum, China

09.2006 – 07.2010 Bachelor study
Applied Chemistry
China University of Petroleum, China

09.2003 – 07.2006 High school study
Beizhen High School, China